

The effect of ocean–atmosphere coupling on the Madden–Julian Oscillation in UK Met Office forecast models

A thesis submitted to the School of Environmental Science
of the University of East Anglia in partial fulfilment
of the requirements for the degree of Doctor of Philosophy

Eliza Karlowska

October 2024

© This copy of the thesis has been supplied on condition that anyone who consults it is understood to recognise that its copyright rests with the author and that use of any information derived there-from must be in accordance with current UK Copyright Law. In addition, any quotation or extract must include full attribution.

© Copyright 2024
Eliza Karłowska

Abstract

The Madden–Julian Oscillation (MJO) is the main mode of intraseasonal weather variability in the tropics. The air–sea interactions during the MJO can modulate the intraseasonal sea surface temperature (SST) anomalies, and influence the MJO through surface flux exchange. Such feedbacks are absent in atmosphere-only Numerical Weather Prediction (NWP) models, potentially leading to a degraded model performance in predicting the MJO. Coupled ocean–atmosphere models can help to understand how these feedbacks affect the MJO, and the MJO prediction skill.

Here, global coupled and atmosphere-only NWP systems of the UK Met Office are assessed to reveal skilful predictions of the MJO in both models at least out to 15 lead days. The coupled model predicts erroneously fast MJO propagation compared with the atmosphere-only model. Numerical experiments reveal that half of the MJO phase speed increase between the models is due to diurnal warm layers (DWLs), unaccounted for in the atmosphere-only model. Enhanced (suppressed) MJO convection weakens (strengthens) DWLs in the coupled model. DWLs rectify intraseasonal SST anomalies such that stronger diurnal warming leads to stronger intraseasonal SST anomalies. The peak response in the MJO convection to these SST anomalies in this coupled model occurs within the next seven days. Such feedback is realistic and consistent with observations, however, the added complexity slightly degrades the model performance in predicting the MJO.

A further analysis of the coupled model shows that ocean advection and net surface heat fluxes are equally important in modulating the intraseasonal mixed layer temperature (MLT) anomalies during the MJO. The net surface heat flux drives the large-scale MLT anomalies in this coupled model, while ocean advection dominates at horizontal scales smaller than 10° . Overall, this work demonstrates the importance of ocean–atmosphere feedbacks during the MJO.

Access Condition and Agreement

Each deposit in UEA Digital Repository is protected by copyright and other intellectual property rights, and duplication or sale of all or part of any of the Data Collections is not permitted, except that material may be duplicated by you for your research use or for educational purposes in electronic or print form. You must obtain permission from the copyright holder, usually the author, for any other use. Exceptions only apply where a deposit may be explicitly provided under a stated licence, such as a Creative Commons licence or Open Government licence.

Electronic or print copies may not be offered, whether for sale or otherwise to anyone, unless explicitly stated under a Creative Commons or Open Government license. Unauthorised reproduction, editing or reformatting for resale purposes is explicitly prohibited (except where approved by the copyright holder themselves) and UEA reserves the right to take immediate 'take down' action on behalf of the copyright and/or rights holder if this Access condition of the UEA Digital Repository is breached. Any material in this database has been supplied on the understanding that it is copyright material and that no quotation from the material may be published without proper acknowledgement.

Acronyms

CCKW	Convectively-Coupled Kelvin Wave
CMIP	Coupled Model Intercomparison Project
EOF	Empirical Orthogonal Functions
ENSO	El Niño-Southern Oscillation
ERA5	ECMWF Reanalysis v5
GA	Global Atmosphere
GC	Global Coupled
GCM	General Circulation Model
GL	Global Land
GO	Global Ocean
GSI	Global Sea Ice
HadGEM	Met Office Hadley Centre Global Environment Model
ITCZ	Intertropical Convergence Zone
IO	Indian Ocean
LST	Local Solar Time
MC	Maritime Continent
MJO	Madden-Julian Oscillation
MLT	Mixed Layer Temperature
NAO	North Atlantic Oscillation
NEMO	Nucleus for European Modelling of the Ocean
NOAA	National Oceanographic and Atmospheric Administration
OLR	Outgoing Longwave Radiation
OSTIA	Operational Sea Surface Temperature and Ice Analysis
RMM	Real-time Multivariate MJO index
SST	Sea Surface Temperature
S2S	Subseasonal-to-Seasonal
UK	United Kingdom
UM	Unified Model

List of incorporated works

Some of the work presented in this thesis has been published, or submitted to academic journals:

- Chapter 2 is based on Karłowska *et al.* (2024a) – “The effect of diurnal warming of sea-surface temperatures on the propagation speed of the Madden–Julian Oscillation”
- Chapter 3 is based on Karłowska *et al.* (2024c) – “Two-way feedback between the Madden–Julian Oscillation and diurnal warm layers in a coupled ocean–atmosphere model”
- Chapter 4 is based on Karłowska *et al.* (2024b), an article in review by the Journal of Geophysical Research: Oceans at the time of the submission of this thesis – “The relative importance of ocean advection and surface heat fluxes during the Madden–Julian Oscillation in a coupled ocean–atmosphere model”

Software

Data analysis and plotting used the following Python packages:

- **Matplotlib** – a 2D graphics environment (Hunter, 2007)
- **Cartopy** – a cartographic python library with a matplotlib interface (Met Office, 2016)
- **Iris** – a Python package for Earth science data (Met Office, 2020)
- **pandas** – a Python data analysis library (McKinney, 2010)
- **cmocean** – beautiful colourmaps for oceanography (Thyng *et al.*, 2016)
- **xarray** – a Python package for labelled multidimensional arrays (Hoyer & Hamman, 2017)
- **gsw** – the Gibbs SeaWater (GSW) Oceanographic Toolbox of TEOS-10 (McDougall & Barker, 2011)

The data used in this thesis were generated on the High Performance Computing Cluster at the UK Met Office in Exeter, Devon.

The data analysis was carried out on JASMIN, the UK's collaborative data analysis environment (www.jasmin.ac.uk).

The data was backed up on the High Performance Computing Cluster supported by the Research and Specialist Computing Support service at the University of East Anglia.

Data availability

All data generated for this thesis are stored on the Managed Archive Storage System at the Met Office.

The following reanalyses and observational datasets were used alongside the model data:

- **CERES SYN1deg dataset** – Rutan *et al.* (2015)
- **ERA5 reanalysis** – Hersbach *et al.* (2020)
- **NOAA OLR interpolated dataset** – Liebmann & Smith (1996)
- **Observed Wheeler–Hendon RMM indices** – Wheeler & Hendon (2004), retrieved from <http://www.bom.gov.au/climate/mjo>
- **OSTIA analysis** – Donlon *et al.* (2012), Fiedler *et al.* (2019), Good *et al.* (2020)

Structure of this thesis

This thesis starts with a general introduction in Chapter 1 that provides an overview of the subject and the literature to date. The motivation for this thesis and the research questions that this thesis endeavours to address are discussed at the end of Chapter 1.

Chapters 2 to 4 present the main results of this thesis as self-contained papers with their own introduction, methodology, results, discussion and conclusion sections. There may be a repetition of the material between each chapter in the introduction and the methodology sections.

In Chapter 5, a synthesis of the results is presented, and future work is discussed in light of the results of this thesis.

Each chapter has acronyms defined within, however, a full acronym glossary is available on page VII.

Acknowledgements

First of all, I would like to thank my supervisory team for an amazing journey throughout these past four years. It is thanks to Adrian, Ben, Tim and Prince that I discovered my love for a discipline I never studied before. Thank you for believing in me and choosing me to do this PhD project four years ago with no prior experience in atmospheric sciences. Your guidance in the past four years shaped the academic person I am today and I will be forever grateful for that.

Secondly, I would like to thank my closest friends who helped me through the personal hardships I encountered during my PhD. Thank you to Ala and Ania for countless video calls between the UK and Poland that kept me sane. Thank you to the tropical squad (Becky, Beth, Dan, Jack and Meg) for becoming my chosen family in the UK, and showing mutual and unconditional support and love in the last four years in Norwich. Shout out to the Good Soup members who adopted me into their group and provided a great escape during the famous lunch breaks at UEA. Thank you to Mollie for supportive coffee breaks and multiple crying sessions on her office floor. Thank you to my online friends that always gave me space to talk (the London and the American folks). Finally, thank you to the volleyball and ballroom communities that kept me active and entertained outside of my PhD in these past four years.

This thesis is dedicated to all the girls in STEM.

Contents

Abstract	v
Acronyms	vii
List of incorporated works	ix
Software	xi
Data availability	xiii
Structure of this thesis	xv
Acknowledgements	xvii
List of figures	xxv
List of tables	xxxvii
1 Introduction	1
1.1 The Madden–Julian Oscillation	1
1.2 The definition of the MJO in data	5
1.3 The MJO in weather and climate models	10
1.4 Ocean–atmosphere interactions during the MJO	14
1.5 Research questions	19
2 The effect of diurnal warming of sea surface temperatures on the propagation speed of the Madden–Julian Oscillation	21
2.1 Preface	21
2.2 Introduction	22
2.3 Data and methods	24
2.3.1 Model specifications	24
2.3.2 Real-time Multivariate MJO index	25
2.3.3 Composites	26
2.3.4 Observational datasets	27
2.4 Results	27
2.4.1 MJO model performance	27
2.4.2 MJO convection in the models and SST-MJO relationship . .	31
2.4.3 Diurnal warming of sea surface temperatures	35
2.4.4 Rectification of diurnal warm layer on daily mean SST . . .	35
2.4.5 Diurnal warm layer strength dependence on MJO phase . .	39
2.4.6 Other potential sources for SST difference between models .	41

2.5	Conclusions	44
3	Two-way feedback between the Madden–Julian Oscillation and diurnal warm layers in a coupled ocean–atmosphere model	51
3.1	Preface	51
3.2	Introduction	52
3.3	Data and methods	54
3.3.1	Model specifications	54
3.3.2	Experimental setup	55
3.3.3	Real-time Multivariate MJO index	57
3.3.4	Composites and observational datasets	58
3.4	Results	58
3.4.1	MJO model performance and diurnal warming	58
3.4.2	MJO convection–diurnal warming–SST relationship	65
3.4.3	Diurnal warming effect on the mean state	73
3.5	Discussion and conclusions	76
4	The relative importance of ocean advection and surface heat fluxes during the Madden–Julian Oscillation in a coupled ocean–atmosphere model	83
4.1	Preface	83
4.2	Introduction	84
4.3	Data and methods	86
4.3.1	Model specifications	86
4.3.2	Real-time Multivariate MJO index	87
4.3.3	Mixed layer depth, barrier layer thickness and thermocline depth diagnostics	88
4.3.4	Composites	88
4.3.5	Target MJO phase	89
4.3.6	Mixed layer temperature tendencies	90
4.3.7	Observations	91
4.4	Results	91
4.4.1	MJO phase 8: Pre-initiation	92
4.4.2	MJO phase 1: Initiation	103
4.4.3	MJO phase 3: Maturity	105
4.4.4	The importance of different horizontal scales in the mixed layer heat budget on the MJO timescales	107
4.5	Discussion and conclusions	109
5	Conclusions	115
5.1	Review of research questions	115
5.1.1	Research question 1	115
5.1.2	Research question 2	116
5.1.3	Research question 3	118
5.2	Future work	119
5.2.1	Convection	119
5.2.2	Mean state	121

5.2.3	Ocean resolution	122
5.2.4	Fieldwork	123
5.3	Concluding remarks	123
A	RMM performance statistics for boreal winter and all seasons	125
B	MJO convection across different MJO phases	129
C	SST and diurnal warming across different MJO phases	133
D	Muted diurnal warming of SST	137
E	Mixed layer heat budget across different MJO phases	143
	References	171

List of figures

1.1	A schematic diagram produced by Madden & Julian (1972) depicting the 40 to 50 day oscillation recorded in the radiosonde measurements across the tropics. Each letter corresponds to a different date of the cycle of this oscillation arriving at Canton Island (3 °S, 172 °W). Cloud symbols depict the convective centre of the oscillation and the arrows indicate the zonal circulation in the lower and upper troposphere. Each diagram also contains sea level pressure disturbance recorded by Madden & Julian (1972) at the bottom of the diagram. <i>Image adapted from Madden & Julian (1972), Figure 16.</i>	2
1.2	Diagram depicting the vertical structure of clouds, temperature and moisture in the convective centre of the Madden–Julian Oscillation (MJO). <i>Image adapted from Jiang et al. (2020), Figure 2.</i>	3
1.3	A schematic diagram depicting the Northern Hemisphere teleconnections of the MJO. The MJO affects the planetary Rossby wave source, leading to differences in the North Atlantic Oscillation (blue and pink shading) and the Pacific–North American Pattern (PNA). Ω indicates the frequency of blocking and atmospheric rivers affected by the MJO. The MJO can also interact with the global monsoon system (dotted shading). <i>Image adapted from Stan et al. (2017), Figure 6.</i>	5
1.4	Eigenvalues of multivariate anomaly fields as a function of longitude for a) EOF1 and b) EOF2 structures. The multivariate anomaly fields are projected onto these EOF structures to obtain indices RMM1 and RMM2 in the Wheeler & Hendon (2004) RMM index. <i>Image reproduced after Gottschalck et al. (2010), Figure 1.</i>	6
1.5	Two dimensional RMM phase space diagram depicting the MJO evolution through RMM phases 1 to 8 for an example MJO event from December 2017 to February 2018. The distance from the centre denotes the RMM amplitude; the MJO is considered active when the amplitude is above 1, i.e. outside the inner circle on the diagram. The colour shading indicates the evolution of the MJO through different months, starting with the brightest blue in December 2017, through January 2018 to the darkest blue in February 2018. <i>Diagram constructed using the observed RMM indices available at http://www.bom.gov.au/climate/mjo and maintained by the Australian Bureau of Meteorology.</i>	7

1.6	Boreal winter composite anomalies of rainfall in eight RMM phases for period 1979–2012. The brown shading denotes below average rainfall anomalies and the green shading denotes above average rainfall anomalies. The rainfall anomalies show an eastward propagation through RMM phases 1 to 8. <i>Image adapted from https://www.climate.gov/news-features/blogs/enso/what-mjo-and-why-do-we-care, produced by the National Oceanographic and Atmospheric Administration.</i>	9
1.7	a) RMM prediction skill (correlation coefficient) between the models and observations; the model is considered skilful when the correlation coefficient is above 0.5; b) RMM amplitude bias between the models and the observations; positive (negative) amplitude bias denotes stronger (weaker) MJO amplitude in the model than in observations; c) RMM phase bias between the models and observations; positive (negative) phase bias indicates faster (slower) MJO in the model than in observations. <i>Image adapted from Kim et al. (2019), Figure 1.</i>	11
1.8	Hövmoller diagrams of zonally averaged 20-to-100 day bandpass filtered precipitation anomalies between 10°S and 10°N. The evolution of the precipitation is obtained by a lag-regression against the reference precipitation time series averaged over 85–95°E and 5°S–5°N. a) TRMM (observations); b) CMIP5 mean; c) CMIP6 mean; d–bo) individual models. The red box in each panel denotes the MC. <i>Image adapted from Ahn et al. (2020a), Figure 1.</i>	13
1.9	Two MJO events observed at the Research Moored Array for African–Asian–Australian Monsoon Analysis and Prediction mooring located at 90°E, 0°N. The left column corresponds to an MJO event that occurred at the end of 2007 and the right column shows an MJO event in January 2011. a) and g) OLR ($W m^{-2}$); b) and h) zonal wind stress ($N m^{-1}$); c) and i) daily precipitation ($mm d^{-1}$); d) and j) temperature ($^{\circ}C$); e) and k) salinity (psu); f) and l) density ($kg m^{-3}$). The grey vertical line denotes the peak MJO convection at the location of the mooring. Circles in panels j and k show the depths of the temperature and salinity sensors, respectively. The mixed layer depth and the isothermal layer depth are plotted as black lines in panels d–f and j–l. <i>Image adapted from Drushka et al. (2014a), Figure 4.</i>	16
2.1	RMM skill statistics as a function of lead day. a) bivariate correlation coefficient; b) root-mean-square error; c) amplitude error; d) phase error. Daily coupled (blue) and atmosphere-only model (red) data are compared for boreal winter season (November–April) and active MJO days only with UM Analysis (solid) and Wheeler-Hendon indices (dashed).	28

2.2	Phase error difference between the coupled and atmosphere-only model for a) all MJO phases combined and b) split by the initial RMM phase that the forecast started in.	28
2.3	RMM skill statistics as a function of lead day split by the initial RMM phase that the forecast started in. a–b) bivariate correlation coefficient; c–d) root-mean-square error; e–f) amplitude error; g–h) phase error.	30
2.4	Hovmöller diagrams of daily mean composites of 20-200 day filtered boreal winter OLR anomaly averaged over the equatorial band (5°S–5°N), for forecasts initialised in MJO phases 1 and 4. a–b) observed; c–d) coupled model; e–f) atmosphere-only model; g–h) difference between coupled and atmosphere-only models. Vertical dashed lines represent equatorial Indian Ocean and central Maritime Continent regions. Initially active MJO forecasts only. Number n denotes the amount of independent events used in the composite (total number of days used displayed in the bracket).	32
2.5	Difference at lead day 7 between composite daily means of coupled and atmosphere-only model 20-200 day filtered boreal winter anomaly of OLR for forecasts initialised in MJO phases a) 1 and b) 4. Initially active MJO forecasts only. Number n denotes the amount of independent events used in the composite (total number of days used is displayed in the bracket). RMM indices from Wheeler-Hendon. EIO – equatorial Indian Ocean; MC – Maritime Continent. The yellow contour outlines differences significant at the 95% level.	33
2.6	Composite daily mean at lead day 1 for a) coupled minus atmosphere-only model MJO-associated SST anomaly difference in MJO phase 1; b) anomalous coupled model diurnal warming of SST in MJO phase 1; c) coupled minus atmosphere-only model MJO-associated SST anomaly difference in MJO phase 4; d) anomalous coupled model diurnal warming of SST in MJO phase 4. Boreal winter and initially active MJO forecasts only.	34
2.7	Composite daily mean at lead day 1 for a) coupled and atmosphere-only model SST difference for all MJO phases; b) coupled model 1500 and 0600 local solar time SST difference for all MJO phases. Boreal winter and initially active MJO forecasts only.	35
2.8	Composite mean vertical section of ocean temperature change, from FOAM initial condition to lead day 1 mean (centred at 12 h lead time), from the coupled model at the equator for all MJO phases. Boreal winter and initially active MJO forecasts only. Model levels are displayed as black dots at 180°E.	36

2.9 Composite lead day 1 daily means for coupled (blue) and atmosphere-only (red) models for: a)–b) sea surface temperatures (SST); c)–d) MJO-associated SST anomalies; e)–f) diurnal warming of SST as a difference between 1500 and 0600 local solar time (LST) SST. EIO and central MC region extents in Figure 2.5. Boreal winter and initially active MJO forecasts only. 38

2.10 Composite lead day 1 daily means for coupled (blue) and atmosphere-only (red) models for a)–b) downward shortwave surface flux (SW flux), observed values from CERES SYN1deg (Rutan *et al.*, 2015); c–d) 10 m windspeed, observed values from ERA5 reanalysis (Hersbach *et al.*, 2020); e–f) mixed layer depth at the equator for reference depth 10 m and $\Delta T = 0.8^\circ\text{C}$. Boreal winter and initially active MJO forecasts only. 40

2.11 Lead day 1 daily mean sea surface temperatures (SST) sensitivity in central Maritime Continent region in a coupled forecast initialisation on 17 January 2017 to downward surface shortwave (SW) flux perturbations achieved with varying cloud erosion parameter and sub-grid variability of cloud water content at the top of the atmosphere. See region extent in Figure 2.5. 42

2.12 Schematic diagram of the Madden–Julian Oscillation (MJO) modulation of the diurnal warm layer strength in the upper ocean and its subsequent rectification of daily mean sea surface temperatures (SST) and MJO-associated SST anomalies, leading to faster eastward MJO propagation within seven forecast days. During enhanced MJO conditions, the diurnal warm layer is suppressed, leading to a colder MJO-associated SST anomaly in a model that resolves the diurnal cycle of SST. This colder anomaly will lead to decreased latent heat flux into the atmosphere and stronger suppression of MJO convection within the next few forecast days. During suppressed MJO conditions, the diurnal warm layer is enhanced, leading to a warmer MJO-associated SST anomaly in a model that resolves the diurnal cycle of SST. This warmer anomaly will lead to enhanced latent heat flux into the atmosphere, leading to more convection ahead of the MJO convective anomalies. Both mechanisms will lead to faster eastward MJO propagation in a model that resolves the diurnal warm layer compared to one that does not. Left panel modified after Yan *et al.* (2021). 47

3.1 Sample evolution of surface diurnal warm layer for one grid point in the Indian Ocean (70.625°E, 0°N) during the first 24 hours of the forecast initialised on May 1, 2016: a) sea surface temperature (SST), and the vertical profiles of ocean temperature at b) 0130 UTC (0610 LST) and c) 1030 UTC (1510 LST). 56

3.2	Real-time Multivariate Madden–Julian Oscillation (MJO) index skill statistics as a function of lead day for CPLD, CPLDmix5m, CPLDmix10m and ATM models: a) bivariate correlation coefficient; b) root-mean-square error; c) amplitude error; d) phase error. Daily mean data are compared for boreal winter season (November–April) and active MJO days only with the Wheeler-Hendon verification indices.	59
3.3	a) Real-time Multivariate Madden–Julian Oscillation (RMM) phase angle difference between the coupled model experiments (CPLD, CPLDmix5m and CPLDmix10m) and the ATM model as a function of lead day; b) RMM phase speed increase (percent) between the coupled model experiments and the ATM model at lead day 7 of the forecast as a function of the mean diurnal warming of sea surface temperatures (dSST, difference between the 1500 and 0600 local solar time sea surface temperature) in the tropics (30°S–30°N) at lead day 1 in the coupled model experiments; c) best fit between the top model level thickness and the mean dSST in the tropics at lead day 1 for $dSST_{max} = 0.18\text{ }^{\circ}\text{C}$ and $H = 4.0\text{ m}$	60
3.4	Composite diurnal warming (dSST; 1500 minus 0600 local solar time SST difference) at lead day 1 for a) CPLD, b) CPLDmix5m and c) CPLDmix10m averaged over all MJO phases (boreal winter and initially active MJO forecasts only). The boxes indicate where area averages are taken later over the equatorial Indian Ocean (EIO) and central Maritime Continent (MC).	62
3.5	Composite 0600 local solar time (LST) SST for CPLD, CPLDmix5m and CPLDmix10m averaged over the tropics (30°S–30°N), and over all MJO phases (boreal winter and initially active MJO forecasts only).	63
3.6	Composite lead day 1 daily means for CPLD, CPLDmix5m, CPLDmix10m and ATM models for: a)–b) diurnal warming of SST (dSST; difference between 1500 and 0600 local solar time SST); c)–d) MJO anomalies of dSST (20–200-day filtered); e)–f) SST; g)–h) MJO anomalies of SST. The EIO and central MC regions are shown in Figure 3.4. Composites are calculated for boreal winter and initially active MJO forecasts only.	66
3.7	Hovmöller diagrams of daily mean composites of MJO anomalous (20–200-day filtered) OLR, averaged over the equatorial band (5°S–5°N), for forecasts initialised in MJO phases 1 and 4: a)–b) observed; c)–d) CPLD model; e)–f) ATM model. Vertical dashed lines represent equatorial Indian Ocean and central Maritime Continent regions. Composites were calculated using boreal winter and initially active MJO forecasts only. Number n denotes the amount of independent events used in the composite (total number of days used displayed in the brackets).	69

3.8	Daily evolution of the model composites of MJO (20–200-day filtered) anomalies of: a–b) dSST; c–d) SST; e–f) OLR (difference from the CPLD model). Panels a, c and e are for the central MC region for initial MJO phase 1. Panels b, d and f are for the equatorial Indian Ocean (EIO) region for initial MJO phase 4. Composites are calculated for boreal winter for active MJO days only. The spatial extent of both regions is shown in Figure 3.4.	70
3.9	Composite daily mean MJO (20–200-day filtered) anomalies of CPLDmix10m minus CPLD difference for: a–b) SST at lead day 1 ; c–d) OLR at lead day 7; e–f) SST at lead day 14. Panels a, c and e are for initial MJO phase 1. Panels b, d and f are for initial MJO phase 4. Composites are calculated from boreal winter data.	72
3.10	Daily average difference for the mean state composites in the warm pool region (40 °E–180 °E, 10 °S–10 °N) between the mixing experiments (CPLDmix5m and CPLDmix10m) and the CPLD model for: a) SST; b) upward latent heat flux into the atmosphere (LH flux); c) downward shortwave flux into the ocean (SW flux); d) downward net heat flux into the ocean Q_{net} ; e) 10 m wind speed; f) OLR. Composites are calculated with boreal winter season data only. Surface variables (SST, heat fluxes and 10 m windspeed) composite averages for sea grid points only.	74
3.11	a) Daily average mean state composite difference in surface precipitation rate over the warm pool region (40 °E–180 °E, 10 °S–10 °N) for CPLDmix5m minus CPLD and CPLDmix10m minus CPLD models; daily average mean state composite difference in surface precipitation rate at lead day 15 for b) CPLDmix5m minus CPLD and c) CPLDmix10m minus CPLD models. Composites are calculated with boreal winter season data only. Warm pool extent in panels b and c.	74

3.12	Schematic diagram of the two-way feedback between the Madden–Julian Oscillation (MJO) and diurnal warm layers in the upper ocean in the coupled ocean–atmosphere Numerical Weather Prediction (NWP) system of the UK Met Office. The MJO conditions in the coupled model modulate the strength of diurnal warm layers at lead day 1 such that enhanced (suppressed) MJO phase leads to suppressed (enhanced) diurnal warm layers. The presence of diurnal warm layers changes the daily mean sea surface temperatures (SST) in the coupled model and enhances daily mean intraseasonal SST anomalies. Stronger (weaker) diurnal warming at lead day 1 leads to warmer (colder) intraseasonal anomalies of SST than in the absence of diurnal warming. The modulated intraseasonal SST anomalies affect the surface fluxes between the ocean and the atmosphere, and ultimately lead to a peak MJO convection response on a 7-lead-day timescale and a $\sim 3\%$ increase in the MJO phase speed. Subsequently, the intraseasonal anomalies of SST respond to these MJO convection changes within the next 3 forecast days.	79
4.1	Composite maps of the 20-to-200 day bandpass filtered anomalies (the Madden–Julian Oscillation, MJO anomalies) of model sea surface temperature (SST) for target MJO phases 8 (panels a–b), 1 (panels c–d) and 3 (panels e–f). Panels a, c and e show composites at forecast day 1 (prior to each MJO phase arrival) and panels b, d and f correspond to forecast day 10 (when each MJO phase arrives in the observations).	92
4.2	Composite maps of model MJO anomalies of outgoing longwave radiation (OLR) for target MJO phases 8 (panels a-b), 1 (panels c-d) and 3 (panels e-f). Lagged composites of the MJO anomalies of OLR in observations Liebmann & Smith (1996) for target MJO phases 8 (panels g-h), 1 (panels i-k) and 3 (panels k-l). Panels a, c, e, g, i and k show composites at forecast day 1 (prior to each MJO phase arrival) and panels b, d, f, h, j and l at forecast day 10 (when each MJO phase arrives in the observations).	93
4.3	a–c) Cumulative change in the composite MJO anomaly of mixed layer temperature (MLT) over forecast days 1 to 10 prior to the arrival of (target) MJO phases 8, 1 and 3 in the western Indian Ocean region; d–f) cumulative change of the MJO anomaly of MLT due to total advection for target MJO phases 8, 1 and 3; g–i) cumulative change of the MJO anomaly of MLT due to vertical mixing for target MJO phases 8, 1 and 3; g–i) cumulative change of the MJO anomaly of MLT due to net heat flux for target MJO phases 8, 1 and 3.	95

4.4	Change in the MJO anomaly of 20° isotherm depth (D20, panels a–c) and the mixed layer depth (MLD, panels d–f) from forecast day 1 to 10 prior to the arrival of (target) MJO phases 8, 1 and 3. Target MJO phase 8 in panels a, d, target MJO phase 1 in panels b, e, and target MJO phase 3 in panels panels c, f.	96
4.5	a–c) Cumulative change in the composite MJO anomaly of mixed layer temperature (MLT) over forecast days 1 to 10 prior to the arrival of (target) MJO phases 8, 1 and 3 in the western Indian Ocean region due to the horizontal advection; d–f) average mean state ocean currents in the mixed layer ($\bar{\mathbf{u}}$) and the average MJO anomaly of MLT (T') over forecast days 1 to 10 in target MJO phases 8, 1 and 3; g–h) MJO anomalous ocean currents (\mathbf{u}') in the mixed layer ($\bar{\mathbf{u}}$) and T' over forecast days 1 to 10 in target MJO phases 8, 1 and 3; j–l) \mathbf{u}' and \bar{T} . \mathbf{u}' is plotted at the 95 % significance level. Yellow outline shows T' at 95 % significance level.	97
4.6	As Figure 4.3 but for central Indian Ocean region.	98
4.7	As Figure 4.3 but for the eastern Maritime Continent region.	99
4.8	a–c) Cumulative change in the MJO anomaly of mixed layer temperature (MLT) due to horizontal advection over forecast days 1 to 10 prior to the arrival of (target) MJO phases 8, 1 and 3; d–f) advection of T' by $\bar{\mathbf{u}}$ over forecast days 1 to 10; g–i) advection of \bar{T} by \mathbf{u}' over forecast days 1 to 10; k–n) advection of T' by \mathbf{u}' over forecast days 1 to 10; m–o) sum of the advection of T' by $\bar{\mathbf{u}}$, the advection of \bar{T} by \mathbf{u}' and the advection of T' by \mathbf{u}' over forecast days 1 to 10.	101
4.9	As in Figure 4.5 but for the eastern Maritime Continent region.	102
4.10	Covariance between the cumulative change in the MJO anomaly of mixed layer temperature, and each temperature tendency term, as a function of the smoothing radius. The temperature tendency terms are $\Delta T_{\text{tot. adv.}}$ (yellow), $\Delta T_{\text{vert. mix.}}$ (pink) and $\Delta T_{Q_{\text{net}}}$ (green). The covariances are calculated over forecast days 1 to 10 prior to the arrival of target MJO phases 8 (left column), 1 (central column) and 3 (right column), for the western Indian Ocean (IO) region (panels a–c), central IO region (panels d–f) and eastern Maritime Continent region (panels g–i).	108
4.11	Schematic diagram of the oceanic processes that drive intraseasonal mixed layer heat budget during the initiation and the evolution of the Madden–Julian Oscillation (MJO) in the coupled ocean–atmosphere Numerical Weather Prediction system of the UK Met Office. MLT – mixed layer temperature. Mean ocean currents and MJO-induced ocean currents not to scale.	110
A1	RMM skill metrics as a function of lead day. As in Figure 2.1 but for all boreal winter season days (November–April).	126

A2	RMM skill metrics as a function of lead day. As in Figure 2.1 but for year-round data.	126
A3	RMM skill metrics as a function of lead day and initial MJO phase. As in Figure 2.3 but for all boreal winter season days (November–April).	127
A4	RMM skill metrics as a function of lead day and initial MJO phase. As in Figure 2.3 but for year-round data.	127
B1	Hovmöller diagrams of daily mean composites of 20-200 day filtered boreal winter OLR anomaly averaged over the equatorial band (5°S–5°N), for forecasts initialised in MJO phases 1 to 4. a–d) observed; e–h) coupled model; i–l) atmosphere-only model; m–p) difference between coupled and atmosphere-only models. Vertical dashed lines represent equatorial Indian Ocean and central Maritime Continent regions. Initially active MJO forecasts only. Number n denotes the amount of independent events used in the composite (total number of days used displayed in the bracket).	130
B2	Hovmöller diagrams of daily mean composites of 20-200 day filtered boreal winter OLR anomaly averaged over the equatorial band (5°S–5°N), for forecasts initialised in MJO phases 5 to 8. a–d) observed; e–h) coupled model; i–l) atmosphere-only model; m–p) difference between coupled and atmosphere-only models. Vertical dashed lines represent equatorial Indian Ocean and central Maritime Continent regions. Initially active MJO forecasts only. Number n denotes the amount of independent events used in the composite (total number of days used displayed in the bracket).	131
B3	Difference at lead day 7 between composite daily means of coupled and atmosphere-only model 20-200 day filtered boreal winter anomaly of OLR for forecasts initialised in MJO phases 1 to 8. Initially active MJO forecasts only. Number n denotes the amount of independent events used in the composite (total number of days used is displayed in the bracket). RMM indices from Wheeler-Hendon. The yellow contour outlines differences significant at the 95% level.	132
C1	Composite daily mean at lead day 1 for coupled minus atmosphere-only model MJO-associated SST anomaly difference for forecasts initialised in MJO phases 1 to 8. Boreal winter and initially active MJO forecasts only. Number n denotes the amount of independent events used in the composite (total number of days used is displayed in the bracket). RMM indices from Wheeler-Hendon. The yellow contour outlines differences significant at the 95% level.	134

C2	Composite daily mean at lead day 1 for coupled model diurnal warming of SST for forecasts initialised in MJO phases 1 to 8. Diurnal warming is defined as 1500 – 0600 local solar time (LST) SST. Boreal winter and initially active MJO forecasts only. Number n denotes the amount of independent events used in the composite (total number of days used is displayed in the bracket). RMM indices from Wheeler–Hendon.	135
D1	Sample evolution of surface diurnal warm layer for one grid point in the Indian Ocean (70.625 °E, 0 °N) during the first 24 hours of the forecast initialised on May 1, 2016: a) sea surface salinity (SSS), and the vertical profiles of ocean salinity at b) 0130 UTC (0610 LST) and c) 1030 UTC (1510 LST).	138
D2	Sample evolution of surface diurnal warm layer for one grid point in the Indian Ocean (70.625 °E, 0 °N) during the first 24 hours of the forecast initialised on May 1, 2016: a) sea surface density, and the vertical profiles of ocean salinity at b) 0130 UTC (0610 LST) and c) 1030 UTC (1510 LST).	138
D3	Hovmöller diagrams of daily mean composites of 20-200 day filtered boreal winter OLR anomaly averaged over the equatorial band (5 °S–5 °N), for forecasts initialised in MJO phases 1 to 4. Panels a, f, k and p) observed; panels b, g, l and q) CPLD model; panels c, h, m and r) CPLDmix5m model; panels d, i, n and s) CPLDmix10m model; panels e, j, o and t) CPLDmix10m model. Vertical dashed lines represent equatorial Indian Ocean and central Maritime Continent regions. Initially active MJO forecasts only. Number n denotes the amount of independent events used in the composite (total number of days used displayed in the bracket). Horizontal dashed lines denote lead days 5 and 10.	139
D4	Hovmöller diagrams of daily mean composites of 20-200 day filtered boreal winter OLR anomaly averaged over the equatorial band (5 °S–5 °N), for forecasts initialised in MJO phases 5 to 8. Panels a, f, k and p) observed; panels b, g, l and q) CPLD model; panels c, h, m and r) CPLDmix5m model; panels d, i, n and s) CPLDmix10m model; panels e, j, o and t) CPLDmix10m model. Vertical dashed lines represent equatorial Indian Ocean and central Maritime Continent regions. Initially active MJO forecasts only. Number n denotes the amount of independent events used in the composite (total number of days used displayed in the bracket). Horizontal dashed lines denote lead days 5 and 10.	140
D5	Composite daily mean MJO (20–200-day filtered) anomalies of CPLDmix10m minus CPLD difference for: a–b) SST at lead day 1 ; c–d) OLR at lead day 7; e–f) SST at lead day 14. Panels a, c and e are for initial MJO phase 2. Panels b, d and f are for initial MJO phase 3. Composites are calculated from boreal winter data.	141

D6	Composite daily mean MJO (20–200-day filtered) anomalies of CPLDmix10m minus CPLD difference for: a–b) SST at lead day 1 ; c–d) OLR at lead day 7; e–f) SST at lead day 14. Panels a, c and e are for initial MJO phase 5. Panels b, d and f are for initial MJO phase 6. Composites are calculated from boreal winter data.	141
D7	Composite daily mean MJO (20–200-day filtered) anomalies of CPLDmix10m minus CPLD difference for: a–b) SST at lead day 1 ; c–d) OLR at lead day 7; e–f) SST at lead day 14. Panels a, c and e are for initial MJO phase 7. Panels b, d and f are for initial MJO phase 8. Composites are calculated from boreal winter data.	142
E1	a–d) Cumulative change in the composite MJO anomaly of mixed layer temperature (MLT) over forecast days 1 to 10 prior to the arrival of (target) MJO phases 8, 1, 2 and 3 in the western Indian Ocean region; e–h) cumulative change of the MJO anomaly of MLT due to total advection for target MJO phases 8, 1, 2 and 3; i–l) cumulative change of the MJO anomaly of MLT due to horizontal mixing for target MJO phases 8, 1, 2 and 3; ; m–p) cumulative change of the MJO anomaly of MLT due to vertical mixing for target MJO phases 8, 1, 2 and 3; q–t) cumulative change of the MJO anomaly of MLT due to net heat flux for target MJO phases 8, 1, 2 and 3; u–x) residual (top row minus sum of the middle rows).	144
E2	a–d) Cumulative change in the composite MJO anomaly of mixed layer temperature (MLT) over forecast days 1 to 10 prior to the arrival of (target) MJO phases 4, 5, 6 and 7 in the western Indian Ocean region; e–h) cumulative change of the MJO anomaly of MLT due to total advection for target MJO phases 4, 5, 6 and 7; i–l) cumulative change of the MJO anomaly of MLT due to horizontal mixing for target MJO phases 4, 5, 6 and 7; ; m–p) cumulative change of the MJO anomaly of MLT due to vertical mixing for target MJO phases 4, 5, 6 and 7; q–t) cumulative change of the MJO anomaly of MLT due to net heat flux for target MJO phases 4, 5, 6 and 7; u–x) residual (top row minus sum of the middle rows).	145
E3	As in Figure E1 but for the central Indian Ocean region.	146
E4	As in Figure E2 but for the central Indian Ocean region.	147
E5	As in Figure E1 but for the eastern Maritime Continent region.	148
E6	As in Figure E2 but for the eastern Maritime Continent region.	149

E7	Covariance as a function of the smoothing radius (degree longitude). Covariance between the cumulative change in the composite MJO anomaly of mixed layer temperature (MLT, ΔT) over forecast days 1 to 10 prior to the arrival of (target) MJO phases 8, 1, 2 and 3 and $\Delta T_{\text{tot. adv.}}$ (yellow), $\Delta T_{\text{vert. mix.}}$ (pink) and $\Delta T_{Q_{\text{net}}}$ (green) for the western Indian Ocean (IO) region (panels a–d), central IO region (panels e–h) and eastern Maritime Continent region (panels i–l).	150
E8	Covariance as a function of the smoothing radius (degree longitude). Covariance between the cumulative change in the composite MJO anomaly of mixed layer temperature (MLT, ΔT) over forecast days 1 to 10 prior to the arrival of (target) MJO phases 4, 5, 6 and 7 and $\Delta T_{\text{tot. adv.}}$ (yellow), $\Delta T_{\text{vert. mix.}}$ (pink) and $\Delta T_{Q_{\text{net}}}$ (green) for the western Indian Ocean (IO) region (panels a–d), central IO region (panels e–h) and eastern Maritime Continent region (panels i–l).	151

List of tables

2.1	Model specifications summary.	24
3.1	Model specifications summary.	55
4.1	Model specifications summary.	87

Chapter 1

Introduction

1.1 The Madden–Julian Oscillation

The Madden–Julian Oscillation (MJO) is an intraseasonal (30–90 day) weather pattern in the tropics, identified originally by Madden & Julian (1971, 1972). The MJO is characterised by envelopes of enhanced and suppressed convection, travelling eastward at $\sim 5 \text{ m s}^{-1}$ phase speed across the tropics. The MJO typically originates in the western equatorial Indian Ocean, crosses the Maritime Continent (MC; Indonesia, Philippines and Papua New Guinea) and dissipates over the western Pacific Ocean.

The MJO was discovered by accident in 1971 by Madden & Julian who analysed 10 years of radiosonde measurements at Canton Island (3°S , 172°W), in the hope of finding theoretical wave-like modes in the tropics. They found, unexpectedly, a strong spectral peak for periods 41 to 53 days. This spectral peak did not match what they expected from the theoretical modes proposed by Matsuno (1966). They found an oscillating signal in the station sea level pressure and the zonal wind components at 850 hPa and 150 hPa. In 1972, Madden & Julian analysed multiple stations in the tropics to find an eastward propagating wave-like disturbance in zonal winds and sea level pressure across the tropics. They hypothesised that this feature is a large-scale convection and circulation pattern moving towards the east in the equatorial plane in the tropics (Figure 1.1). Later, this weather phenomenon was named after them as the Madden–Julian Oscillation, the MJO.

As Figure 1.1 shows, the MJO is characterised by an overturning circulation, with a convective centre (the active phase) and a suppressed convection to the

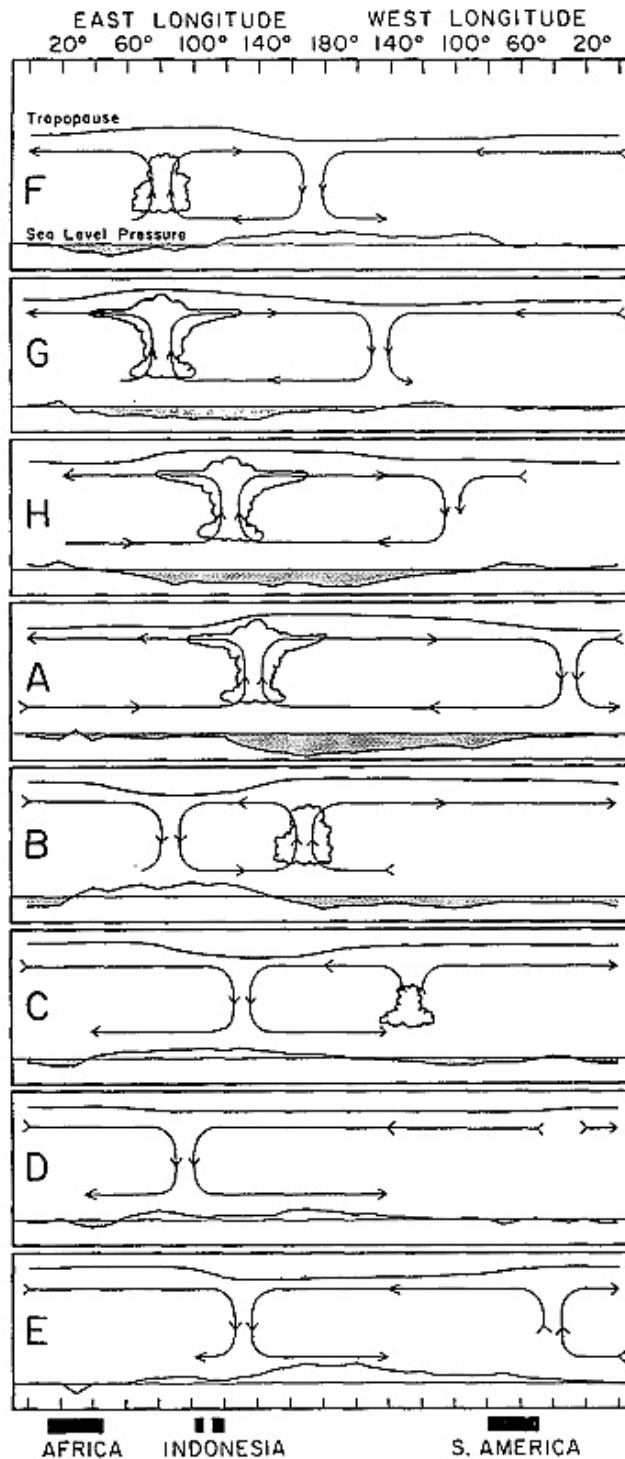


Figure 1.1: A schematic diagram produced by Madden & Julian (1972) depicting the 40 to 50 day oscillation recorded in the radiosonde measurements across the tropics. Each letter corresponds to a different date of the cycle of this oscillation arriving at Canton Island (3°S , 172°W). Cloud symbols depict the convective centre of the oscillation and the arrows indicate the zonal circulation in the lower and upper troposphere. Each diagram also contains sea level pressure disturbance recorded by Madden & Julian (1972) at the bottom of the diagram. *Image adapted from Madden & Julian (1972), Figure 16.*

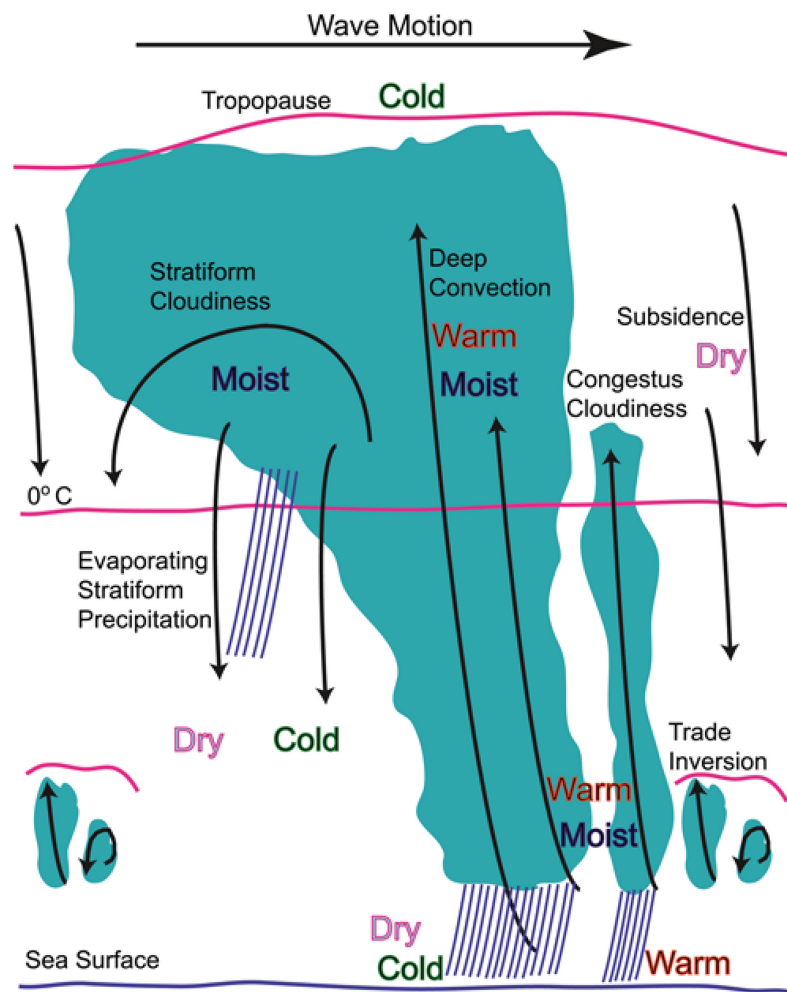


Figure 1.2: Diagram depicting the vertical structure of clouds, temperature and moisture in the convective centre of the Madden–Julian Oscillation (MJO). Image adapted from Jiang *et al.* (2020), Figure 2.

east and to the west of the convective phase (the suppressed phase). In the lower troposphere, the MJO consists of easterly wind anomalies located to the east of the convective centre, and strong westerlies to the west of the convective centre resulting in the wind convergence. A reverse pattern is observed in the upper troposphere, where the wind divergence occurs.

The active phase of the MJO is characterised by deep convective clouds with strong upward motions, enhanced precipitation and enhanced moisture in the column (Figure 1.2). To the east of the convective centre, shallow cumulus clouds can be observed (e.g., Chen & Del Genio, 2009; Tromeur & Rossow, 2010; Xu & Rutledge, 2014), with a boundary layer convergence anomaly (e.g., Kiladis *et al.*, 2005; Sperber, 2003), and a positive moisture anomaly in the lower troposphere due to warm sea surface temperatures (SSTs) (e.g., Tian *et al.*, 2010; Johnson & Ciesielski, 2013). To the west of the convective centre, the MJO consists of

the trailing layered stratiform clouds (e.g., Kiladis *et al.*, 2005; Lin *et al.*, 2004). Additionally, a negative moisture anomaly is present in the lower troposphere to the west of the convective centre. This anomaly occurs due to the evaporation of precipitation from stratiform clouds (Lin *et al.*, 2004).

There are four major theories that explain the dynamics of the MJO: the skeleton theory (Majda & Stechmann, 2009), the moisture mode theory (e.g., Adames & Kim, 2016), the gravity wave theory (Yang & Ingersoll, 2014), and the trio-interaction theory (e.g., Wang & Rui, 1990). A comprehensive summary of these theories can be found in Zhang *et al.* (2020). Most theories for the MJO state that moist processes are key to its eastward propagation and its growth. The moisture mode theory postulates that the MJO eastward propagation is regulated by the background moist static energy (MSE) advected by the MJO circulation. Enhanced MSE to the east of the MJO convection and a decrease in the MSE to the west is found to promote the eastward propagation of the MJO (e.g., Arnold *et al.*, 2015; Sobel *et al.*, 2014; Jiang, 2017).

The MJO has a significant effect on the precipitation in the tropics, however, it also modulates weather and climate systems across the globe through teleconnections (e.g., Zhang, 2013; Stan *et al.*, 2017; Schreck, 2021). The MJO can lead to an increase in tornado occurrences in America (Thompson & Roundy, 2013) and an increase in tropical cyclone genesis in the Southern Indian Ocean (Bessafi & Wheeler, 2006), affect the monsoon systems (e.g., Pai *et al.*, 2011; Lorenz & Hartmann, 2006), trigger warm El Niño–Southern Oscillation events (ENSO) (e.g., Zhang & Gottschalck, 2002), and affect the planetary Rossby waves that influence the weather at mid-latitudes across the globe (e.g., Seo *et al.*, 2016). Stan *et al.* (2017) provides a comprehensive summary of the MJO influence around the globe.

Figure 1.3 presents a schematic diagram of some of the extratropical teleconnections of the MJO in the Northern Hemisphere. The most prominent teleconnection known of the MJO is the influence it exerts on the North Atlantic Oscillation (NAO), the weather pattern that modulates the atmospheric variability in North America and Europe (Wallace & Gutzler, 1981). Observations show that a positive NAO pattern (higher air pressure and fewer cold-air outbreaks) is more likely to occur 15 days after the MJO reaches the MC (e.g., Cassou, 2008; Yadav & Straus, 2017). While the MJO teleconnections are not the focus of this thesis, the effects of the MJO extend globally, and therefore, understanding and improving the MJO predictability is an important task for weather modelling centres. In the next section, I will provide an overview of

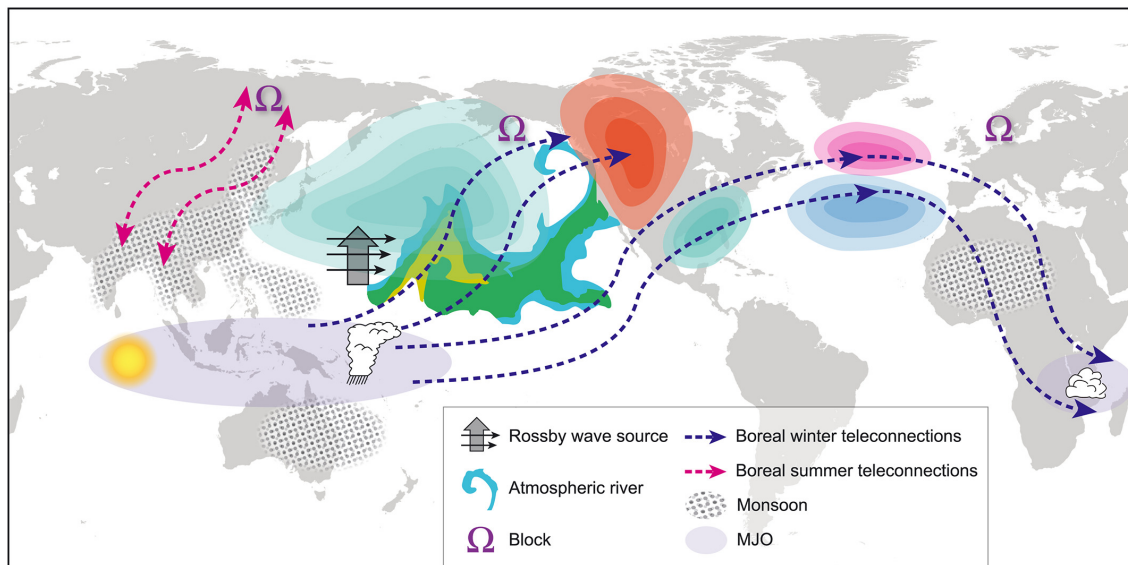


Figure 1.3: A schematic diagram depicting the Northern Hemisphere teleconnections of the MJO. The MJO affects the planetary Rossby wave source, leading to differences in the North Atlantic Oscillation (blue and pink shading) and the Pacific–North American Pattern (PNA). Ω indicates the frequency of blocking and atmospheric rivers affected by the MJO. The MJO can also interact with the global monsoon system (dotted shading). Image adapted from Stan et al. (2017), Figure 6.

how the MJO is extracted from the data and how well state-of-the-art numerical weather prediction (NWP) models simulate the MJO.

1.2 The definition of the MJO in data

The first three decades since the discovery of the MJO resulted in many studies of this weather phenomenon (for review, see Zhang, 2005). However, no consensus was achieved on how to define and extract the MJO signal from the data. The MJO was mostly extracted using a spectral analysis, however the period used varied from study to study, making it harder to interpret the MJO behaviour in observations, and across different models. Initially, the MJO was defined as a 40 to 50 day oscillation (Madden & Julian, 1972). Some subsequent studies extended the period to 30 to 60 days (e.g., Weickmann, 1991; Yanai *et al.*, 2000; Straus & Lindzen, 2000), some argued for even shorter periods of 20 to 30 days (e.g., Hartmann *et al.*, 1992; Chongyin *et al.*, 2005).

The methodology to extract the MJO signal was standardised in 2004, when Wheeler & Hendon created the Real-Time Multivariate MJO (RMM) index, the most common MJO index used in the past two decades. The RMM index uses

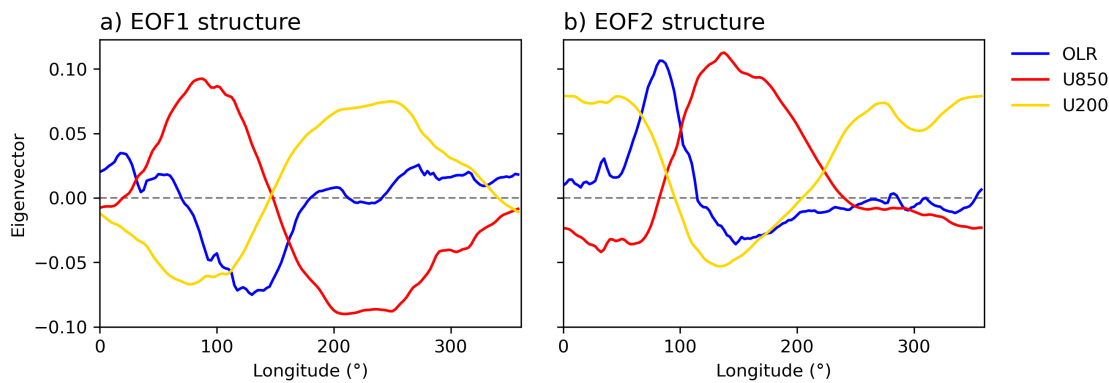


Figure 1.4: Eigenvalues of multivariate anomaly fields as a function of longitude for a) EOF1 and b) EOF2 structures. The multivariate anomaly fields are projected onto these EOF structures to obtain indices RMM1 and RMM2 in the Wheeler & Hendon (2004) RMM index. *Image reproduced after Gottschalck et al. (2010), Figure 1.*

zonally averaged anomalies of top-of-atmosphere outgoing longwave radiation (OLR) and zonal winds at 200 hPa and 850 hPa between 15 °S and 15 °N. These anomalies are constructed by the removal of the seasonal cycle and the long-term variability linked to ENSO (Lin *et al.*, 2008), and normalised by their standard deviation in observations (for details, see Gottschalck *et al.*, 2010).

The RMM1 and RMM2 indices are created using the principal component time series of the dominant spatial structures of the data (the empirical orthogonal functions, EOFs). EOF1 and EOF2 represent the first two dominant multivariate spatial structures of the data, accounting for 25 % of the variability on intraseasonal timescales (Wheeler & Hendon, 2004). The EOF1 structure represents the convective phase of the MJO and is described by a negative OLR anomaly centred around 120 °E (Figure 1.4a). During the convective phase of the MJO, the zonal winds at 850 hPa display westerly anomalies to the west of the MJO convection, and easterly anomalies to the east. At 200 hPa, the zonal wind anomalies reverse. The EOF2 structure represents the suppressed phase of the MJO (positive OLR anomaly, Figure 1.4b). The suppressed phase of the MJO is characterised by a positive OLR anomaly located over the Indian Ocean around 60 °E, with westerly zonal wind anomalies at 850 hPa located to the east of the peak suppressed MJO convection and the easterly zonal wind anomalies to the west. At 200 hPa, the zonal wind anomalies reverse.

The multivariate anomaly fields of zonal winds and OLR are projected onto the canonical MJO structures (EOF1 and EOF2) to obtain the RMM1 and RMM2 indices. The combination of the RMM1 and RMM2 indices defines eight MJO phases in the tropics. Figure 1.5 shows an example MJO event between December

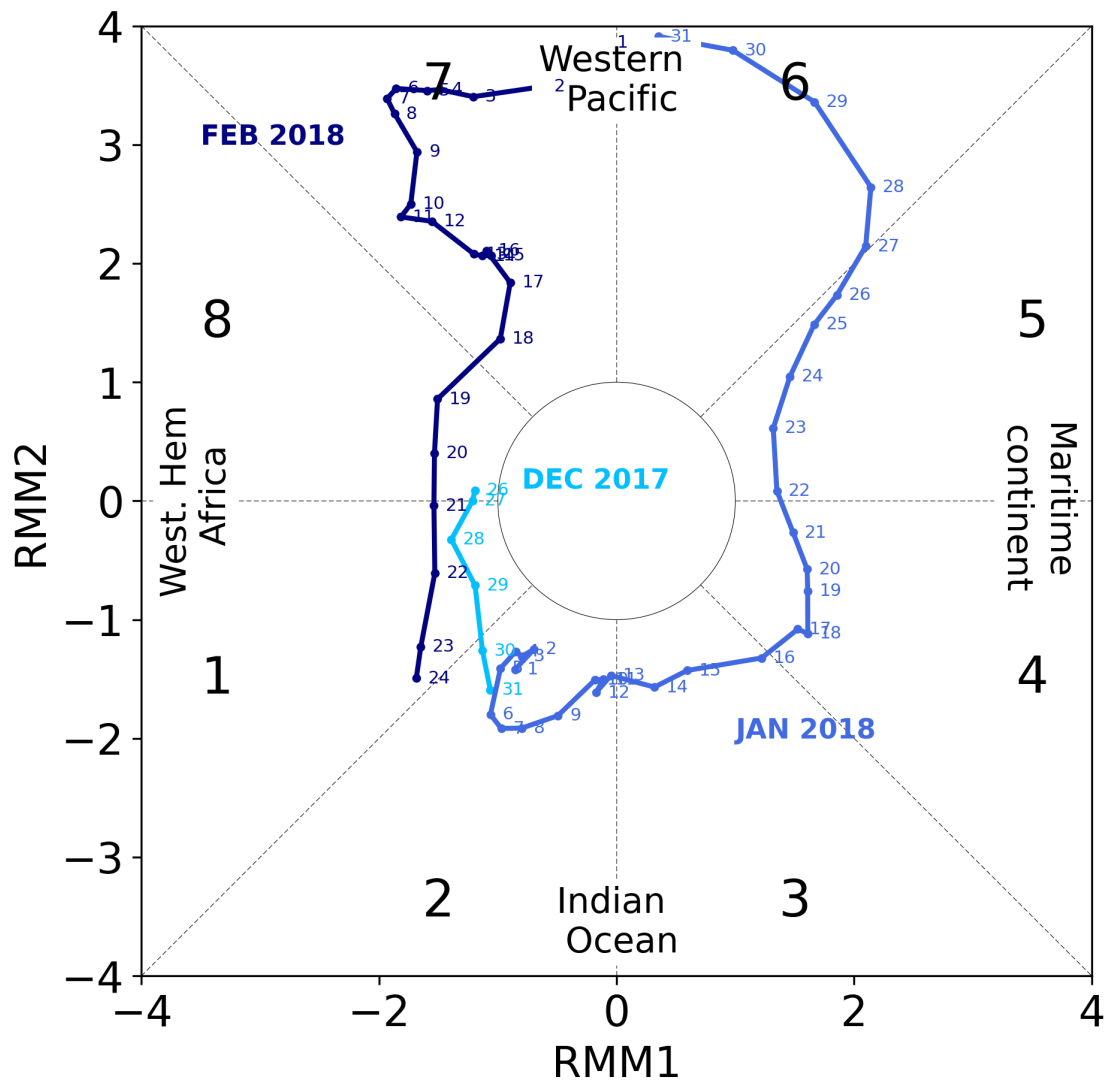


Figure 1.5: Two dimensional RMM phase space diagram depicting the MJO evolution through RMM phases 1 to 8 for an example MJO event from December 2017 to February 2018. The distance from the centre denotes the RMM amplitude; the MJO is considered active when the amplitude is above 1, i.e. outside the inner circle on the diagram. The colour shading indicates the evolution of the MJO through different months, starting with the brightest blue in December 2017, through January 2018 to the darkest blue in February 2018. Diagram constructed using the observed RMM indices available at <http://www.bom.gov.au/climate/mjo> and maintained by the Australian Bureau of Meteorology.

2017 and February 2018. This MJO event initiated in the western hemisphere and Africa in RMM phase 1, with both RMM indices displaying negative values at the end of December 2017. Then, the MJO travelled eastward across the tropical Indian Ocean through RMM phase 2 in January 2018. On January 14, 2018, the RMM2 index became positive and the MJO crossed into RMM phase 3. On January 16, 2018, the MJO reached RMM phase 4 and the MC. As the MJO reached RMM phase 5 on January 22, 2018, the RMM1 index became positive. By RMM phase 7, the MJO reached the western Pacific, and at the beginning of February 2018, the RMM1 index became negative again when the MJO reached RMM phase 8, and the western hemisphere. This particular event continued to be active in RMM phase 1 following phase 8, without losing its amplitude. Such MJO events are called “successive MJO events” (Matthews, 2008), as opposed to the “primary MJO events” that start in RMM phase 1 without a preceding active MJO in RMM phase 8.

Figure 1.6 depicts a composite analysis of boreal winter precipitation anomalies for 1979–2012 period split into different phases from the RMM index. The green and the blue shading indicates positive rainfall anomalies associated with the MJO. These anomalies originate in the western Indian Ocean in RMM phase 1 and propagate eastward through subsequent RMM phases across the tropics until they reach the Pacific in RMM phase 8.

The widespread use of the RMM index in the literature is partially due to its simplicity. The RMM index requires only two parameters, the phase and the amplitude, to define the location and the strength of the MJO. Additionally, the RMM index was constructed for real-time applications, making it an appealing method to use at operational centres for assessing daily model predictions. The index is not, however, without its limitations. It does not account for the changes in the MJO structure from event to event, and can be contaminated by the high frequency signal originating from Convectively Coupled Equatorial Kelvin and Rossby Waves (Roundy *et al.*, 2009).

Stachnik & Chrisler (2020) provides a review of other indices available in the literature to extract the MJO signal: the OLR-based MJO index (OMI, Kiladis *et al.*, 2014), the filtered OMI and the velocity potential MJO index (Ventrice *et al.*, 2013). All aforementioned indices use an EOF analysis on different 2D fields, and each index shows analogous spatial structures of the MJO, with slight differences in the daily variations of the MJO amplitude. Ultimately, each index has its own advantages and it is up to the author’s choice which index is appropriate to use in each study. The RMM index is the index of choice used throughout this

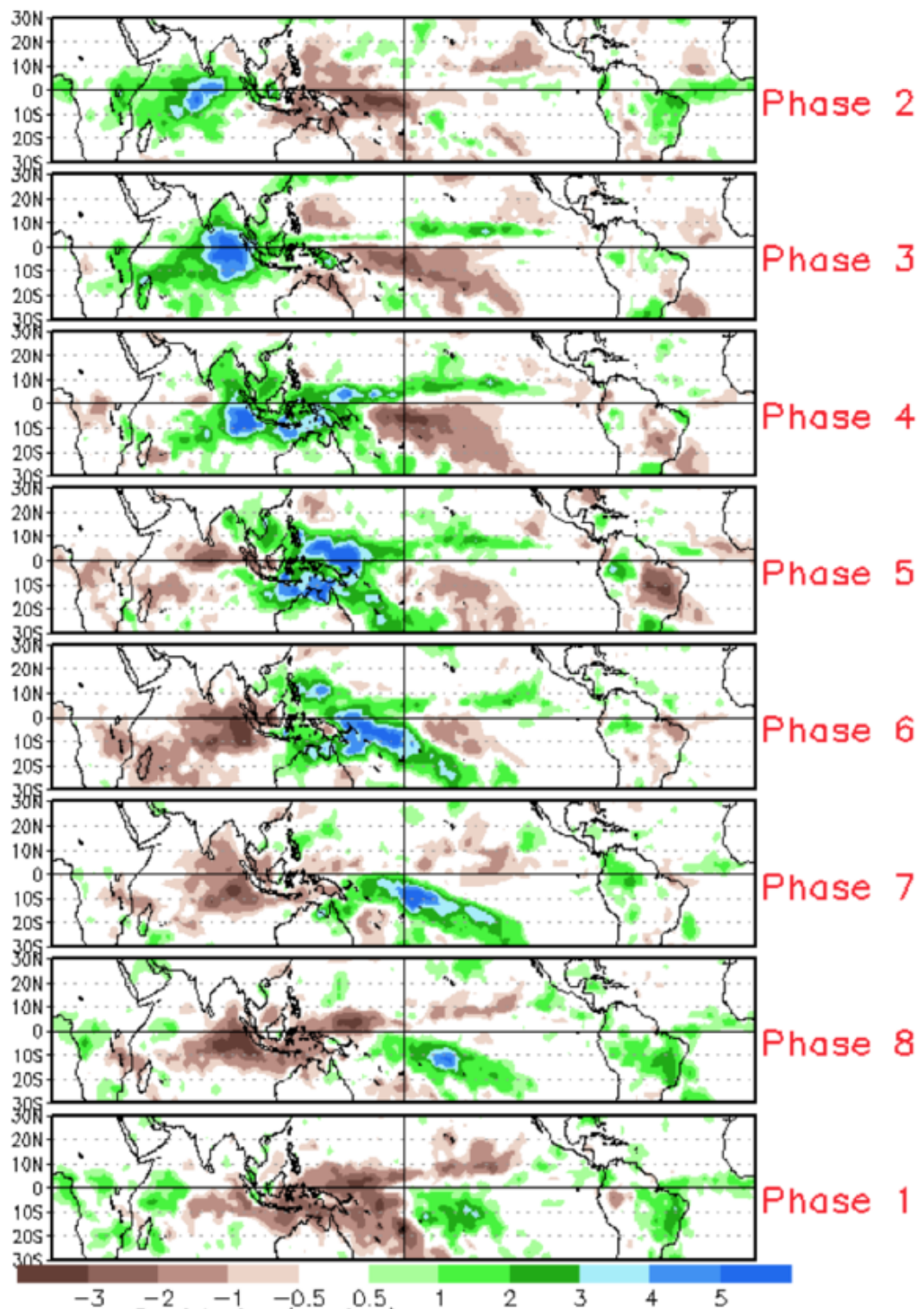


Figure 1.6: Boreal winter composite anomalies of rainfall in eight RMM phases for period 1979–2012. The brown shading denotes below average rainfall anomalies and the green shading denotes above average rainfall anomalies. The rainfall anomalies show an eastward propagation through RMM phases 1 to 8. *Image adapted from <https://www.climate.gov/news-features/blogs/enso/what-mjo-and-why-do-we-care>, produced by the National Oceanographic and Atmospheric Administration.*

thesis, and the most common index used to assess the forecast skill in the models discussed in the following section of this chapter.

1.3 The MJO in weather and climate models

The MJO is the main source of tropical weather predictability on subseasonal timescales (2 to 4 weeks) (Lau & Waliser, 2011), and therefore, it bridges the gap between the weather and climate. Despite the influence the MJO has on the global climate system (e.g., Zhang, 2013), current general circulation models (GCMs) suffer from certain limitations in representing the MJO (e.g., Vitart, 2017; Ahn *et al.*, 2017, 2020a). In this section, I will provide an overview of the MJO in GCMs over the past three decades and discuss the model limitations in simulating the MJO.

In the late 1990s, dynamical models produced poor skill in predicting the MJO, with an inability to predict the MJO skilfully past lead day 10 (e.g., Hendon *et al.*, 2000; Jones *et al.*, 2000). The empirical and statistical models in the early 2000s outperformed dynamical models at the time, skilfully predicting the MJO out to 12–20 days (e.g., Seo *et al.*, 2009; Waliser *et al.*, 1999; Wheeler & Weickmann, 2001; Jones *et al.*, 2004; Jiang *et al.*, 2008). In 2010s, dynamical models substantially improved due to the increase in the horizontal resolution, the improvements in the initial conditions, better forecast calibration, and the rise of coupled ocean–atmosphere models and ensemble forecasting. By the end of the 2010s, the MJO predictive skill of dynamical models surpassed the 20 day mark, and overtook the skill of empirical and statistical models (e.g., Fu *et al.*, 2013; Vitart, 2017; Kim *et al.*, 2019; Rashid *et al.*, 2011; Wang *et al.*, 2014; Li *et al.*, 2019).

Under perfect model assumptions, the MJO should be predicted skilfully out to 7 weeks (Neena *et al.*, 2014). Current subseasonal to seasonal (S2S) models fall short of that, with a skilful prediction out to 3–4.5 weeks (Kim *et al.*, 2014; Vitart, 2017; Kim *et al.*, 2019). Figure 1.7 shows the RMM prediction skill of eight S2S models analysed by Kim *et al.* (2019). Most of the analysed models show a decline in the MJO amplitude with forecast lead day compared with observations (negative amplitude bias in Figure 1.7b), and much slower MJO propagation than the observations suggest (negative phase bias in Figure 1.7c). It is also reported that models tend to perform better during boreal winter when the MJO is most active, or when the forecasts are initialised during strong MJO events (Rashid *et al.*, 2011; Kim *et al.*, 2014; Xiang *et al.*, 2015; Liu *et al.*, 2017).

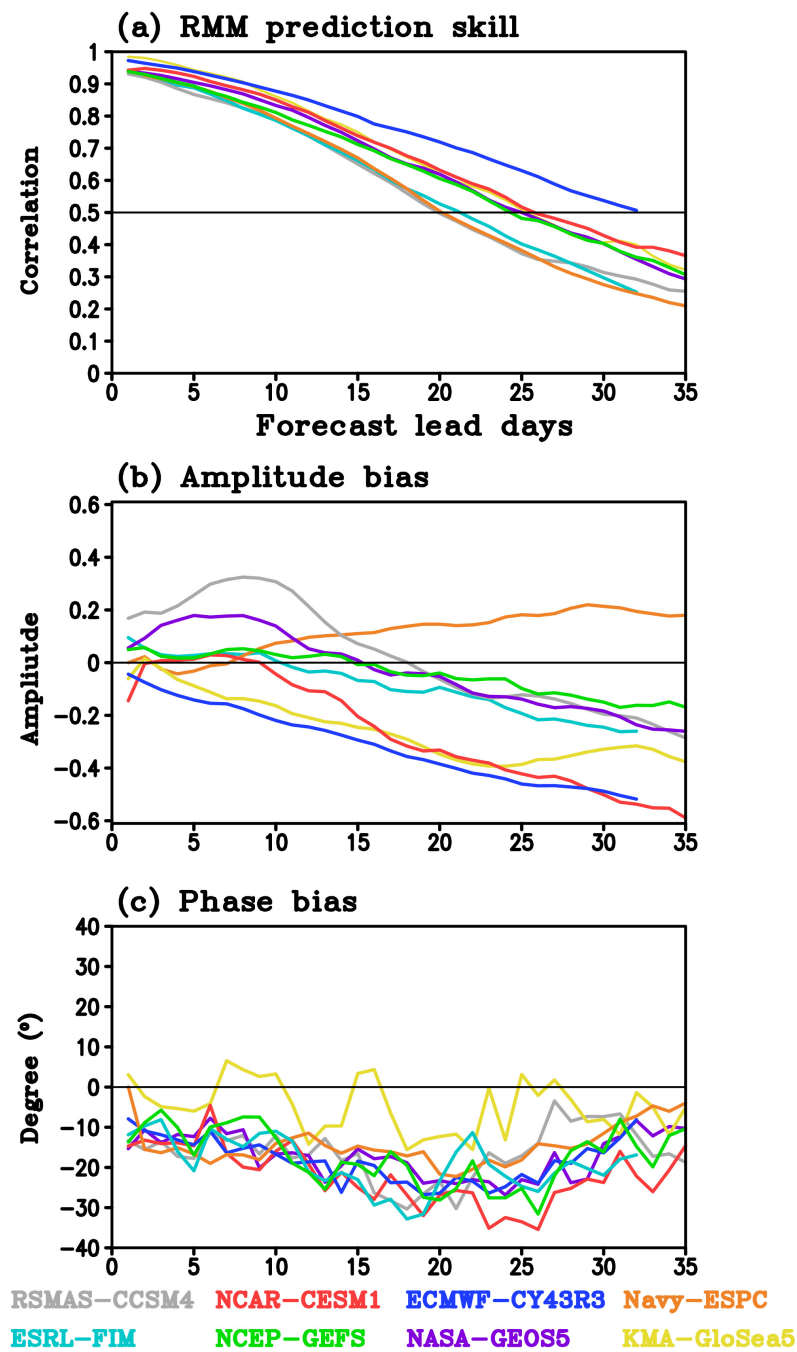


Figure 1.7: a) RMM prediction skill (correlation coefficient) between the models and observations; the model is considered skillful when the correlation coefficient is above 0.5; b) RMM amplitude bias between the models and the observations; positive (negative) amplitude bias denotes stronger (weaker) MJO amplitude in the model than in observations; c) RMM phase bias between the models and observations; positive (negative) phase bias indicates faster (slower) MJO in the model than in observations. *Image adapted from Kim et al. (2019), Figure 1.*

Half of the MJO events in observations do not cross the MC, and $>75\%$ of the events that cross into the MC, weaken during the passage (Zhang & Ling, 2017). This is known as the “MC barrier effect”, and it is exaggerated in most models in the literature (e.g., Seo *et al.*, 2009; Kim *et al.*, 2014, 2019; Liu *et al.*, 2017; Vitart, 2017; Xiang *et al.*, 2015). Figure 1.8 shows Hövmoller diagrams of the MJO-filtered precipitation anomaly from 34 climate models from the Coupled Model Intercomparison Project (CMIP) phase 5 and 6 (Ahn *et al.*, 2020a). Many models fail to represent the evolution of the MJO-associated rainfall over the red box in the MC in Figure 1.8a. The multimodel mean for CMIP6 shows an improvement in the precipitation over the MC compared with the previous generation of the models, CMIP5 (Figure 1.8c,b). The improvement in the CMIP6 models was found to be due to the reduction of the dry bias in the Indo-Pacific warm pool region that many climate models display. Accurate representation of the horizontal moisture gradient is believed to be the key process in propagating the MJO across the MC (Ahn *et al.*, 2020a; Kang *et al.*, 2021; Gonzalez & Jiang, 2019). However, other mechanisms have been proposed to explain the barrier effect: land-locked convection over the MC preventing the MJO passage (e.g., Hagos *et al.*, 2016; Savarin & Chen, 2022a), topography blocking (e.g., Inness & Slingo, 2006; Kim *et al.*, 2017), ENSO-related westward propagating dry anomalies from the central Pacific Ocean (DeMott *et al.*, 2018), and weaker mesoscale circulation over land during the active phase of the MJO over the MC (Birch *et al.*, 2016).

The representation of atmospheric convection presents another challenge in predicting the MJO in NWP models. At coarser horizontal resolutions than ~ 10 km, NWP models use parameterisation schemes for the atmospheric convection. The two main schemes for triggering atmospheric convection used by GCMs are atmospheric instability (local buoyancy) driven schemes and moisture content driven schemes. Moisture based convection schemes are found to improve the eastward propagation of the MJO (Jia *et al.*, 2010; Chang *et al.*, 2019). It is not ubiquitous that the upgrades to the convection schemes will improve the MJO. Often times, they can also degrade the model mean state at the expense of a better MJO (e.g., Kim *et al.*, 2011). The MJO–mean state trade off can be, however, mitigated by the inclusion of parameterisation for the mesoscale convection in the models (Ahn *et al.*, 2019).

At higher horizontal resolutions, typically 4–5 km, models start to explicitly resolve convection. Convection-permitting models can improve the simulations of the MJO (e.g., Howard *et al.*, 2024; Holloway *et al.*, 2013; Zhu *et al.*, 2017).

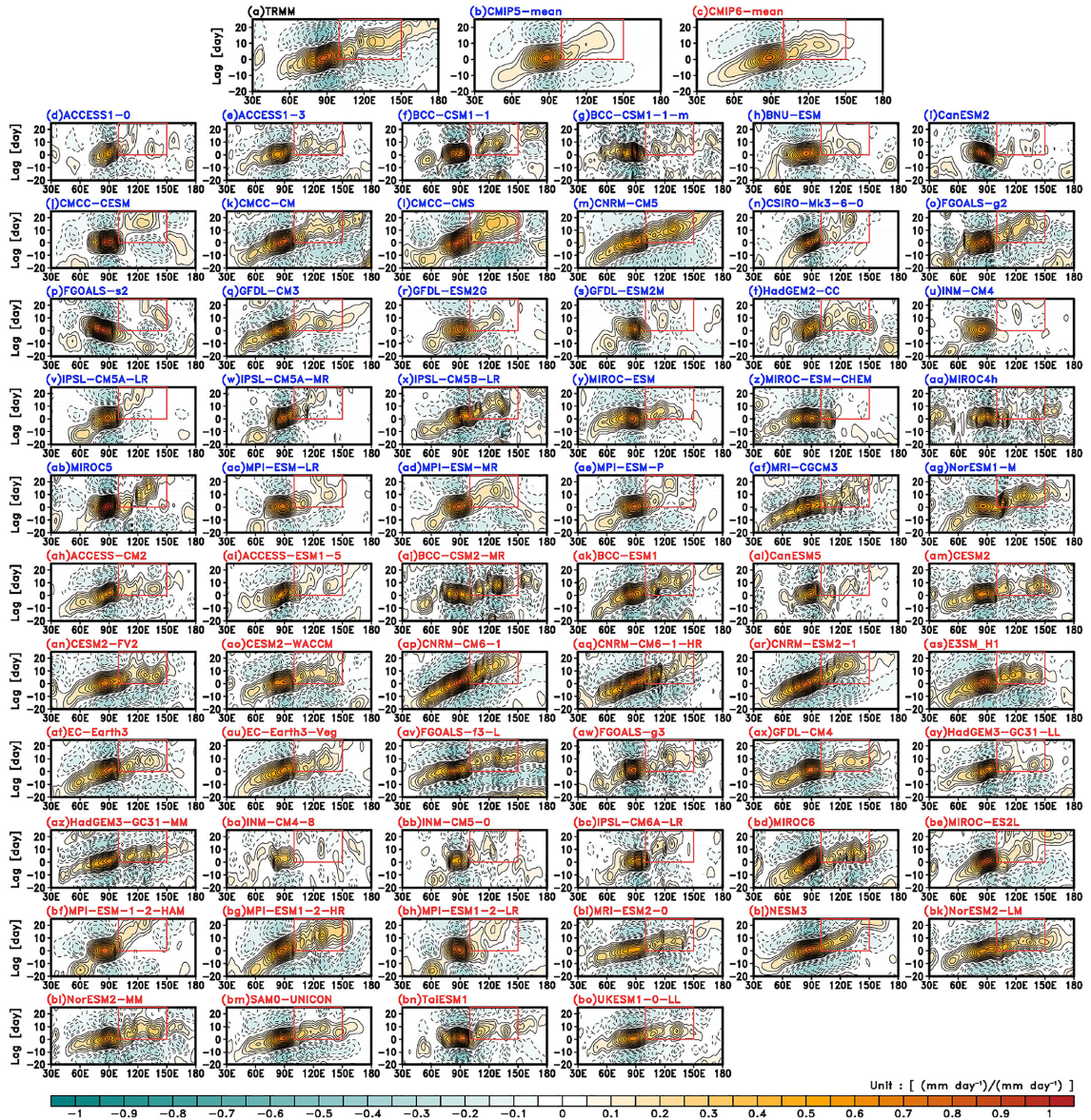


Figure 1.8: Hövmoller diagrams of zonally averaged 20-to-100 day bandpass filtered precipitation anomalies between 10°S and 10°N. The evolution of the precipitation is obtained by a lag-regression against the reference precipitation time series averaged over 85–95°E and 5°S–5°N. a) TRMM (observations); b) CMIP5 mean; c) CMIP6 mean; d–bo) individual models. The red box in each panel denotes the MC. Image adapted from Ahn et al. (2020a), Figure 1.

However, Holloway *et al.* (2013) demonstrated that the increase in the horizontal resolution alone does not necessarily result in a better MJO. The choice of the convection scheme still plays a large role at convection-permitting horizontal resolution, and hence new, scale-aware convection schemes are needed to be developed for convection-permitting models (Kendon *et al.*, 2021). One such scheme, CoMorph, is being developed at the UK Met Office to allow for the interactions between the resolved mechanisms and the parameterised convection in the model (Lavender *et al.*, 2024).

The MJO itself is changing with global climate change and has grown in amplitude over the past century (Subramanian *et al.*, 2014; Jones & Carvalho, 2006; Maloney *et al.*, 2019). Due to more regular occurrences of the MJO and its strengthening amplitude, the MJO predictability at lead day 40 is more skilful now than at the beginning of the 20th century (Du *et al.*, 2024). Climate projections suggest an increase in the MJO precipitation under the climate change scenarios (Bui *et al.*, 2023). Increasing our predictive skill of the MJO is of utmost importance in order to mitigate the risks of extreme precipitation events under global warming effects.

1.4 Ocean–atmosphere interactions during the MJO

Decades of study suggest that the MJO is mainly an atmospheric phenomenon, and the main features of the MJO can be reproduced by models that do not include time-varying ocean components (e.g., Gill, 1980; Wang & Li, 1994; Majda & Stechmann, 2011; Thual *et al.*, 2014). However, there is a growing evidence that ocean feedbacks cannot be neglected during the MJO (for review, see DeMott *et al.*, 2016). In this section, I will provide an overview of the air–sea interactions during the MJO in observations and numerical models.

Reanalysis shows that intraseasonal SST anomalies evolve alongside the eastward propagating MJO (Hendon & Glick, 1997; Woolnough *et al.*, 2000). Warm SST anomalies develop one week prior to the MJO convection in the western Indian Ocean region, enhancing evaporation into the atmosphere and destabilising the atmosphere, leading to atmospheric convection. When the MJO convection develops, the increase in the surface winds and the cloud cover leads to a reduction in the shortwave radiation into the ocean and an increase in the wind-driven mixing, cooling the intraseasonal SST anomalies. Cool intraseasonal SST anomalies inhibit the development of the MJO convection and promote

the suppressed MJO conditions. The suppressed MJO conditions favour the development of warm intraseasonal SST anomalies. The relationship between the MJO and the intraseasonal SST anomalies manifests as eastward propagating SST anomalies of order 0.1 °C, leading the MJO by a quarter of its cycle.

The MJO influence extends further than the SSTs, modulating the ocean surface mixed layer as well (Sui *et al.*, 1997; Drushka *et al.*, 2012; Liu *et al.*, 2021; Savarin & Chen, 2022b). The ocean surface mixed layer is characterised by uniform profiles of temperature and salinity extending from the ocean surface to 10 m–100 m depth in the tropics (de Boyer Montégut *et al.*, 2004). Enhanced MJO convection is associated with deepening of the mixed layer that leads to the cooling of SSTs (Sui *et al.*, 1997; Drushka *et al.*, 2012; Liu *et al.*, 2021; Savarin & Chen, 2022b). An example of the MJO-associated deepening of the mixed layer recorded from a mooring at (90 °E, 0 °N) is presented in Figure 1.9d,j (the mixed layer is denoted by the shallower black line in the diagram). The MJO convection arrives on December 24, 2017 at the location of the mooring (Figure 1.9a), and the MJO passage leads to the deepening of the mixed layer and cooling of the SSTs. Observations show that suppressed MJO conditions lead to the shoaling of the mixed layer, which contributes to warming of the SSTs (Drushka *et al.*, 2014a; Savarin & Chen, 2022b).

Mixed layer heat budgets are conducted in the literature to quantify the relative importance of subsurface oceanic processes within the mixed layer in modulating the intraseasonal mixed layer temperature anomalies (Chi *et al.*, 2014; Drushka *et al.*, 2012; McPhaden & Foltz, 2013; Halkides *et al.*, 2015). Some studies raise the importance of the ocean advection in driving the upper ocean temperature changes during the MJO (Chi *et al.*, 2014; McPhaden & Foltz, 2013; Chandra *et al.*, 2024), while others suggest that the net heat flux is the most prominent driver of the mixed layer temperature changes on the MJO timescales in the tropics (Drushka *et al.*, 2012; Halkides *et al.*, 2015). Observational studies are limited to a select few locations that may not be representative of the tropics (Chi *et al.*, 2014; McPhaden & Foltz, 2013), while reanalyses rely on imperfect ocean models to fill gaps in sparse observational datasets and can be limited by the lack of mesoscale eddy contribution to the mixed layer heat budget (Halkides *et al.*, 2015). *The importance of ocean advection during the MJO is, therefore, still debated in the scientific community, and needs to be further examined in both observations and models.*

The MJO can also affect the formation of barrier layers in the tropics (e.g., Halkides *et al.*, 2015; McPhaden & Foltz, 2013; Drushka *et al.*, 2014a). Barrier

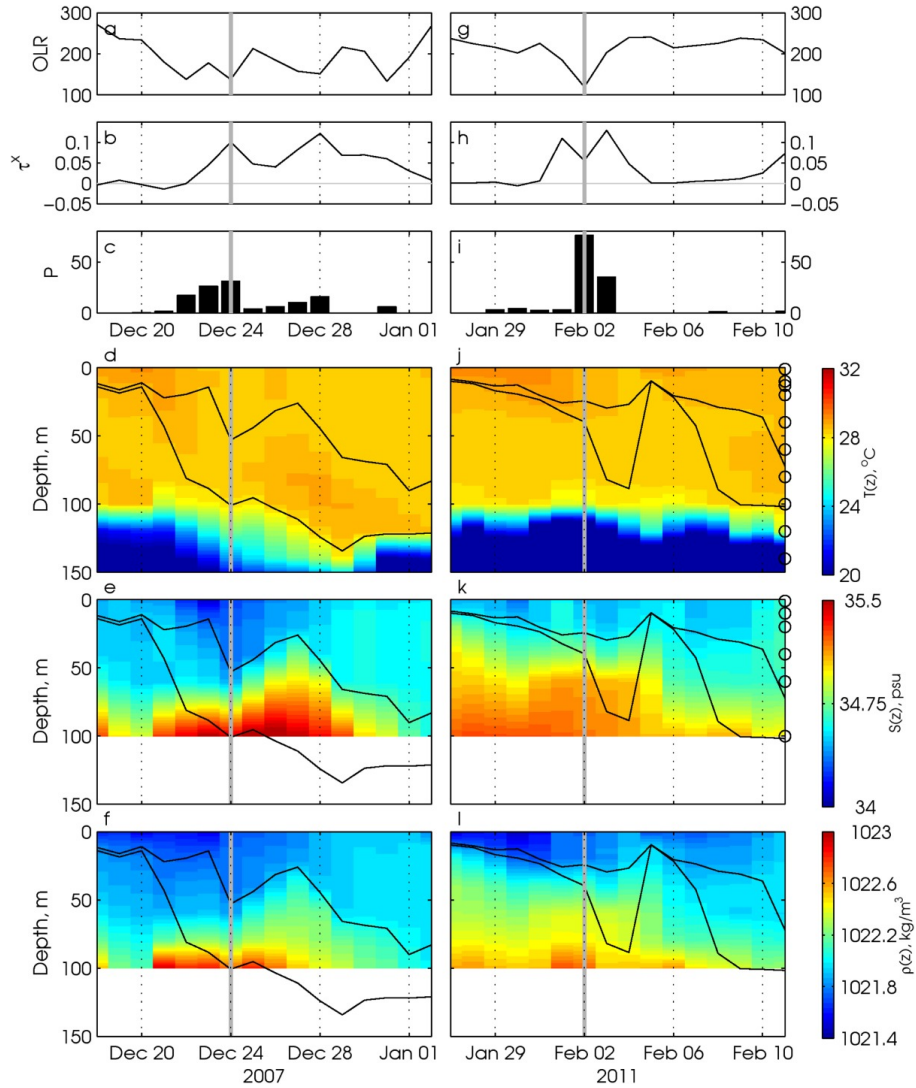


Figure 1.9: Two MJO events observed at the Research Moored Array for African–Asian–Australian Monsoon Analysis and Prediction mooring located at 90°E , 0°N . The left column corresponds to an MJO event that occurred at the end of 2007 and the right column shows an MJO event in January 2011. a) and g) OLR (W m^{-2}); b) and h) zonal wind stress (N m^{-1}); c) and i) daily precipitation (mm d^{-1}); d) and j) temperature ($^{\circ}\text{C}$); e) and k) salinity (psu); f) and l) density (kg m^{-3}). The grey vertical line denotes the peak MJO convection at the location of the mooring. Circles in panels j and k show the depths of the temperature and salinity sensors, respectively. The mixed layer depth and the isothermal layer depth are plotted as black lines in panels d–f and j–l. *Image adapted from Drushka et al. (2014a), Figure 4.*

layers form typically due to the influx of fresh water into the ocean, creating two distinct layers of different salinities within the isothermal layer in the upper ocean. Barrier layers shelter the mixed layer from the thermocline, concentrating the impact of the surface fluxes within the mixed layer. The MJO-associated precipitation can lead to the freshening of the surface mixed layer and result in the formation of strong barrier layers of thickness ~ 50 m in the tropics (Drushka *et al.*, 2014a; Moteki *et al.*, 2018; Savarin & Chen, 2022b). Figure 1.9e shows an example development of a barrier layer at a mooring located at (90 °E, 0 °N) (the barrier layer is shown as the layer between the two black lines in panel e). The precipitation of $>20 \text{ mm d}^{-1}$ associated with the arrival of the enhanced MJO convection on December 24, 2018 (Figure 1.9c) leads to the influx of fresh water into the mixed layer, and to the development of a barrier layer of thickness 50 m at its peak (Figure 1.9e). Thick barrier layers can prevent the intrusion of colder waters from below the mixed layer, leading to a faster recovery of SSTs post the MJO passage (Moteki *et al.*, 2018; Savarin & Chen, 2022b).

In recent years, observational studies have shown that the diurnal variability in the upper ocean temperature can be linked to the MJO (Yan *et al.*, 2021; Itterly *et al.*, 2021). The diurnal variability of SST is influenced by the development of diurnal warm layers. Such layers develop in the upper few metres of the ocean during the afternoon due to a strong daytime increase in the solar radiation at the ocean surface and due to low surface winds (Price *et al.*, 1986; Fairall *et al.*, 1996; Kawai & Wada, 2007). These layers are characterised by an exponential decay in temperature with depth and can increase daily mean SSTs by even up to 1 °C (Matthews *et al.*, 2014). At night, the mixing within the mixed layer and overnight cooling leads to the destruction of these diurnal warm layers. Reanalysis data validated with surface drifters shows that diurnal warm layers can be strong in the tropics, with the diurnal amplitude of SST larger than 0.5 °C (Bellenger & Duvel, 2009). Suppressed MJO convection (sunny weather and low winds) favours the development of diurnal warm layers, while enhanced MJO convection inhibits the development of diurnal warm layers in the tropics. The diurnal variability of SST rectifies the intraseasonal SST variability in the tropics, potentially affecting weather patterns like the MJO (Yan *et al.*, 2021; Itterly *et al.*, 2021). The increase in the diurnal variability of SST in coupled models can lead to a stronger MJO response (Bernie *et al.*, 2007, 2008; Seo *et al.*, 2014; Hsu *et al.*, 2019). *It has been hypothesised that diurnal warm layers affect the MJO, however, there is no composite study to date addressing how this feedback manifests in models and what is its strength.*

On longer timescales, MJO-induced westerly wind bursts can trigger equatorial oceanic Kelvin and Rossby waves. The westerly wind anomalies during the MJO lead to Ekman convergence at the equator, resulting in eastward-propagating downwelling Kelvin waves and westward-propagating upwelling Rossby waves (Battisti, 1988; Giese & Harrison, 1990). These equatorial waves create sea surface height anomalies of 10 cm order, and can lead to substantial changes in the thermocline depth, with disturbances of even 40 m amplitude in the tropics (McPhaden, 1999). There is a growing evidence that these waves influence the upper ocean heat content during the MJO (Rydbeck *et al.*, 2019, 2021, 2023). Webber *et al.* (2010) showed that the westerly wind anomalies associated with the MJO force a downwelling equatorial oceanic Kelvin wave that travels eastward from the western Indian Ocean towards the MC. This wave reflects off the coast of Sumatra as a downwelling equatorial oceanic Rossby wave. This westward travelling Rossby wave arrives ~ 100 days later in the western Indian Ocean, advecting warm SST anomalies there, and leading to the MJO convection initiation in this region. This mechanism was presented by Webber *et al.* (2012b) as a triggering mechanism for primary MJO events.

Subsurface upper ocean processes are difficult to observe with satellite measurements, therefore, there is a need for more in-situ measurements of the upper ocean during the MJO. Two major field campaigns were conducted in years 1992–1993 (Webster & Lukas, 1992) and 2011–2012 (Yoneyama *et al.*, 2013), pointing at the importance of air–sea interactions during the MJO. Many numerical studies show that coupling of the atmosphere to an ocean model can improve the MJO representation in these models (e.g., Kemball-Cook *et al.*, 2002; Woolnough *et al.*, 2007; Kim *et al.*, 2008; Marshall *et al.*, 2008; Fu *et al.*, 2015; Savarin & Chen, 2022a).

There are still gaps in understanding to what extent the upper ocean modulates the MJO. Namely, how does the presence of diurnal warm layers affect the MJO in a coupled ocean–atmosphere model; and what is the importance of ocean advection during the MJO? These gaps motivate the following research questions addressed in the next section of this chapter of this thesis.

1.5 Research questions

The UK Met Office developed a global deterministic coupled ocean–atmosphere model, running in near real-time since 2016, alongside their operational global atmosphere-only NWP system. In May 2022, the Met Office replaced the atmosphere-only model with the coupled model for global forecasting in the operational mode. The work carried out in this thesis was motivated by this replacement to investigate the benefits of the dynamically evolving 3D ocean in predicting the MJO in the tropics, and to examine the air–sea interactions during the evolution of the MJO. The following key research questions are addressed throughout this thesis:

1. *Will coupling the Met Office forecast model to an ocean model improve the MJO predictions in the tropics?*

The introduction of a 3D ocean brings more complexity into the coupled model, and therefore, has a potential to unleash new biases. Chapter 2 investigates why the coupled model predicts faster MJO propagation than the observations and the atmosphere-only model, and presents a hypothesis for a feedback between the upper ocean and the MJO that motivates the next research question addressed in this thesis.

2. *How does the upper 10 m of the ocean modulate the MJO in the coupled model?*

Chapter 3 presents a set of numerical experiments to confirm the hypothesised feedback between diurnal warm layers in the ocean and the MJO. This chapter demonstrates that the presence of diurnal warm layers in the coupled model leads to an increase in the phase speed of the MJO compared with the atmosphere-only model that does not simulate this feedback. Half of the overall increase in the MJO phase speed between the coupled and the atmosphere-only model can be explained by the presence of diurnal warm layers. The remaining half motivates the next research question addressed in this thesis.

3. *How do subsurface oceanic processes within the ocean mixed layer modulate MJO-associated changes in the mixed layer temperature in the tropics?*

Subsurface oceanic processes such as ocean advection and ocean mixing can contribute to intraseasonal changes in the upper ocean temperature in the tropics. These processes are investigated in Chapter 4, where a mixed layer heat budget is conducted to investigate the relative importance of net surface heat flux forcing and subsurface oceanic processes in modulating intraseasonal changes in upper ocean temperature in the tropical Indian Ocean and the Maritime Continent during the MJO.

These three questions will be revisited in Chapter 5, after a thorough examination in their respective chapters.

Chapter 2

The effect of diurnal warming of sea surface temperatures on the propagation speed of the Madden–Julian Oscillation

2.1 Preface

This chapter is an extended version of an article published by the Quarterly Journal of Royal Meteorological Society (Karlowska *et al.*, 2024a) and reformatted into a thesis chapter. This chapter is the sole work of the candidate, with the supervisory team listed as co-authors for their supervisory role. The main body of the article was not altered for this thesis. Footnotes 1, 2 and 4 were added into the thesis chapter, with extra figures in Appendices A, B and C, expanding some of the figures to all MJO phases 1 to 8. These additional figures do not alter the overall conclusions of this chapter.

This chapter presents a hypothesised mechanism by which the upper 10 m of the ocean modulate the propagation speed of the MJO, leading to a faster MJO propagation speed in the coupled model of the UK Met Office compared with the atmosphere-only version of this model.

2.2 Introduction

The Madden–Julian Oscillation (MJO) is the main mode of intraseasonal (30–90 days) weather variability in the tropics (Madden & Julian, 1971). It is comprised of regions of enhanced and suppressed convection ($O(10,000 \text{ km})$) propagating eastward with a phase speed of 5 m s^{-1} across the tropics. The MJO convective anomalies typically originate in the west equatorial Indian Ocean, cross the Maritime Continent (Indonesia, Philippines and Papua New Guinea) and dissipate over the Pacific Ocean. The MJO interacts with many global weather and climate patterns (for review, see Zhang, 2013), and remains a challenge in subseasonal model predictability (e.g., Vitart, 2017; Kim *et al.*, 2019). In the past decade, the rise of coupled ocean–atmosphere Numerical Weather Prediction (NWP) and climate models has led to improvements in MJO predictions and simulations compared with atmosphere-only models (e.g., Ahn *et al.*, 2017; Vitart, 2017). Current coupled ocean–atmosphere seasonal to subseasonal models predict the MJO out to 3–4.5 weeks (Kim *et al.*, 2019), however, many underestimate its propagation speed and amplitude, especially over the Maritime Continent (Kim *et al.*, 2014, 2019; Xiang *et al.*, 2015; Vitart, 2017).

Ocean–atmosphere feedbacks play an important role in MJO propagation across the tropics (DeMott *et al.*, 2015; Li *et al.*, 2013b). During suppressed MJO conditions, reduced cloud cover leads to increased solar radiation at the ocean surface and decreased wind-driven mixing in the surface ocean mixed layer. The surface mixed layer, with typical depths of 10–100 m in the tropics (de Boyer Montégut *et al.*, 2004), is characterised by nearly uniform profiles of temperature and salinity. During the reduced mixing conditions associated with the suppressed phase of the MJO, the mixed layer shoals, leading to a reduction of its heat capacity and enhancing the increase in sea surface temperatures (SSTs) associated with the increased solar radiation. Warm SSTs moisten the low level atmosphere via increased evaporation, creating atmospheric instability and promoting convection. During enhanced convective MJO conditions, lower incoming solar radiation at the ocean surface and increased upward latent heat flux due to strong surface winds leads to increased mechanical mixing, cooling of SST and deepening of the ocean surface mixed layer (Drushka *et al.*, 2012; Liu *et al.*, 2021).

Diurnal changes in solar radiation and surface winds can lead to the development of diurnal warm layers a few metres deep, superimposed on the deeper, residual mixed layer. Seaglider observations during suppressed MJO

conditions show that such layers can increase the temperature of the top few meters in the ocean by 0.8°C , with a daily mean increase of 0.2°C (Matthews *et al.*, 2014). The diurnal warm layer reaches a maximum at approximately 1500 local solar time, and then disappears overnight due to nocturnal mixing. In line with observations, increased diurnal variability of SST is found to increase mean SST in the tropics in coupled model simulations (Bernie *et al.*, 2008; Seo *et al.*, 2014; Hsu *et al.*, 2019). Large diurnal variability of SST can lead to increased specific humidity in the lower troposphere, affecting some simulated MJO events (Hsu *et al.*, 2019). Increased vertical resolution in the upper ocean has also been shown to improve MJO predictions (Ge *et al.*, 2017; Ma & Jiang, 2021). More frequent coupling in coupled models can also lead to stronger diurnal variability of SST and better onset and evolution of MJO convection (Seo *et al.*, 2014). The cooling in the upper ocean due to the passage of the MJO in coupled simulations can also lead to improved eastward MJO propagation (Savarin & Chen, 2022b). Accurate representation of two-way feedbacks between the upper ocean and atmospheric convection is essential for future improvements in MJO predictions.

While coupled ocean–atmosphere climate models are widely used, there are only a few operational short to extended range NWP systems that use coupled configurations (Mogensen *et al.*, 2017; Smith *et al.*, 2018). Recently, the UK Met Office has developed a deterministic coupled ocean–atmosphere model, running in real-time since 2016, alongside the atmosphere-only version of the model. Early hindcast experiments of Shelly *et al.* (2014) showed that the coupled model outperformed the atmosphere-only model during two strong MJO events in 2009 and 2010. However, results of Vellinga *et al.* (2020) over three boreal winters showed little difference between the models in terms of MJO prediction skill. The main difference between the models was found in MJO propagation speed, with the coupled model predicting faster MJO propagation than the atmosphere-only model. In this paper, we examine MJO performance using five years of data from real-time coupled and atmosphere-only NWP systems of the UK Met Office, expanding on the study of Vellinga *et al.* (2020), and using process-based diagnostics to determine the mechanism(s) which lead to the different MJO simulations in the coupled and atmosphere-only models. In section 2.3, the model specifications, data and methodology are described. In section 2.4, we present general MJO performance for both models and mechanisms leading to performance differences between the coupled and atmosphere-only model. Discussion and conclusions follow in section 2.5.

Table 2.1: Model specifications summary.

Start date	End date	Atmosphere horizontal resolution	Atmosphere no. of levels in coupled (atmosphere-only) model	Ocean horizontal resolution	Ocean no. of levels	Global atmosphere (GA) version	Global land (GL) version	Global ocean (GO) version	Global sea ice (GSI) version
1 May 2016	11 July 2017	N768	L85 (L70)	ORCA025	L75	GA6.1	GL6.1	GO5	CSI6
12 July 2017	25 September 2018	N1280	L85 (L70)	ORCA025	L75	GA6.1	GL6.1	GO5	CSI6
26 September 2018	31 December 2019	N1280	L70 (L70)	eORCA025	L75	GA6.1	GL8.1	GO6.0	CSI8.0
1 January 2020	8 December 2020	N1280	L70 (L70)	eORCA025	L75	GA7.2	GL8.1	GO6.0	CSI8.0
9 December 2020	31 May 2021	N1280	L70 (L70)	eORCA025	L75	GA7.2.1	GL8.1	GO6.0	CSI8.1

References: GA6.1 and GL6.1 (Walters *et al.*, 2017); GA7.2, GA7.2.1 and GL8.1 (Walters *et al.*, 2019); GO5 (Megann *et al.*, 2014); GO6.0 (Storkey *et al.*, 2018); CSI6 (Rae *et al.*, 2015); CSI8.0 and CSI8.1 (Ridley *et al.*, 2018)

2.3 Data and methods

2.3.1 Model specifications

The data used in this study were simulated with coupled ocean–atmosphere and atmosphere-only NWP systems of the UK Met Office running daily since 1 May 2016. The atmosphere-only model was the operational forecast model at the time at the Met Office, and the ocean component of the coupled model was the operational ocean forecast model. Models were initialised at 0000 UTC in real-time out to 10 and 7 day lead times for coupled and atmosphere-only models, respectively. Both models yield 1857 forecast initialisations between 1 May 2016 and 31 May 2021. The models use the same atmosphere and land components, with the addition of ocean and sea ice models for the coupled version. Table 4.1 shows a summary of changes in resolution, number of vertical levels and model components (and their references) that occurred during this study.

Both models use a mass-flux convection scheme (Gregory & Rowntree, 1990; Gregory & Allen, 1991) that allows shallow, mid-level and deep convection. For the first 15 months of the data period, the atmosphere and land components used a horizontal resolution of N768 (0.2348° longitude and 0.1568° latitude). From 12 July 2017 the models were upgraded to N1280 (0.148° longitude and 0.098° latitude; ~ 15 km and ~ 10 km at the equator). Prior to September 2018, the coupled model used an extra 15 vertical levels in the stratosphere, later changed to match the atmosphere-only model number of levels. The ocean component of the coupled model uses the Nucleus for European Modelling of the Ocean (NEMO) consortium ocean model (Madec *et al.*, 2017), with horizontal resolution of 0.25° and 75 vertical levels, 8 of which are in the top 10 m of the ocean. The ocean–sea ice and atmosphere–land components are initialised with uncoupled data assimilation (DA) systems. The atmosphere–land component uses a 4D-Var DA system (Rawlins *et al.*, 2007) (hereafter, “UM

Analysis”), initialised at 0000 UTC, with SST and sea ice concentrations from the Operational Sea Surface Temperature and Ice Analysis (OSTIA) (Donlon *et al.*, 2012) assimilation system, updated by Fiedler *et al.* (2019) and Good *et al.* (2020). The initial SST and sea ice concentrations are held constant throughout the atmosphere-only forecasts. The ocean-sea ice component uses Forecast Ocean Assimilating Model (FOAM)-NEMOVAR DA system from Blockley *et al.* (2014) and Waters *et al.* (2015) (hereafter, “FOAM”). The coupled model exchanges information between ocean–sea ice and atmosphere–land components every 1 h. For more detailed description of model configurations, see section 2 in Vellinga *et al.* (2020).

2.3.2 Real-time Multivariate MJO index

MJO performance is quantified using the Real-time Multivariate MJO index (RMM) index, originally from Wheeler & Hendon (2004). Full methodology on how the indices are calculated can be found in Gottschalck *et al.* (2010), with references therein. The index uses daily anomalies of top-of-atmosphere outgoing longwave radiation (OLR) and zonal winds at 850 hPa and 200 hPa. The indices RMM1 and RMM2 represent the principal component time series of the dominant spatial structures (Empirical Orthogonal Functions, EOFs) of the data. The combination of RMM1 and RMM2 defines 8 MJO phases depending on the location of the MJO convection in the tropics, with phases 8 and 1 being in the Western Hemisphere and Africa, phases 2 and 3 in the Indian Ocean, phases 3 and 4 in the Maritime Continent and phases 6 and 7 in the Western Pacific. The amplitude of the MJO is defined as $\sqrt{\text{RMM1}^2 + \text{RMM2}^2}$. Here, the active MJO is defined by days when amplitude ≥ 1.0 .

We use two RMM indices for model verification: the Wheeler-Hendon index (Wheeler & Hendon (2004), retrieved from <http://www.bom.gov.au/climate/mjo>) and RMM indices calculated from the UM Analysis, using daily means from runs initialised at 0000 UTC and 1200 UTC. RMM indices for both models are calculated from runs initialised at 0000 UTC. The model indices are compared with these two datasets using four standard scalar metrics following Lin *et al.* (2008) and Rashid *et al.* (2011): bivariate anomaly correlation coefficient, root-mean-square error (RMSE), amplitude error and phase error. The bivariate anomaly correlation coefficient corresponds to the spatial correlation between forecasts and observations. A model is considered skilful when $\text{RMSE} < \sqrt{2}$ and correlation > 0.5 (Lin *et al.*, 2008). Amplitude error is negative (positive)

when the model underestimates (overestimates) MJO RMM amplitude. Phase error in the (RMM1, RMM2) plane is defined as an angle (in degrees) and is positive (negative) when the MJO is ahead of (behind) the observations. The RMM statistics are calculated for the boreal winter season (November–April) for active MJO days between 1 May 2016 and 31 May 2021. The same analysis was performed for all available data and winter season only data. Qualitatively, no notable difference was observed in RMM skill metrics between these two periods¹.

2.3.3 Composites

Composite maps are calculated from daily means of meteorological variables. The high resolution original model data is regrided to N180 ($1^\circ \times 1^\circ$) horizontal resolution before processing. Anomalies in this paper are obtained by subtracting the seasonal cycle (comprised of the annual mean and first three harmonics) for 2017–2020. The MJO anomalies are temporally filtered anomalies with a 20–200 day bandpass Lanczos filter (Duchon, 1979). Data from each lead day is processed separately by concatenation of all days at a given lead time from separate forecast initialisations. Composites are split by MJO phases on lead day 1 according to Wheeler–Hendon RMM indices. Lead days from consecutive forecast initialisations with the same initial RMM phase are treated as one event and averaged before compositing. The statistical significance of composite differences between the models at 95 % significance level are calculated using a Student’s t-test. All composites are for initially active MJO forecasts during boreal winter season (November–April) for 1 November 2016 to 22 January 2021 (or 7 January 2021 for OLR based on observed data availability). Missing days were interpolated between the nearest previous and next day forecast.

Subsurface ocean data were processed along an equatorial transect to study the vertical profile of ocean–atmosphere interaction in the coupled model. The mixed layer depth is defined following Drushka *et al.* (2014a), as the depth where the potential density (σ) change from the potential density at a reference depth of 10 m is greater than a threshold given by:

$$\Delta\sigma = \sigma(T_{\text{ref}} - \Delta T, S_{\text{ref}}, P_0) - \sigma(T_{\text{ref}}, S_{\text{ref}}, P_0), \quad (2.1)$$

where T_{ref} and S_{ref} are the temperature and salinity at the reference depth 10 m,

¹Skill metrics for boreal winter season and year-round data are displayed in Appendix A (Figures A1–A4).

P_0 is surface pressure, and $\Delta T = 0.8^\circ\text{C}$ is chosen as the optimal value following Kara *et al.* (2000). The reference depth of 10 m was chosen deliberately to remove the effects of the diurnal cycle of temperature on mixed layer depth (e.g., de Boyer Montégut *et al.*, 2007; Hosoda *et al.*, 2010). Temperature and salinity from the coupled model were interpolated in depth to every 1 m resolution between 0 m and 1000 m before calculating mixed layer depth. Potential density calculations were obtained using Python package gsw v3.4.0 based on definitions from Gibbs SeaWater Oceanographic Toolbox of TEOS-10 (McDougall & Barker, 2011). The coupled model diurnal warming (dSST) is defined as the difference between 1500 and 0600 local solar time SST.

2.3.4 Observational datasets

Observed daily interpolated OLR was obtained from National Oceanic and Atmospheric Administration (NOAA) at $2.5^\circ \times 2.5^\circ$ resolution (Liebmann & Smith, 1996). ERA5 reanalysis data was used for hourly 10 m windspeed (Hersbach *et al.*, 2020) at $0.25^\circ \times 0.25^\circ$ resolution. NOAA OLR and ERA5 winds were interpolated onto a $1^\circ \times 1^\circ$ grid for comparison with model data. Daily mean shortwave radiation was obtained from the CERES SYN1deg dataset at $1^\circ \times 1^\circ$ resolution (Rutan *et al.*, 2015).

2.4 Results

2.4.1 MJO model performance

Both the coupled and the atmosphere-only models are skilful in predicting the MJO, with bivariate correlation coefficients above 0.94 within the first 7 lead days, reaching just above 0.88 for the coupled model by lead day 10 (Figure 2.1a). Regardless of the analysis dataset used to compare the models, there is little difference between the models in the bivariate correlation coefficients. The RMSE for Wheeler–Hendon indices (Figure 2.1b, dashed lines) is twice as large as the UM Analysis RMSE on lead day 1 (Figure 2.1b, solid lines). As both models are initialised from the UM Analysis, the initial RMSE is expected to be low in this case, but it converges towards the Wheeler–Hendon RMSE later in the forecast. Overall, both models are within the skilful RMSE threshold, reaching 0.62 by lead day 7. The extended forecasts from the coupled model reach 0.90 RMSE by lead day 10, still within the threshold. The MJO is too weak in both models at all lead

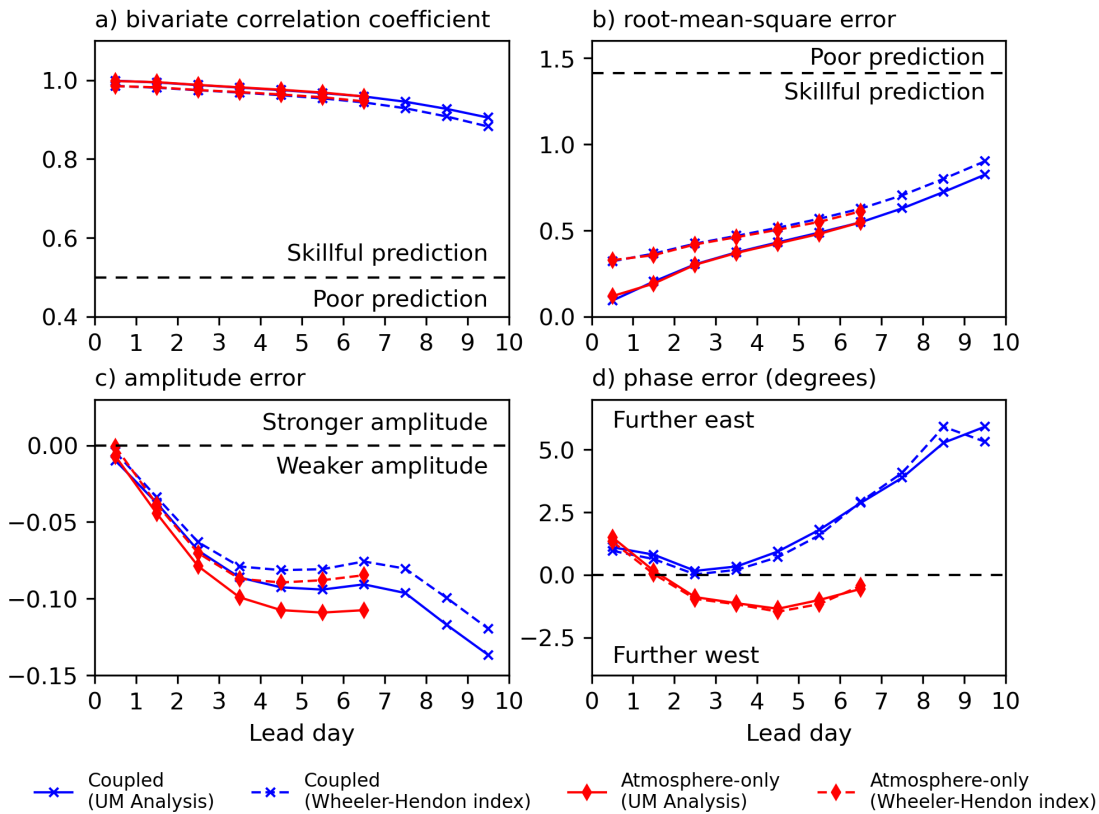


Figure 2.1: RMM skill statistics as a function of lead day. a) bivariate correlation coefficient; b) root-mean-square error; c) amplitude error; d) phase error. Daily coupled (blue) and atmosphere-only model (red) data are compared for boreal winter season (November–April) and active MJO days only with UM Analysis (solid) and Wheeler-Hendon indices (dashed).

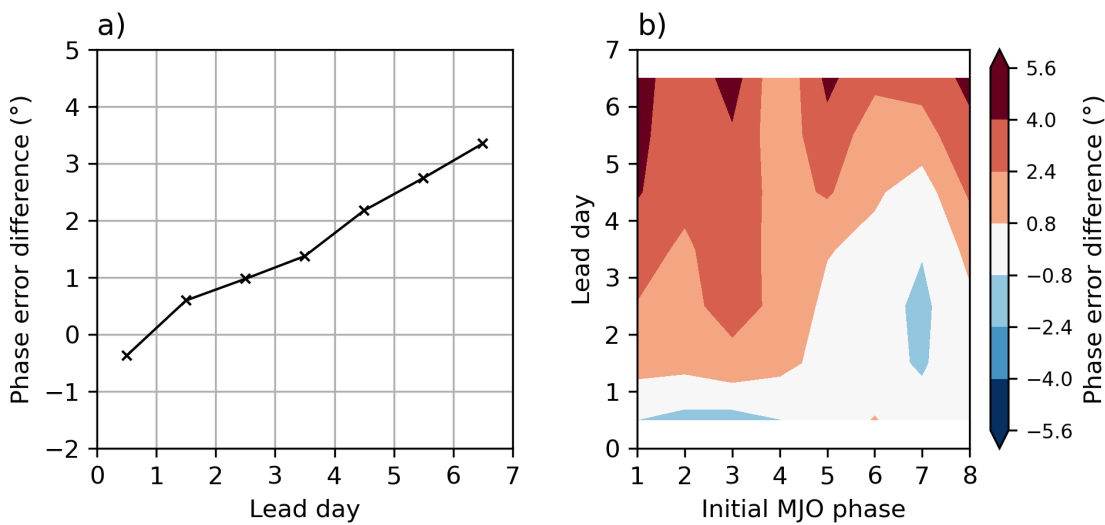


Figure 2.2: Phase error difference between the coupled and atmosphere-only model for a) all MJO phases combined and b) split by the initial RMM phase that the forecast started in.

times (Figure 2.1c), with smaller amplitude errors for the coupled model than the atmosphere-only model at lead day 3 and beyond.

The largest difference between the models is observed in phase error (Figure 2.1d). At lead day 1, both models predict the MJO to the east of the verification datasets. Afterwards, the coupled model tends to predict the MJO further east, with a linear increase in phase error reaching $>5^\circ$ (in RMM phase space) by lead day 10. The atmosphere-only model predicts the MJO further west than the verification datasets at lead day 2 and beyond, with a constant phase error at around -1.5° (in RMM phase space). This implies correct MJO propagation speed in the atmosphere-only model from lead day 2, albeit with the MJO anomalies placed too far to the west. Phase error in the coupled model linearly increases at a rate $\sim 0.6^\circ \text{d}^{-1}$ (in RMM phase space) compared to the atmosphere-only model (Figure 2.2a). The positive phase error difference can be interpreted as the coupled model MJO anomalies located to the east of the MJO anomalies simulated by the atmosphere-only model. During the study period, the average RMM phase speed of the MJO was 5.2°d^{-1} (and 4.9°d^{-1} for MJO events that stayed active crossing into the MC, i.e. RMM phase 5). The increase in phase angle error between the models of $\sim 0.6^\circ \text{d}^{-1}$ (in RMM phase space) is equivalent to $\sim 12\%$ per day increase in MJO phase speed in the coupled model compared with the atmosphere-only model.

The same forecast skill analysis was performed for forecasts split by initial MJO phase (from phase 1 to 8 defined by the Wheeler–Hendon indices, hereafter referred to as MJO phases). The bivariate correlation coefficient (Figure 2.3a-b) and RMSE (Figure 2.3c-d) are similar between the models within 7 lead days across all phases. Forecasts initialised in phases 4–6 perform better than forecasts initialised in other phases. In particular, forecasts starting in phases 1–3 show skill that drops below 0.88 after lead day 8 for the coupled model. During MJO phases 1 to 3, the enhanced convection is present over the Indian Ocean. By lead day 8 the convective envelope moves eastward, reaching the MC. The MC is known to produce a so-called “barrier effect” that leads to a weaker MJO or its total disappearance (e.g., Zhang & Ling, 2017). The barrier effect tends to be stronger in models than observed (Seo *et al.*, 2009; Kim *et al.*, 2014, 2019; Liu *et al.*, 2017; Vitart, 2017; Xiang *et al.*, 2015). The decrease in coupled model performance at lead day 8 and beyond in initial MJO phases 1 to 3 is likely a result of the barrier effect present in the model.

Variations in amplitude error are larger when individual phases are considered (Figure 2.3e–f). Generally, amplitude is underestimated in phases 5–8

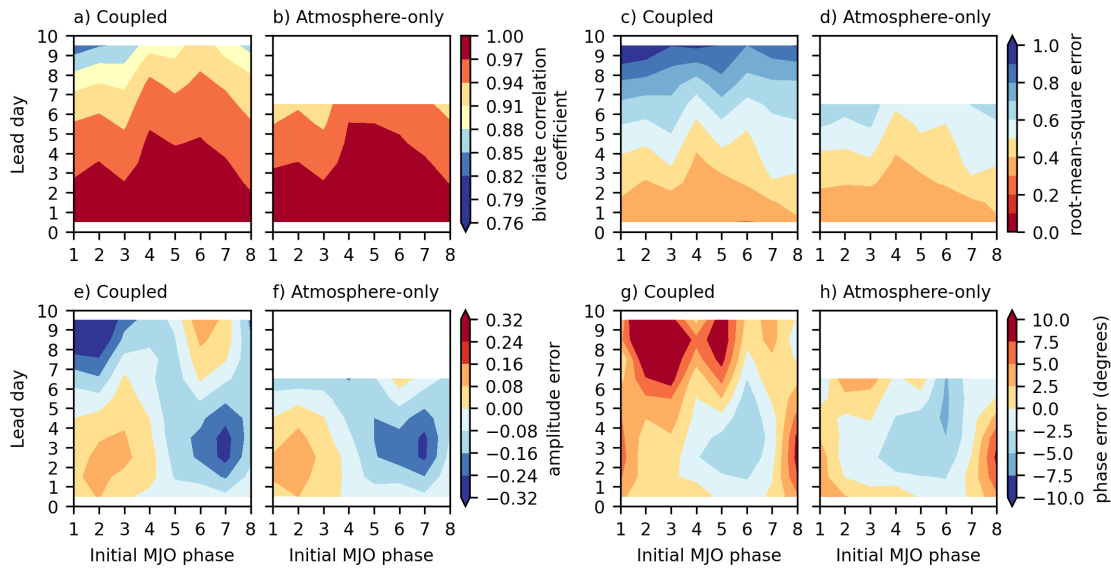


Figure 2.3: RMM skill statistics as a function of lead day split by the initial RMM phase that the forecast started in. a–b) bivariate correlation coefficient; c–d) root-mean-square error; e–f) amplitude error; g–h) phase error.

up to lead day 7 and in phases 1–3 after lead day 7. This coincides with active MJO convection over the MC, where both models display weaker convection and circulation than observed. The phase error shows that the atmosphere-only model simulates the MJO too far to the west across most phases (Figure 2.3h), consistent with the slow propagation seen in Figure 2.1d. The coupled model simulates the MJO too far to the east across all MJO phases at lead day 7 and beyond (Figure 2.3g). The phase error difference between the coupled and atmosphere-only model in phases 1–3 displays a similar trend to the average in Figure 2.2a, with $\sim 0.6^\circ$ increase per day in RMM phase space (Figure 2.2b). In phase 4, the increasing trend is observed up to lead day 4. Afterwards, the phase error difference between the models is steady and positive, implying that both models simulate MJO at a similar speed, with the coupled model anomalies located to the east of the atmosphere-only model anomalies. In initial phases 5–8, the coupled model MJO anomalies are located to the west of the atmosphere-only MJO anomalies until lead day 3, contrary to the average trend. Afterwards, the phase error difference linearly increases between the models, consistent with the average behaviour in Figure 2.2a.

2.4.2 MJO convection in the models and SST-MJO relationship

Both models predict the MJO well with slight differences in MJO convective (OLR) anomalies by lead day 7 in different initial MJO phases. In initial MJO phase 1, the observed MJO shows enhanced convection (negative OLR anomalies) over the equatorial Indian Ocean region (EIO, 5°S–5°N, 70°E–90°E) and suppressed MJO convection (positive OLR anomalies) in the western MC (Figure 2.4a)². Both models capture this convection pattern well (Figure 2.4c, e). By lead day 3, the coupled model exhibits stronger convection than the atmosphere-only model in the active convective EIO region (negative OLR differences of up to 5.5 W m⁻² by lead day 7; Figure 2.4g). In the convectively suppressed central MC region (120°E–135°E), convection in the coupled model is less suppressed than in the atmosphere-only model from lead day 3, leading to a negative 6.5 W m⁻² OLR difference between the models by lead day 7 (Figure 2.4g). In initial MJO phase 4, observations show reversed convective anomalies to those of phase 1, with enhanced MJO convection over the EIO and the MC regions (Figure 2.4b). As the MJO propagates eastward in initial phase 4, the EIO becomes a region of suppressed convection from lead day 4 onward. Again, both models simulate this fairly well (Figure 2.4d,f). However, from lead day 3, the coupled model suppresses convection faster in the EIO region than the atmosphere-only model, reaching a positive OLR difference of 5.9 W m⁻² between the models by lead day 7 (Figure 2.4h).

These two initial MJO phases display the largest spatial differences in OLR anomalies between the coupled and atmosphere-only model at lead day 7 (Figure 2.5, other phases are displayed in Figure B3 in Appendix B). In initial phase 1, both the EIO and central MC regions display a spatially coherent difference in OLR anomaly between the models at 95% significance level (Figure 2.5a). In initial phase 4, the OLR anomaly difference is at the 95% significance level across almost the entire EIO region. Since both models use the same land and atmosphere components (and hence the same cumulus parameterisation scheme), the OLR anomaly differences must be driven by different ocean boundary conditions (i.e. SSTs) in the models.

Already at lead day 1 daily mean, the models exhibit differences in MJO-associated SST anomalies³ in initial phases 1 and 4 (Figure 2.6a and

²Hovmöller diagrams for initial MJO phases 1 to 8 are provided in Appendix B (Figures B1–B2).

³20–200-day filtered SST anomalies from the mean and the first three harmonics of the annual cycle averaged over each MJO phase

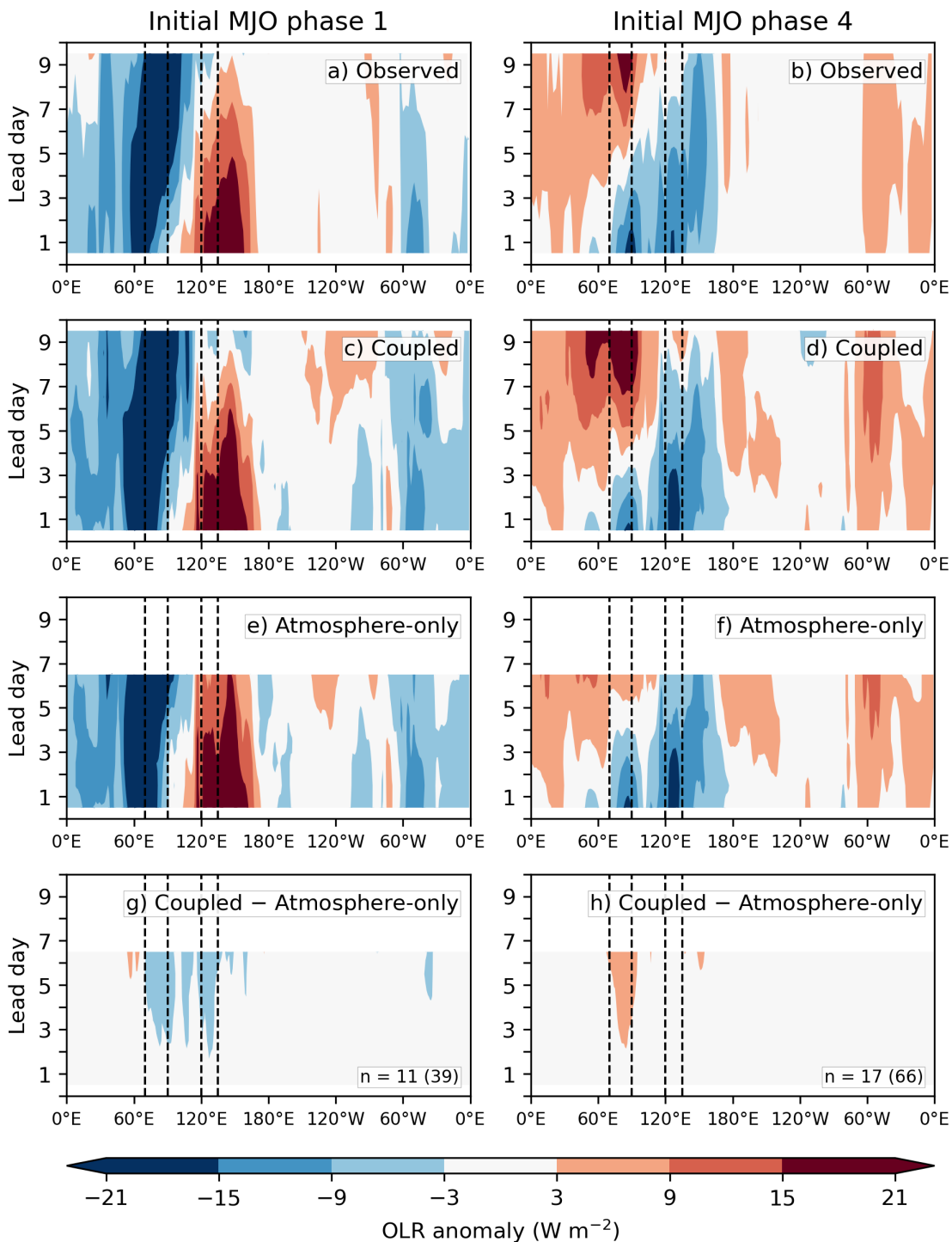


Figure 2.4: Hovmöller diagrams of daily mean composites of 20-200 day filtered boreal winter OLR anomaly averaged over the equatorial band (5°S – 5°N), for forecasts initialised in MJO phases 1 and 4. a–b) observed; c–d) coupled model; e–f) atmosphere-only model; g–h) difference between coupled and atmosphere-only models. Vertical dashed lines represent equatorial Indian Ocean and central Maritime Continent regions. Initially active MJO forecasts only. Number n denotes the amount of independent events used in the composite (total number of days used displayed in the bracket).

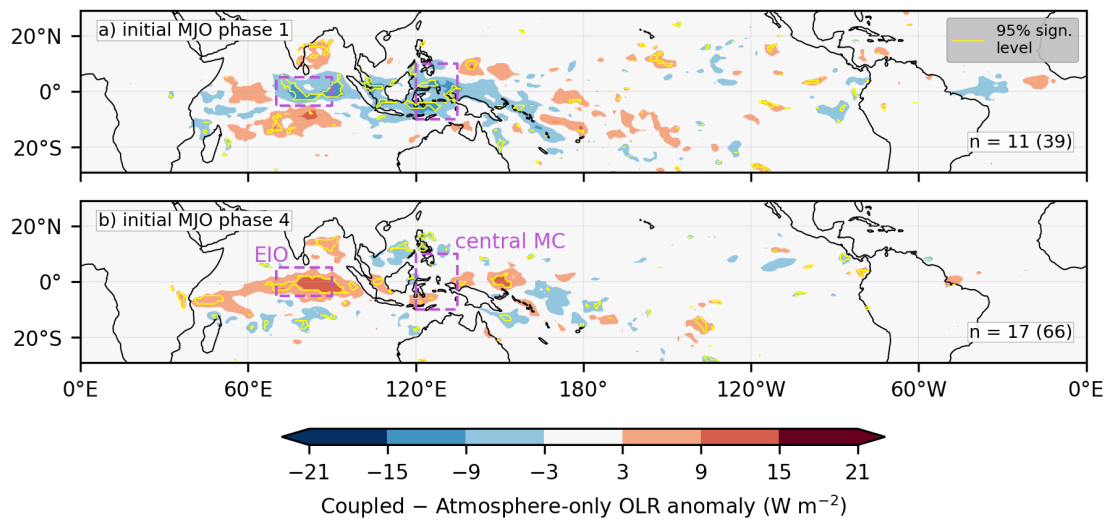


Figure 2.5: Difference at lead day 7 between composite daily means of coupled and atmosphere-only model 20-200 day filtered boreal winter anomaly of OLR for forecasts initialised in MJO phases a) 1 and b) 4. Initially active MJO forecasts only. Number n denotes the amount of independent events used in the composite (total number of days used is displayed in the bracket). RMM indices from Wheeler-Hendon. EIO – equatorial Indian Ocean; MC – Maritime Continent. The yellow contour outlines differences significant at the 95% level.

c)⁴. These differences remain fairly constant throughout the forecast and their evolution is consistent with the differences in OLR that develop between the models by lead day 7 (Figure 2.5). In initial phase 1 at lead day 1, the coupled model develops warmer MJO-associated SST anomalies in the central MC region compared with the atmosphere-only model persisted SST by $0.12\text{ }^{\circ}\text{C}$ (Figure 2.6a). During the suppressed convective conditions of MJO phase 1 in the central MC (Figure 2.4c), warm MJO-associated SST anomalies will lead to enhanced latent heat (LH) flux into the atmosphere in the region. The evaporation linked to this LH flux exchange will moisten the low level atmosphere, and in line with the moisture mode theory for eastward MJO propagation (e.g., Sobel & Maloney, 2013), this moisture anomaly will lead to more convection in the coupled model ahead of the main MJO convective envelope. Therefore, these increased warm MJO-associated SST anomalies in the central MC region at lead day 1 will lead to increased MJO propagation in the coupled model by lead day 7.

In initial phase 4, the coupled model shows colder MJO-associated SST anomalies in the EIO region than the atmosphere-only model at lead day 1 by

⁴For completeness, the difference in the MJO anomaly of SST between the coupled and the atmosphere-only model at lead day 1 for initial MJO phases 1 to 8 is displayed in Appendix C (Figure C1).

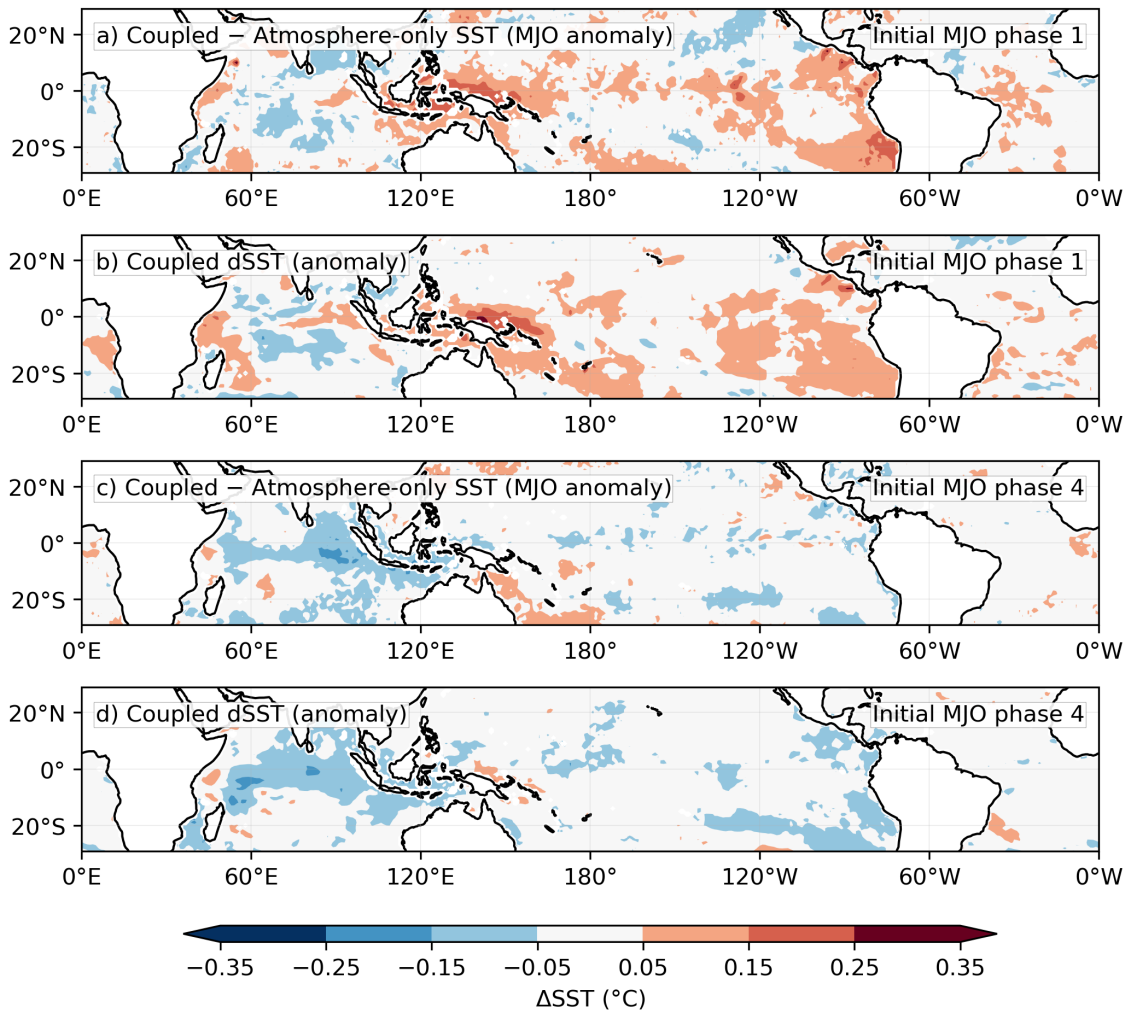


Figure 2.6: Composite daily mean at lead day 1 for a) coupled minus atmosphere-only model MJO-associated SST anomaly difference in MJO phase 1; b) anomalous coupled model diurnal warming of SST in MJO phase 1; c) coupled minus atmosphere-only model MJO-associated SST anomaly difference in MJO phase 4; d) anomalous coupled model diurnal warming of SST in MJO phase 4. Boreal winter and initially active MJO forecasts only.

0.08°C (Figure 2.6c). This region is in suppressed MJO conditions in phase 4 at lead day 1 (Figure 2.4d), and the colder MJO-associated SST anomalies will lead to inhibited convection in the coupled model there, causing a stronger suppressed MJO phase behind the main MJO convective envelope (Figure 2.5b). Therefore, these SST differences between the models will consistently lead to faster propagation in the coupled model, consistent with the phase speed differences we observe in Figure 2.2. The next question to address is how these SST differences arise.

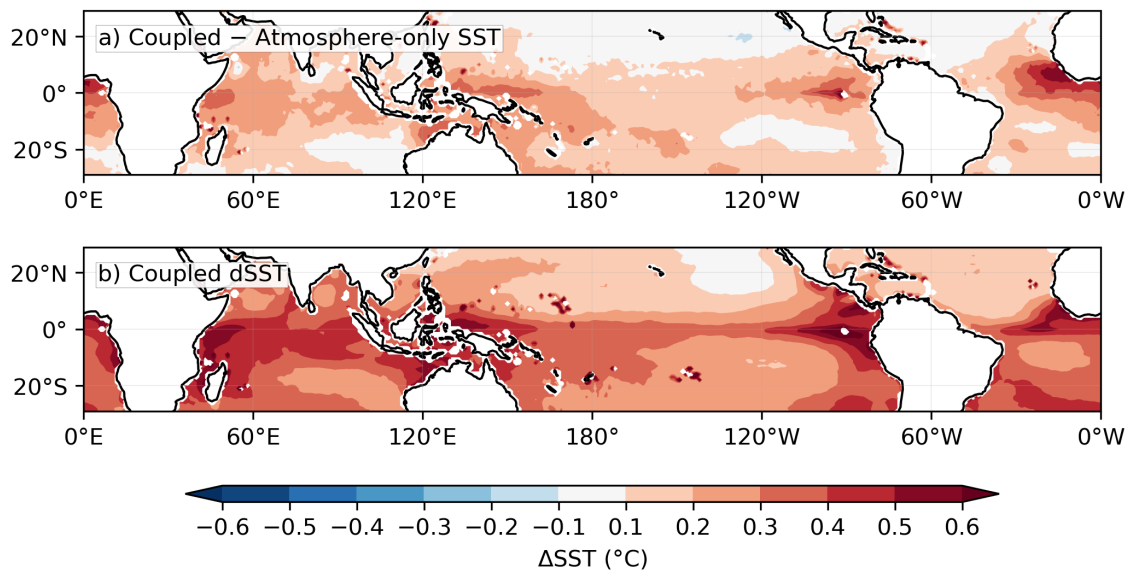


Figure 2.7: Composite daily mean at lead day 1 for a) coupled and atmosphere-only model SST difference for all MJO phases; b) coupled model 1500 and 0600 local solar time SST difference for all MJO phases. Boreal winter and initially active MJO forecasts only.

2.4.3 Diurnal warming of sea surface temperatures

In this section, the role of the diurnal cycle in SST in the coupled model is examined, as a potential explanation of the SST differences between the coupled and atmosphere-only model.

2.4.4 Rectification of diurnal warm layer on daily mean SST

The atmosphere-only model is initialised from the previous day OSTIA foundation SSTs, corresponding to bulk 10 m night-time ocean temperature which excludes the effects of diurnal warming. The coupled model initial SST is the FOAM Analysis 0000 UTC instantaneous ocean temperature at the top model level at 0.51 m. Hence, the coupled model initial SSTs refer to a shallower depth than the atmosphere-only initial SSTs. Additionally, the coupled model initial SSTs will have an extra component of longitudinal variation as incoming solar radiation depends on local solar time (LST) at 0000 UTC. The initialisation difference in SST between the models is, however, insignificant (not shown).

The coupled model SSTs are warmer than the atmosphere-only SSTs at lead day 1 across the tropics by 0.1–0.4 °C (Figure 2.7a). The diurnal warming of SST in the coupled model (dSST; Figure 2.7b), defined here as the difference between

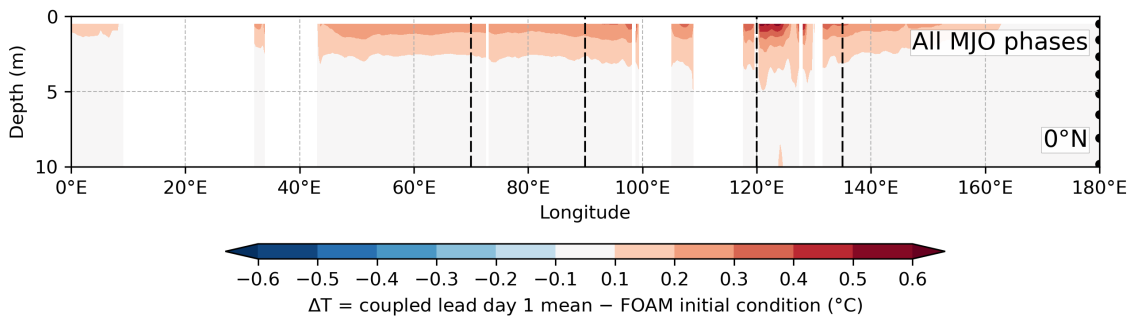


Figure 2.8: Composite mean vertical section of ocean temperature change, from FOAM initial condition to lead day 1 mean (centred at 12 h lead time), from the coupled model at the equator for all MJO phases. Boreal winter and initially active MJO forecasts only. Model levels are displayed as black dots at 180°E.

1500 and 0600 LST SST, displays a similar spatial pattern to the SST difference between the models seen in Figure 2.7a (spatial correlation coefficient between the two patterns is 0.65 over the warm pool region 60–180°E). The difference between the models is around half the magnitude of the dSST because the model difference is calculated from daily mean SSTs. The strongest dSST occurs close to the equator, peaking in the central MC and north of New Guinea at 0.5–0.6°C. The largest positive SST difference between the models is also recorded there, at 0.2–0.3°C. The dSST is weaker in the Indian Ocean basin (up to 0.5°C), where a weaker SST difference also occurs, albeit still positive at 0.1–0.3°C. Hence, the zonal gradient in dSST compounds the effects of the underlying zonal gradient in the background SST in the coupled model, leading to a larger zonal gradient in the daily mean SST in the coupled model, when compared to the foundation SST used in the atmosphere-only model. This stronger SST gradient across the Indo-Pacific warm pool could improve the propagation of the MJO in the coupled model (Hu *et al.*, 2022). The spatial pattern of the dSST across the tropics in the coupled model (Figure 2.7b) is broadly consistent with moored buoy array observations (Yan *et al.*, 2021) and reanalysis data validated with surface drifters (Bellenger & Duvel, 2009). Stronger dSST over the MC can be attributed to the minimum in surface winds in that region present in the coupled model, and ERA5 reanalysis (not shown). This is consistent with glider observations that show that weaker winds and stronger SW flux into the ocean lead to stronger diurnal warming (e.g., Matthews *et al.*, 2014).

Further evidence of the role of the diurnal warm layer can be gained by examining profiles of temperature in the upper ocean. While sub-daily vertical profiles of ocean temperature are not available from the coupled model output, the difference between lead day 1 daily mean temperature and the FOAM initial

condition can capture the diurnal warm layer evolution over the warm pool region (between 60 °E and 150 °E at the equator). The FOAM initial condition is at 0000 UTC, corresponding to 0400 LST at 60 °E and 1000 LST at 150 °E. Hence, over the warm pool region, these initial conditions coincide approximately with the cool phase of the diurnal warm layer. The day 1 daily mean from the forecast model corresponds to the average of the diurnal cycle. Therefore, this daily mean in the warm pool region will be warmer than the FOAM initial condition, and correspond approximately to the daily-mean strength of the diurnal warm layer. In the western hemisphere, the model is initialised during the peak diurnal warm layer strength, therefore, the daily mean temperature profile in this region will be colder than the initial condition.

The coupled model ocean temperature shows an increase of >0.1 °C in the top 5 m of the Indo-Pacific Ocean basin from the initial condition to the day 1 daily mean (Figure 2.8). Crucially, the warming is not uniform across the region; the strongest and deepest warming occurs over the MC (0.4–0.6 °C), while in the EIO region, the warming is weaker at 0.1–0.3 °C. This is consistent with the patterns of SST difference between the models and the coupled model dSST in Figure 2.7a and b. Subsequent daily mean changes (after day 1) in warm pool SST and upper ocean temperature in the coupled model are much smaller (less than 0.1 °C; not shown). We also note that the western hemisphere records a cooling in the upper 5 m of similar magnitude to the warming seen in Figure 2.8; local time in the western hemisphere at this time corresponds to the cooling phase of the diurnal warm layer. Hence, the coupled model resolves the diurnal warm layer formation in the upper 5 m of the ocean model. This process leads to elevated daily mean SST in the coupled model, and contributes to faster eastward MJO propagation via surface flux exchange.

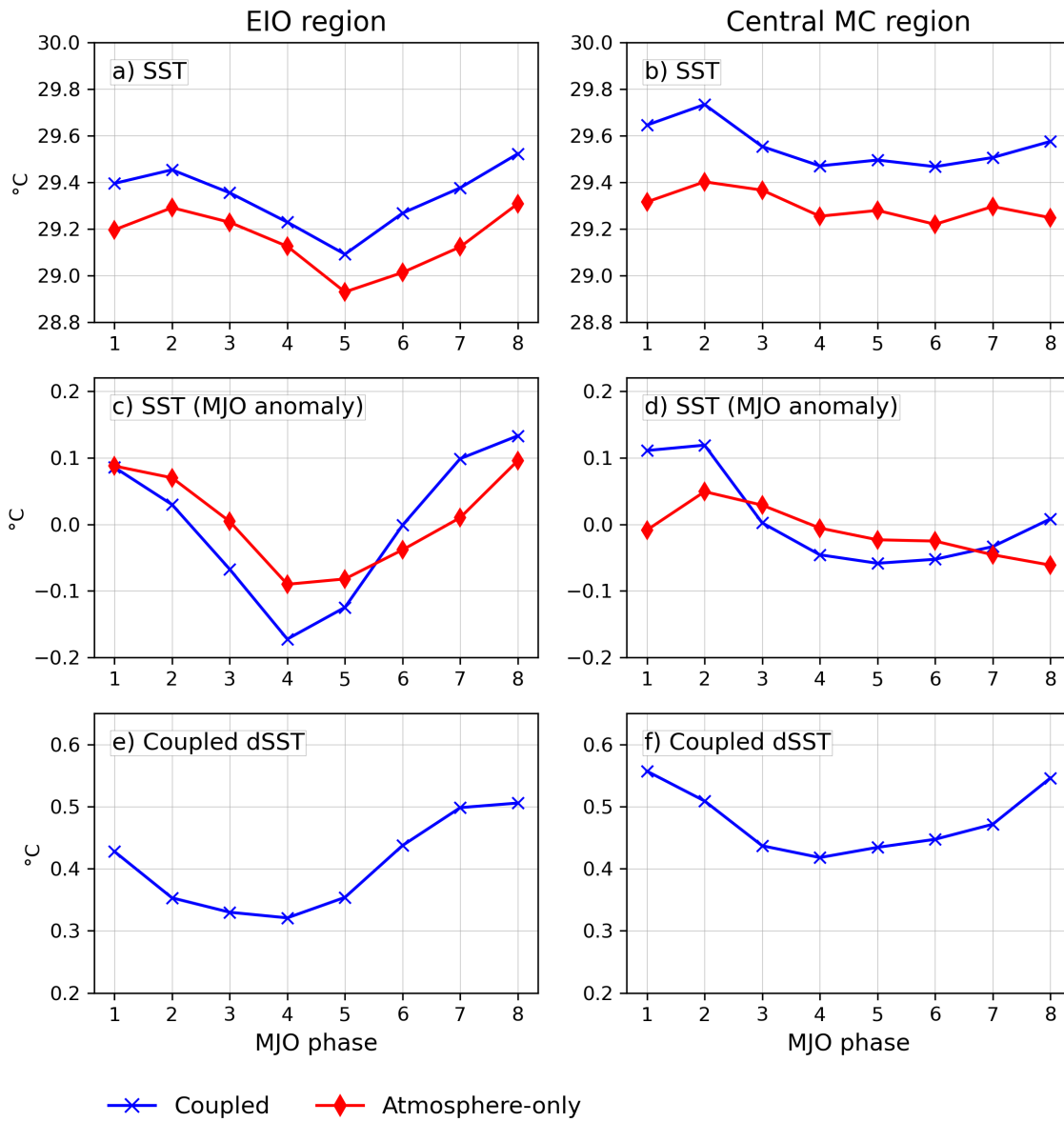


Figure 2.9: Composite lead day 1 daily means for coupled (blue) and atmosphere-only (red) models for: a)–b) sea surface temperatures (SST); c)–d) MJO-associated SST anomalies; e)–f) diurnal warming of SST as a difference between 1500 and 0600 local solar time (LST) SST. EIO and central MC region extents in Figure 2.5. Boreal winter and initially active MJO forecasts only.

2.4.5 Diurnal warm layer strength dependence on MJO phase

The systematic warming in the coupled model SSTs at lead day 1 compared with the atmosphere-only model SSTs is present across all MJO phases. It has magnitude $\sim 0.2^\circ\text{C}$ in the EIO region (Figure 2.9a) and $\sim 0.3^\circ\text{C}$ in the central MC region (Figure 2.9b), and this magnitude is approximately constant across all MJO phases. However, there is considerable variation across MJO phases in the MJO-associated SST anomalies after the removal of the mean and annual cycle, and 20-200 day bandpass temporal filtering applied (Figure 2.9c–d). These MJO-associated SST anomalies will lead to MJO convection anomalies (Matthews, 2004; Woolnough *et al.*, 2001). Moored buoy array observations show that diurnal warming indirectly rectifies MJO-associated SSTs (Yan *et al.*, 2021). The atmosphere-only MJO-associated SST anomalies at lead day 1 roughly correspond to OSTIA dataset of MJO-associated SSTs anomalies⁵ and by definition exclude any diurnal warming effects. The coupled model resolves the diurnal warm layer formation, therefore, according to findings of Yan *et al.* (2021), the dSST in the coupled model may indirectly affect its MJO-associated SST anomalies. Indeed the coupled model dSST values (Figure 2.9e–f) correlate well with the MJO-associated SST anomalies in the coupled model (blue lines in Figure 2.9c–d); the coldest MJO-associated SST anomalies in the coupled model in both regions occur during the time of the weakest dSST (around MJO phase 3–5), and conversely, the warmest MJO-associated SST anomalies are present when the coupled model exhibits the strongest dSST (around MJO phase 8–2).

The dSST is indicative of diurnal warm layer strength in the ocean as seen in Figure 2.7b and Figure 2.8. This layer develops on days with weak surface winds and strong incoming solar radiation conditions. In the EIO region, the strongest diurnal warming is observed in phase 8 (Figure 2.9e) when low 10 m wind speed (Figure 2.10c) and high surface shortwave radiation (SW) flux into the ocean occur (Figure 2.10a). In phase 4, however, this region experiences the highest winds and moderate SW flux into the ocean, resulting in the weakest dSST of all MJO phases here. The same pattern can be observed in the central MC, where the largest dSST and largest warm MJO-associated SST anomalies occur during phase 1 (Figure 2.10f, d), with the lowest 10 m wind speeds (Figure 2.10d) and highest SW flux into the ocean (Figure 2.10b).

⁵The atmosphere-only model in operational mode uses previous day OSTIA SSTs as the initial condition. Therefore, the persisted SSTs used by the atmosphere-only model are OSTIA dataset lagged by 1 day.

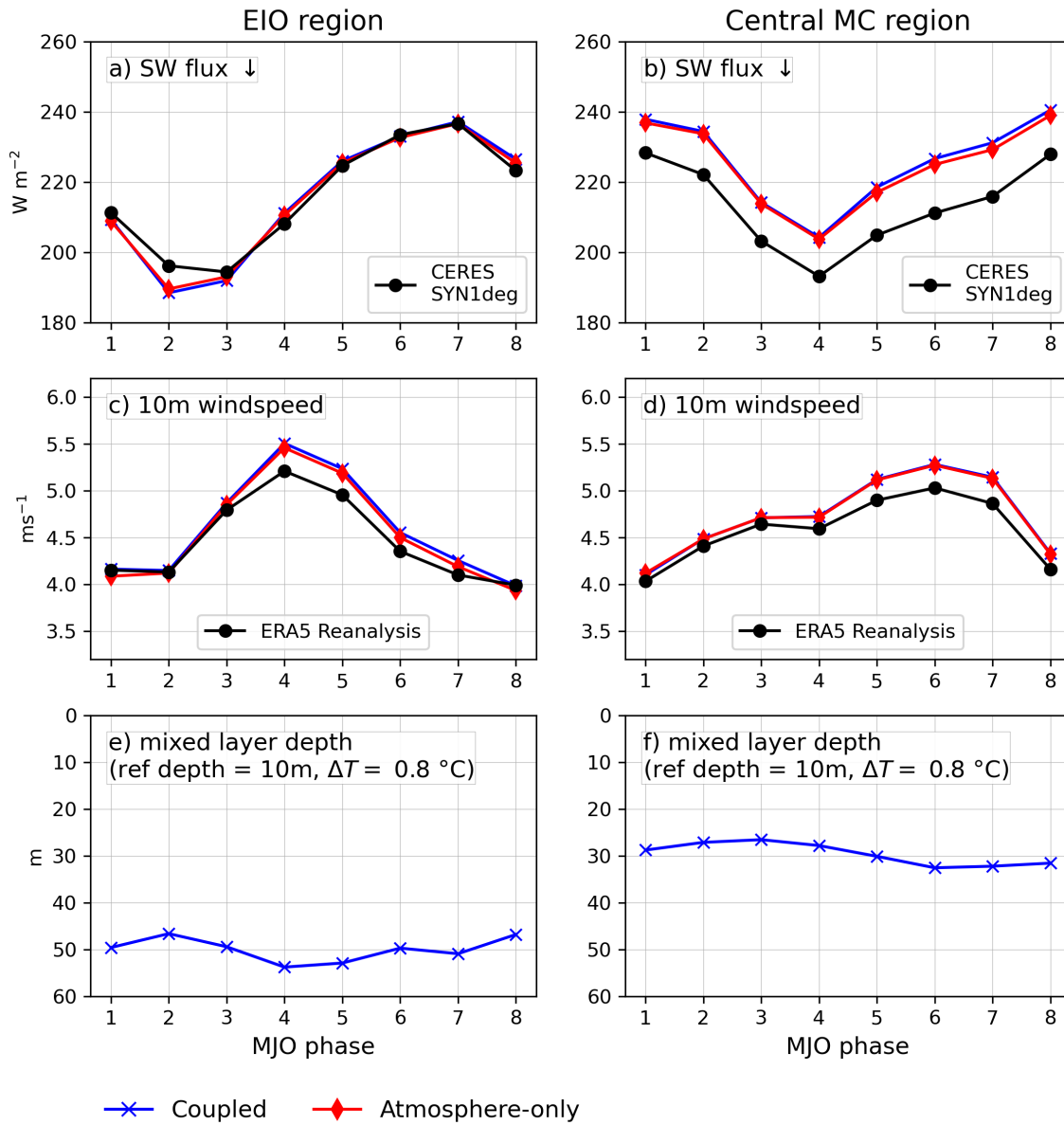


Figure 2.10: Composite lead day 1 daily means for coupled (blue) and atmosphere-only (red) models for a)–b) downward shortwave surface flux (SW flux), observed values from CERES SYN1deg (Rutan *et al.*, 2015); c–d) 10 m windspeed, observed values from ERA5 reanalysis (Hersbach *et al.*, 2020); e–f) mixed layer depth at the equator for reference depth 10 m and $\Delta T = 0.8^\circ\text{C}$. Boreal winter and initially active MJO forecasts only.

The pattern of anomalous dSST in the coupled model at lead day 1 also correlates well spatially with the difference in MJO-associated SST anomalies between the models (Figure 2.6a,b for initial MJO phase 1, and Figure 2.6c,d for initial MJO phase 4, other MJO phases are displayed in Figure C2 in Appendix C). The magnitude of the anomalous dSST in each MJO phase appears to explain the majority of the difference in the MJO-associated SST anomaly between the coupled and atmosphere-only model at lead day 1. At lead day 1, the atmosphere-only model MJO-associated SST anomalies can be roughly regarded as OSTIA dataset of non-diurnally resolving MJO-associated SST anomalies. At longer lead times, both the coupled model and the OSTIA MJO-associated SST anomalies evolve, albeit any cooling or warming recorded in the coupled model is stronger than OSTIA (not shown). The majority of the difference between the two on a sub-weekly time scale can be explained by the magnitude of the anomalous dSST in the coupled model (not shown). The diurnal warm layer formation in the coupled model is therefore the main process that modulates the MJO-associated SST anomalies at lead day 1. The MJO conditions at lead day 1 enhance or suppress the strength of the diurnal warm layer in the coupled model, rectifying daily mean SST and modulating the MJO-associated SST anomalies. These in turn lead to MJO convection differences between the models within the next 7 forecast days.

2.4.6 Other potential sources for SST difference between models

Other potential mechanisms were considered for SST differences between the coupled and atmosphere-only model at lead day 1: surface shortwave (SW) radiation flux bias, mixed layer depth variations, 10 m windspeed bias and latent heat flux bias. None of these were able to produce a significant magnitude change in SST. Details follow below.

2.4.6.1 Surface shortwave flux bias

Surface SW flux biases could lead to a change in SST in the coupled model through direct heating of the ocean mixed layer. Although daily mean SW flux into the ocean is remarkably well reproduced in the EIO region across all MJO phases at lead day 1 compared to the CERES SYN1deg observed SW flux (Figure 2.10a), there is a systematic bias of approximately 10 W m^{-2} in the central MC

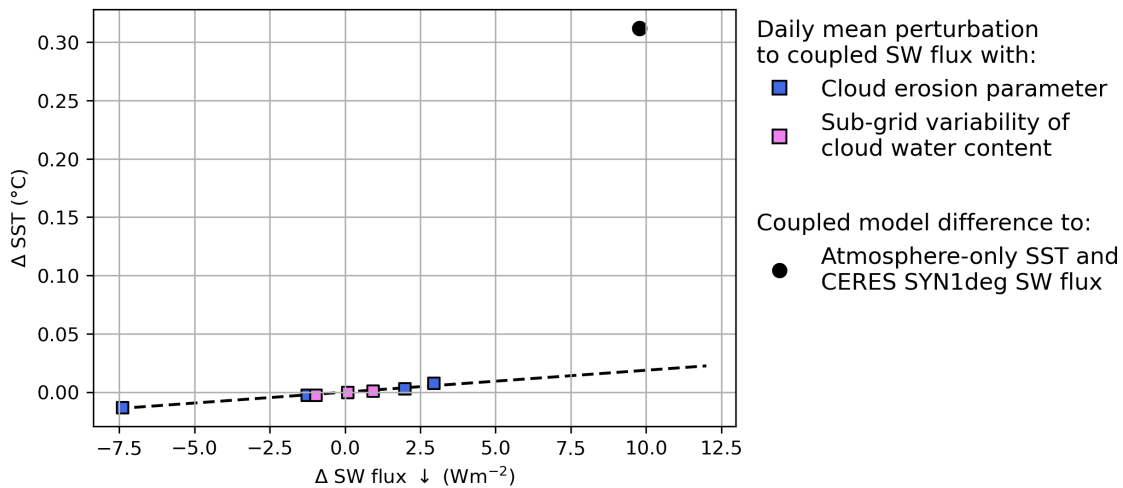


Figure 2.11: Lead day 1 daily mean sea surface temperatures (SST) sensitivity in central Maritime Continent region in a coupled forecast initialisation on 17 January 2017 to downward surface shortwave (SW) flux perturbations achieved with varying cloud erosion parameter and sub-grid variability of cloud water content at the top of the atmosphere. See region extent in Figure 2.5.

region (Figure 2.10b). An experimental case study was designed to test the magnitude of SW flux changes on SST in the coupled model in the first 24 h of the forecast. Forecasts were initialised on 17 January 2017, when an active MJO was in phase 1 (suppressed convection conditions in the central MC region). The experiments involved changing top of the atmosphere radiation sub-grid variability of cloud water content and tuning shallow cumulus clouds (“cloud erosion parameter”) to artificially force a change in surface SW flux. Seven experiments showed a linear relationship between SW flux and SST daily mean changes from the control coupled run (Figure 2.11):

$$\Delta \text{SST} = 0.001874 \times \Delta \text{SW flux} + 1.682 \times 10^{-6}. \quad (2.2)$$

Hence, for the 9.78 W m^{-2} SW flux daily mean bias in the coupled model that was present for the 17 January 2017 control run, the expected SST increase due to the SW flux change would be $0.018 \text{ }^\circ\text{C}$. However, the daily mean difference in SST between the coupled and atmosphere-only model in the central MC region on 17 January 2017 stands at $0.31 \text{ }^\circ\text{C}$ (Figure 2.11), an order of magnitude larger than what the linear regression suggests. The coupled model response to this SW flux bias is therefore not large enough to explain the much larger difference in SST between the models.

2.4.6.2 Mixed layer depth variations in the coupled model

A large change in mixed layer depth in the coupled model would lead to surface fluxes being distributed over a greater or smaller depth, and subsequent mixed layer depth temperature changes (and therefore SST changes) being significantly smaller or larger, respectively. Figure 2.10e–f shows mixed layer depth calculated at the equator for a reference depth of 10 m and a temperature change of $\Delta T = 0.8^\circ\text{C}$, at lead day 1 for the EIO and central MC regions. There is no strong relationship between mixed layer depth and MJO phase at lead day 1, with variations of mixed layer depth of 10-20 % in both regions across different MJO phases. The mixed layer temperature tendency due to surface heat fluxes over a 24 h period can be estimated as follows:

$$\frac{\partial T}{\partial t} = \frac{Q_{net}}{\rho_0 C_p h'} \quad (2.3)$$

where Q_{net} is the net surface heat flux (W m^{-2}), ρ_0 is seawater density (1025 kg m^{-3}), h is mixed layer depth (m) and C_p is specific heat of sea water ($3850 \text{ J kg}^{-1} \text{ }^\circ\text{C}^{-1}$). Using the coupled model daily mean Q_{net} at the equator and mixed layer depth at lead day 1, we find that changes in water column temperature over 24 h in the coupled model are $<0.02^\circ\text{C}$ in the EIO region and $<0.06^\circ\text{C}$ in the central MC region. These temperature tendencies are an order of magnitude smaller than the difference between the coupled and atmosphere-only model SST at lead day 1 at the equator, accounting for $<9\%$ of the SST difference in the EIO region and 11-20 % in the central MC region. We also note that there are no large fluctuations in mixed layer depth that could produce substantial changes in mixed layer temperature through entrainment of colder waters from beneath the mixed layer. We conclude that mixed layer processes in the coupled model are not enough to explain the majority of the SST increase in the coupled model compared to the atmosphere-only model.

The coupled model also simulates a barrier layer below the mixed layer. The simulated barrier layer is of 5 m thickness and does not vary across different initial MJO phases on lead day 1 (not shown). Observations show that barrier layers thicker than 10 m, can lead to faster SST recovery post MJO passage due to a decreased entrainment of cold water from below the barrier layer into the mixed layer (Moteki *et al.*, 2018; Drushka *et al.*, 2014a). This mechanism is simulated in the coupled model in EIO region in initial phase 4 at lead day 5 and beyond. The barrier layer thickens from ~ 5 m at lead day 5 to ~ 10 m at lead

day 10 through shoaling of the mixed layer. However, this small change in the barrier layer thickness will have a minor, secondary effect on the SST change.

2.4.6.3 Surface wind speed and latent heat flux biases

Latent heat flux exchange between the ocean and atmosphere acts as a cooling mechanism in the upper ocean. Latent heat flux is proportional to 10 m windspeed, therefore, we calculate the fractional wind speed bias in the coupled model compared to the ERA5 reanalysis and multiply it by the coupled model surface latent heat flux to obtain the latent heat flux bias that would result from the coupled model wind speed bias. Equation 2.3 can be used then to calculate the latent heat flux contribution to the mixed layer temperature tendency, with Q_{net} replaced by latent heat flux bias. The coupled model has generally stronger winds than ERA5 by up to 7% and 15% in the EIO and central MC regions, respectively, at lead day 1 at the equator (Figure 2.10c–d). Stronger winds will lead to an increase in latent heat flux into the atmosphere and increase the cooling effect in the upper ocean. In the EIO region this bias yields a negative temperature tendency up to $-0.005\text{ }^{\circ}\text{C}$ for MJO phases 2–8, with MJO phase 1 yielding a positive temperature tendency of $0.001\text{ }^{\circ}\text{C}$. In the central MC region, the temperature tendency due to wind speed bias is negative for all MJO phases, up to $-0.01\text{ }^{\circ}\text{C}$. Therefore, this latent heat flux bias due to the wind speed bias will lead to a slight cooling in the coupled model and cannot explain the observed increase in SST compared to the atmosphere-only model.

2.5 Conclusions

The coupled ocean–atmosphere NWP system of the UK Met Office has been running daily since 1 May 2016. In May 2022, the coupled model was switched to an operational mode, replacing the atmosphere-only NWP system that was previously used for operational global forecasting at the Met Office. Our study reveals that the addition of an ocean model introduces new complications for the MJO forecasting in this NWP system. The inclusion of the diurnal warming of SST ($dSST$) in the coupled model makes it more realistic, however, its subsequent feedbacks with the MJO ultimately lead to a stronger than desired increase in the MJO propagation speed.

Both the coupled and atmosphere-only NWP models of the Met Office predict the MJO skilfully out to at least 7 lead days. However, the coupled model

simulates faster eastward MJO propagation than the atmosphere-only model by 12% (in RMM phase space). This increase is caused by the coupled model's ability to resolve the diurnal warm layer formation in the upper ocean, the effects of which are not present in the atmosphere-only model that utilises foundation (night-time) SSTs. The dSST pattern in the coupled model correlates spatially well with the SST difference between the models. Both patterns are positive across the Indo-Pacific warm pool with peak values over the Maritime Continent. This uneven distribution of dSST across the Indo-Pacific warm pool leads to a stronger SST gradient in the coupled model in the region of MJO convection. The distribution of the dSST in the coupled model across the tropics is broadly consistent with observations (Yan *et al.*, 2021; Bellenger & Duvel, 2009). Glider observations also show that weak surface winds and large SW flux lead to stronger diurnal warming (Matthews *et al.*, 2014). Consistently, the strongest dSST in the coupled model is recorded over the MC, coinciding with the weakest surface winds in the model, and ERA5 reanalysis. An accurate representation of the SST gradient across the Indian Ocean is found to favour more moisture to the east of the MJO convection in coupled model simulations, and leads to better eastward propagation of the MJO (Hu *et al.*, 2022). Hence, this stronger SST gradient in the Met Office's coupled model could lead to more coherent MJO propagation.

Observations show that the dSST in the Indo-Pacific warm pool rectifies onto the intraseasonal SSTs (Yan *et al.*, 2021). Strong dSST leads to more moist static energy ahead of the active MJO phase, leading to an earlier onset of MJO convection (Itterly *et al.*, 2021). This feedback is simulated by the Met Office's coupled model. The MJO conditions in the coupled model dictate the strength of the dSST. The dSST rectifies onto the MJO-associated SST anomalies and those anomalies feed back into the MJO convection within the next few forecast days and lead to MJO propagation speed changes in the coupled model. This mechanism is similar to existing theories of the MJO atmosphere-ocean interaction (for review, see DeMott *et al.*, 2015), and amplifies the SST patterns associated with these processes. More detailed description of this two-way feedback between the MJO and dSST is described as follows, with a visual summary displayed in Figure 2.12:

1. During the convective phase of the MJO, the cloud cover is increased and wind-driven mixing is enhanced, causing the suppression of diurnal warm layer strength (and dSST). This happens for example in MJO phase 4 in the equatorial Indian Ocean region. The suppressed dSST leads to colder

MJO-associated SST anomalies in the coupled model at lead day 1. These colder MJO-associated SST anomalies will tend to inhibit convection in that region later in the forecast. By lead day 7, this region is in the suppressed MJO phase, to the west of the MJO convective anomalies. This mechanism will therefore result in stronger suppression behind the MJO convective envelope, and lead to increased eastward MJO propagation.

2. During the suppressed MJO phase, low surface winds and high incoming solar radiation lead to an enhanced dSST in the coupled model. This happens for example during MJO phase 1 in the central Maritime Continent region located to the east of the MJO convective anomalies at lead day 1. The enhanced dSST in this region leads to warmer MJO-associated SST anomalies in the coupled model at lead day 1. These warmer MJO-associated SST anomalies will then increase moisture and convection ahead of the MJO convective anomalies, leading to faster eastward MJO propagation.

The MJO is a major source of predictability on 1–3 week time scales (e.g., Gottschalck *et al.*, 2010), and therefore, it is crucial for models to predict it well. Atmosphere-only models can skilfully predict the MJO out to 10 lead days (Woolnough *et al.*, 2007), but over longer lead times, the coupled NWP systems tend to outperform the atmosphere-only ones (e.g., Kim *et al.*, 2014; Vitart, 2017). There is still much room for improvement as models generally tend to simulate an MJO that erroneously decreases in propagation speed with lead time (Vitart, 2017). Previous studies showed that diurnal variability of SST in coupled models can lead to improved MJO predictions and simulations (Bernie *et al.*, 2007, 2008; Seo *et al.*, 2014; Tseng *et al.*, 2015; Ge *et al.*, 2017; Hong *et al.*, 2017). High vertical resolution near the ocean surface is found to be the key to stronger dSST in coupled models and increased intraseasonal SST variability that feeds into MJO convection (Ge *et al.*, 2017; Tseng *et al.*, 2015; Hsu *et al.*, 2019). Consistent with these studies, we show that the dSST plays a crucial role in representing the MJO, and should be considered for model improvements, especially for those models that struggle to simulate eastward propagation of the MJO.

Particular care should be taken with different SST datasets used by models. Foundation SSTs are often used for comparisons with model-simulated SSTs. Such comparison could lead to misleading conclusions: a naive analysis could suggest that the Met Office's coupled model needs to correct the "warm bias" in the tropics. Instead, this "warm bias" is a manifestation of a real mechanism,

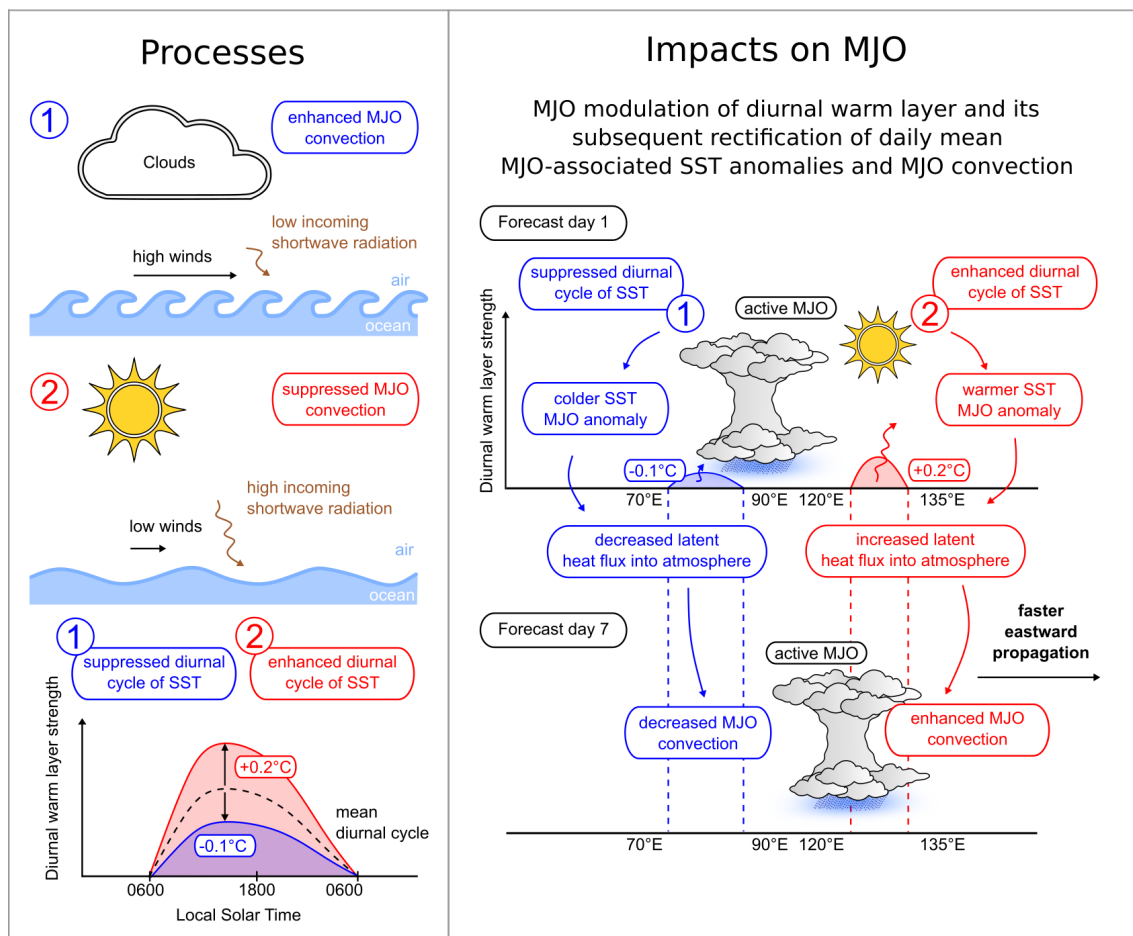


Figure 2.12: Schematic diagram of the Madden–Julian Oscillation (MJO) modulation of the diurnal warm layer strength in the upper ocean and its subsequent rectification of daily mean sea surface temperatures (SST) and MJO-associated SST anomalies, leading to faster eastward MJO propagation within seven forecast days. During enhanced MJO conditions, the diurnal warm layer is suppressed, leading to a colder MJO-associated SST anomaly in a model that resolves the diurnal cycle of SST. This colder anomaly will lead to decreased latent heat flux into the atmosphere and stronger suppression of MJO convection within the next few forecast days. During suppressed MJO conditions, the diurnal warm layer is enhanced, leading to a warmer MJO-associated SST anomaly in a model that resolves the diurnal cycle of SST. This warmer anomaly will lead to enhanced latent heat flux into the atmosphere, leading to more convection ahead of the MJO convective anomalies. Both mechanisms will lead to faster eastward MJO propagation in a model that resolves the diurnal warm layer compared to one that does not. Left panel modified after Yan *et al.* (2021).

the diurnal layer formation in the upper ocean, that is not represented in the OSTIA dataset. This mechanism may be, however, too strong in the coupled model, leading to erroneously fast MJO propagation speed. Coupled models that lack high vertical resolution near the ocean surface could potentially benefit from parameterising this mechanism. Many climate models from the Coupled Model Intercomparison Project Phase 6 (CMIP6) have the top ocean model level

thickness larger than 5 m (see Table 1 in Wang *et al.*, 2022) and hence are unlikely to accurately simulate diurnal variability in the upper ocean.

The Met Office uses different configurations of the same model for weather predictions and climate simulations. The too-fast eastward propagating MJO is also present in the seasonal configuration of this coupled NWP system ($\sim 5^\circ$ phase error for the first 4 weeks of the forecast; Vitart, 2017) and in the CMIP6 climate configuration (HadGEM3 model; Ahn *et al.*, 2020b). Both the seasonal forecast system and the climate model are at a lower atmospheric horizontal resolution (N216) than the coupled NWP model analysed here. All three configurations, however, use the same vertical and horizontal resolution in the ocean component of the model. It is likely that the two-way feedback between the MJO and the diurnal warm layer is present across all those configurations, irrespective of the atmospheric horizontal resolution. The high resolution coupled NWP system of the Met Office predicts the MJO skilfully to at least 10 forecast days, however, the too-fast propagating MJO may present challenges for weather predictions past 2 weeks, and for longer term climate projections. The increase in MJO speed in the coupled model can lead to faster onset of teleconnection patterns; for example, the CMIP6 HadGEM3 model is found to underestimate the North Atlantic Oscillation response to the MJO (Skinner *et al.*, 2022). The North Atlantic Oscillation is a key component of northern Europe variability, thus improving the MJO will improve seasonal predictions and climate projections over the UK. Lastly, the next generations of coupled models will be at higher atmospheric horizontal resolution and ultimately convection permitting. Our findings demonstrate the importance of investigating how the diurnal warm layer manifests in these models and the subsequent effects on the MJO.

The goal of this chapter was to answer the first research question:

Will coupling the Met Office forecast model to an ocean model improve the MJO predictions in the tropics?

The short answer is no, the coupled model does not improve the MJO predictions. More realistic SSTs in the coupled model (simulated due to the presence of diurnal warm layers) degrade the MJO model performance. This is likely due to the convection scheme that was developed for a model with persistent SSTs, overestimating the convection response to diurnally changing SSTs. The next chapter will investigate to what extent the hypothesised feedback

between the MJO and diurnal warm layers increases the MJO phase speed in this coupled model.

Chapter 3

Two-way feedback between the Madden–Julian Oscillation and diurnal warm layers in a coupled ocean–atmosphere model

3.1 Preface

This chapter is an extended version of an article published by the Quarterly Journal of Royal Meteorological Society (Karlowska *et al.*, 2024c) and reformatted into a thesis chapter. This chapter is the sole work of the candidate, with the supervisory team listed as co-authors for their supervisory role. The main body of the article was not altered for this thesis. Footnotes 1, 3 and 4 were added into this thesis chapter, with extra figures displayed in Appendix D. These additional figures do not alter the overall conclusions of this chapter.

This chapter investigates the feedback between diurnal warm layers and the MJO in the coupled NWP system of the UK Met Office, as hypothesised in Chapter 2. A set of numerical experiments is conducted on the coupled model to show that the presence of diurnal warm layers in the coupled model leads to a faster MJO propagation speed across the tropics.

3.2 Introduction

The Indo-Pacific warm pool region is the largest region of warm sea surface temperatures (SSTs) on Earth, spanning the equatorial Indian Ocean, the Maritime Continent (MC; Indonesia, Borneo, New Guinea) and the equatorial western Pacific. It is characterised by SSTs exceeding 28 °C (e.g., Yan *et al.*, 1992), and plays a major role in modulating the global atmospheric circulation (e.g., Kim *et al.*, 2020). The intraseasonal SST anomalies over the warm pool region influence intraseasonal weather patterns such as the Madden–Julian Oscillation (MJO). The MJO comprises an envelope of enhanced and suppressed convection, and is the major component of the tropical weather variability on intraseasonal timescales (Madden & Julian, 1971, 1972). It originates in the western Indian Ocean and travels eastward at a $\sim 5 \text{ m s}^{-1}$ phase speed, often crossing into the MC and dissipating over the Pacific.

The canonical evolution of the MJO can be described by a phase-lag relationship between the MJO convective anomalies and the intraseasonal SST anomalies over the warm pool region (e.g., Hendon & Glick, 1997; Woolnough *et al.*, 2000). Positive SST anomalies destabilise the atmosphere via surface flux exchanges, increasing the near-surface moisture and temperature gradients, and promoting moist convection. Such SST anomalies are observed approximately 1 week prior to the MJO convection over the warm pool region. During the convectively active phase of the MJO, decreased solar radiation (due to higher cloud cover) and increased latent heat flux (due to higher surface winds) lead to cooler anomalies of SST, located to the west of the MJO. This pattern of warm SST anomalies to the east and cold SST anomalies to the west evolves along the eastward propagating MJO, lagging the MJO by a quarter of the MJO cycle. This canonical evolution of the MJO convective signal can be reproduced in atmosphere-only models forced with MJO-like SST anomalies (Woolnough *et al.*, 2001; Matthews, 2004).

There is a growing evidence that short-timescale (diurnal) variations in the SSTs affect the ocean–atmosphere interactions on the MJO time scales. For example, the study by Yan *et al.* (2021) of the global tropical moored buoy array revealed that the diurnal variability of SST rectifies the intraseasonal variability of SST. Itterly *et al.* (2021) showed that the diurnal air-sea exchanges in the warm pool region influence the moist static energy budget prior to the onset of the MJO convection. To add to the complexity, the MJO conditions themselves alter the diurnal variability of the SST (Anderson *et al.*, 1996; Bellenger & Duvel, 2009;

Matthews *et al.*, 2014; Itterly *et al.*, 2021). The top few meters of the ocean are prone to the development of diurnal warm layers on days with low cloud cover and low surface windspeeds (Matthews *et al.*, 2014). Such layers often increase the daily mean SST by $>1^{\circ}\text{C}$ and are predicted to develop on approximately 30% of the days in the warm pool region (Matthews *et al.*, 2014). Suppressed MJO conditions favour the development of such layers (e.g., Itterly *et al.*, 2021). Observations show that the increase in the daily mean SST associated with the development of diurnal warm layers affects turbulent air-sea fluxes, leading to an increase in the moist static energy ahead of the MJO and to the formation of cumulus convection (Ruppert & Johnson, 2015).

The diurnal variability of the SST can be artificially altered in coupled ocean–atmosphere models by changing the coupling frequency (e.g., Bernie *et al.*, 2007; Seo *et al.*, 2014; Hsu *et al.*, 2019) or changing the near-surface vertical resolution of the ocean model (e.g., Woolnough *et al.*, 2007; Tseng *et al.*, 2015; Ge *et al.*, 2017). For example, Bernie *et al.* (2007) showed that an increase in the coupling frequency generates a stronger variability of SST, leading to a stronger MJO response. Following this study, Bernie *et al.* (2008) found that an increased diurnal variability of SST in a coupled climate model led to a higher daily mean SST and stronger MJO projections compared to the atmosphere-only version of this model. Increased coupling frequency can also improve the phase of the diurnal cycle of surface fluxes (Hsu *et al.*, 2019; Seo *et al.*, 2014). While a more accurate diurnal cycle of surface fluxes in the study of Seo *et al.* (2014) led to stronger SST variability and stronger MJO convection in their coupled model, Hsu *et al.* (2019) found that the near-surface resolution of their ocean model led to stronger changes in the SSTs (and surface fluxes) than the effects the coupling frequency had on the SSTs. High near-surface resolution of the ocean generally increases daily mean SSTs, and improves the MJO predictions in models (e.g., Woolnough *et al.*, 2007; Tseng *et al.*, 2015; Ge *et al.*, 2017). In particular, higher near-surface resolution can increase the SSTs ahead of the MJO resulting in the preconditioning of deep convection through increased low-level moisture (Tseng *et al.*, 2015).

MJO prediction still remains a challenge in the modelling community (e.g., Vitart, 2017; Ahn *et al.*, 2020b). Many models simulate a slower MJO than observations suggest (e.g., Kim *et al.*, 2014; Xiang *et al.*, 2015; Vitart, 2017; Kim *et al.*, 2019). However, Karlowska *et al.* (2024a) showed that the global coupled ocean–atmosphere Numerical Weather Prediction (NWP) model of the UK Met Office, contrary to most models, predicts the MJO to propagate faster than both

observations and the atmosphere-only version of this model. An increase of 12% in the MJO phase speed was recorded in the coupled model compared with the atmosphere-only model over a 7-lead-day period. Karlowska *et al.* (2024a) hypothesised that this increase in the MJO phase speed was caused by a strong diurnal cycle of SST present in the coupled model, absent from the atmosphere-only model that utilises persisted foundation SST. In this study, we confirm their hypothesis through model sensitivity experiments. We impose instantaneous mixing in the top 5 m or 10 m of the ocean model component to mute the diurnal warming of SST in the coupled model, and quantify its contribution to the MJO phase speed increase between the coupled and the atmosphere-only models. In section 3.3, the model specifications, data, methodology and experimental setup are described. In section 3.4, we present the MJO performance for all model runs, describe a two-way feedback between the MJO and diurnal warm layers in the coupled model and investigate the diurnal warming effect on the mean state of the coupled model. Discussion and conclusions follow in section 3.5.

3.3 Data and methods

3.3.1 Model specifications

The data used in this study were generated with the coupled ocean–atmosphere and the atmosphere-only NWP systems of the UK Met Office. Both models were run in a hindcast mode for a 5 year period between May 1, 2016 and May 31, 2021, yielding 1857 forecast initialisations. Each model was initialised at 0000 UTC and integrated out to 15 lead days. Both models used the same atmosphere and land components, with the addition of the ocean and sea ice component for the coupled version. Due to computational expense, the models used in this study were of lower atmospheric horizontal resolution than the operational versions of these models running at the time at the Met Office. Some of the operational changes were applied to the models on September 25, 2018 (see Table 4.1 for detailed model versions and their references). The horizontal resolution of the atmosphere component was N216 (0.83° longitude and 0.56° latitude) from May 1, 2016 to September 24, 2018, then N320 (0.57° longitude and 0.38° latitude) from September 25, 2018 to May 31, 2021. The same cumulus parameterisation scheme, with shallow, mid-level and deep convection (Gregory & Rowntree, 1990; Gregory & Allen, 1991), is used across all the horizontal resolutions studied

Table 3.1: Model specifications summary.

Start date	End date	Atmosphere horizontal resolution	Atmosphere no. of levels in coupled (atmosphere-only) model	Ocean horizontal resolution	Ocean no. of levels	Global atmosphere (GA) version	Global land (GL) version	Global ocean (GO) version	Global sea ice (GSI) version
May 1, 2016	Sep 24, 2018	N216	L85 (L70)	ORCA025	L75	GA6.1	GL6.1	GO5	GSI6
Sep 25, 2018	May 31, 2021	N320	L70 (L70)	eORCA025	L75	GA7.2	GL8.1	GO6.0	GSI8.0

References: GA6.1 and GL6.1 (Walters *et al.*, 2017); GA7.2, GA7.2.1 and GL8.1 (Walters *et al.*, 2019); GO5 (Megann *et al.*, 2014); GO6.0 (Storkey *et al.*, 2018); GSI6 (Rae *et al.*, 2015); GSI8.0 and GSI8.1 (Ridley *et al.*, 2018)

here and in Karłowska *et al.* (2024a).

The atmosphere component of the coupled model is coupled to the Nucleus for European Modelling of the Ocean (NEMO) consortium ocean model (Madec *et al.*, 2017). The NEMO ocean model, at a horizontal resolution of 0.25° , is comprised of 75 vertical levels, with 8 model levels in the upper 10 m of the ocean. A 1 h coupling frequency is used in the coupled model to exchange the information between the ocean–sea ice and the atmosphere–land components. The ocean–sea ice and atmosphere–land components are initialised separately, with their own data assimilation (DA) systems. The coupled model uses the Forecast Ocean Assimilating Model (FOAM)-NEMOVAR DA system from Blockley *et al.* (2014) and Waters *et al.* (2015) to initialise its SST and sea ice concentrations. The atmosphere–land component is initialised with the 4D-Var DA system (Rawlins *et al.*, 2007) that uses SST and sea ice concentrations from the Operational Sea Surface Temperature and Ice Analysis (OSTIA) (Donlon *et al.*, 2012) assimilation system, updated by Fiedler *et al.* (2019) and Good *et al.* (2020). More detailed model descriptions are available in section 2 of Vellinga *et al.* (2020).

3.3.2 Experimental setup

To artificially suppress the diurnal cycle of SST in the NEMO ocean model, vertical eddy diffusivity was increased to a very large, unrealistic value ($10\text{ m}^2\text{ s}^{-2}$) over a specific mixing depth, such that the water column was instantaneously mixed over this mixing depth at each time step. Two mixing depths were chosen in this study, 5 m and 10 m, and the model runs for these mixing depths will be hereafter referred to as CPLDmix5m and CPLDmix10m, respectively. The control coupled and atmosphere-only models will be referred to as the CPLD and ATM models, respectively. The 5 m mixing depth was chosen because the typical e-folding depth of the observed diurnal warm layers is 4–5 m (Matthews *et al.*, 2014). The 10 m mixing depth was selected for more direct comparisons of the coupled model against the ATM model that uses bulk

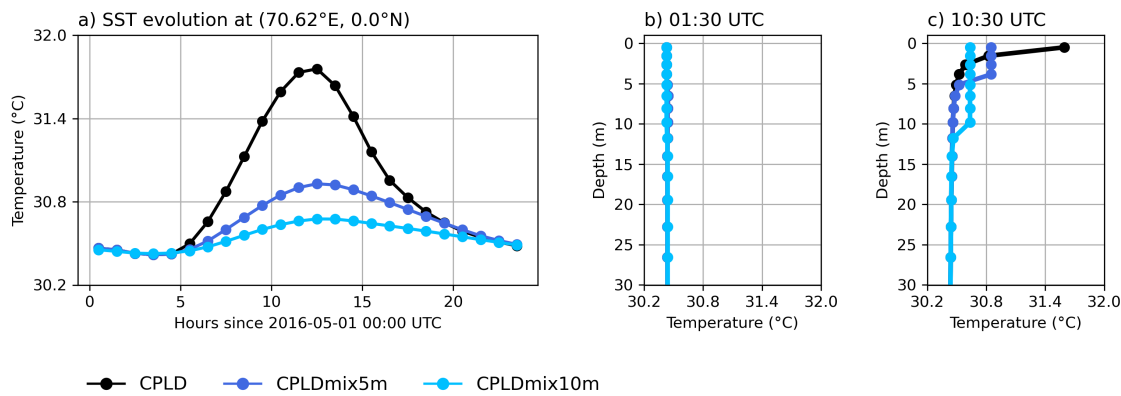


Figure 3.1: Sample evolution of surface diurnal warm layer for one grid point in the Indian Ocean (70.625°E, 0°N) during the first 24 hours of the forecast initialised on May 1, 2016: a) sea surface temperature (SST), and the vertical profiles of ocean temperature at b) 0130 UTC (0610 LST) and c) 1030 UTC (1510 LST).

10 m SSTs from the OSTIA dataset. Mixing depths deeper than 10 m were not considered for the experiments, as the entrainment of cold water from below the mixed layer in some regions, such as the MC, would lead to the daily mean SST being lower than the expected night-time SST in these regions (not shown).

An example evolution of the SST for a grid point in the Indian Ocean in the CPLD model and in the mixing experiments for the first 24 h of the forecast initialised on May 1, 2016 is displayed in Figure 3.1a. The additional mixing mutes the amplitude of the diurnal cycle of SST during this forecast. The maximum SST during this forecast is reduced by 0.8°C in the CPLDmix5m model, and by >1°C in the CPLDmix10m model run. The effect of the enhanced mixing on the near-surface temperature profiles can be seen in Figures 3.1b,c. During the night, e.g., 0130 UTC in the Indian Ocean, any surface diurnal warm layer will have disappeared due to background mixing. Hence, the night-time temperature profiles are similar between the CPLD model and the mixing experiments (Figure 3.1b). During the afternoon (1030 UTC in the Indian Ocean) the CPLD model develops a strong diurnal warm layer (Figure 3.1c). However, in the instantaneous mixing experiments, the ocean temperature in the upper half of the mixing depth decreases compared with the CPLD model. In the lower half of the mixing depth, the ocean temperature increases compared with CPLD, such that the instantaneous mixing conserves the energy of the system, and distributes it equally within the specified mixing depth. Therefore, the instantaneous mixing effectively degrades the vertical resolution of the ocean model, creating a homogeneous top model layer of the same thickness as the mixing depth.

Salinity changes in the mixing experiments are on the order of 0.01 psu¹, similar in magnitude to the observed values of the diurnal cycle of salinity in the tropics (Drushka *et al.*, 2014b). The equivalent density change for a 1 °C change in temperature requires a salinity change of 0.5 psu at a typical tropical SST (27 °C). Such salinity change would impact barrier layers and mixing from below the mixed layer. The imposed mixing does not extend beyond the mixed layer in our experiments and the changes in the salinity are small. Therefore, the changes to salinity stratification due to the imposed mixing will not have a substantial effect on the SSTs in our experiments.

3.3.3 Real-time Multivariate MJO index

The Wheeler & Hendon (2004) Real-time Multivariate MJO index (RMM) index is used to quantify the MJO performance (full methodology available in Gottschalck *et al.* (2010), with references therein). Daily anomalies of top-of-atmosphere outgoing longwave radiation (OLR) and zonal winds at 850 hPa and 200 hPa are used to construct the index. The RMM1 and RMM2 indices are the principal component time series corresponding to the dominant spatial structures of the data. The RMM indices define the location of the MJO convection in the tropics with 8 phases. In phases 8 and 1, the MJO is located over the western hemisphere and Africa. During phases 2 and 3 the MJO convective anomalies propagate across the Indian Ocean, reaching the MC in phases 3 and 4. During phases 6 and 7, the MJO is located over the western Pacific. In this study, days with an active MJO are defined as those for which the RMM amplitude $\sqrt{\text{RMM1}^2 + \text{RMM2}^2} \geq 1.0$.

Model indices are verified against the Wheeler-Hendon index (Wheeler & Hendon (2004), retrieved from <http://www.bom.gov.au/climate/mjo>). Four standard scalar statistics are used for model performance between the model indices and the Wheeler-Hendon indices, following Lin *et al.* (2008) and Rashid *et al.* (2011): bivariate anomaly correlation coefficient, root-mean-square error (RMSE), amplitude error and phase error. The first two correspond to the spatial correlation between the models and the verification dataset. A skilful prediction is found for $\text{RMSE} < \sqrt{2}$ and correlation > 0.5 (Lin *et al.*, 2008). A negative (positive) amplitude error in the model signifies underestimated (overestimated) RMM amplitude. The phase error is the angle in degrees in RMM phase space

¹Equivalent figures for ocean salinity and density to Figure 3.1 are displayed in Appendix D (Figures D1–D2).

and is positive (negative) when the MJO in the model is located to the east (to the west) of the verification dataset. The active MJO days between May 1, 2016 and May, 31 2021 for the boreal winter season (November–April) are used for each lead day to calculate the RMM statistics.

3.3.4 Composites and observational datasets

Composite maps are calculated for daily means of meteorological variables regridded to N180 ($1^\circ \times 1^\circ$) horizontal resolution. Separate forecast initialisations are concatenated at a given lead time for further processing. Anomalies are calculated by the removal of the seasonal cycle (annual mean and first three harmonics) for the period 2017-2020 at a given lead time. The MJO anomalies are then obtained by a temporal filtering of the anomalies with a 20 to 200 day bandpass Lanczos filter (Duchon, 1979) at each lead time. The composites are split by the initial MJO phase from the Wheeler-Hendon indices at lead day 1. Consecutive forecast initialisations with the same initial MJO phase are averaged before compositing and treated as one event. Unless otherwise stated, the initially active MJO forecasts during the November–April season are used for the composite analysis for the period November 1, 2016 to January 15, 2021. The composites for daily interpolated OLR from the National Oceanic and Atmospheric Administration (NOAA) at $2.5^\circ \times 2.5^\circ$ resolution (Liebmann & Smith, 1996) were calculated until January 7, 2021 based on the observed data availability. Mean state composites of all meteorological variables in section 3.4.3 were calculated for the boreal winter period from November 1, 2016 to January 15, 2021, including both active and non-active MJO days. Missing days (less than 1 %) were interpolated between the nearest previous and next day forecast initialisations.

3.4 Results

3.4.1 MJO model performance and diurnal warming

In the following section, the overall MJO performance is discussed with the RMM skill statistics averaged across all MJO phases for the CPLD, CPLDmix5m, CPLDmix10m and ATM models. The data used here spans the boreal winter season, and active MJO days only. Qualitatively, no significant difference in the RMM skill statistics was found for year-round data.

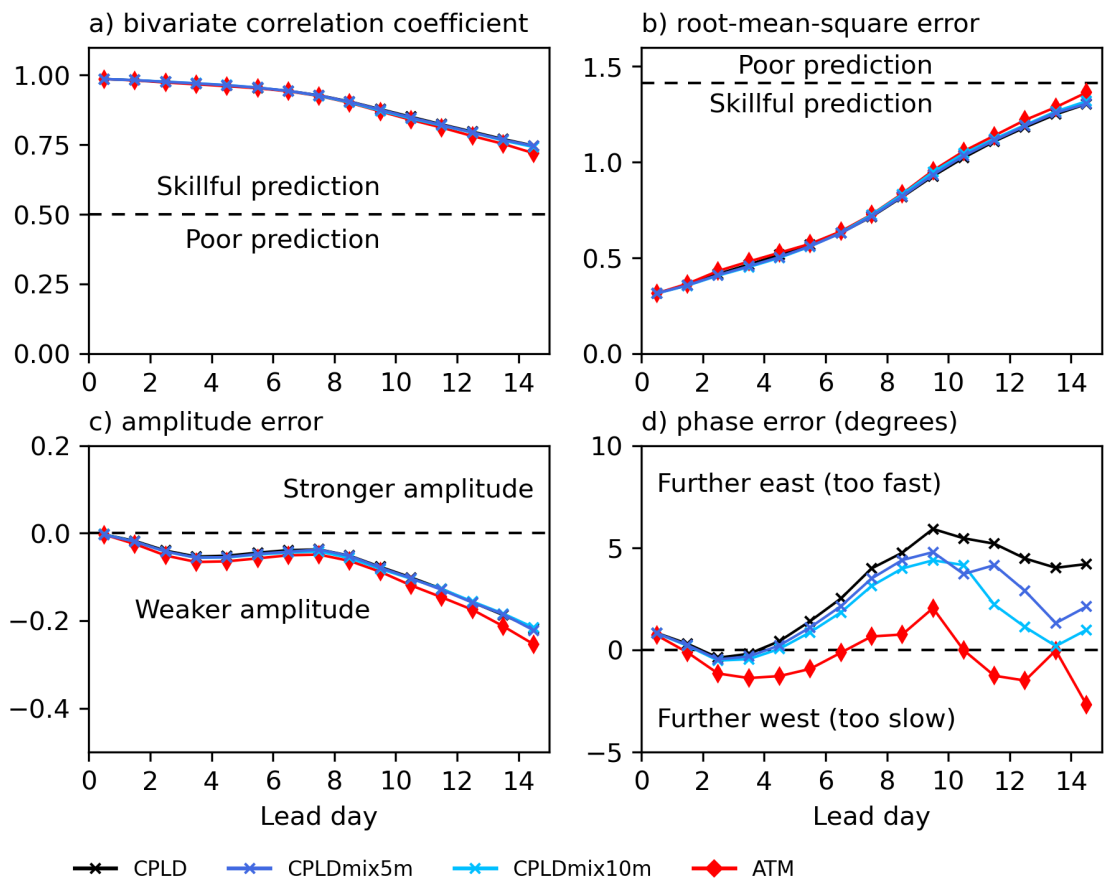


Figure 3.2: Real-time Multivariate Madden-Julian Oscillation (MJO) index skill statistics as a function of lead day for CPLD, CPLDmix5m, CPLDmix10m and ATM models: a) bivariate correlation coefficient; b) root-mean-square error; c) amplitude error; d) phase error. Daily mean data are compared for boreal winter season (November–April) and active MJO days only with the Wheeler-Hendon verification indices.

The CPLD, CPLDmix5m, CPLDmix10m and ATM models predict the MJO skilfully out to 15 lead days, with the bivariate correlation coefficients above 0.70 at all times during the forecast (Figure 3.2a). There is little difference between the models in bivariate correlation coefficients, with the exception of the ATM model that produces slightly smaller coefficients than the coupled model runs at lead day 15. All models are within the skilful RMSE threshold out to 15 forecast days (Figure 3.2b). The ATM model predicts slightly larger RMSE than the coupled runs from lead day 12 onward. At lead day 15, the RMSE for all models reaches close to the threshold for poor prediction, suggesting that at longer lead times these models may not be skilful in predicting the MJO. The RMM amplitude decreases in all models with lead time, reaching -0.25 amplitude error by lead day 15 (Figure 3.2c). The coupled model runs show slightly better amplitude error than the ATM model from lead day 10 onward.

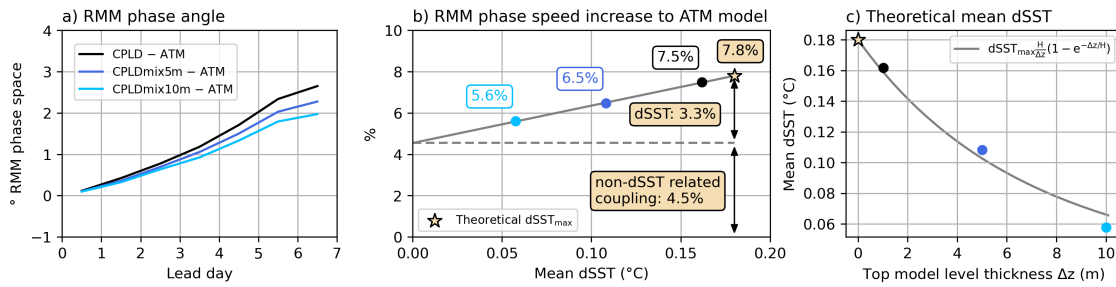


Figure 3.3: a) Real-time Multivariate Madden–Julian Oscillation (RMM) phase angle difference between the coupled model experiments (CPLD, CPLDmix5m and CPLDmix10m) and the ATM model as a function of lead day; b) RMM phase speed increase (percent) between the coupled model experiments and the ATM model at lead day 7 of the forecast as a function of the mean diurnal warming of sea surface temperatures (dSST, difference between the 1500 and 0600 local solar time sea surface temperature) in the tropics (30°S–30°N) at lead day 1 in the coupled model experiments; c) best fit between the top model level thickness and the mean dSST in the tropics at lead day 1 for $\text{dSST}_{\text{max}} = 0.18^\circ\text{C}$ and $H = 4.0\text{ m}$.

The largest difference between the models is recorded in the RMM phase error (Figure 3.2d). At lead day 1, all models predict the MJO to the east of the verification dataset, i.e., too fast eastward propagation. Afterwards, the ATM model predicts the MJO to the west of the verification dataset (i.e., too slow eastward propagation), at -1.5° phase error for lead days 3 to 6. At longer lead times, the ATM model phase error varies between -2.5° and 2.5° , reaching -2.1° at lead day 15. During the first 7 lead days, the ATM model predicts the MJO with approximately correct phase speed, likely due to compensating biases present in the ATM model. At the same time, all coupled models simulate a too-fast MJO compared with the verification dataset. The phase errors for the CPLD, CPLDmix5m and CPLDmix10m models evolve similarly within the first 7 lead days of the forecast. However, the additional mixing in the upper ocean reduces the phase speed in the CPLDmix5m and CPLDmix10m compared with the CPLD model such that deeper mixing causes a stronger reduction in the MJO phase speed, and as a result a stronger reduction in the RMM phase error. This is particularly evident at lead days longer than 10, likely due to secondary feedbacks between the ocean and the atmosphere. Those feedbacks are explored in section 3.4.2.2.

All three coupled model runs show a linear growth in the RMM phase angle compared to the ATM model during the first 7 lead days of the forecast (Figure 3.3a). The CPLD model displays the strongest increase in the RMM phase angle compared with the ATM model, at a rate of 0.44°d^{-1} (in RMM phase space). The CPLDmix5m and CPLDmix10m models show a weaker increase in the RMM

phase angle compared to the ATM model at 0.38°d^{-1} and 0.33°d^{-1} (RMM phase space), respectively. The average RMM phase speed during the study period in the ATM model was 5.9°d^{-1} (RMM phase space). Therefore, the equivalent increase in the RMM phase speed for the coupled runs compared with the ATM model stands at 7.5%, 6.5% and 5.6% for the CPLD, CPLDmix5m and CPLDmix10m models, respectively. This is lower than the 12% recorded by Karłowska *et al.* (2024a) for a higher resolution version of the CPLD model, although they used the observed RMM phase speed in their comparison, which is slightly slower than the ATM model RMM phase speed. Qualitatively, the choice of ATM rather than OBS as a baseline makes little difference in the quoted values (e.g., 8.5% instead of 7.5% for the CPLD model). The exact increase in speed is likely to vary between models, but we expect the key finding to remain: coupling increases the speed of the MJO, and a substantial component of this speed up is due to the representation of the diurnal cycle of SST.

To further understand the increase in the MJO phase speed in the coupled model, it is important to understand the main differences between the models, that is the nature of SSTs in each model. The ATM model utilises persisted SSTs from the OSTIA dataset that correspond to the bulk 10 m night-time ocean temperature. Therefore, this dataset does not include any diurnal warming effects on the SSTs, nor the air-sea interactions due to the diurnal cycle. The ocean component of the CPLD model is comprised of 8 model levels in the top 10 m of the ocean and has the capacity to produce diurnal warm layers (Figure 3.1c, also see Karłowska *et al.* (2024a) for diurnal warm layer formation in the CPLD model). The CPLD model SSTs correspond to the top model level centred at 0.51 m, bounded by 0.0 m and 1.02 m depth. The CPLDmix5m and CPLDmix10m model runs are a variation of the CPLD model run and are capable of developing diurnal warm layers, but with greatly reduced diurnal amplitude. The additional mixing reduces the amplitude of the diurnal warming in these model runs and increases the effective thickness of the SST layer from 1.02 m to 5 m and 10 m for the CPLDmix5m and CPLDmix10m models, respectively.

The boreal winter composite of active MJO days for the diurnal warming of SST (dSST), defined here as the difference between the 1500 and 0600 local solar time (LST) SST, is positive at lead day 1 in the CPLD model across the tropics (Figure 3.4a). The strongest dSST is recorded near the equator, with mean values $>0.4^\circ \text{C}$. The dSST is the largest in the western Indian Ocean, over the MC and in the eastern Pacific. The mean dSST at lead day 1 in the tropics (30°S - 30°N) in the CPLD model stands at 0.16°C . The dSST in the CPLDmix5m is reduced across

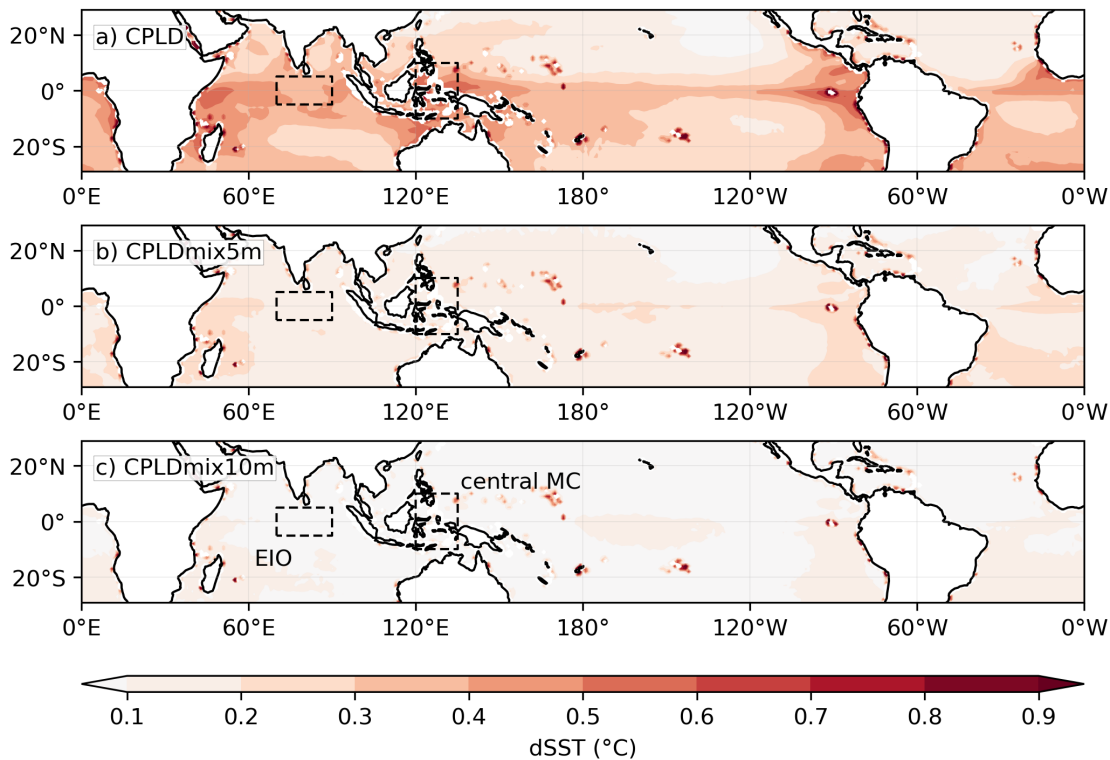


Figure 3.4: Composite diurnal warming (dSST; 1500 minus 0600 local solar time SST difference) at lead day 1 for a) CPLD, b) CPLDmix5m and c) CPLDmix10m averaged over all MJO phases (boreal winter and initially active MJO forecasts only). The boxes indicate where area averages are taken later over the equatorial Indian Ocean (EIO) and central Maritime Continent (MC).

the tropics to a mean value of 0.11 °C (Figure 3.4b). A further reduction in the mean tropical dSST is observed in the CPLDmix10m model, with values <0.1 °C across the majority of the tropics and a mean value of 0.06 °C (Figure 3.4c). The night-time tropical SST (at 0600 LST) does not vary substantially between all coupled experiments over 15 lead days of the forecast (Figure 3.5). The difference in the night-time SST between the coupled experiments at lead day 15 is <0.01 °C. Therefore, the mixing experiments successfully suppress the diurnal variations of SST with minimal side effects on other processes, such as the evolution of the ocean mixed layer.

The percentage increase in the RMM phase speed between the coupled model runs and the ATM model out to lead day 7 is linearly correlated with the mean dSST in the tropics at lead day 1 in each coupled model run (Figure 3.3b). Theoretically, if the diurnal warming effects were entirely removed from the CPLD model (dSST = 0 °C), the intersect of the linear fit between the mean tropical dSST and the RMM phase speed increase between the coupled models

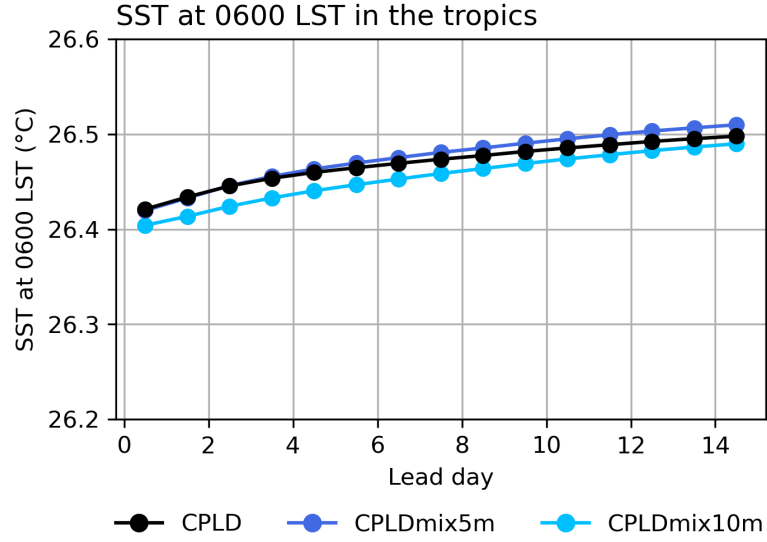


Figure 3.5: Composite 0600 local solar time (LST) SST for CPLD, CPLDmix5m and CPLDmix10m averaged over the tropics (30°S-30°N), and over all MJO phases (boreal winter and initially active MJO forecasts only).

and the ATM model would correspond to all other coupling effects unrelated to the dSST. Those effects would be present in all the coupled model runs, regardless of the dSST strength.

Ignoring the cool skin effect, it is straightforward to calculate what the theoretical maximum of dSST in the CPLD model would be as the thickness of the top model level decreases towards the skin depth of the water surface. Ocean glider observations of diurnal warm layers in the Indian Ocean show that the additional diurnal warming with respect to the foundation temperature at the base of the diurnal warm layer can be described by an exponential decay with depth, with a caveat that such decay is observed on days with sunny weather and weak surface winds and not during enhanced MJO convection (Matthews *et al.*, 2014). The bulk temperature profile $T(z)$ with a superimposed diurnal warm layer can be described as:

$$T(z) = T^* + \text{dSST}_{\max} e^{-z/H}, \quad (3.1)$$

where T^* is the foundation SST, dSST_{\max} is the theoretical maximum dSST and H is the scale depth of the diurnal warm layer. The modelled surface temperature T_{sfc} is then a vertical average of this temperature profile for each model run over

the SST layer thickness (Δz):

$$T_{\text{sfc}} = \frac{1}{\Delta z} \int_0^{\Delta z} T^* + \text{dSST}_{\text{max}} e^{-z/H} dz = T^* + \text{dSST}_{\text{max}} \frac{H}{\Delta z} \left(1 - e^{-\Delta z/H} \right). \quad (3.2)$$

Therefore the theoretical dSST contribution to the surface temperature is:

$$\text{dSST}(\Delta z) = \text{dSST}_{\text{max}} \frac{H}{\Delta z} \left(1 - e^{-\Delta z/H} \right). \quad (3.3)$$

A least squares regression was fit to obtain the optimum dSST_{max} and H for the Δz and the mean tropical dSST in all coupled model runs (Figure 3.3c). The optimum dSST_{max} and H were found at 0.18°C and 4.0 m , close to the values recorded from observations collected by ocean gliders in the central Indian Ocean ($\text{dSST}_{\text{max}} = 0.22^\circ\text{C}$; $H = 4.2\text{ m}$) by Matthews *et al.* (2014). Theoretically, the mean dSST would tend to the value of dSST_{max} with increasing vertical ocean resolution. Therefore, the theoretical maximum MJO phase speed increase in the CPLD model compared with the ATM model can be extrapolated to 7.8% for $\text{dSST}_{\text{max}} = 0.18^\circ\text{C}$ (Figure 3.3b). This value is slightly larger than the value for the CPLD model at the current vertical resolution in the ocean model. This shows that the $\sim 1\text{ m}$ vertical resolution in this coupled model is sufficient to capture almost all of the effects of the diurnal warm layer on the MJO and there is no need to increase this vertical resolution further.

On a 7-lead-day timescale, the presence of the dSST contributes approximately 40% of the MJO phase speed increase between the CPLD and the ATM model. The representation of the dSST is therefore important for the eastward propagation of the MJO in this coupled NWP system. The remaining 60% is contributed by other coupling effects unrelated to diurnal warming, e.g. mixed layer and barrier layer contributions. The mixed layer in the coupled model at lead day 1 is deeper than the maximum depth of the imposed mixing in all coupled experiments across the tropics at a mean value of $\sim 30\text{ m}$. The mixed layer depth evolution throughout the forecast happens at the same rate in all coupled model runs (not shown), and hence, the suppression of the diurnal warming has a minimal effect on the mixed layer evolution in these experiments. The coupled model also simulates barrier layers, however, they are less than 10 m thick (not shown). Observations show that barrier layers larger than 10 m can increase the SST recovery post the MJO passage (Drushka *et al.*, 2014a; Moteki *et al.*, 2018). Therefore, barrier layer contributions to the SST changes will be

minor in this coupled model.

3.4.2 MJO convection–diurnal warming–SST relationship

The mixing experiments show that muting the diurnal warming of SST (dSST) in the CPLD model can lead to a substantial reduction in the MJO phase speed over a 15-lead-day forecast. In this section, we examine the relationship between MJO convection, dSST and SST anomalies to investigate how a better representation of dSST leads to faster MJO propagation across different MJO phases in the CPLD model. The following section focuses on two regions that display the largest differences in the MJO convection between the CPLD and the ATM models: the equatorial Indian Ocean region (EIO; 70 °S-90 °N, 5 °S-5 °N) and the central MC region (120 °S-135 °N, 10 °S-10 °N). The spatial extent of these regions is displayed in Figure 3.4c.

3.4.2.1 MJO impact on diurnal warming and daily mean SST

Karłowska *et al.* (2024a) showed that the MJO conditions in a higher horizontal atmospheric resolution version of the CPLD model set the strength of the dSST. During suppressed MJO conditions, low surface winds and high shortwave (SW) flux into the ocean lead to stronger than average dSST in the coupled model. Conversely, during the active MJO convection, cloud cover and stronger winds lead to weaker than average dSST. The same mechanism occurs in the lower horizontal atmosphere resolution version of the coupled model used in the experiments here. During initial MJO phases 6–1, the suppressed MJO convection over the EIO region (not shown) leads to stronger dSST than in phases 2–5 (Figure 3.6a), when MJO convection is enhanced. The same relationship between the dSST and the MJO convection occurs in the central MC region (Figure 3.6b). The strongest dSST is recorded in initial MJO phases 7–2 during the suppressed MJO convection over the MC. During initial MJO phases 3–6, the MJO convection is located over the MC and thus the CPLD model generates a weaker dSST.

The CPLD model dSST at lead day 1 varies in each region between 0.3 and 0.6 °C across different MJO phases (Figure 3.6a-b). Both mixing experiments show a reduction in the dSST in each region to ~ 0.2 °C and ~ 0.1 °C for the CPLDmix5m and CPLDmix10m models, respectively. Both mixing experiments also show a smaller phase-to-phase variation in the dSST than the CPLD model.

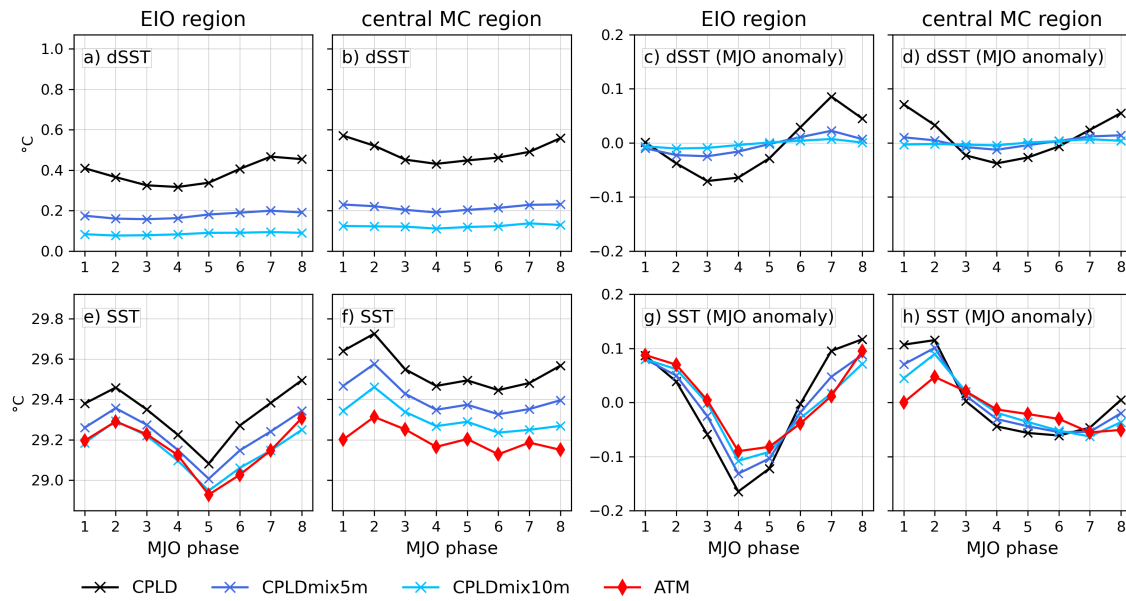


Figure 3.6: Composite lead day 1 daily means for CPLD, CPLDmix5m, CPLDmix10m and ATM models for: a)–b) diurnal warming of SST (dSST; difference between 1500 and 0600 local solar time SST); c)–d) MJO anomalies of dSST (20–200-day filtered); e)–f) SST; g)–h) MJO anomalies of SST. The EIO and central MC regions are shown in Figure 3.4. Composites are calculated for boreal winter and initially active MJO forecasts only.

Muted dSST in the coupled model at lead day 1 leads to a reduction in the lead day 1 daily mean SST in each region (Figure 3.6e–f, as colder water is mixed up to the surface as in Figure 3.1c). The additional mixing in the CPLDmix5m model leads to a 0.1–0.2°C reduction in the daily mean SST in both regions across different initial MJO phases. The CPLDmix10m model displays a further reduction in the daily mean SST of 0.05–0.1°C compared with the CPLDmix5m model daily mean SST. The reduction in the daily mean SST in the mixing experiments corresponds to approximately half of the reduction in the dSST. The CPLDmix10m effectively degrades the CPLD model to a 10 m top level, such that the reduction in the dSST causes the SSTs to systematically cool down towards the foundation SST at lead day 1 (Figure 3.6e–f)². Overall, the presence of the dSST in the CPLD model leads to an increase in the daily mean SST compared with the ATM model that uses foundation SST and does not resolve the diurnal warming effects.

Diurnal warm layers form during the day and are destroyed overnight due to the night-time heat loss. After removal of the mean, and subsequent 20–200-day bandpass filtering, the dSST anomalies are hereafter referred to as

²ATM model uses persisted foundation SSTs from the previous day OSTIA SST in the hindcast mode. Therefore, the ATM model SST at lead day 1 is similar to the foundation SST, albeit lagged by 2 days (not shown).

“MJO anomalies”. Non-zero MJO anomalies of dSST emerge in the CPLD model at lead day 1 in both regions across different MJO phases, as a result of the systematic modulation of dSST by the MJO (Figure 3.6c-d). During the suppressed MJO conditions, the CPLD model produces positive MJO anomalies of dSST, and during the enhanced MJO convection, the CPLD model simulates negative MJO anomalies of dSST. The MJO anomalies of the dSST in the CPLDmix5m model are reduced compared to the CPLD model, however, with a similar, but much reduced, phase-to-phase variation in the amplitude. The CPLDmix10m MJO anomalies of dSST are further reduced, being below 0.02°C across all initial MJO phases. The MJO anomalies of SST between the models reflect the behaviour seen in the MJO anomalies of the dSST (Figure 3.6g-h, c-d). More positive (negative) MJO anomalies of dSST lead to stronger positive (negative) MJO anomalies of SST in the coupled model. Moreover, the strong reduction in the MJO anomalies of dSST in the CPLDmix10m model yields MJO anomalies of SST that are closer in value to the ATM model MJO anomalies of SST, especially in the EIO region (Figure 3.6g). The additional mixing in the central MC region reduces the MJO anomalies of SST in the coupled model towards those of the ATM model, except for in phases 1 and 2, where a difference of around 0.1°C remains (Figure 3.6h).

Thus, the dSST in the CPLD model is modulated by the MJO conditions. The dSST then rectifies the daily mean SST and the daily mean MJO anomalies of SST. This mechanism, hypothesised by Karłowska *et al.* (2024a), is confirmed by the mixing experiments carried out in this study. We now consider how the relationship between the MJO, the dSST and the SST manifests over 15 lead days of the forecast to yield a faster MJO in the dSST resolving coupled model.

3.4.2.2 Two-way feedback between the MJO and diurnal warm layers

In this section, two initial MJO phases 1 and 4 were chosen to describe the relationship between the MJO, the diurnal warming and the SST in the CPLD model over 15 lead days of the forecast.

In initial MJO phase 1, the observations show negative MJO anomalies of OLR (enhanced MJO convection) over the Indian Ocean and positive MJO anomalies of OLR (suppressed MJO convection) over the MC (Figure 3.7a)³. Both the CPLD and the ATM models simulate this pattern well (Figure 3.7c,e). The CPLD model

³Hovmöller diagrams for all models and all MJO phases are provided in Appendix D (Figures D3–D4).

simulates the onset of the MJO convection over the MC better than the ATM model at lead days 7 and beyond. The suppressed MJO convection over the MC leads to positive MJO anomalies of dSST in the central MC region (Figure 3.8a). The positive MJO anomalies of dSST in all coupled models lead to stronger positive MJO anomalies of SST compared with the ATM model (Figure 3.8c). The CPLDmix5m and CPLDmix10m MJO anomalies of SST at lead day 1 are reduced compared with the CPLD model SST due to the reduction in the MJO anomalies of dSST. The initially positive MJO anomalies of SST in all coupled models grow, peaking 3, 5 and 7 days later for the CPLD, CPLDmix5m and CPLDmix10m models, respectively. The early arrival of the MJO anomaly of SST occurs due to the addition of diurnal warming on top of the canonical evolution of the MJO anomalies of SST due to the changes in the net heat flux into the ocean (Q_{net}) throughout the life cycle of the MJO. In the absence of diurnal warming in the CPLDmix10m model, the MJO anomalies of SST peak around lead day 7 when the MJO anomaly of Q_{net} is close to zero (not shown). The presence of strong MJO anomalies of dSST in the CPLD model adds an extra, time-varying component to the MJO anomalies of SST such that the CPLD model displays an earlier peak in positive MJO anomalies of SST in this region compared with the CPLDmix5m and CPLDmix10m models.

By lead day 7, the active MJO convection propagates into the central MC region (Figure 3.7a). Accordingly, the positive MJO anomalies of dSST weaken with lead day in each coupled model run, until lead day 7, when all models display MJO anomalies of dSST close to zero (Figure 3.8a). The difference in the MJO anomalies of SST between the CPLD model and the mixing experiments is small during this time of weakest dSST (Figure 3.8c). By lead day 7, the MJO convection differences between the CPLD and mixing experiments reaches a maximum in response to the differences in MJO SST anomalies over the preceding days (Figure 3.8e). The MJO convection reaches the MC by lead day 7 (Figure 3.7a), and accordingly, the dSST regime shifts to negative MJO anomalies of dSST growing past lead day 7 (Figure 3.8a).

The CPLD model displays the strongest decline in the MJO anomaly of SST compared with the mixing experiments due to the strongest negative MJO anomalies of dSST. This decline takes approximately 3 lead days (from lead day 7 to 10). Afterwards, all coupled models' MJO anomalies of SST evolve in parallel to each other. This is a spatially coherent pattern in the coupled model. Colder MJO anomalies of SST over the MC at lead day 1 (Figure 3.9a), lead to less convection at lead day 7 in the CPLDmix10m model compared with the CPLD

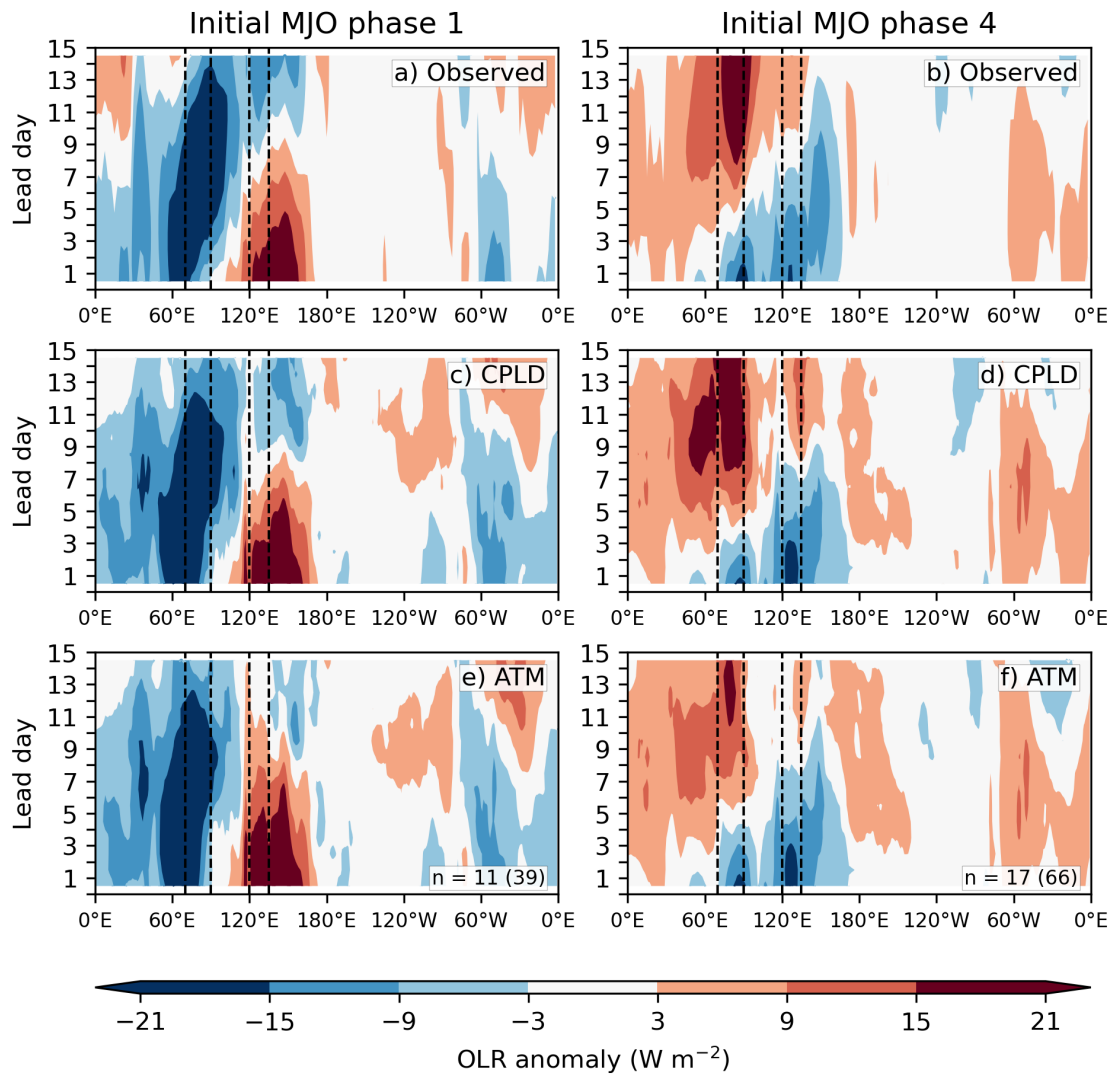


Figure 3.7: Hovmöller diagrams of daily mean composites of MJO anomalous (20–200-day filtered) OLR, averaged over the equatorial band (5°S – 5°N), for forecasts initialised in MJO phases 1 and 4: a–b) observed; c–d) CPLD model; e–f) ATM model. Vertical dashed lines represent equatorial Indian Ocean and central Maritime Continent regions. Composites were calculated using boreal winter and initially active MJO forecasts only. Number n denotes the amount of independent events used in the composite (total number of days used displayed in the brackets).

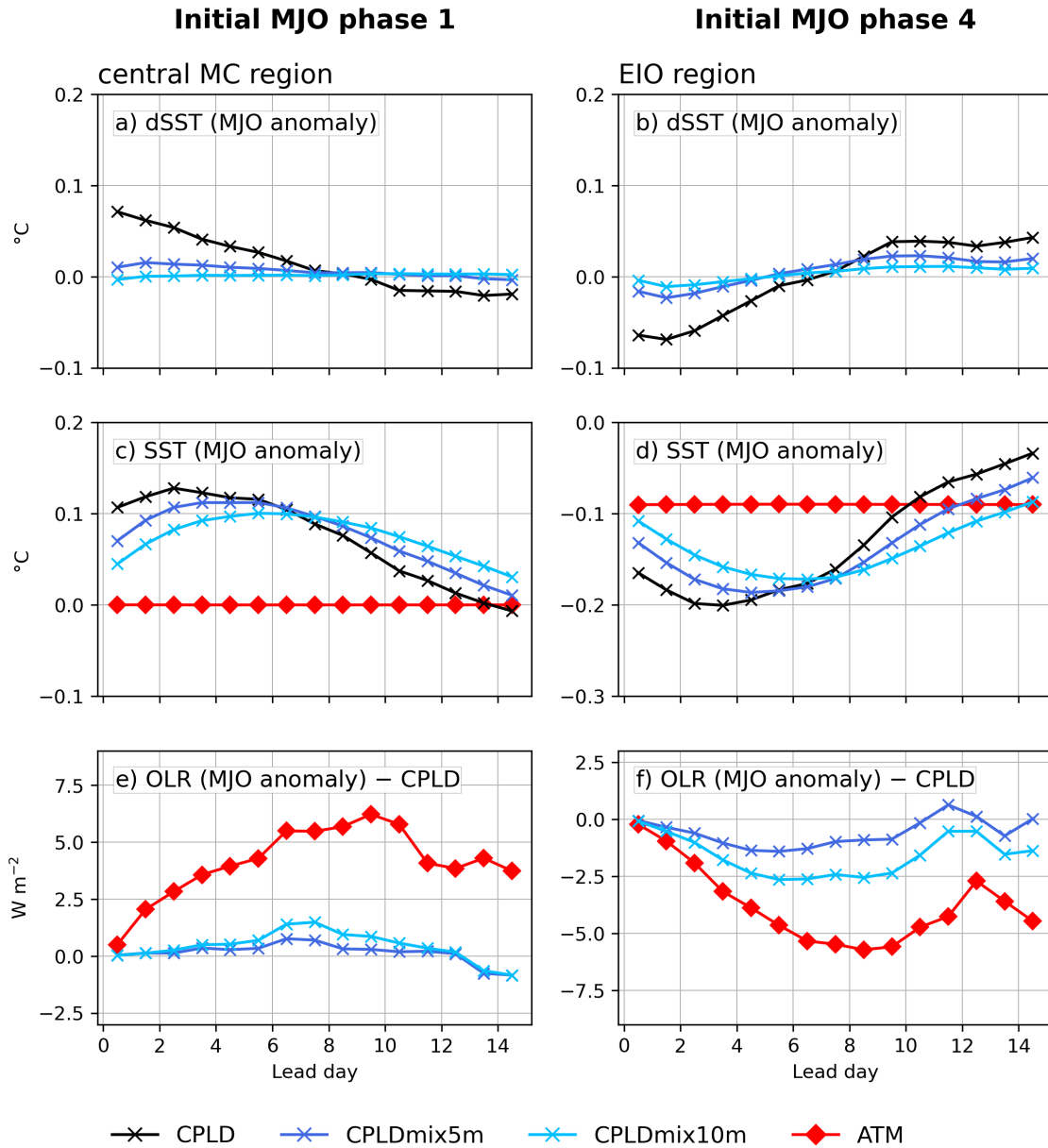


Figure 3.8: Daily evolution of the model composites of MJO (20–200-day filtered) anomalies of: a–b) dSST; c–d) SST; e–f) OLR (difference from the CPLD model). Panels a, c and e are for the central MC region for initial MJO phase 1. Panels b, d and f are for the equatorial Indian Ocean (EIO) region for initial MJO phase 4. Composites are calculated for boreal winter for active MJO days only. The spatial extent of both regions is shown in Figure 3.4.

model (Figure 3.9c) during the convective MJO phase in that region (Figure 3.7c). The MJO anomalies of SST respond quickly to that change in the MJO convection, and by lead day 14, less convection in the CPLDmix10m model leads to warmer MJO anomalies of SST compared with the control (Figure 3.9e)⁴.

In initial MJO phase 4 at lead day 1, the enhanced MJO convection spans most of the eastern Indian Ocean and the MC (Figure 3.7b). Both the CPLD and the ATM models reproduce this MJO convection well across the tropics (Figure 3.7d,f). However, at longer lead days, the CPLD model overestimates the suppressed MJO convection over the western Indian Ocean. At the same time, the ATM model underestimates the suppressed MJO convection over the MC. The enhanced convection over the Indian Ocean leads to negative MJO anomalies of dSST in the CPLD model in the EIO region in MJO phase 4 at lead day 1 (Figure 3.8b). The mixing experiments show smaller, albeit still negative, MJO anomalies of dSST in this region at lead day 1. The stronger the MJO anomalies of dSST, the more negative the MJO anomaly of SST is generated in the coupled model (Figure 3.8d). The negative MJO anomalies of SST at lead day 1 grow in the coupled model runs, peaking 3, 5 and 7 days later for the CPLD, CPLDmix5m and CPLDmix10m models, respectively. Similarly to the positive anomalies in Figure 3.8c, the negative MJO anomalies of SST in the EIO region grow by a similar increment between the coupled model runs each lead day until they reach their negative peak. The earlier arrival of negative MJO anomalies of SST in the CPLD model is associated with the stronger negative peak in the MJO anomaly of dSST that is superimposed on the MJO anomalies of SST seen in the CPLDmix10m simulation in the absence of diurnal warming.

As the forecast reaches lead day 7, the approaching suppressed MJO convection (Figure 3.7d) over the EIO region leads to a weaker negative MJO anomaly of dSST, reaching close to zero for all models at lead day 7 (Figure 3.8b). Consequently, during the weakest MJO anomaly of dSST at lead day 7, the MJO anomalies of SST in all coupled model runs are the closest to each other throughout the forecast (Figure 3.8d). At the same time, the difference in MJO convection between the mixing experiments and the CPLD model peaks (Figure 3.8f). That difference is larger when deeper mixing is imposed. The MJO anomalies of SST in the EIO region for initial MJO phase 4 recover from the MJO passage post lead day 7, and display a warming trend towards the end of the forecast (Figure 3.8d). The CPLD MJO anomalies of SST recover the fastest

⁴For completeness, equivalent Figure 3.9 for other MJO phases is in Appendix D (Figures D5–D7).

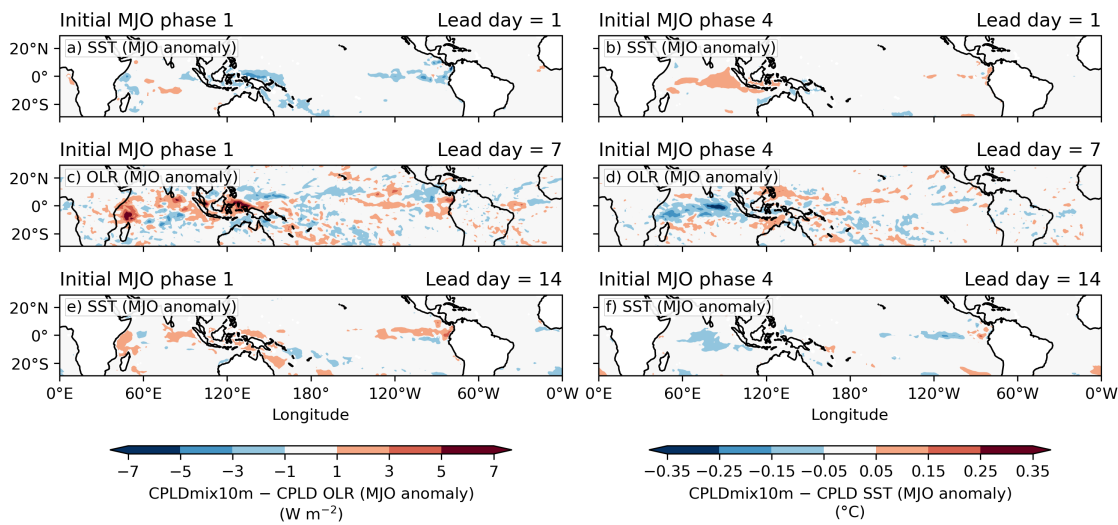


Figure 3.9: Composite daily mean MJO (20–200-day filtered) anomalies of CPLDmix10m minus CPLD difference for: a–b) SST at lead day 1 ; c–d) OLR at lead day 7; e–f) SST at lead day 14. Panels a, c and e are for initial MJO phase 1. Panels b, d and f are for initial MJO phase 4. Composites are calculated from boreal winter data.

between lead days 7 and 11 compared with the mixing experiments. Afterwards, all coupled models' MJO anomalies of SST evolve in parallel to each other until day 15.

The spatial extent of this feedback can be seen in Figure 3.9b,d,f. The additional mixing in the CPLDmix10m reduces the negative MJO anomalies of SST over the Indian Ocean compared with the CPLD model, leading to a positive SST difference (Figure 3.9b). By lead day 7, an organised enhanced MJO convection response is observed in the CPLDmix10m model in response to the warmer SSTs compared with the control over the preceding days. At lead day 7, the CPLDmix10m model simulates more convection over the central Indian Ocean compared with the CPLD model (Figure 3.9d) during the suppressed MJO phase (Figure 3.7d). By lead day 14, the CPLDmix10m model generates colder MJO SST anomalies compared with the CPLD model due to the relatively enhanced MJO convection at lead day 7 in the CPLDmix10m model (Figure 3.9d).

The mechanism described in this section is a two-way feedback between the MJO convection and diurnal warm layers. At lead day 1, the MJO conditions in the coupled model dictate the strength of the dSST. The dSST rectifies the daily mean SST and daily mean MJO anomalies of SST. The addition of diurnal warming shifts the peak of the MJO anomalies of SST earlier in the forecast, and by lead day 7, there is a coherent response in the MJO convection in the coupled model to the preceding MJO anomalies of SST. That convection has

an instantaneous effect on the dSST, and within the next 3 lead days the MJO anomalies of SSTs respond to that convection change. The stronger the MJO anomalies of dSST in the coupled model, the faster the MJO anomalies of SST recover post the MJO transition from active to suppressed phase, and vice-versa. Ultimately, more extreme anomalies of dSST in the coupled model lead to faster MJO phase speed through the modulation of the convection via MJO anomalies of SST.

3.4.3 Diurnal warming effect on the mean state

Analyses of NWP and climate models show that a steeper background horizontal moisture gradient results in improved eastward propagation of the MJO across the MC (Lim *et al.*, 2018; Ahn *et al.*, 2020b). The key process in simulating a realistic MJO eastward propagation is the existence of a realistic background moisture distribution and the advection of this by the MJO winds (e.g., Jiang, 2017). NWP models that are prone to the development of dry mean state biases in the lower troposphere over the Indo-Pacific warm pool, tend to produce a reduced mean horizontal moisture gradient and display a poorer MJO prediction skill (Kim *et al.*, 2019). Observations show that the presence of diurnal warming of SST (dSST) can increase the latent heat (LH) flux into the atmosphere by approximately 4 W m^{-2} (Fairall *et al.*, 1996; Matthews *et al.*, 2014). This increase can lead to changes in the mean state of the model, and have subsequent effects on the MJO. Therefore, to understand the effect of the dSST on the mean state and the MJO, we analyse in this section the evolution of mean state composite meteorological variables for six boreal winters in the warm pool region (40°E – 180°E , 10°S – 10°N) between November 1, 2016 and January 15, 2021 for the CPLD, CPLDmix5m and CPLDmix10m models.

Muted dSST leads to cooler mean state SST in the mixing experiments compared with the CPLD model over the warm pool region (Figure 3.10a). The cooling decreases from lead day 1 to lead day 15, starting at -0.1°C and -0.16°C for the CPLDmix5m and CPLDmix10m models at lead day 1 and reaching -0.05°C and -0.12°C for these models by lead day 15. The lead day 1 mean state SST difference between the mixing experiments and the CPLD model is reflected in the the upward latent heat (LH) flux into the atmosphere at lead day 1 (Figure 3.10b). Increased mixing in the upper ocean leads to cooler SSTs. Cooler SSTs will generally lead to less evaporation into the atmosphere, and hence lower LH flux is observed in the mixing experiments compared with the CPLD model. The

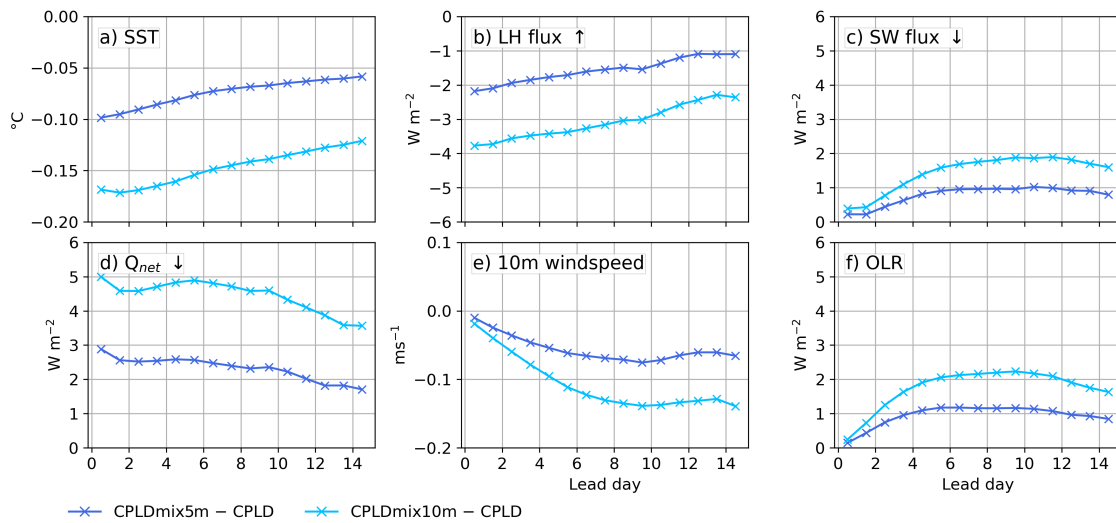


Figure 3.10: Daily average difference for the mean state composites in the warm pool region (40°E–180°E, 10°S–10°N) between the mixing experiments (CPLDmix5m and CPLDmix10m) and the CPLD model for: a) SST; b) upward latent heat flux into the atmosphere (LH flux); c) downward shortwave flux into the ocean (SW flux); d) downward net heat flux into the ocean Q_{net} ; e) 10 m wind speed; f) OLR. Composites are calculated with boreal winter season data only. Surface variables (SST, heat fluxes and 10 m windspeed) composite averages for sea grid points only.

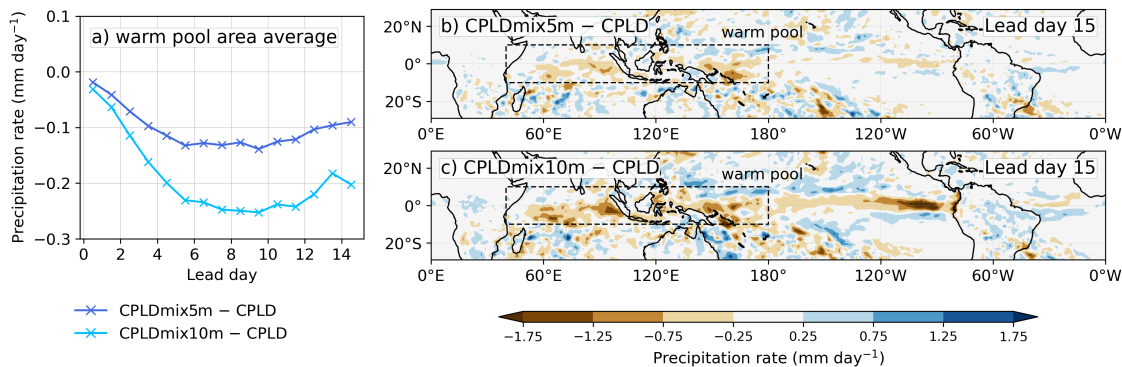


Figure 3.11: a) Daily average mean state composite difference in surface precipitation rate over the warm pool region (40°E–180°E, 10°S–10°N) for CPLDmix5m minus CPLD and CPLDmix10m minus CPLD models; daily average mean state composite difference in surface precipitation rate at lead day 15 for b) CPLDmix5m minus CPLD and c) CPLDmix10m minus CPLD models. Composites are calculated with boreal winter season data only. Warm pool extent in panels b and c.

pattern of the difference in the mean state SST and the difference in the mean state LH flux between mixing experiments and the CPLD model is spatially correlated with 0.95 correlation coefficient (not shown).

The mean state downward shortwave (SW) flux at the surface at lead day 1 is similar between all coupled model runs (Figure 3.10c). At longer lead

times, convection is suppressed in response to the cooler SSTs, such that the mixing experiments display more SW flux into the ocean compared with the CPLD model, reaching 1 W m^{-2} and 2 W m^{-2} difference by lead day 7 for the CPLDmix5m and CPLDmix10m models, respectively. The downward net heat flux, Q_{net} , shows a positive difference of $\sim 5 \text{ W m}^{-2}$ at lead day 1 between the CPLDmix10m and CPLD model (Figure 3.10d). The majority of the Q_{net} difference in the warm pool region is due to the SW and LH fluxes. The Q_{net} difference between the models gets smaller with lead day due to a decreasing difference in the LH flux and the increase in the positive SW flux difference.

The mean state difference in OLR evolves similarly to the SW flux difference, with less convection in the warm pool region by lead day 7 in both mixing experiments compared with the control (Figure 3.10f). The difference in OLR is approximately the same as the SW flux difference. The mean state 10m windspeed weakens steadily during the forecast, until lead day 9–10 when it reaches approximately -0.07 m s^{-1} and -0.14 m s^{-1} difference for the CPLDmix5m and CPLDmix10m models, respectively (Figure 3.10e). This corresponds to weaker 10m windspeed by 1.2% and 2.6% in the CPLDmix5m and CPLDmix10m models, respectively. The similar evolution in time of the windspeed and OLR differences suggests that the weaker windspeeds in the mixing experiments are due to the weakening of the Walker circulation.

The mean state precipitation rate at the surface at lead day 1 is similar between all coupled model runs (Figure 3.11a). Both mixing experiments display a steady decline in the surface precipitation rate compared with the CPLD model until lead day 7. At lead day 7, the difference between the mixing experiments and the CPLD model reaches approximately -0.12 mm d^{-1} and -0.25 mm d^{-1} for the CPLDmix5m and CPLDmix10m models, respectively, and stays steady until lead day 15. At lead day 15, the majority of the warm pool region in the mixing experiments displays a smaller surface precipitation rate than the CPLD model (Figure 3.11b-c). The strongest decrease in the surface precipitation rate between the mixing experiments and the CPLD model at lead day 15 is approximately 2 mm d^{-1} and is located west of Sumatra and east of New Guinea. Biases of such magnitude over the warm pool region can be linked to weaker moisture advection in NWP models, and ultimately weaker RMM amplitude (Kim *et al.*, 2019). A drier mean state lower troposphere in the CPLDmix10m model would indicate less background moisture, and might be expected to lead to a weaker MJO amplitude (Kim *et al.*, 2019). However, all coupled models investigated here display a very similar MJO amplitude over the 15 lead days

of the forecast (Figure 3.2c). We hypothesise that on a 15-lead-day timescale in this coupled NWP model it is unlikely that there are substantial changes to the strength of the MJO due to diurnal warming effects on the low level background moisture.

In summary, the mean state changes resulting from the suppression of the diurnal cycle of SST represent a weakening of convection and associated circulation patterns, and weaker surface precipitation, linked to reduced evaporation at the sea surface. On a 15-lead-day timescale, these mean state differences do not seem to affect the MJO amplitude in the coupled model. A stronger Walker circulation has been hypothesised to decelerate the MJO (Suematsu & Miura, 2022). All coupled models investigated here display a deceleration in the MJO phase speed from lead day 10, with the strongest deceleration recorded by the CPLDmix10m model (Figure 3.2d). Contrary to the results of Suematsu & Miura (2022), the CPLDmix10m simulates the weakest Walker circulation and the strongest deceleration of the MJO past lead day 10. Further study is necessary, beyond the scope of this paper, to separate the effects the diurnal warm layer on the MJO and on the mean state–MJO relationship in this coupled model.

3.5 Discussion and conclusions

The hindcast experiments of the coupled ocean–atmosphere and the atmosphere-only NWP models of the UK Met Office reveal skilful MJO predictions out to 15 lead days. The coupled model predicts a faster MJO than the atmosphere-only model, consistent with a previous study of Karłowska *et al.* (2024a) that analysed higher horizontal atmospheric resolution versions of these models. They hypothesised that the addition of the diurnal warming of SST (dSST) in the coupled model, compared with the atmosphere-only model, leads to stronger MJO anomalies⁵ of SST, and ultimately to a faster MJO. They proposed that stronger positive MJO anomalies of SST encourage the MJO convection ahead of the MJO, while stronger negative MJO anomalies of SST behind the MJO inhibit the MJO convection to the west. Using experiments which imposed instantaneous mixing in the upper few metres of the ocean, we reveal that this feedback does indeed lead to a faster MJO in the coupled NWP system of the UK Met Office. Reduction in the dSST leads to a reduction in the daily mean MJO

⁵20–200-day bandpass filtered anomalies

anomalies of SST and those SSTs lead to differences in MJO convection, slowing the MJO down over 15 lead days during the forecast.

The increase in the MJO phase speed in the coupled model compared with the atmosphere-only model over the first 7 lead days of the forecast is related to the mean tropical dSST in the coupled model. The stronger the mean dSST is produced in the coupled model at lead day 1, the larger the increase in the MJO phase speed is observed over the next 7 days. On a 7-lead-day timescale, representing the tropical dSST in the coupled model increases the MJO phase speed by $\sim 3\%$ relative to the atmosphere-only model. Coupling processes unrelated to the dSST contribute a further $\sim 5\%$ phase speed increase, resulting in a $\sim 8\%$ faster MJO phase speed in the coupled model compared with the atmosphere-only model. Karłowska *et al.* (2024a) reported a larger, 12%, increase in the MJO phase speed between these models at higher horizontal atmosphere resolution. The mean tropical dSST, however, does not differ substantially between the different versions of the coupled model, with a mean difference of $< 0.0002\text{ }^{\circ}\text{C}$ (not shown). It is likely that the coupled NWP system of the UK Met Office is more sensitive to the SST variability at a higher atmospheric horizontal resolution, or that the MJO speed increase unrelated to the dSST increases in this model with a higher horizontal resolution of the atmosphere component. Hence, about half of the MJO phase speed increase in this coupled model compared with the atmosphere-only version of the model on a 7 lead-day timescale can be attributed to the dSST, and the other half to other coupling processes. While the proportion of the phase speed increase due to dSST may differ in the observed MJO, it is worth noting that coupled models that struggle with the eastward propagation of the MJO may improve their skill by increasing the near-surface vertical resolution in the ocean model.

Diurnal warming of the ocean on calm, sunny days can be characterised by an exponential decay over the top few meters of the ocean (Matthews *et al.*, 2014). The coupled NWP model of the UK Met Office simulates that exponential decay. The mean tropical dSST in the coupled model decreases with the increase in the effective top model layer thickness. Theoretically, we estimate that a maximum dSST in the coupled model in the tropics at lead day 1 stands at $0.18\text{ }^{\circ}\text{C}$, close to the observed value in the Indian Ocean reported by Matthews *et al.* (2014) of $0.22\text{ }^{\circ}\text{C}$. The scaling depth of the exponential decay is found to be 4 m, very similar to the 4.2 m value observed in the Indian Ocean (Matthews *et al.*, 2014). At the current vertical resolution in the ocean component of the coupled model (approximately 1 m near the surface), the mean tropical dSST is close to

the theoretical maximum at 0.16°C . The small difference between these two values suggests that little can be gained towards a better representation of the dSST in this coupled model should the near-surface vertical resolution be further increased. Additionally, the similarity of the spatial pattern of the dSST from Figure 3.4a to the spatial patterns of dSST from the reanalysis data validated with surface drifters for 1979–2002 period from Bellenger & Duvel (2009) suggests that this coupled model simulates realistic diurnal warm layers. However, we conclude that models with a coarser vertical resolution in the near surface ocean (of the order of 10 m as is often used in climate models) may benefit from the parameterisation of diurnal warm layers.

The mixing experiments presented in this study provide an insight into the time-scale and the magnitude of the two-way feedback between the MJO and the dSST. The MJO conditions alter the strength of the dSST in the coupled model such that stronger dSST is observed during suppressed MJO conditions, consistent with observations (Anderson *et al.*, 1996; Bellenger & Duvel, 2009; Matthews *et al.*, 2014; Itterly *et al.*, 2021). At lead day 1, the presence of the dSST increases the daily mean SST in the coupled model compared with the foundation SST used by the atmosphere-only model. The magnitude of the dSST and the resultant daily mean SST increase varies systematically with MJO phase, resulting in MJO anomalies in dSST that are positive (negative) in suppressed (active) convective conditions. The dSST then rectifies the MJO anomalies of SST in the coupled model such that stronger MJO anomalies of dSST lead to stronger MJO anomalies of SST. Observations show that the dSST rectifies the intraseasonal SSTs (Yan *et al.*, 2021; Itterly *et al.*, 2021), and this coupled NWP system simulates this mechanism.

At longer lead times, the coupled model produces a faster MJO due to the interactions between the MJO, the dSST and the SST anomalies (see summary in Figure 3.12). Changes in the MJO regime lead to changes in the MJO anomalies of dSST. Changes in the MJO anomalies of dSST lead to changes in the amplitude of MJO SST anomalies. Stronger MJO anomalies of dSST at the beginning of the forecast can shift the peak of the MJO anomalies of SST earlier by a few forecast days. The peak response in the MJO convection to the initial changes in the MJO anomalies of SST is observed on a 7 lead-day timescale in the coupled model. Subsequently, the MJO anomalies of SST respond to these changes in the MJO convection within 3 days. A stronger warming (or cooling) post the active-to-suppressed MJO transition (or suppressed-to-active MJO transition) is observed for stronger MJO anomalies of dSST. The overall effects of a muted

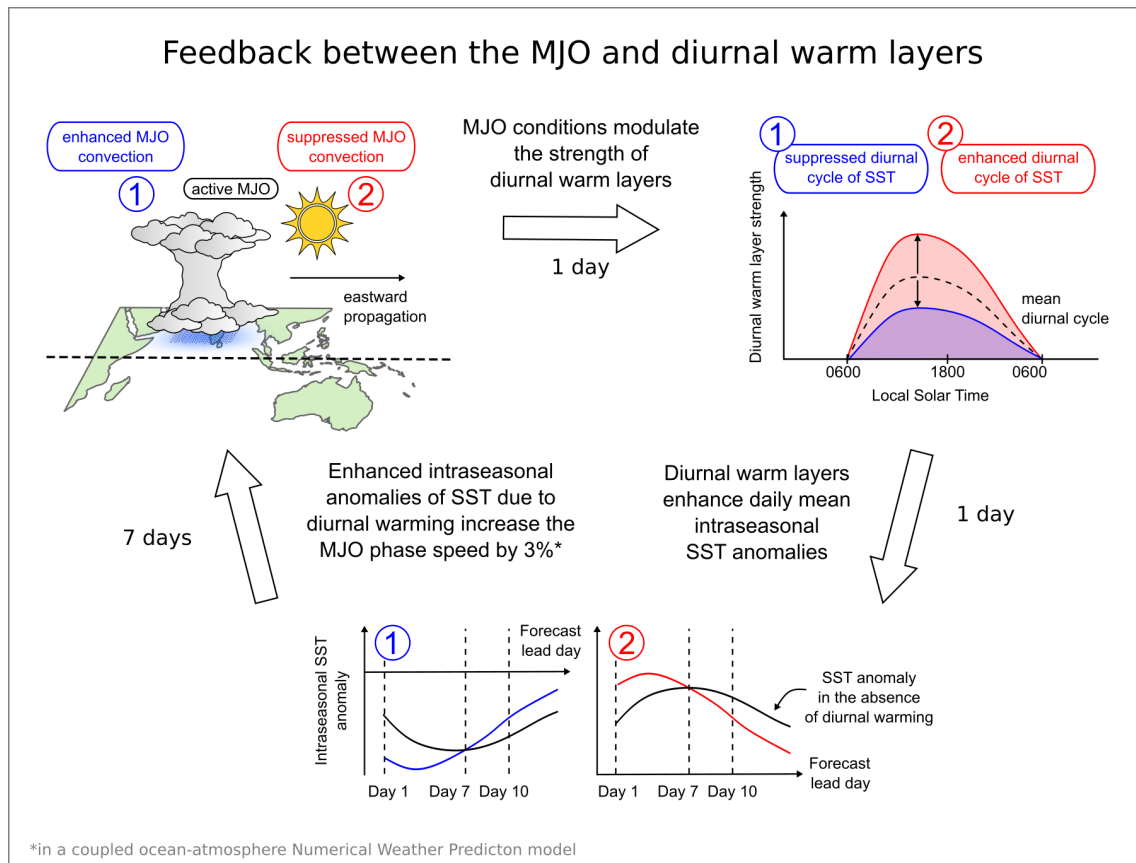


Figure 3.12: Schematic diagram of the two-way feedback between the Madden–Julian Oscillation (MJO) and diurnal warm layers in the upper ocean in the coupled ocean–atmosphere Numerical Weather Prediction (NWP) system of the UK Met Office. The MJO conditions in the coupled model modulate the strength of diurnal warm layers at lead day 1 such that enhanced (suppressed) MJO phase leads to suppressed (enhanced) diurnal warm layers. The presence of diurnal warm layers changes the daily mean sea surface temperatures (SST) in the coupled model and enhances daily mean intraseasonal SST anomalies. Stronger (weaker) diurnal warming at lead day 1 leads to warmer (colder) intraseasonal anomalies of SST than in the absence of diurnal warming. The modulated intraseasonal SST anomalies affect the surface fluxes between the ocean and the atmosphere, and ultimately lead to a peak MJO convection response on a 7-lead-day timescale and a $\sim 3\%$ increase in the MJO phase speed. Subsequently, the intraseasonal anomalies of SST respond to these MJO convection changes within the next 3 forecast days.

dSST in the coupled model are thus muted MJO anomalies of SST prior and post the MJO passage, ultimately leading to a slower eastward propagation of the MJO. DeMott *et al.* (2016) showed that stronger fluctuations in SSTs ahead of the MJO lead to more moist static energy there, encouraging the MJO convection. Seo *et al.* (2014) showed that higher dSST in a coupled model leads to higher mean SST and higher latent heat flux prior to convection, thus influencing the MJO. This mechanism is similar to that seen here in the coupled model and we confirm the early hypotheses of Bernie *et al.* (2008) and Woolnough *et al.* (2007) that indeed the presence of the dSST does alter the simulated MJO in a coupled model.

Ultimately, the presence of the dSST in this coupled NWP model leads to prediction of an erroneously fast MJO. The atmosphere-only model predicts a more accurate MJO phase speed than the coupled model according to the verification dataset. The coupled model became the operational forecast model at the Met Office in May 2022, taking over from the atmosphere-only model. The coupled model is more realistic but introduces more complexity. The convection in the Unified Model (UM; the atmosphere component of the coupled and the atmosphere-only models) is parameterised and may have been tuned to produce a good diurnal cycle of convection with the diurnally fixed SSTs. It is possible that the parameterisation scheme over-simulates the diurnal cycle of convection in response to diurnally evolving SSTs in the coupled model, leading to too-fast MJO propagation in this model. Several studies demonstrate the importance of the diurnal cycle of convection and precipitation over the MC (e.g., Peatman *et al.*, 2014; Birch *et al.*, 2016; Hagos *et al.*, 2016; Baranowski *et al.*, 2019; Wei *et al.*, 2020). Generally, the diurnal cycle of precipitation is represented better in convection-permitting models than in the models that parameterise convection (Prein *et al.*, 2015). Senior *et al.* (2023) showed that the regional version of the UM at a convection-permitting horizontal resolution improves extreme rainfall compared with the global lower resolution model that uses a parameterised convection. This improvement was associated with the modulation of the diurnal cycle of convection by convectively coupled Kelvin Waves, often associated with the MJO (e.g., Neena *et al.*, 2022). If the convection-permitting model improves the diurnal cycle of convection, would the too-fast MJO manifest in this coupled NWP system as well?

Our study also provides implications for climate projections of the MJO. Ahn *et al.* (2020b) analysed over 30 Coupled Model Intercomparison Project Phase 5 (CMIP5) and Phase 6 (CMIP6) models to reveal that the improvement in the

eastward propagation of the MJO in the CMIP6 models compared with the CMIP5 models is associated with a stronger horizontal moisture gradient in the lower troposphere across the warm pool region. They showed that the climate configuration of the coupled model examined here (HadGEM3) generates an accurate amplitude of the MJO-associated rainfall over the MC. However, similar to our results, the MJO in the HadGEM3 model propagates faster to the east than the observations suggest. The climate model uses the same horizontal resolution in the ocean and the atmosphere as the coupled model here, therefore, this too-fast propagating MJO in the climate setting is likely to be partially caused by the presence of diurnal warm layers in the upper ocean. Unlike the models of the UK Met Office, the majority of the ocean models from the CMIP6 do not have a 1 m near-surface resolution (see Table 1 in Wang *et al.*, 2022). Would the MJO improve or degrade in CMIP models should the near-surface vertical resolution be increased?

In summary, the mechanisms discussed in this paper show that the diurnal warming of SST has an important impact on the air–sea interactions on MJO timescales in an NWP setting. The two-way feedback between the MJO and diurnal warm layers should be further verified with in-situ observations of the diurnal cycle of SST, and the representation of the diurnal cycle of SST should be considered in future model developments in order to achieve better MJO predictions.

The goal of this chapter was to answer the second research question:

How does the upper 10 m of the ocean modulate the MJO in the coupled model?

Diurnal warm layers in the coupled model rectify daily mean SST and intraseasonal SST anomalies. Stronger intraseasonal SST anomalies due to the presence of diurnal warming in the upper 10 m of the ocean component of the coupled model lead to an increase in the MJO phase speed by a few percent between the coupled and the atmosphere-only model. Not all of the increase in the MJO phase speed between the models can be explained by diurnal warming alone. Therefore, the next chapter will investigate other oceanic processes that can modulate the intraseasonal SST anomalies in this coupled model.

Chapter 4

The relative importance of ocean advection and surface heat fluxes during the Madden–Julian Oscillation in a coupled ocean–atmosphere model

4.1 Preface

This chapter was submitted to the *Journal of Geophysical Research: Oceans*, and at the time of the thesis submission, pending review. This chapter is the sole work of the candidate, with the supervisory team listed as co-authors for their supervisory role. The main body of the article was not altered for this thesis. Footnotes 1 and 2 were added into the thesis chapter, with extra figures displayed in Appendix E. These additional figures do not alter the overall conclusions of this chapter.

The results of Chapter 3 showed that net heat flux-driven diurnal warm layers rectify intraseasonal SST anomalies in the coupled model of the UK Met Office. Other oceanic processes such as ocean advection and ocean mixing can also modulate these SST anomalies, therefore, this chapter presents an intraseasonal mixed layer heat budget in the context of the MJO to investigate these processes and their relative importance.

4.2 Introduction

The ocean surface mixed layer is a layer of approximately constant temperature and salinity, typically from the surface to between 10–100 m depth in the tropics (de Boyer Montégut *et al.*, 2004). The depth of the ocean surface mixed layer varies due to changes in incoming solar radiation at the ocean surface, wind-driven mechanical mixing and the influx of freshwater into the ocean. Intraseasonal variations of the mixed layer temperature (MLT; closely related to sea surface temperature) in the tropics can be linked to the evolution of the Madden–Julian Oscillation (MJO) (Chi *et al.*, 2014; Drushka *et al.*, 2012; McPhaden & Foltz, 2013; Halkides *et al.*, 2015), the dominant mode of intraseasonal (30–90 days) atmospheric variability in the tropics. The canonical MJO event is comprised of large-scale ($\sim 10\,000$ km) enhanced and suppressed convective anomalies travelling eastward in the tropics at $\sim 5\text{ m s}^{-1}$ phase speed (Madden & Julian, 1971, 1972). The MJO originates in the western Indian Ocean and travels through the Maritime Continent (MC; Indonesia, Philippines and Papua New Guinea), until it dissipates over the western Pacific.

The suppressed phase of the MJO is characterised by calm, cloud free and sunny conditions, leading to a reduction in mechanical mixing in the surface ocean, shoaling of the mixed layer and enhancement of sea surface temperatures (SSTs). Warm SSTs promote evaporation into the atmosphere and lead to instability and atmospheric convection. Observations show that warm intraseasonal SST anomalies occur 1 week prior to the MJO convection over the Indo-Pacific warm pool region (Hendon & Glick, 1997; Woolnough *et al.*, 2000). The development of the convective MJO anomalies is associated with an increase in cloud cover and surface winds, leading to a decrease in solar radiation at the ocean surface and an increase in mechanical mixing. This in turn leads to the deepening of the mixed layer and cooling of the SST (Drushka *et al.*, 2012; Liu *et al.*, 2021). Thus, the MJO suppressed phase promotes warm intraseasonal SST anomalies and the MJO convective phase contributes to the cooling of intraseasonal SST anomalies in the Indo-Pacific warm pool (Yan *et al.*, 2021; Itterly *et al.*, 2021). As a result, a coupled feedback mechanism exists whereby convective and SST anomalies both propagate eastwards, out of phase by a quarter of a cycle, with anomalies in the atmosphere and ocean reinforcing each other.

The role of ocean dynamics in the initiation and sustenance of the MJO is still debated in the scientific community (e.g., Zhang, 2005; Sobel *et al.*, 2010;

DeMott *et al.*, 2015). The MJO is predominantly an atmospheric phenomenon, and atmosphere-only models are able to successfully reproduce an eastward propagating MJO without a dynamically evolving ocean (e.g., Woolnough *et al.*, 2007; Karłowska *et al.*, 2024a). However, air–sea interactions are known to play an important role during the MJO (DeMott *et al.*, 2015; Li *et al.*, 2013b). Mixed layer heat budgets are conducted to investigate the relative importance of oceanic subsurface processes and heat flux forcing on the intraseasonal changes of the MLT during the MJO (Chi *et al.*, 2014; Drushka *et al.*, 2012; McPhaden & Foltz, 2013; Halkides *et al.*, 2015). Drushka *et al.* (2012) conducted a mixed layer heat budget using in-situ observations of Argo floats in the Indo-Pacific warm pool region and showed that the net heat flux changes associated with the eastward propagating MJO convective envelope are the main driver of the intraseasonal MLT changes. Contrary to the results of Drushka *et al.* (2012), the analyses of moorings by Chi *et al.* (2014) and McPhaden & Foltz (2013) showed that the horizontal advection and the formation of barrier layers can have a substantial effect on the MLT changes during the MJO.

Halkides *et al.* (2015) analysed 18 years of a heat-conserving ocean state estimate to reveal that wind-driven horizontal advection is the largest contributor to the intraseasonal MLT variability near the equator. Away from the equator, they found that vertical subsurface processes (vertical mixing and vertical advection) and net heat fluxes dominate the MJO mixed layer heat budget. Chandra *et al.* (2024) used an updated version of this dataset at a higher temporal frequency to state that horizontal advection is the main driver of intraseasonal ocean heat content anomalies in the upper 200 m of the tropical Indian Ocean. They argued that the surface heat fluxes play a minor role in the upper ocean heat content variability during the MJO, with a caveat that their study included both the mixed layer and the thermocline. They showed that positive intraseasonal anomalies of the ocean heat content over the Indian Ocean prior to the MJO convection over the MC are partially driven by equatorial oceanic Rossby waves. These waves are generated by equatorial oceanic Kelvin waves that are reflected off the coast of Sumatra and travel westward towards the African coast and bring warm SSTs to the western Indian Ocean basin. This is consistent with previous studies that shown that oceanic Rossby waves contribute to the intraseasonal changes in the upper ocean heat content (Rydbeck *et al.*, 2019, 2023). Rossby waves have also been hypothesised to trigger primary MJO events in the tropics (Webber *et al.*, 2012b).

The MJO-related upper ocean heat budget studies provided in the literature

suffer from certain limitations, and hence, there is no consensus on the relative importance of different ocean heat budget terms during the MJO. For example, Drushka *et al.* (2012) argued that the net heat flux is the main driver of the MJO related MLT changes, however, their heat budget did not close. Halkides *et al.* (2015) provided a closed heat budget, however, their study was limited by the lack of eddy activity in their ocean state estimate. Chandra *et al.* (2024) updated the study of Halkides *et al.* (2015) by adding a parameterisation scheme for the eddy transport, however, their analysis was extended to the thermocline, hence reducing the relative net surface heat flux contributions to the budget. In this paper, a mixed layer heat budget is conducted in the context of the MJO using a global coupled ocean–atmosphere Numerical Weather Prediction (NWP) model of the UK Met Office. An eddy-permitting coupled model is used to address the relative importance of ocean advection and the net heat flux forcing in modulating the MJO-related mixed layer temperature changes in the tropical Indian Ocean and the MC. In section 4.3, model specifications, data and methodology are described. In section 4.4, the mixed layer heat budget is conducted targeting three different MJO phases (pre-initiation, initiation and maturity), and a novel approach is presented to separate different horizontal scales at which oceanic processes contribute to the changes in the intraseasonal MLT. Discussion and conclusions follow in section 4.5.

4.3 Data and methods

4.3.1 Model specifications

The data used in this study were generated with the coupled ocean–atmosphere NWP system of the UK Met Office. The model was run in a hindcast mode for a 5 year period between May 1, 2016 and May 31, 2021, and initialised at 0000 UTC each day, yielding 1857 forecasts. Each model run was integrated out to 15 forecast days. The model used in this study is a version of the operational Met Office model running at the time, hence, some of the operational changes were applied to this model on September 24, 2018 (see Table 4.1 for detailed model versions and their references). The horizontal resolution of the atmosphere component was N216 from May 1, 2016 to September 24, 2018 (0.83° longitude and 0.56° latitude). Afterwards, the horizontal resolution of the atmosphere component was N320 (0.57° longitude and 0.38° latitude). The atmosphere component of the coupled model uses a convective parameterisation

Table 4.1: Model specifications summary.

Start date	End date	Atmosphere horizontal resolution	Atmosphere no. of levels	Ocean horizontal resolution	Ocean no. of levels	Global atmosphere (GA) version	Global land (GL) version	Global ocean (GO) version	Global sea ice (GSI) version
May 1, 2016	Sep 24, 2018	N216	L85	ORCA025	L75	GA6.1	GL6.1	GO5	GSI6
Sep 25, 2018	May 31, 2021	N320	L70	eORCA025	L75	GA7.2	GL8.1	GO6.0	GSI8.0

References: GA6.1 and GL6.1 (Walters *et al.*, 2017); GA7.2, GA7.2.1 and GL8.1 (Walters *et al.*, 2019); GO5 (Megann *et al.*, 2014); GO6.0 (Storkey *et al.*, 2018); GSI6 (Rae *et al.*, 2015); GSI8.0 and GSI8.1 (Ridley *et al.*, 2018)

scheme, with separate representations of shallow, mid-level and deep convection (Gregory & Rowntree, 1990; Gregory & Allen, 1991).

The ocean component of the coupled model is the Nucleus for European Modelling of the Ocean (NEMO) consortium ocean model (Madec *et al.*, 2017). The NEMO ocean model is comprised of 75 vertical levels, with 8 model levels in the top 10 m of the ocean. The horizontal resolution of the NEMO ocean model is 0.25°. The NEMO ocean model uses a turbulent kinetic energy scheme for the parameterisation of the vertical and horizontal mixing in the ocean model (Madec *et al.*, 2017). The model exchanges information between the ocean–sea ice and the atmosphere–land components with a 1 h coupling frequency. The ocean–sea ice and atmosphere–land components are initialised separately, with their own data assimilation (DA) systems. The NEMO ocean model uses the Forecast Ocean Assimilating Model (FOAM)-NEMOVAR DA system from Blockley *et al.* (2014) and Waters *et al.* (2015) to initialise its SST and sea ice concentrations. The atmosphere–land component is initialised with the 4D-Var DA system (Rawlins *et al.*, 2007) that uses SST and sea ice concentrations from the Operational Sea Surface Temperature and Ice Analysis (OSTIA) (Donlon *et al.*, 2012) assimilation system, updated by Fiedler *et al.* (2019) and Good *et al.* (2020). More detailed model descriptions are available in section 2 of Vellinga *et al.* (2020).

4.3.2 Real-time Multivariate MJO index

The Wheeler & Hendon (2004) Real-time Multivariate MJO (RMM) index is used in this study to define the state of the MJO in the tropics. The index is constructed with daily anomalies of top-of-atmosphere outgoing longwave radiation (OLR) and zonal winds at 850 hPa and 200 hPa (full methodology available in Gottschalck *et al.* (2010), with references therein). The indices RMM1 and RMM2 split the tropics into 8 phases: phases 8 and 1 when the MJO convection is located over Africa and the western hemisphere; phases 2 and 3 when the MJO convection is located over the Indian Ocean; phases 4 to 5 when the MJO travels across the Maritime Continent and phases 6 and 7 when the

MJO convection is located over the western Pacific. Observed indices are used in this study, retrieved from <http://www.bom.gov.au/climate/mjo> (Wheeler & Hendon, 2004). Days with an active MJO are defined for those with RMM amplitude: $\sqrt{\text{RMM1}^2 + \text{RMM2}^2} \geq 1.0$. For a detailed MJO performance analysis in this coupled model, see Karłowska *et al.* (2024c).

4.3.3 Mixed layer depth, barrier layer thickness and thermocline depth diagnostics

Mixed layer heat budgets were conducted for selected regions in the tropics in the context of the MJO. Subsurface ocean data were processed to study the evolution of ocean variables in the mixed layer in the coupled model of the UK Met Office. The mixed layer depth was defined following Drushka *et al.* (2014a) as the depth where the potential density (σ) change from the potential density at a reference depth of 10 m is greater than a threshold given by:

$$\Delta\sigma = \sigma(T_{\text{ref}} - \Delta T, S_{\text{ref}}, P_0) - \sigma(T_{\text{ref}}, S_{\text{ref}}, P_0), \quad (4.1)$$

where T_{ref} and S_{ref} are the temperature and salinity at the reference depth 10 m, P_0 is surface pressure. ΔT values of 0.25 °C, 0.5 °C and 0.8 °C were explored and 0.5 °C was chosen as the optimal value for ΔT (not shown). The reference depth of 10 m was chosen to remove the effects of the diurnal cycle of temperature on mixed layer depth (de Boyer Montégut *et al.*, 2007; Hosoda *et al.*, 2010). Temperature and salinity were interpolated in depth to 1 m resolution between 0 m and 200 m before calculating the mixed layer depth. Potential density calculations were obtained using Python package gsw v3.4.0 based on definitions from Gibbs SeaWater Oceanographic Toolbox of TEOS-10 (McDougall & Barker, 2011). The barrier layer thickness was calculated as the difference between the isothermal layer depth, defined by the depth where the temperature equals $T_{\text{ref}} - \Delta T$, and the mixed layer depth. The 20° isotherm depth (D20) was extracted from the model data by a linear interpolation between model levels.

4.3.4 Composites

Vertical profiles of ocean temperature, temperature tendencies and ocean currents were vertically averaged within the mixed layer, and weighted by the layer thickness, before further processing. Composite maps were calculated

for daily means of mixed layer averages of subsurface ocean variables using the ocean model grid at 0.25° in each region. Separate forecast initialisations were concatenated at a given lead time for further processing. Anomalies of all variables are calculated by the removal of the seasonal cycle (annual mean and first three harmonics) for the period 2017-2020. The MJO anomalies are then obtained by a temporal filtering of the anomalies with a 20–200 day bandpass Lanczos filter (Duchon, 1979). Although the MJO produces spectral peaks between 30 to 90 days, this wide bandpass filter is used to avoid spurious maxima and minima before and after an MJO event that are introduced by narrower filter bands such as 30–70 days (Matthews, 2000).

Mean state composites of the MLT (\bar{T}) and the mixed layer averaged ocean currents ($\bar{\mathbf{u}}$) were calculated for the boreal winter period from November 1, 2016 to January 15, 2021 for active MJO days. Apart from the mean state composites, every variable in this study refers to an MJO anomaly. Missing forecast initializations (less than 1%) were interpolated between the nearest previous and next day forecast initialisations. The statistical significance of the composite MJO anomalies of the mixed layer averaged ocean currents and the mixed layer averaged temperature at the 95% significance level were calculated using a Student's t-test.

4.3.5 Target MJO phase

Composites for each MJO phase were defined using a “target” MJO phase. The target MJO phase was set to be at T+10 days within any given forecast run, such that the evolution of the ocean processes that generate the SSTs prior to the target MJO phase can be studied in this coupled model. This timescale was chosen as the typical timescale of the coupling between the MJO convection and the intraseasonal SST anomalies in the tropics (Woolnough *et al.*, 2000). For example, for target MJO phase 3, an initial list of all the days that fall into MJO phase 3 from the RMM indices was first created. A second list was created by subtracting 10 days from all the days in the first list. The composite for the target MJO phase 3 was then calculated using all the forecasts initialised on the days in the second list. Consecutive forecast initialisations with the same target MJO phase at T+10 days were averaged before compositing and treated as one event. Only active MJO forecasts at T+10 days during the November–April season are used for the composite analysis.

4.3.6 Mixed layer temperature tendencies

The model provides temperature tendencies due to different oceanic processes: ocean advection (zonal, meridional and vertical), ocean mixing (horizontal and vertical), penetrating solar flux and non-solar fluxes, all calculated at the model time step. The following equation describes the temperature tendency in the model:

$$\frac{\partial T}{\partial t} = \underbrace{\left. \frac{\partial T}{\partial t} \right|_{\text{zonal adv.}} + \left. \frac{\partial T}{\partial t} \right|_{\text{merid. adv.}} + \left. \frac{\partial T}{\partial t} \right|_{\text{vert. adv.}}}_{\text{total advection}} + \left. \frac{\partial T}{\partial t} \right|_{\text{vert. mix.}} + \left. \frac{\partial T}{\partial t} \right|_{\text{horiz. mix.}} + \underbrace{\left. \frac{\partial T}{\partial t} \right|_{\text{solar flux}} + \left. \frac{\partial T}{\partial t} \right|_{\text{non-solar flux}}}_{Q_{\text{net}}}, \quad (4.2)$$

where T is the ocean temperature, t is time and Q_{net} is the net heat flux. The temperature tendencies due to ocean advection are calculated in the model as the divergence of the advective fluxes. The total temperature tendency due to ocean advection is a sum of the temperature tendencies due to zonal, meridional and vertical advection. Vertical mixing is parameterized in the model using a turbulent kinetic energy scheme that provides vertical eddy viscosity and diffusivity coefficients through time evolution of the turbulent kinetic energy (Madec *et al.*, 1997, 2017). Horizontal mixing is parameterized in a similar manner to vertical mixing, with the horizontal mixing coefficient varying in 2D space based on the mesh grid size in the model. The temperature tendency due to penetrating solar flux is calculated in the model using the Paulson & Simpson (1977) expression for the attenuation of solar radiation that assumes a constant chlorophyll concentration of 0.05 mg m^{-3} and exponential decay of downward irradiance with depth. The model splits the attenuation of solar radiation into three color bands for wavelengths 400–700 nm (red, green and blue), and one band for wavelengths longer than 700 nm. The model assumes an e-folding depth of 23 m for wavelengths 400–700 nm, and 0.35 m depth for wavelengths longer than 700 nm. The non-solar flux (comprised of longwave radiation, latent and sensible heat fluxes, Q_{nsr}) is distributed in the model within the top model level only. The temperature tendency due to Q_{nsr} is equal to $\frac{Q_{\text{nsr}}}{\rho_0 C_p h}$, where $\rho = 1026 \text{ kg m}^{-3}$, $C_p = 4000 \text{ J/kg}^\circ\text{C}$ and $h = 1.02 \text{ m}$. The horizontal mixing and residual temperature tendencies are not presented in this paper as they are negligible; a typical contribution from the horizontal mixing and the residual to

the MJO anomaly of MLT over 10 days of the forecast is $0.0001\text{ }^{\circ}\text{C}$, three orders of magnitude smaller than the changes in MLT (order $0.1\text{ }^{\circ}\text{C}$).

MLT tendencies in the model are stored as daily accumulations and all composites of the change in the MJO anomaly of MLT (ΔT) in this paper are summed from forecast day 1 to 10 to understand the changes in the MLT prior to the arrival of a specific MJO phase in the forecast at T+10 days. The composites of MLT and ocean currents correspond to daily means centred at 1200 UTC, therefore, all composites of the MLT and the ocean currents (u) in this study correspond to an average between forecast day 1 and 10.

4.3.7 Observations

Observed values of the daily interpolated OLR were obtained from the National Oceanic and Atmospheric Administration (Liebmann & Smith, 1996).

4.4 Results

In the following section, three target MJO phases (8, 1, and 3) were chosen to evaluate different oceanic processes contributing to the MJO anomaly of mixed layer temperature (MLT) prior to the arrival of each of these MJO phases at T+10 days. These phases were chosen to represent the pre-initiation, the initiation and the maturity of the MJO enhanced convective anomalies over the Indian Ocean. Three regions were chosen for the mixed layer heat budget in the context of the MJO: the western Indian Ocean region ($37\text{--}60\text{ }^{\circ}\text{E}$, $10\text{ }^{\circ}\text{S}\text{--}10\text{ }^{\circ}\text{N}$), the central Indian Ocean region ($65\text{--}85\text{ }^{\circ}\text{E}$, $10\text{ }^{\circ}\text{S}\text{--}5\text{ }^{\circ}\text{N}$) and the eastern MC region ($120\text{--}150\text{ }^{\circ}\text{E}$, $10\text{ }^{\circ}\text{S}\text{--}10\text{ }^{\circ}\text{N}$). The extent of each region is shown in Figure 4.1c. These regions were chosen as they display the largest changes over the equatorial belt in the MJO anomalies of SST prior to the initiation of the MJO convection over the western Indian Ocean (i.e., phases 8 and 1; Figure 4.1a-d).

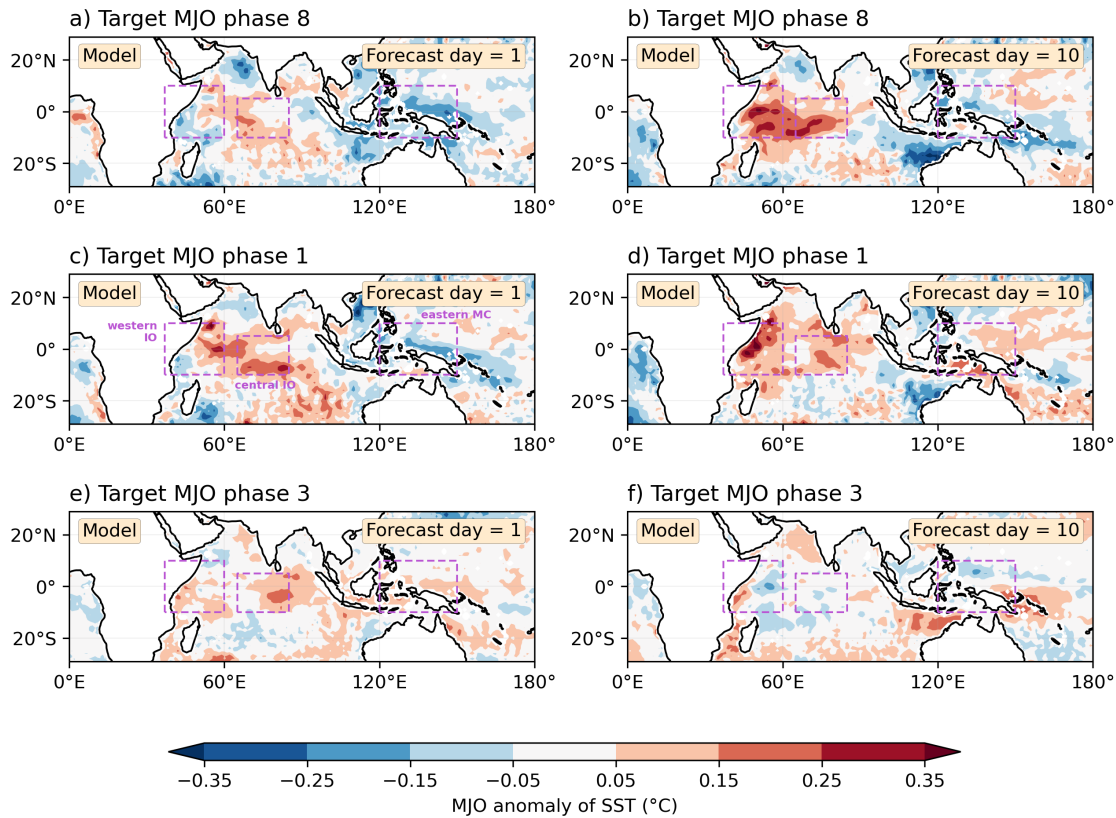


Figure 4.1: Composite maps of the 20-to-200 day bandpass filtered anomalies (the Madden–Julian Oscillation, MJO anomalies) of model sea surface temperature (SST) for target MJO phases 8 (panels a–b), 1 (panels c–d) and 3 (panels e–f). Panels a, c and e show composites at forecast day 1 (prior to each MJO phase arrival) and panels b, d and f correspond to forecast day 10 (when each MJO phase arrives in the observations).

4.4.1 MJO phase 8: Pre-initiation

MJO phase 8 represents the pre-initiation stage of the MJO enhanced convective anomalies in the western Indian Ocean region. Observations show that 40% of the primary MJO events initiate in the Indian Ocean, and such events are preceded by warm SST anomalies in that area (Matthews, 2008). In this section, a detailed analysis of the processes driving the warming tendency in SST prior to MJO phase 8 is presented to understand what leads to the development of the subsequent MJO enhanced convective anomalies.

Ten days prior to MJO phase 8 (at forecast day 1), the coupled model simulates a positive MJO anomaly of OLR over the Indian Ocean (suppressed MJO convection) and a negative MJO anomaly of OLR over the western Pacific (enhanced MJO convection) (Figure 4.2a). The suppressed MJO convection travels eastward into the MC when the MJO is in phase 8 at forecast day 10

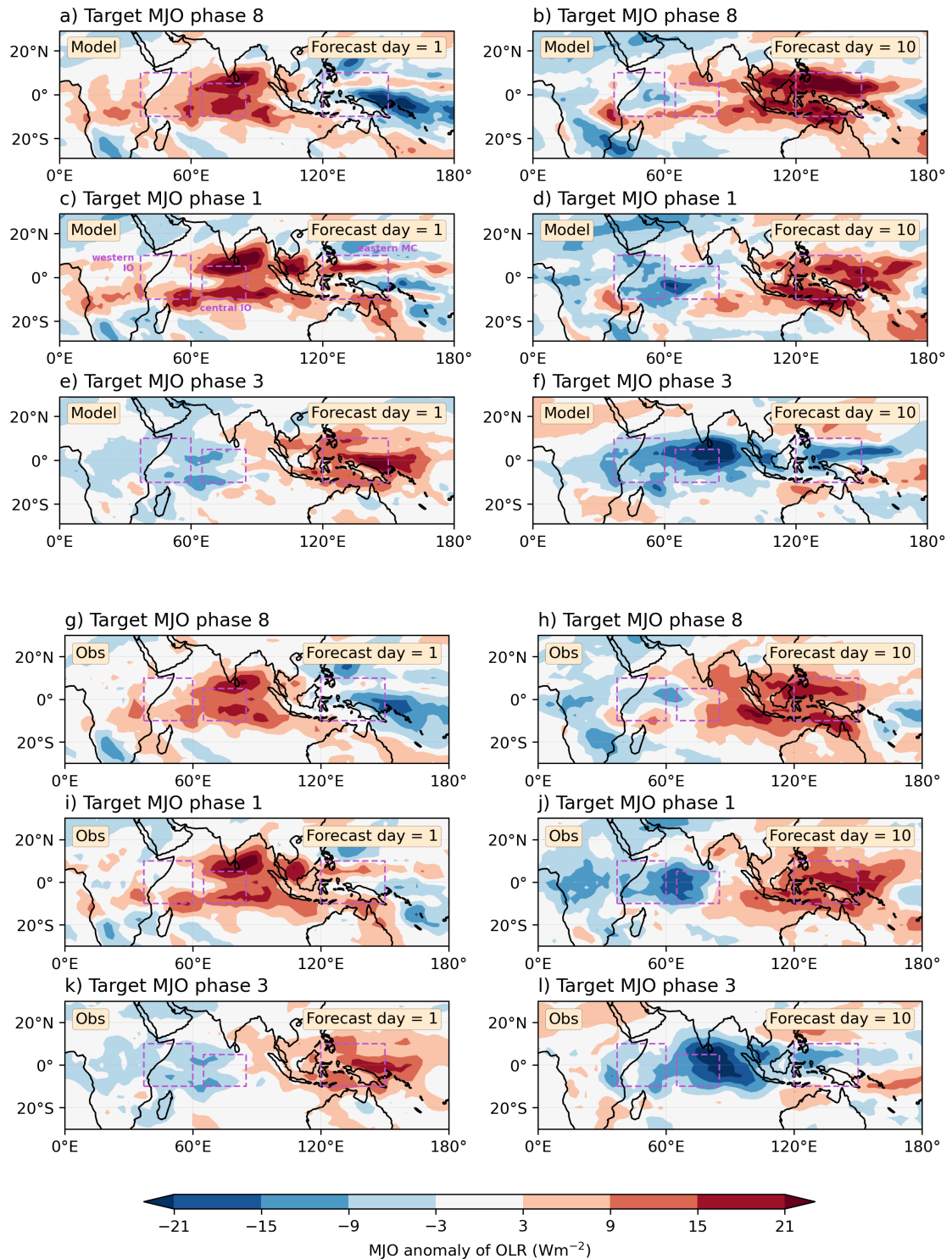


Figure 4.2: Composite maps of model MJO anomalies of outgoing longwave radiation (OLR) for target MJO phases 8 (panels a-b), 1 (panels c-d) and 3 (panels e-f). Lagged composites of the MJO anomalies of OLR in observations Liebmann & Smith (1996) for target MJO phases 8 (panels g-h), 1 (panels i-k) and 3 (panels k-l). Panels a, c, e, g, i and k show composites at forecast day 1 (prior to each MJO phase arrival) and panels b, d, f, h, j and l at forecast day 10 (when each MJO phase arrives in the observations).

(Figure 4.2b). Additionally, by forecast day 10, a weak enhanced MJO convection develops over the western Indian Ocean. The evolution of the MJO convection prior to MJO phase 8 in the coupled model is consistent with the observed pattern (Figure 4.2g-h), albeit with a stronger suppressed MJO convection over the MC at forecast day 10 in the model compared with observations (Figure 4.2b, h).

The MJO anomalies of SST prior to the MJO phase 8 are warm (cold) over the Indian Ocean (the MC) at forecast day 1 (Figure 4.1a). Warm MJO anomalies of SST in the western and central Indian Ocean intensify by forecast day 10 when the MJO phase 8 arrives (Figure 4.1b). These anomalies, of over 0.4°C , are likely to increase the low level moisture via evaporation and destabilise the atmosphere, which will ultimately lead to more MJO convection in this region later in the forecast and thus support the initiation of the MJO enhanced convective anomalies in phases 8 and 1.

The cumulative change in the MJO anomaly of MLT prior to the MJO phase 8 is positive over the western Indian Ocean region, with up to 0.5°C increase in the MJO anomaly of MLT ahead of MJO phase 8 (Figure 4.3a). Total advection, vertical mixing and Q_{net} all contribute to this warming (Figure 4.3d,g,j). The Q_{net} contributes the large scale warming pattern (Figure 4.3j), whereas the ocean advection and vertical mixing contribute at smaller horizontal scales (Figure 4.3d,g). The warming due to the Q_{net} prior to the MJO phase 8 in this region is consistent with the shoaling of the mixed layer (Figure 4.4d), which will in turn enhance the magnitude of the heat flux driven warming. The total ocean advection reinforces the Q_{net} in this region, contributing up to 0.4°C to the tumescent column of the MJO anomaly of MLT (Figure 4.3d). Suppressed vertical mixing leads to a 0.25°C warming near the equator at 55°E (Figure 4.3g). However, this warming tendency is cancelled by the cooling associated with the total advection at this location (Figure 4.3d).

Ocean advection prior to MJO phase 8 in the western Indian Ocean is the strongest at the equator near the coast of Africa (Figure 4.3d). The horizontal advection (zonal and meridional) dominates the total advection term (Figure 4.5a), consistent with Halkides *et al.* (2015). The average MJO anomaly of MLT in this region prior to MJO phase 8 is positive to the east of 45°E and negative near the coast (Figure 4.5g). The mean ocean currents in the coupled model are westward at the equator and south-westward along the coast of Africa between 5°S and 5°N (Figure 4.5d). These currents will advect this warm MJO anomaly of MLT westward toward the coast of Africa prior to the MJO convection initiation in this region. Advection of the MJO MLT anomalies by the mean currents

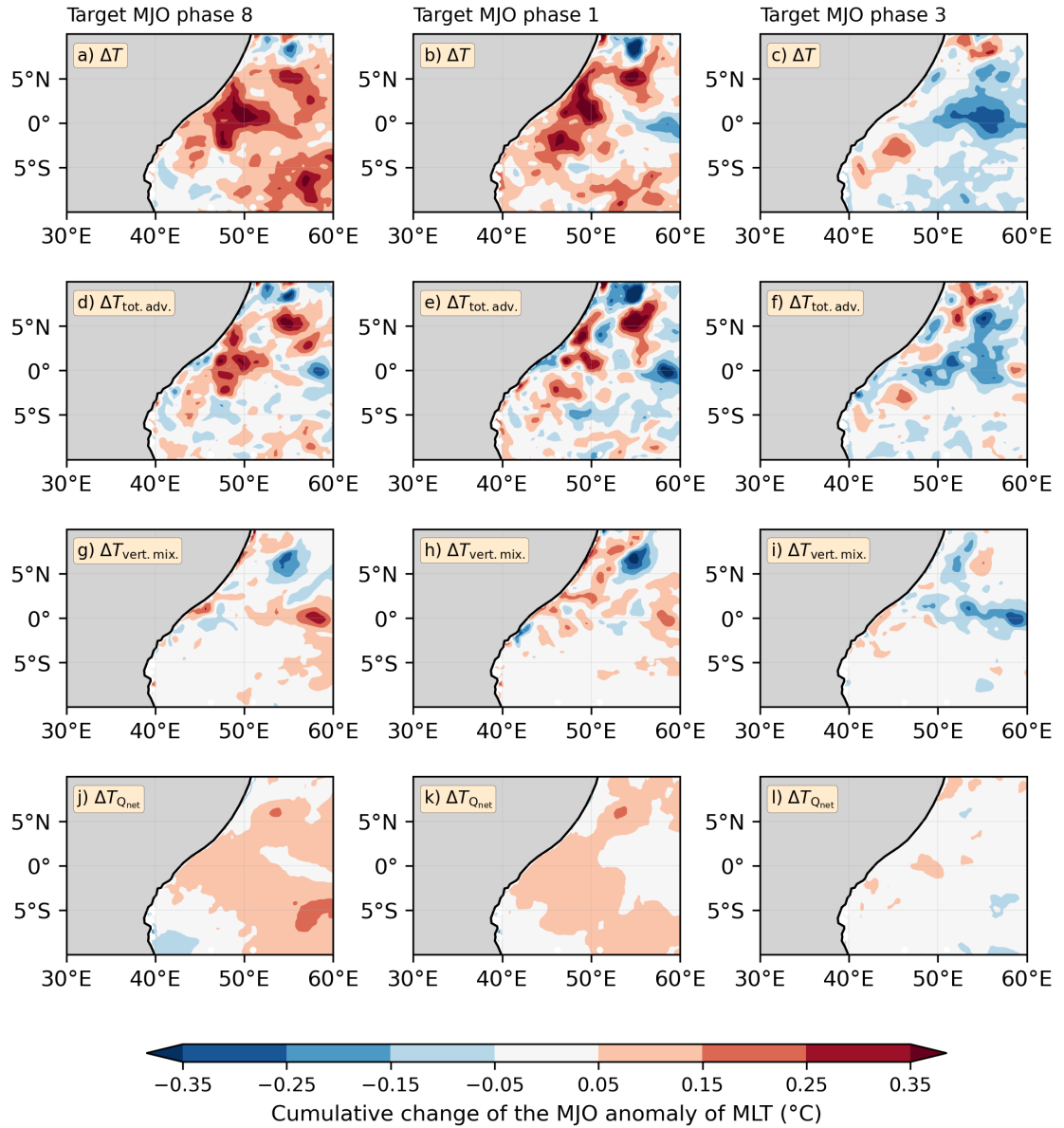


Figure 4.3: a–c) Cumulative change in the composite MJO anomaly of mixed layer temperature (MLT) over forecast days 1 to 10 prior to the arrival of (target) MJO phases 8, 1 and 3 in the western Indian Ocean region; d–f) cumulative change of the MJO anomaly of MLT due to total advection for target MJO phases 8, 1 and 3; g–i) cumulative change of the MJO anomaly of MLT due to vertical mixing for target MJO phases 8, 1 and 3; j–l) cumulative change of the MJO anomaly of MLT due to net heat flux for target MJO phases 8, 1 and 3.

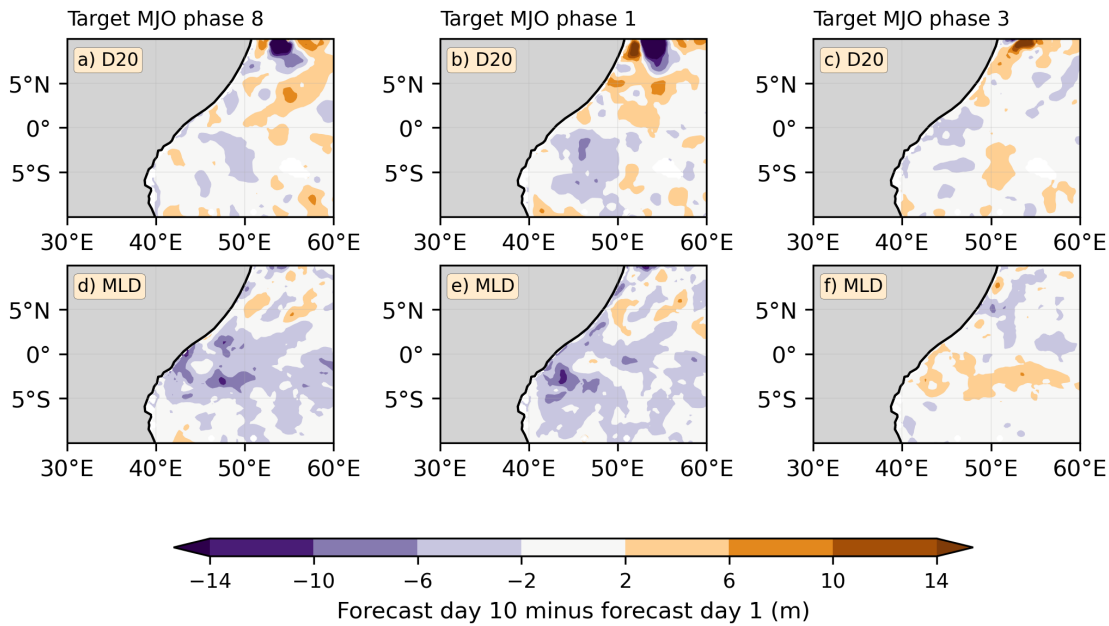


Figure 4.4: Change in the MJO anomaly of 20° isotherm depth (D20, panels a–c) and the mixed layer depth (MLD, panels d–f) from forecast day 1 to 10 prior to the arrival of (target) MJO phases 8, 1 and 3. Target MJO phase 8 in panels a, d, target MJO phase 1 in panels b, e, and target MJO phase 3 in panels panels c, f.

appears to be the leading cause of the anomalous warming due to horizontal advection, thus implying that this process is key in generating the warm SST anomalies that precede the initiation of convection here in MJO phases 8 and 1.

Deepening of the D20 and warm MLT tendency ahead of the MJO initiation can be associated with a downwelling oceanic equatorial Rossby wave (Webber *et al.*, 2012a). Such waves have a period of ~ 100 d, and they can produce a signal in the MJO anomalous ocean currents. There are statistically significant westward MJO anomalies of ocean currents at 45–50°E (Figure 4.5g). However, the MJO winds are weak prior to the MJO phase 8 in this area (not shown). There are also no notable changes in the MJO anomaly of D20 over 10 forecast days prior to the arrival of the MJO phase 8 (Figure 4.4a). Therefore, there is little evidence that MJO induced equatorial oceanic waves contribute substantially to the advection-driven warming in these composites.

Over the central Indian Ocean region, the MJO anomaly of MLT shows a warming tendency prior to MJO phase 8 (Figure 4.6a). This warming is mostly driven by Q_{net} (Figure 4.6j). The total advection term is noisy in this region (Figure 4.6d). The most coherent signal is the negative change in the MJO anomaly of MLT of up to 0.25°C at the equator near 65°E. This is likely caused by the advection of colder MJO anomalies of MLT towards the east from 70°E

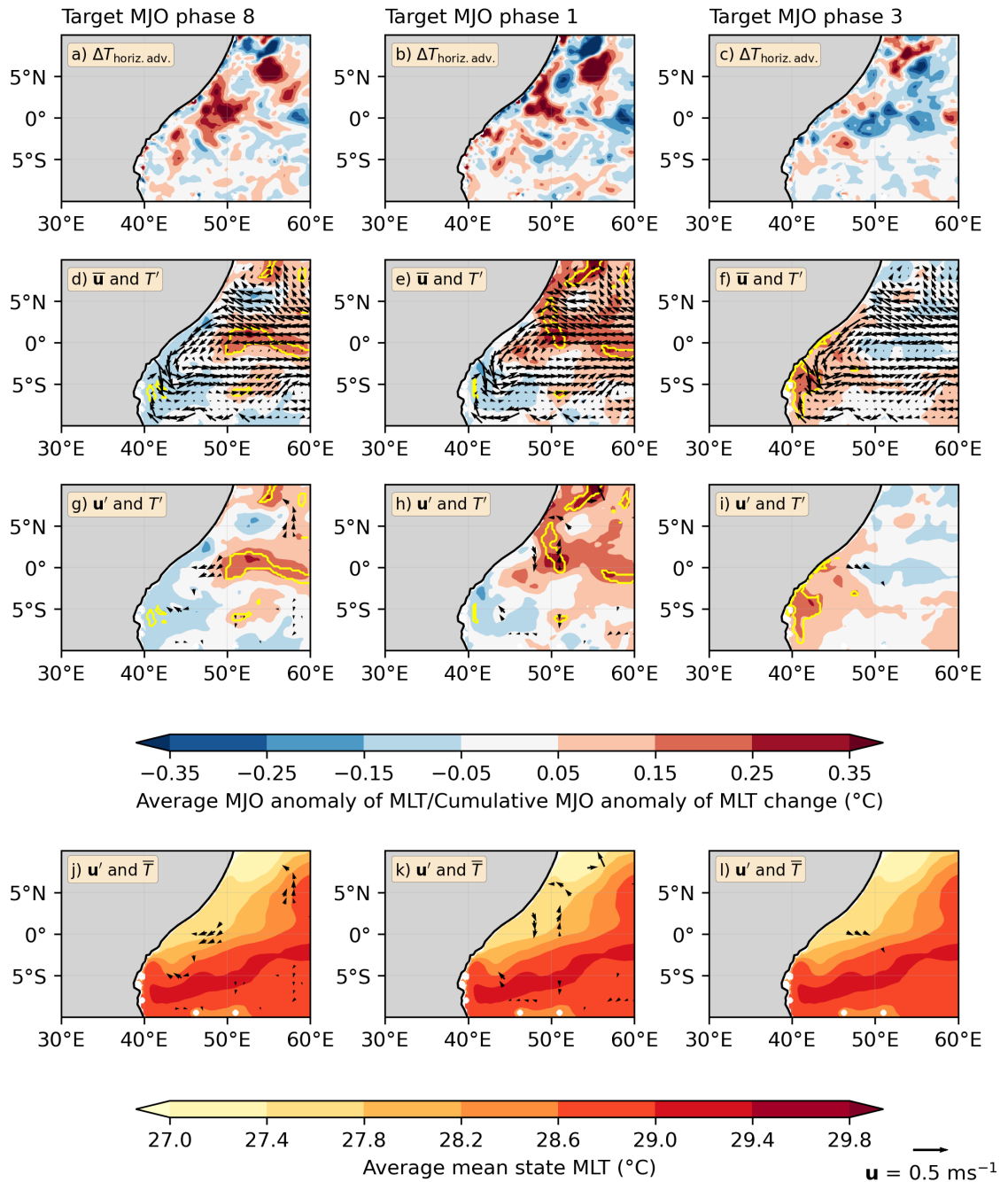


Figure 4.5: a–c) Cumulative change in the composite MJO anomaly of mixed layer temperature (MLT) over forecast days 1 to 10 prior to the arrival of (target) MJO phases 8, 1 and 3 in the western Indian Ocean region due to the horizontal advection; d–f) average mean state ocean currents in the mixed layer (\bar{u}) and the average MJO anomaly of MLT (T') over forecast days 1 to 10 in target MJO phases 8, 1 and 3; g–i) MJO anomalous ocean currents (u') in the mixed layer (\bar{u}) and T' over forecast days 1 to 10 in target MJO phases 8, 1 and 3; j–l) u' and \bar{T} . u' is plotted at the 95% significance level. Yellow outline shows T' at 95% significance level.

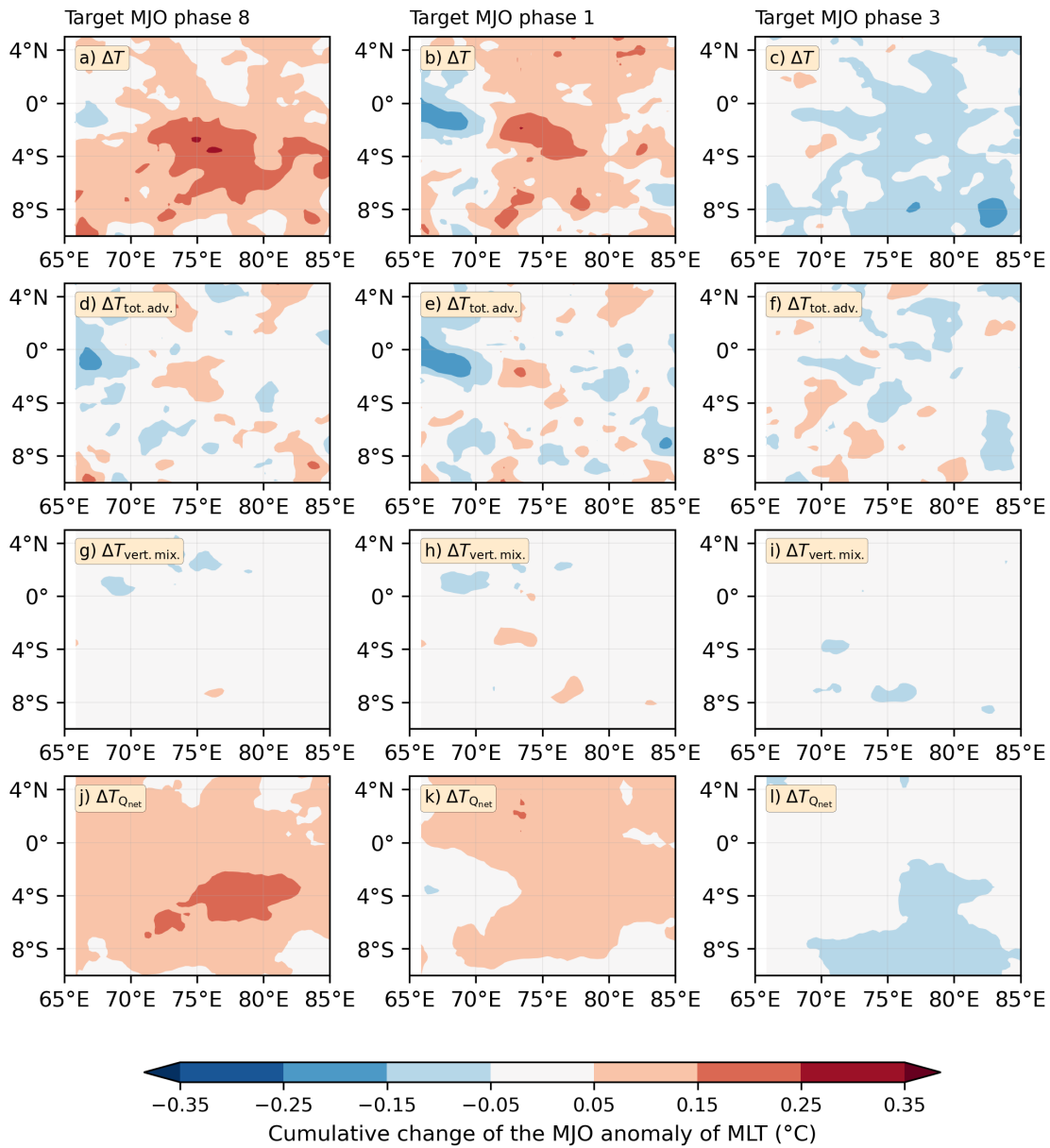


Figure 4.6: As Figure 4.3 but for central Indian Ocean region.

by the mean state ocean currents (not shown). The MJO anomalies of D20 and the mixed layer depth display shoaling in the central Indian Ocean region by up to 6 m prior to the MJO phase 8 (not shown). The mixed layer in this region is at an average depth of 33 m, and a change of 20% in the mixed layer depth is significant. The shoaling of the mixed layer will enhance the warming due to the Q_{net} in this region. The vertical mixing contribution to the MJO anomaly of MLT in this region is negligible prior to MJO phase 8 (Figure 4.6g).

The eastern MC experiences a cooling of up to -0.25 °C in the MJO anomaly of MLT prior to MJO phase 8 across most of the region (Figure 4.7a). The total

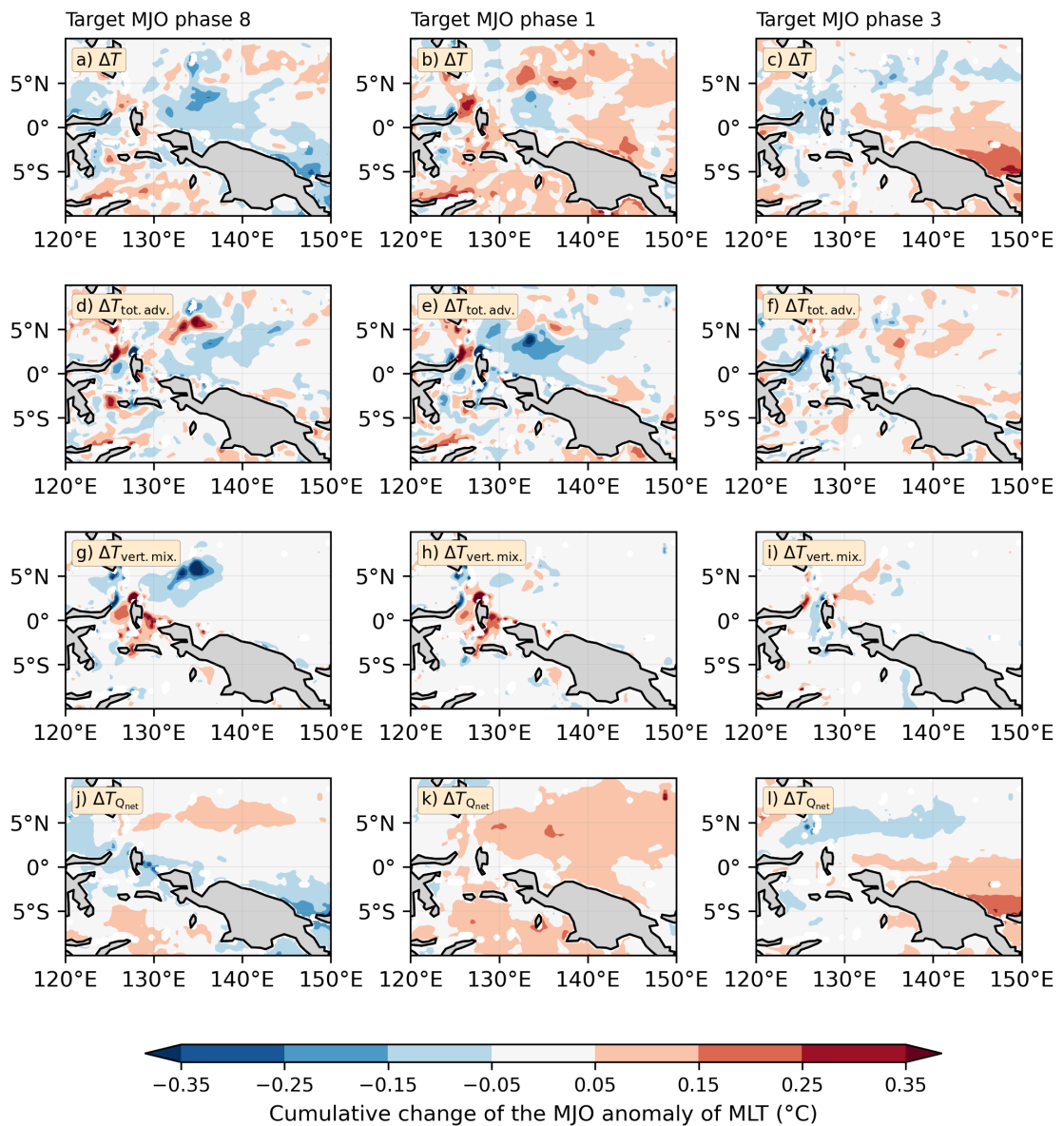


Figure 4.7: As Figure 4.3 but for the eastern Maritime Continent region.

advection is the main driver of this cold MJO anomaly of MLT (up to -0.15°C , Figure 4.7d). There is also a negative contribution from the vertical mixing anomalies in this area of up to -0.7°C (Figure 4.7g), and a positive contribution from the Q_{net} of up to 0.15°C (Figure 4.7j).

The horizontal advection is the main contributor to the total advection term in the eastern MC region prior to the MJO phase 8 arrival (Figure 4.8a). To further understand the horizontal advection term in this region, Reynolds decomposition is applied to the mean state variables and the MJO anomalies of

ocean variables as follows:

$$\Delta T_{\text{horiz. adv.}} = \bar{\mathbf{u}} \cdot \nabla T' + \mathbf{u}' \cdot \nabla \bar{T} + \mathbf{u}' \cdot \nabla T' + \text{residual} \quad (4.3)$$

where prime denotes the MJO anomalies of oceanic variables and bar denotes the mean state values (for boreal winter and active MJO). Note that the $\bar{\mathbf{u}} \cdot \nabla \bar{T}$ term is omitted from the equation because it does not affect anomalies. The horizontal advection term in the eastern MC region is reproduced well with Reynolds decomposition in each target MJO phase (Figure 4.8a,m, Figure 4.8b,n, Figure 4.8c,o).

Earlier, we showed that the mean state currents advect the MJO anomalies of MLT in the Indian Ocean to modulate the total MLT tendency in the context of the MJO prior to the MJO phase 8. In contrast, in the eastern MC, the MJO induced ocean current anomalies advecting the mean temperature gradients ($\mathbf{u}' \cdot \nabla \bar{T}$) are the main driver of the cooling due to the advection in this region prior to the MJO phase 8 (Figure 4.8g). The other terms, $\bar{\mathbf{u}} \cdot \nabla T'$ and $\mathbf{u}' \cdot \nabla T'$, do not produce a spatially coherent pattern of cooling in this region prior to the MJO phase 8 (Figure 4.8d,j).

The mean state ocean currents off the coast of New Guinea show the South Equatorial Current that travels northwest from New Guinea towards the Banda Sea and the Philippines (Figure 4.9d). The anti-cyclonic curvature present in the mean state ocean currents near 130–140°E is likely associated with the semi-permanent and anti-cyclonic Halmahera eddy that the coupled model starts to resolve. The MJO induced mixed layer ocean current anomalies prior to MJO phase 8 oppose the South Equatorial Current here, reducing the advection of warm water from New Guinea towards Mindanao, thus contributing to the net cooling in this region (Figure 4.9j). These ocean current anomalies are consistent with the MJO anomalous surface winds in this region prior to the MJO phase 8 (not shown).

Overall, prior to the MJO phase 8, the mixed layer experiences warming in the western and central Indian Ocean and cooling over the MC. The net heat flux drives the large scale warming pattern over the Indo-Pacific warm pool. In the western Indian Ocean, the mean state ocean currents advect the MLT warming due to the net heat flux and produce regions of enhanced warming that may seed the initial development of convection here. The ocean advection contribution is weaker over the central Indian Ocean where the net heat flux dominates. Over the MC, the MJO-induced ocean current anomalies suppress the mean westward

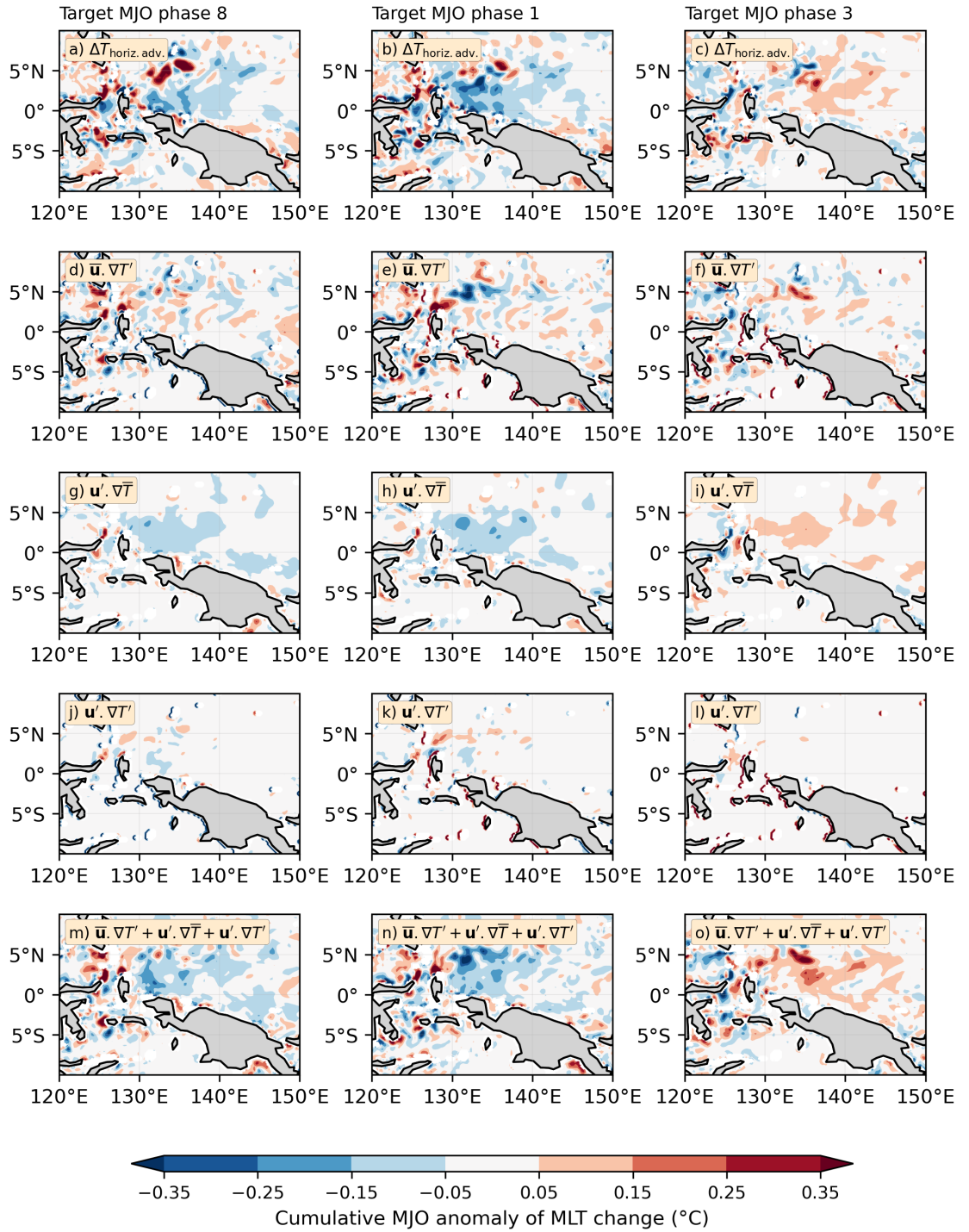


Figure 4.8: a–c) Cumulative change in the MJO anomaly of mixed layer temperature (MLT) due to horizontal advection over forecast days 1 to 10 prior to the arrival of (target) MJO phases 8, 1 and 3; d–f) advection of T' by \bar{u} over forecast days 1 to 10; g–i) advection of \bar{T} by u' over forecast days 1 to 10; k–n) advection of T' by u' over forecast days 1 to 10; m–o) sum of the advection of T' by \bar{u} , the advection of \bar{T} by u' and the advection of T' by u' over forecast days 1 to 10.

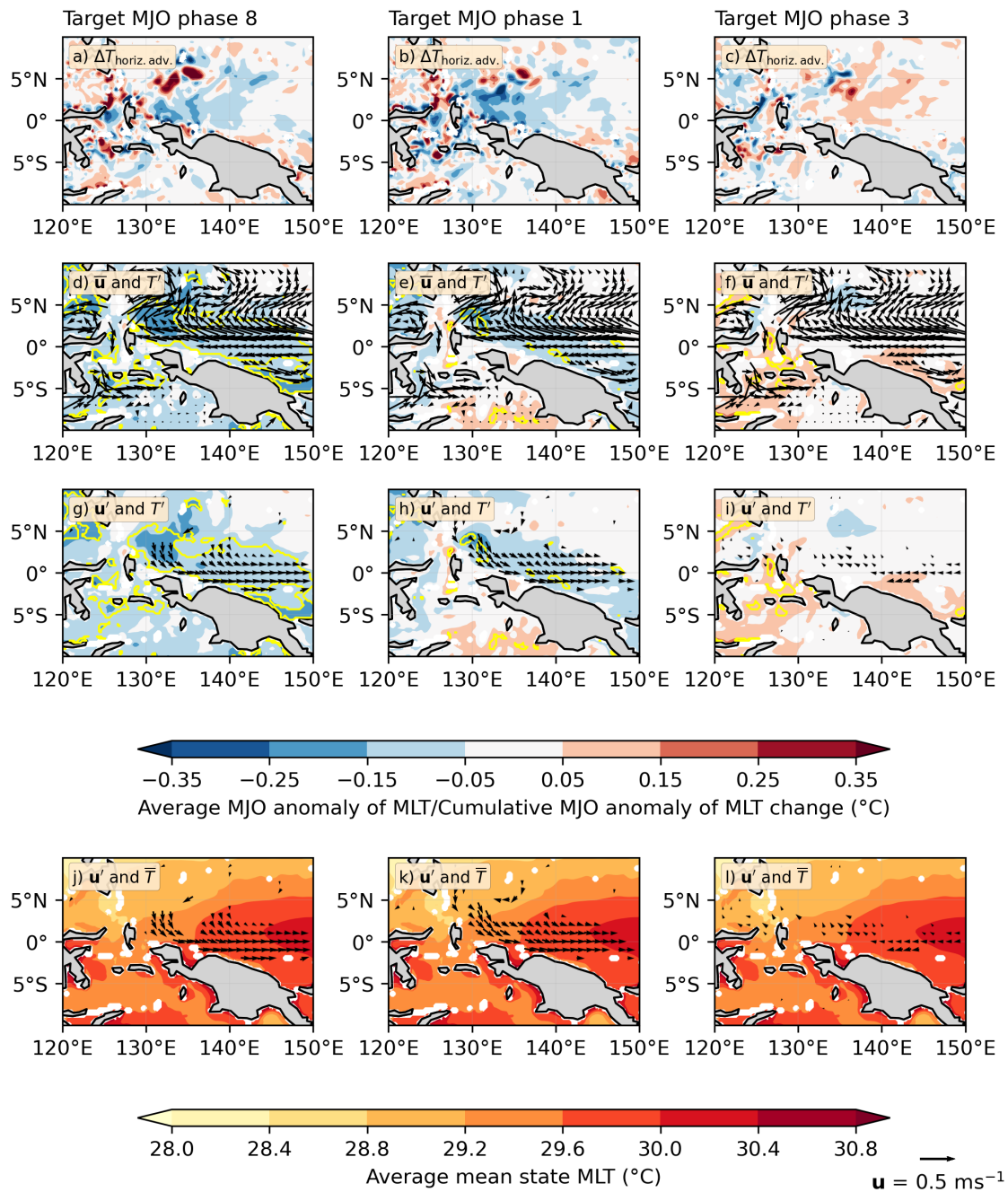


Figure 4.9: As in Figure 4.5 but for the eastern Maritime Continent region.

advection of warm MLT and thus contribute to cooling the MLT in this region, and promoting suppressed MJO convection over the MC.

4.4.2 MJO phase 1: Initiation

MJO phase 1 represents the initiation stage of the MJO enhanced convective anomalies over the western Indian Ocean region. MJO phase 1 is often associated with the lowest forecast skill compared with other MJO phases (e.g., Kim *et al.*, 2014; Karłowska *et al.*, 2024a). In order to understand why models may predict MJO phase 1 with a worse skill, it is important to study the evolution of the SSTs during the growth of the MJO enhanced convective anomalies in the western Indian Ocean region prior to MJO phase 1.

Prior to MJO phase 1, the coupled model simulates suppressed MJO convection over the central Indian Ocean and the western MC at forecast day 1 in the forecast (Figure 4.2c). By forecast day 10, the canonical MJO phase 1 develops in the tropics, with enhanced MJO convective anomalies of -20 W m^{-2} over the western and central Indian Ocean and a suppressed MJO convective signal over the MC (Figure 4.2d). The coupled model reproduces the observed pattern well in this MJO phase (Figure 4.2i,j), albeit slightly underestimating the enhanced MJO convection over the central Indian Ocean region at forecast day 10 (Figure 4.2d,j).

The development of the MJO convection over the Indian Ocean in the coupled model is preceded by warm MJO anomalies of SST in this region at forecast day 1 (i.e., 10 days prior to phase 1; Figure 4.1c). The warm MJO anomaly of SST in this region intensifies by forecast day 10 (i.e., the middle of phase 1; Figure 4.1d). Over the MC, the negative SST anomalies at forecast day 1 contribute to the development of suppressed MJO convection by forecast day 10 (Figure 4.2d).

Similar to MJO phase 8, the development of the MJO convection over the Indian Ocean prior to MJO phase 1 is associated with a warming in the MJO anomaly of MLT in all three regions considered here (Figure 4.3b, 4.6b, 4.7b). However, the strongest warming, of up to 0.5°C , occurs in the western Indian Ocean (Figure 4.3b). This warming is especially strong close to the African coast. The central Indian Ocean region experiences a warming of up to 0.25°C ahead of MJO phase 1 (Figure 4.6b). Over the eastern MC, the warming is less spatially coherent, and weaker than in the Indian Ocean, reaching a maximum of 0.15°C (Figure 4.7b). The large scale warming pattern recorded across all regions

considered prior to MJO phase 1 is contributed by the Q_{net} (Figure 4.3k, 4.6k, 4.7k). All regions display a uniform warming due to the Q_{net} of up to 0.15°C prior to MJO phase 1. This is in response to the large scale suppressed MJO conditions over the tropics at forecast day 1 (Figure 4.2c). This is also consistent with the shoaling of the MJO anomalies of the mixed layer in all three regions by up to 14 m (western Indian Ocean in Figure 4.4e; other regions not shown).

Similar to target MJO phase 8, ocean advection is the second most important term driving the MJO anomalies of MLT prior to the start of MJO phase 1. Total advection produces strong positive MLT anomalies of up to 0.5°C in the western Indian Ocean along the coast of Africa (Figure 4.3e). Horizontal advection dominates the total advection term in the western Indian Ocean prior to MJO phase 1 (Figure 4.5b). This MLT warming is likely driven by the mean state ocean currents advecting warm MJO anomalies of MLT towards and along the coast of Africa (Figure 4.5e). These warm MJO anomalies of MLT are significant at the 95% significance level (yellow outline in Figure 4.5h). The MJO-induced anomalous ocean currents are noisy, and dominated by eddy-like circulations (not shown); the relatively short (5-year) dataset is not sufficiently long to robustly determine if these anomalous currents consistently contribute to the advection term here.

A strong negative MJO anomaly of MLT is recorded in the coupled model at the equator between 60°E and 70°E prior to the MJO phase 1 (Figure 4.3b, 4.6b). This decrease of 0.25°C in MLT is driven by ocean advection (Figure 4.3e, 4.6e). This is consistent with the development of the SST anomalies in these regions prior to MJO phase 1 (Figure 4.1c–d). Warm SST anomalies of up to 0.25°C at forecast day 1 are advected west from the central Indian Ocean region towards the African coast. These anomalies are replaced in the central Indian Ocean region by relatively colder SST anomalies ($<0.05^\circ\text{C}$, white shading in Figure 4.1c,d) that are advected from further east.

The ocean advection tendency reinforces Q_{net} along the African coast (Figure 4.3e,k), however, over the eastern MC, advective MLT cooling (Figure 4.7e) opposes warming due to Q_{net} anomalies (Figure 4.7k). There is strong advective cooling of MLT located near the Halmahera eddy, north of the equator at around 130°E . MJO wind anomalies induce southeastward ocean current anomalies that weaken the South Equatorial Current off the coast of New Guinea. These anomalous currents are directed up the mean gradient in MLT (Figure 4.9k), thus producing anomalous cooling there (Figure 4.8h). The other terms, $\bar{\mathbf{u}} \cdot \nabla T'$ and $\mathbf{u}' \cdot \nabla T'$, do not produce a spatially coherent pattern of cooling in this region prior

to the MJO phase 1 (Figure 4.8e,k).

The vertical mixing contributions to the changes in the MJO anomaly of MLT prior to the MJO phase 1 are negligible in the central Indian Ocean region (Figure 4.6h) and the eastern MC (Figure 4.7h). The only region where the vertical mixing takes a larger role prior to MJO phase 1 is the western Indian Ocean region. The vertical mixing tendency of up to 0.25°C locally reinforces the contributions of ocean advection and Q_{net} near the African coast (Figure 4.3h). Vertical mixing opposes the ocean advection at the location of the Great Whirl off the coast of Somalia at 8°N , 55°E (see mean state ocean currents in Figure 4.5e). This is consistent with the shoaling of the MJO anomaly of D20 in this region (Figure 4.4b) that will promote the entrainment of colder water by increasing the vertical temperature gradient below the mixed layer.

Overall, prior to the MJO phase 1, net heat flux is the dominant driver of the large scale warming in the Indo-Pacific warm pool. Horizontal advection of MLT anomalies reinforces the net heat flux warming near the African coast prior to the MJO phase 1. Over the MC, the MJO-induced ocean current anomalies produce MLT cooling, opposing the large scale warming tendency associated with the net heat flux in this region.

4.4.3 MJO phase 3: Maturity

MJO phase 3 represents the maturity stage of the MJO enhanced convective anomalies over the western Indian Ocean region. This phase was chosen to study processes that drive the evolution of the SSTs once the MJO enhanced convective anomalies are established over the western Indian Ocean, and when these anomalies travel eastward into the central Indian Ocean and start to develop over the Maritime Continent in MJO phase 3.

Ten days prior to MJO phase 3, there is a weak enhanced MJO convection over the western and central Indian Ocean and a suppressed MJO convection over the MC in the coupled model (Figure 4.2e). By forecast day 10, MJO phase 3 arrives with a strong MJO convective anomaly over the whole tropical Indian Ocean and most of the MC (Figure 4.2f). The observations show a similar evolution of the MJO convective anomalies prior to MJO phase 3 (Figure 4.2k,l), albeit with a less elongated pattern of enhanced MJO convection over the Indian Ocean at forecast day 10.

The development of the MJO convective anomalies over the Indian Ocean is

preceded by warm MJO SST anomalies of $0.25\text{ }^{\circ}\text{C}$ in the central Indian Ocean at forecast day 1 (Figure 4.1e). These warm SST anomalies weaken over the Indian Ocean due to the intensification of the MJO convection that enhances cloud cover and increases mechanical mixing due to stronger surface winds (Figure 4.1f, 4.2f).

The change in the MJO anomaly of MLT over 10 days prior to the arrival of the MJO phase 3 is negative over the western Indian Ocean (Figure 4.3c). The cold MLT anomalies of up to $-0.35\text{ }^{\circ}\text{C}$ are centred around the equator in this region and are driven by the total advection (Figure 4.3f) and vertical mixing terms (Figure 4.3i), with a negligible contribution from Q_{net} (Figure 4.3l). There is a negative MJO anomaly of MLT located at the equator in the western Indian Ocean prior to MJO phase 3 (Figure 4.5f). It is likely that the mean state ocean currents advect this cool MLT anomaly westwards toward the African coast, contributing to the cooling west of 50°E . There is a small (approximately $3^{\circ} \times 1.75^{\circ}$) region of statistically significant current anomalies at the equator near the African coast, which would advect the colder mean state MLT off the coast of Africa toward the east, thus contributing to this negative MLT tendency (Figure 4.5l). However, it is unclear what causes the cooling tendency around 55°E , which may be driven by statistically insignificant eddy-driven heat fluxes. There are no coherent changes in the MJO anomaly of D20 prior to MJO phase 3 in this region (Figure 4.4c). The MJO anomaly of mixed layer depth shows a deepening of up to 6 m south of the equator in this region (Figure 4.4f), but this does not appear to contribute to the cooling tendency from vertical mixing along the equator (Figure 4.3i).

The MJO anomaly of MLT in the central Indian Ocean region and the eastern MC is mostly driven by Q_{net} prior to MJO phase 3 (Figure 4.6c,l and 4.7c,l). The central Indian Ocean experiences an MLT cooling of up to $-0.15\text{ }^{\circ}\text{C}$ prior to MJO phase 3, consistent with the development of MJO convection in this region from forecast day 1 to 10. The eastern MC region displays a warming in MLT near New Guinea, and cooling in the Sulawesi sea. The warming due to Q_{net} is consistent with the shoaling of the mixed layer in this region prior to MJO phase 3 by up to 10 m (not shown). Warm advection produces up to $0.15\text{ }^{\circ}\text{C}$ of warming north of New Guinea, near the location of the Halmahera eddy (Figure 4.7f). The Reynolds decomposition suggests that this warming is due to the MJO anomalous ocean currents strengthening the mean state currents that advect relatively warm mean state MLT from the equator northwards towards the Philippines (Figure 4.8i, 4.9l). The other terms, $\bar{\mathbf{u}} \cdot \nabla T'$ and $\mathbf{u}' \cdot \nabla T'$, do not produce a spatially coherent pattern of warming in this region prior to the MJO

phase 3 (Figure 4.8f,n). The vertical mixing contributions to the changes in the MJO anomaly of MLT prior to MJO phase 3 are negligible in the central Indian Ocean region (Figure 4.6i) and the eastern MC (Figure 4.7i). The total advection term in the central Indian Ocean region is noisy prior to MJO phase 3 and no coherent features can be inferred (Figure 4.6f).

Overall, prior to the MJO convection over the central Indian Ocean in phase 3, the MJO-induced MLT tendency is dominated by ocean advection and vertical mixing in the western Indian Ocean and by net heat flux in the central Indian Ocean and over the MC.

4.4.4 The importance of different horizontal scales in the mixed layer heat budget on the MJO timescales

The coupled model shows that Q_{net} dominates the large scale changes in the MJO anomalies of MLT. However, ocean advection and vertical mixing can substantially modulate the total MJO anomaly of MLT, reinforcing or opposing the changes due to Q_{net} . To determine the relative importance of these oceanic processes in the MJO mixed layer heat budget across a range of spatial scales, a Gaussian smoothing was applied to the two-dimensional MLT tendency anomaly fields for a selection of smoothing radii (1° , 2° , 4° , 8° , 16° , 32°). The covariance was then calculated between each budget term and the total MLT change (Figure 4.10)¹.

Prior to MJO phase 8, the ocean advection is the dominant term at smoothing radii smaller than 4° across all regions considered here (Figure 4.10a,d,g). At larger horizontal scales, Q_{net} displays the largest covariance in the western Indian Ocean region and over the eastern MC. In the central Indian Ocean, ocean advection and Q_{net} show a similar covariance to the total MLT change at larger horizontal scales.

Prior to MJO phase 1, the transition in dominance between ocean advection and Q_{net} happens at a larger horizontal scale in the Indian Ocean compared with target MJO phase 8, closer to 16° (Figure 4.10b,e). This change could be associated with large scale equatorial oceanic Kelvin and Rossby waves that advect MJO anomalies of MLT across the Indian Ocean. However, the signal is not robust enough in the ocean current anomalies in this coupled model. The covariance of

¹For completeness, equivalent Figure 4.10 for all target MJO phases is in Appendix E (Figures E7–E8).

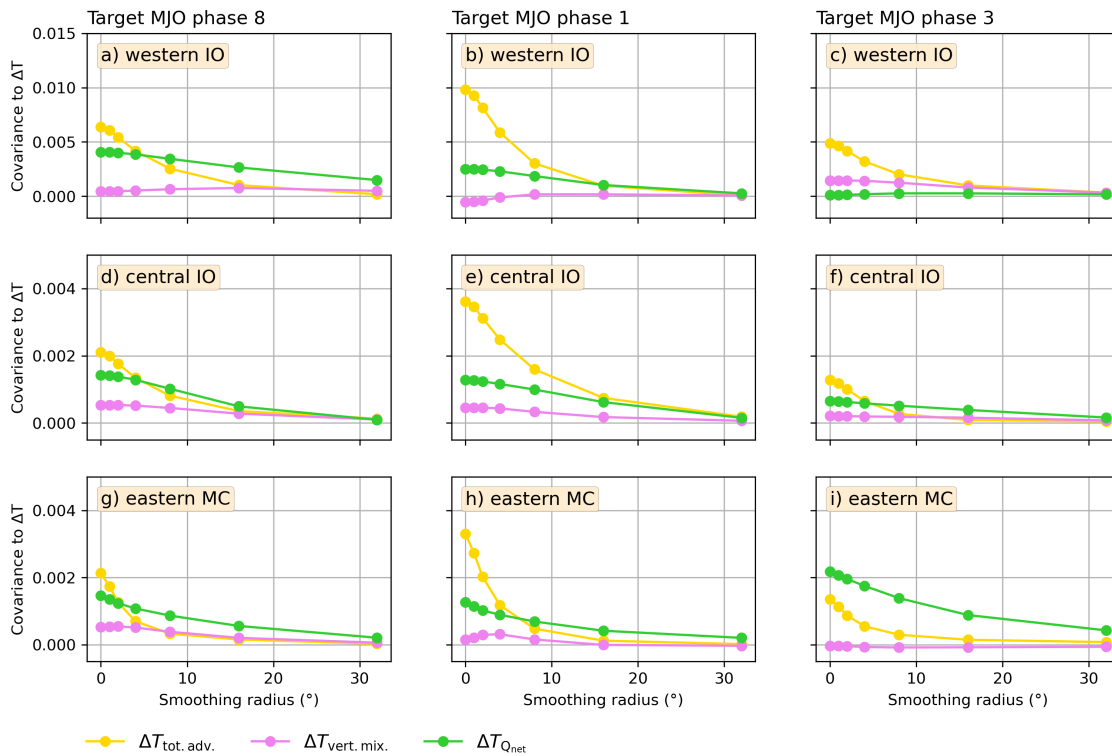


Figure 4.10: Covariance between the cumulative change in the MJO anomaly of mixed layer temperature, and each temperature tendency term, as a function of the smoothing radius. The temperature tendency terms are $\Delta T_{\text{tot. adv.}}$ (yellow), $\Delta T_{\text{vert. mix.}}$ (pink) and $\Delta T_{Q_{\text{net}}}$ (green). The covariances are calculated over forecast days 1 to 10 prior to the arrival of target MJO phases 8 (left column), 1 (central column) and 3 (right column), for the western Indian Ocean (IO) region (panels a–c), central IO region (panels d–f) and eastern Maritime Continent region (panels g–i).

the advection term in target MJO phase 1 is approximately three times stronger than the covariance of the Q_{net} term (Figure 4.10b,e,h). In contrast, in target MJO phase 8, the covariance of the advection term is only slightly larger than the Q_{net} covariance, thus the transition in dominance between ocean advection and Q_{net} is at a smaller horizontal scale in target MJO phase 1 than target MJO phase 8.

Prior to MJO phase 3, each region displays a more complex interplay between the three processes than in phase 8 or 1. In the western Indian Ocean region, ocean advection is dominant at all horizontal scales, with vertical mixing displaying the second largest covariance and Q_{net} being negligible at all horizontal scales (Figure 4.10c). In the central Indian Ocean, ocean advection dominates at smaller horizontal scales ($<4^\circ$) and Q_{net} has the largest covariance at horizontal scales $>4^\circ$ (Figure 4.10f). Finally, in the eastern MC, Q_{net} dominates at all horizontal scales prior to MJO phase 3, with advection having a secondary contribution to the changes in the MJO anomaly of MLT there (Figure 4.10i).

4.5 Discussion and conclusions

The mixed layer heat budget of the coupled ocean–atmosphere Numerical Weather Prediction model of the UK Met Office reveals that ocean advection plays an important role in modulating intraseasonal mixed layer temperature (MLT) anomalies in the Indo-Pacific warm pool region. The coupled model shows that net heat fluxes drive the large-scale (order 10°) changes to the intraseasonal MLT anomalies, but ocean advection dominates at smaller horizontal scales (order 1°) and contributes significant changes to these MLT anomalies. Figure 4.11 shows a graphical summary of the oceanic processes that drive the intraseasonal MLT changes during the MJO in this coupled model.

Prior to the MJO initiation over the western Indian Ocean (RMM phase 1), the mixed layer shoals and the net surface heat fluxes (distributed over a shallower mixed layer) lead to an overall warming over the Indo-Pacific warm pool. The advection of the intraseasonal MLT anomalies by the mean state ocean currents in the western Indian Ocean reinforces the warming in this region due to the net surface heat flux. Over the Maritime Continent, the MJO-induced ocean current anomalies oppose the mean state ocean currents (and mesoscale eddy circulation) to resulting in anomalous cooling from the reduced advection of warm mean state MLT from the east, thus reducing the warming due to the net heat flux in this region.

When the MJO convection is developing over the central Indian Ocean (RMM phase 3), the situation is more complex. The western Indian Ocean experiences cooling after the MJO passage. This cooling is likely associated with the mean state ocean currents advecting cold MJO anomaly of MLT towards the coast of Africa. In the central Indian Ocean region, the cooling due to the development of the MJO convective phase is driven by the net heat fluxes only. Over the eastern Maritime Continent, the net heat fluxes are driving the most of the total MLT changes on MJO timescales. However, there is a small and positive contribution in this region from the MJO-induced ocean current anomalies that strengthen the mean currents in this region.

RMM phases 8, 1 and 3 were investigated in this study to represent different stages of the evolution of the MJO enhanced convective anomalies in the western Indian Ocean region. The mixed layer heat budget was conducted for all RMM phases and the results are as follows. The intraseasonal mixed layer heat budget in the western Indian Ocean region is dominated by ocean advection at small

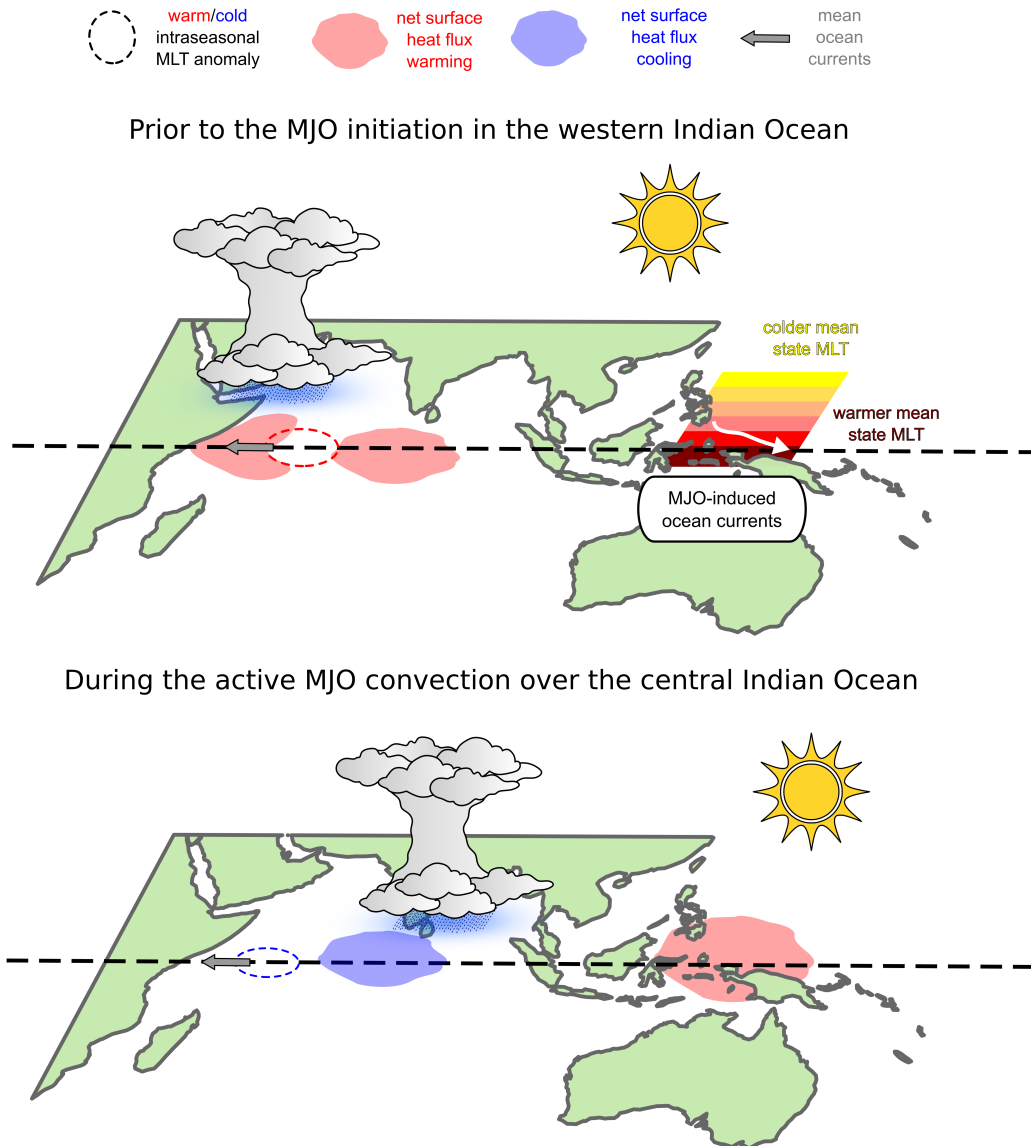


Figure 4.11: Schematic diagram of the oceanic processes that drive intraseasonal mixed layer heat budget during the initiation and the evolution of the Madden-Julian Oscillation (MJO) in the coupled ocean-atmosphere Numerical Weather Prediction system of the UK Met Office. MLT – mixed layer temperature. Mean ocean currents and MJO-induced ocean currents not to scale.

scales across all target MJO phases (Figures E1–E8 in Appendix E). In this region, the net heat flux contributes to the large-scale warming (cooling) of the intraseasonal MLT anomaly prior to MJO phases 8 to 2 (6 to 7) (Figures E1–E2 in Appendix E). Prior to MJO phases 6 and 7, the net heat flux cooling occurs off the equator, whereas prior to MJO phases 8 to 2 the warming pattern occurs both at the equator and off the equator. The net heat flux is not important in this region prior to MJO phases 3 to 5. The net heat flux is the dominant driver of the intraseasonal MLT changes in the central Indian Ocean region across all target MJO phases (Figures E3–E4 in Appendix E). In the eastern MC, the cooling due to ocean advection in the area of the Halmahera eddy occurs only prior to MJO phases 7 to 2 (Figures E5–E6 in Appendix E). The net heat flux, however, drives the large scale warming and cooling patterns in this region across all target MJO phases.

The MJO mixed layer heat budget we have conducted using the coupled NWP model of the UK Met Office is broadly consistent with the ocean state estimate mixed layer heat budget of Halkides *et al.* (2015). Halkides *et al.* (2015) demonstrated that the net heat fluxes are the most dominant off the equator during the MJO, while the horizontal advection is the biggest driver of the intraseasonal MLT changes at the equator during the MJO. Our results broadly corroborate the results of Halkides *et al.* (2015), however, the horizontal advection contribution in some places in this study extends some distance away from the equator (western Indian Ocean region; Figure 4.5a–c), while in others, no dominant signal is found in the advective term (central Indian Ocean region; Figure 4.6d–f). Our forecast model suggests that both the ocean advection and the net heat fluxes are important, but they act on different horizontal scales to modulate the intraseasonal changes in the MLT. The net heat flux dominates at larger horizontal scales (order 10°), while ocean advection dominates at smaller horizontal scales (order 1°).

The westerly wind bursts associated with the MJO increase the cyclonic eddy generation in the Banda Sea during boreal winter season (Hao *et al.*, 2023). The coupled model of the UK Met Office shows important contributions from the ocean advection in the Halmahera eddy region to the MJO anomalies of MLT over the eastern Maritime Continent region. The MJO-induced ocean currents in the model lead to a cyclonic circulation in phases 1 and 8 in this region. The Halmahera eddy is known to be weaker during boreal winter (Ramadhan *et al.*, 2020), therefore, our results pose the question of whether the MJO reduces the anti-cyclonic circulation in this region, and whether the MJO

affects the vertical heat transfer from below the mixed layer towards the surface within the area of this eddy. An *in situ* mixed layer heat budget of Vijith *et al.* (2020) corroborates our findings, showing that ocean advection has a significant contribution to the mixed layer heat budget at small horizontal scales north of the central Indian Ocean region, in Bay of Bengal. The boreal summer intraseasonal oscillation (BSISO) that propagates northwards over the Bay of Bengal is one of the triggering mechanism for the onset of the Asian summer monsoon (Li *et al.*, 2013a). Akin to the MJO, the BSISO can modulate the wind stress and the heat flux at the ocean surface, affecting the mixed layer depth and the MLT over the Bay of Bengal (Jia *et al.*, 2023). A potential future study should extend our analysis of the coupled NWP model of the UK Met Office to the Bay of Bengal to understand different processes governing the evolution of the MLT in this forecast model during the northward propagation of the BSISO.

The MJO is also reported to modulate the strength of the Indonesian Throughflow, which in turn regulates the exchange of water between the eastern Indian Ocean basin and the western tropical Pacific Ocean basin (Gordon *et al.*, 2019; Tamasiunas *et al.*, 2021). Tamasiunas *et al.* (2021) shown that 50% of the Indonesian Throughflow transport is regulated by the MJO, and the convective (suppressed) phase of the MJO leads to a reduction (enhancement) of the Indonesian Throughflow transport. Our forecast model suggests that the MJO does modulate ocean currents in the Indonesian Throughflow area, raising implications for the heat and water transport between these ocean basins in models that do not resolve the interaction between the MJO and the mesoscale eddy circulations in this region. Additionally, vertical mixing is found to contribute a substantial cooling near the area of the Great Whirl off the coast of Africa prior to the MJO phases 8 and 1 in this coupled model. The thermocline shoals in this region prior to the MJO phases 8 and 1, and consistently, the model records entrainment of cooler water from below the mixed layer there. Computer resources already allow for global models to use eddy-resolving ocean resolutions (Roberts *et al.*, 2016). Therefore, the interactions between the mesoscale eddies and the MJO should be investigated further in future studies.

In conclusion, the mixed layer heat budget of the coupled model of the UK Met Office reveals important contributions from the subsurface ocean processes to the intraseasonal MLT anomalies in the Indo-Pacific warm pool region. Ocean advection drives the small scale changes in the intraseasonal MLT anomalies, while the net heat flux provides large scale warming and cooling patterns. Overall, ocean advection should be well-simulated to accurately forecast the

MJO.

The goal of this chapter was to answer the third, and final research question:

How do subsurface oceanic processes within the ocean mixed layer modulate MJO-associated changes in the mixed layer temperature in the tropics?

The results of this chapter demonstrate that ocean advection is important in modulating the intraseasonal MLT anomalies during the MJO in the coupled model of the UK Met Office. The ocean advection dominates at horizontal scales of order 1° , whereas the net surface heat flux dominates the intraseasonal mixed layer heat budget at larger horizontal scales, order 10° . The mean state ocean currents are responsible for the advective cooling and warming in the western Indian Ocean region during the MJO. Over the Maritime Continent, the MJO-associated ocean current anomalies reduce or strengthen the mean state ocean currents, leading to cooling or warming of the MLT during the MJO. Ocean advection is not as prominent in the central Indian Ocean region, where the net surface heat flux dominates.

Chapter 5

Conclusions

The research carried out in this thesis was motivated by the importance of the air–sea interactions during the Madden–Julian Oscillation (MJO). Specifically, this thesis was focused on assessing how the air–sea interactions affect the predictive skill of the MJO in the coupled ocean–atmosphere Numerical Weather Prediction (NWP) system of the UK Met Office in comparison to the atmosphere-only version of this model. Within this theme, three research questions were posed in Section 1.5, and the following section provides a synthesis of the answers to these research questions based on the work carried out in this thesis. Future work and concluding remarks are discussed at the end.

5.1 Review of research questions

5.1.1 Research question 1

Will coupling the Met Office forecast model to an ocean model improve the MJO predictions in the tropics?

The UK Met Office developed a global coupled ocean–atmosphere model, in the hope of improving their model skill compared to the atmosphere-only model, the operational model at the time at the Met Office. The coupled model became the operational model for global forecasting at the Met Office in 2022, and thus the question was posed whether the new model improves the MJO predictions compared with the atmosphere-only model. Chapter 2 of this thesis demonstrates that increasing the model complexity does not necessarily lead to

an improvement in the MJO predictions, in fact, the model performance can be degraded because of this added complexity.

Both high resolution global NWP models of the UK Met Office provide skilful MJO predictions out to lead day 7 in the tropics (Figure 2.1). The spatial extent of the MJO and the MJO amplitude are almost identical between the models within 7 lead days of the forecast. The main difference between the models was found in the eastward propagation of the MJO. The coupled model erroneously predicts the MJO faster than the observations (Figure 2.1d). The atmosphere-only model predicts approximately correct MJO phase speed out to lead day 7, and thus performs better than the coupled model.

The nature of the sea surface temperatures (SSTs) in these two models led to the answer to why adding an ocean in this forecast model leads to a degraded performance in predicting the MJO. The atmosphere-only model uses persisted SSTs that do not include the effects of the diurnal cycle of SST. Such effects are known to be strong in the tropics (Matthews *et al.*, 2014; Bellenger & Duvel, 2009). The coupled model SSTs change throughout the simulation, and the daily mean SST in the coupled model can be influenced by the diurnal cycle of SST.

In Chapter 2, a two-way feedback between the MJO and diurnal warm layers in the ocean is proposed: the MJO sets the strength of the diurnal cycle of SST, the diurnal cycle of SST modulates the intraseasonal SST anomalies, and these anomalies modulate surface fluxes that affect the eastward propagation of the MJO. A stronger (weaker) than average diurnal cycle of SST leads to more positive (negative) intraseasonal SST anomalies in this coupled model. These anomalies modulate the latent heat flux release into the atmosphere in the coupled model, and promote (inhibit) convection ahead of (behind) the enhanced convection of the MJO, leading to a faster eastward propagation of the MJO in the coupled model compared with the atmosphere-only model (Figure 2.12). Observations show that the diurnal variability of SST rectifies the intraseasonal SST variability (Yan *et al.*, 2021; Itterly *et al.*, 2021). Thus, the proposed feedback is a realistic mechanism. However, more realism leads to a degraded model performance in predicting the MJO. The next research question of this thesis presents, therefore, a detailed analysis of this feedback.

5.1.2 Research question 2

How does the upper 10 m of the ocean modulate the MJO in the coupled model?

A set of numerical experiments was carried out in Chapter 3 to test the hypothesised feedback between the MJO and diurnal warm layers in the upper 10 m of the ocean model. Two control model runs were carried out out to 15 lead days (the coupled and the atmosphere-only control model runs), and two coupled experiments were conducted with instantaneous vertical mixing over the top 5 m and 10 m of the ocean component of the coupled model to test the feedback. The instantaneous mixing experiments led to a substantial reduction in the diurnal cycle of SST by creating a vertically homogeneous layer of equal temperature and salinity in the top 5 m and 10 m of the ocean component of the coupled model.

The mean diurnal warming of SST (dSST; difference between 1500 and 0600 local solar time SST) was reduced substantially in the mixing experiments compared with the control coupled run (Figure 3.4). The reduction in the dSST in the coupled model led to a systematic reduction in the MJO phase speed during the first 7 lead days of the forecast (Figure 3.2d). The reduction in the dSST did not lead to changes in the spatial extent of the MJO or the MJO amplitude (Figure 3.2a–c). About half of the MJO phase speed increase between the coupled and the atmosphere-only model was found to be due to the presence of diurnal warm layers in the coupled model (Figure 3.3b).

As hypothesised in Chapter 2, the dSST impacts the intraseasonal SST anomalies (Figure 3.6g–h). Stronger dSST leads to more extreme intraseasonal SST anomalies, such that stronger (weaker) than average dSST leads to more positive (negative) intraseasonal SST anomalies in this coupled model. On a 15 lead day timescale, the feedback between the MJO and diurnal warm layers emerges in the coupled model as follows: the MJO conditions rectify the strength of the dSST, the dSST rectifies daily mean intraseasonal SST anomalies, the MJO convection responds to these SST anomalies, with a peak response within 7 days, and the intraseasonal SST anomalies subsequently respond to this MJO convection change within the next 3 days.

It is promising that the coupled model simulates the rectification of the diurnal variability of SST onto the intraseasonal variability of SST. However, more realism leads to a slightly degraded model performance in predicting the MJO. We speculate that the answer lies in the convection parameterisation scheme used by these two models. The convection scheme was developed for the atmosphere-only model such that it simulates a realistic diurnal cycle of convection with SSTs that do not display diurnal changes. Now that the SSTs show significant diurnal variations in the coupled model, the scheme is likely to

overestimate the convection response to diurnally changing SSTs.

Finally, the reduction in the $dSST$ in the coupled model leads to substantial differences in the mean state of the model by lead day 15 (Figure 3.10, 3.11). Most notably, a reduction of 4 W m^{-2} is observed in the latent heat flux into the atmosphere, but also a reduction in the top-of-atmosphere convection, weaker surface circulation and a reduction in the mean state precipitation of up to 2 mm d^{-1} in some regions over the Indo-Pacific warm pool region. These results indicate that models that do not resolve diurnal warm layers may underestimate tropical precipitation, and the lack of diurnal warm layers may be one of the reasons why some climate models display a dry bias in this region (e.g., Ahn *et al.*, 2020a).

5.1.3 Research question 3

How do subsurface oceanic processes within the ocean mixed layer modulate the MJO-associated changes in the mixed layer temperature in the tropics?

The work carried out in Chapters 2 and 3 demonstrated that the atmosphere-only model of the UK Met Office can predict the MJO skilfully out to 15 lead days. The addition of the air–sea interactions in the coupled model modulates the eastward propagation of the MJO. The first two research questions of this thesis examined the upper 10 m of the ocean model and diurnal warm layer formation. When diurnal warm layer effects are removed from the coupled model, the MJO is still faster than the observations and the atmosphere-only model. Therefore, the final research question was posed to investigate the subsurface oceanic processes that contribute to the mixed layer temperature (MLT) changes during the MJO in this coupled model, and address to what extent ocean advection modulates the MLT anomalies during the MJO.

Chapter 4 presents a mixed layer heat budget to examine the intraseasonal changes in MLT in the tropics in this coupled model. The mixed layer heat budget reveals that ocean advection is equally important as the net heat flux forcing in modulating MLT changes on MJO timescales. Prior to the MJO convection initiation over the western Indian Ocean region, the mean state ocean currents advect warm intraseasonal MLT anomaly towards the coast of Africa and reinforce the net heat flux warming in this region. Over the MC, the MJO-related anomalous ocean currents, located north of New Guinea, act in the opposite direction to the mean state ocean currents, resulting in a cooling trend

and a reduction of the net heat flux warming ahead of the MJO convection there.

When the MJO convection develops over the central Indian Ocean region, the net heat flux forcing does not produce substantial changes in the intraseasonal MLT anomalies in the western Indian Ocean region. Ocean advection and vertical mixing are two major contributors to the cooling of intraseasonal MLT in this region post the MJO passage. The net heat flux dominates the mixed layer heat budget over the central Indian Ocean during the active MJO convection. Over the MC, the net heat flux contributes the most to the intraseasonal MLT changes, however, MJO-related anomalous ocean currents strengthen the mean state ocean currents north of New Guinea, resulting in a positive advective contribution to the intraseasonal MLT anomaly in that region.

A scale analysis at the end of Chapter 4 reveals different horizontal scales at which ocean advection and net heat fluxes operate during the MJO to modulate intraseasonal MLT. Ocean advection dominates at smaller horizontal scales, typically less than 10° , while net heat fluxes provide broader changes in intraseasonal MLT, order 10° . The results of this chapter indicate that ocean advection is important during the MJO, and there is a benefit in using an atmosphere model coupled to a fully dynamic 3D ocean model in predicting the MJO.

5.2 Future work

The work carried out in this thesis provides a few potential ideas for future work.

5.2.1 Convection

All models used in this thesis were of a horizontal resolution in the atmosphere component that does not allow explicit resolution of atmospheric convection at the grid spacing. As such, the coupled model at 15 km and 60 km horizontal resolution simulates the MJO similarly well, with no notable differences between these two configurations. The atmosphere-only model used in this study is available at a convection-permitting horizontal resolution (N2560) at the Met Office, and select few case studies have been published of this model in literature (Tomassini *et al.*, 2023). The N2560 horizontal resolution of the model uses a 5 km grid length in latitude across the globe, and 7.8 km grid length in longitude at the equator, 5 km in the midlatitudes and 4 km near the poles. The horizontal spacing

at the equator in this configuration is within the grey zone for the atmospheric convection. To address this issue, the Met Office developed CoMorph, a new convection scheme that is adaptable at different horizontal scales (Lavender *et al.*, 2024).

The case studies of Tomassini *et al.* (2023) demonstrated that the atmosphere-only model performs better with a scale-aware convection scheme than when the convection scheme is switched off, or when the convection is fully parameterised in the model. One of the case studies in Tomassini *et al.* (2023) was carried out during an MJO event in January 2018. The convection-permitting simulations show an improvement in the Maritime Continent barrier effect compared with the operational atmosphere-only model at the time at the Met Office. Additionally, the scale-aware convection scheme performed better in predicting the Kelvin-like disturbances, and Rossby and Mixed Rossby-Gravity waves during this MJO event.

Chapters 2 and 3 of this thesis indicate that the diurnal cycle of convection may be the reason why the MJO is too fast in the coupled model. There is some evidence that the diurnal cycle of convection is represented better in the tropics in the atmosphere component of the coupled model at a convection-permitting horizontal resolution in a regional version of this model (Adams *et al.*, 2019). The current convection scheme used by the coupled model was developed for a much coarser grid, and may not be applicable at convection-permitting horizontal resolutions. Future work should examine the MJO skill of the coupled model using the CoMorph convection scheme at a convection-permitting horizontal resolution. In particular, the fidelity of the diurnal cycle of convection should be investigated in the model in the context of diurnally changing SSTs.

To address that, we propose several model experiments that will compliment model runs that are already planned at the Met Office. The Met Office plans to run one year of coupled forecasts at a convection-permitting resolution using the CoMorph convection scheme, initialised every 3 days from September 2020. The atmosphere component of this coupled run will be at N2560 horizontal resolution, coupled to the ORCA12 configuration of the ocean model at $1/12^\circ$ grid spacing (an eddy-resolving ocean model). A control coupled model run will be carried out at N1280 horizontal resolution of the atmosphere component and ORCA025 version of the ocean component ($1/4^\circ$ grid spacing). This control coupled model run is equivalent to the high resolution coupled model run used in Chapter 2, albeit with a newer version of the coupled model, GC5, instead of GC2 and GC3. We propose to carry out two model runs with

the N2560–ORCA12 configuration of the coupled model, muting the diurnal cycle of SST (as presented in Chapter 3). The MJO phase speed, the diurnal cycle of SST and the diurnal cycle of convection should be investigated across all of these model runs, and compared with the high resolution model runs presented in Chapter 2. Convection-permitting models might alter the biases in the atmospheric model such that coupling to the ocean and the simulation of diurnal warming has a different effect on model skill. Furthermore, high resolution atmospheric models might respond more sensitively to the small-scale SST anomalies produced by ocean advection (identified in Chapter 4), and hence, affect the MJO simulations in these models.

Global convection-permitting simulations are computationally expensive, however, recent efforts have been made to run global atmosphere-only models at 5 km horizontal resolution out to 40 days (DYAMOND project, Feng *et al.*, 2023). All models within the DYAMOND project were run during boreal summer, and no active MJO event was present during that time. The Met Office is in the process of developing a new atmosphere component of the model, LFRic, named after the pioneering weather forecaster Lewis Fry Richardson (Adams *et al.*, 2019). This model was developed to allow for better scalability of the model with higher horizontal resolutions and faster running time using Graphical Processing Units, instead of the slower Central Processing Units used by the Unified Model, the current atmosphere component of the coupled model. The Met Office plans to submit the N2560–ORCA12 configuration of GC5 version of the coupled model to the DYAMOND project phase 3. This phase is likely to cover a boreal winter as well as a boreal summer, and hopefully during an active MJO event. With the development of LFRic, global coupled model experiments suggested in this section are more likely to be feasible in the future at the Met Office, and hopefully come to fruition.

5.2.2 Mean state

The experiments carried out in Chapter 3 showed that there are important differences in the mean state of the coupled model when the diurnal warming effects are reduced. The Met Office uses a seamless approach to weather predictions and climate projections, using the same core of the model in NWP and climate settings. The climate version of the coupled model investigated in this thesis also displays a faster MJO than observations suggest (Ahn *et al.*, 2020a). We speculate that the mean state of the climate model would also change if the

diurnal warming effects were removed. A future study should investigate how the changes in the mean state identified in Chapter 3 affect the MJO projections in this coupled climate model. For example, there is some evidence that the mean state changes due to the presence of diurnal warm layers diminish by lead day 15 in this coupled NWP model (Figure 3.10). Coupled climate model experiment with muted diurnal warming effects would demonstrate whether diurnal warming modulates the mean state of the model on longer timescales than investigated here.

The mean state of the climate model can affect the MJO (e.g., Ahn *et al.*, 2019), and furthermore, a better mean state moisture gradient can result in a better eastward propagation of the MJO (Ahn *et al.*, 2020b). We propose four climate model experiments equivalent to the experiments carried out in Chapter 3 to address these speculations. The comparison of the mean state in these four experiments would allow to isolate the diurnal warming effects and other coupling effects on the model mean state, and the MJO propagation speed.

Diurnal warming leads to a faster MJO in this coupled model on a 15 lead day timescale, therefore, it has a potential to affect the onset of the MJO teleconnections in the extratropics. For example, negative North Atlantic Oscillation (NAO) pattern is likely to occur three weeks after MJO is in phases 2 and 3 (Lin *et al.*, 2021). The experiments proposed in this section would enable to investigate the coupling between the MJO and the NAO. Finally, diurnal warming can affect other coupled weather patterns beyond the context of the MJO, e.g. ENSO, Indian Ocean Dipole, monsoons, etc. It would be of scientific interest to investigate other parts of the Earth system affected by this phenomenon.

5.2.3 Ocean resolution

The ocean component of the coupled model investigated in this thesis uses an eddy-permitting horizontal resolution. The model is available at a higher horizontal resolution of $1/12^\circ$, an eddy-resolving horizontal resolution. Chapter 4 demonstrated that the MJO modulates the mesoscale eddy circulation in this coupled model, leading to changes in the intraseasonal heat transport in the Indonesian Throughflow area. The Met Office has run one year of forecasts using the $1/12^\circ$ horizontal resolution in the ocean component of the coupled model. Based on the results of this thesis, the $1/12^\circ$ ocean forecast data should be investigated in the future to evaluate the mesoscale eddy interaction with

the MJO and to determine if the results presented here are dependent on the horizontal resolution of the ocean model.

5.2.4 Fieldwork

The research carried out in this thesis shows that ocean feedbacks cannot be neglected during the MJO and there is a need for more in-situ observations of air–sea interactions during the MJO. There are sparse observations of upper ocean processes during the MJO over the MC, despite the fact that this region has a significant effect on the global climate system (e.g., Kim *et al.*, 2020). The *TerraMaris* field campaign was planned in years 2018–2025 to rigorously investigate the scale interactions between the land and the ocean over the MC using various data collection methods: a research aircraft, an atmospheric radar, radiosondes, land-based measurements on the islands, and autonomous underwater and surface vehicles in the seas. Unfortunately, the global pandemic in years 2020–2022 prevented this fieldwork campaign from coming to fruition. The data that would have been collected during this campaign would have been complementary to the work carried out in this thesis, to validate the diurnal warming over the MC in the coupled model and to investigate the diurnal cycle of convection over the MC. This author can only hope that one day a similar campaign will go ahead and we will be able to further our understanding of these ocean–atmosphere interactions over the MC.

5.3 Concluding remarks

The research carried out in this thesis has furthered our understanding of air–sea interactions during the Madden–Julian Oscillation (MJO) in the coupled ocean–atmosphere model of the UK Met Office. Several processes within the upper ocean were identified throughout this thesis to be of importance during the MJO.

Diurnal warm layer formation was long hypothesised to increase the eastward propagation of the MJO (Bernie *et al.*, 2007, 2008). The numerical experiments carried out in this thesis proved that diurnal warm layers affect the intraseasonal sea surface temperature anomalies in the tropics such that their presence leads to an increase in the MJO phase speed by a few percent in the coupled model of the UK Met Office. This leads to a degraded model

performance, likely caused by an overestimated response of the diurnal cycle of convection to diurnally changing sea surface temperatures. *One recommendation of this thesis is, therefore, to investigate this relationship further in this coupled ocean–atmosphere model.*

We also demonstrated the importance of ocean advection during MJO initiation and MJO growth. Ocean advection is found to dominate at smaller horizontal scales ($<10^\circ$) in modulating the intraseasonal mixed layer temperature anomalies. Ocean advection can work in tandem with net heat fluxes during the MJO. It can also oppose the net heat flux to modulate the intraseasonal mixed layer temperature anomalies over the Indo-Pacific warm pool region. Previous studies in the literature do not agree which process is the most important during the MJO (e.g., Drushka *et al.*, 2012; Chi *et al.*, 2014; Halkides *et al.*, 2015; Chandra *et al.*, 2024). This thesis demonstrates that *both* processes are important, and they modulate the intraseasonal mixed layer temperature anomalies at different horizontal scales.

The detailed analysis of the upper ocean processes during the MJO carried out in this thesis will be of significance to weather forecasting centres aiming to improve the representation of the MJO in their Numerical Weather Prediction systems. *Ultimately, this thesis demonstrates that coupled modelling should be used to fully represent the coupled ocean–atmosphere system that produces the MJO.*

Appendix A

RMM performance statistics for boreal winter and all seasons

RMM performance statistics from Chapter 2 were performed for boreal winter season and year-round data for the high resolution operational coupled and atmosphere-only NWP models of the UK Met Office. Qualitatively, no notable difference was found compared with the boreal winter and active MJO analysis performed in Chapter 2.

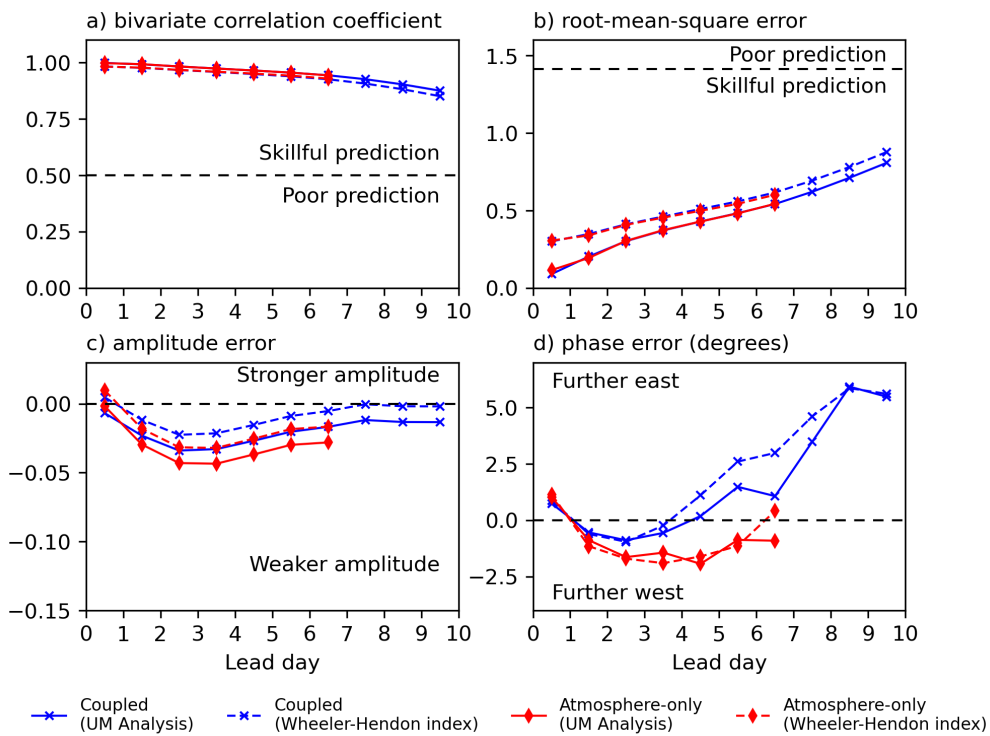


Figure A1: RMM skill metrics as a function of lead day. As in Figure 2.1 but for all boreal winter season days (November–April).

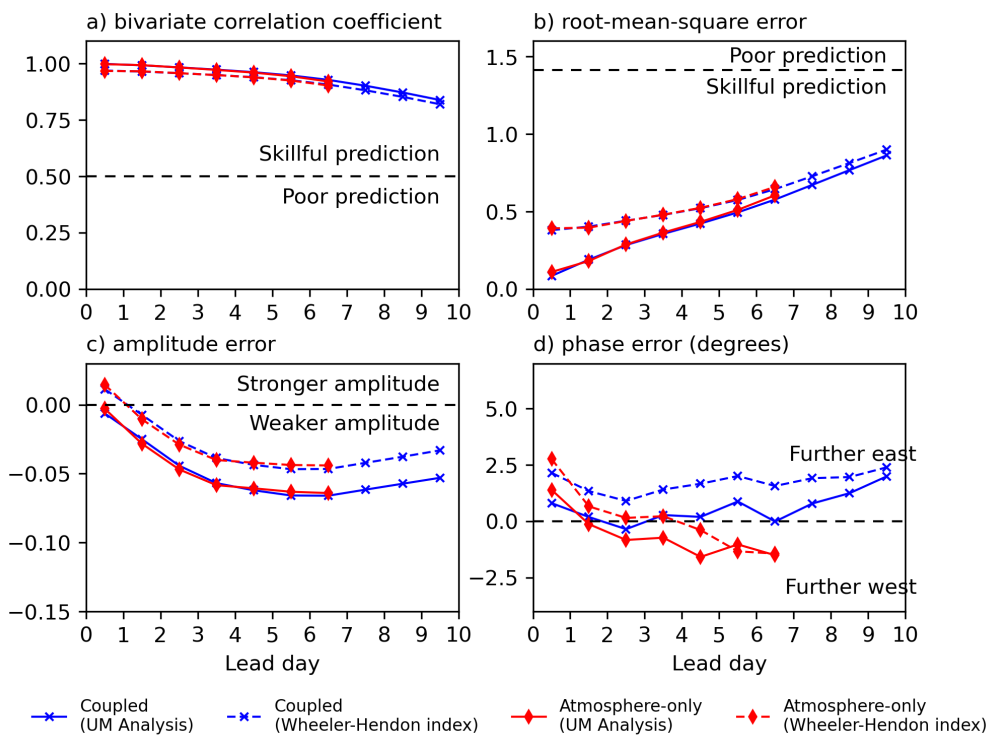


Figure A2: RMM skill metrics as a function of lead day. As in Figure 2.1 but for year-round data.

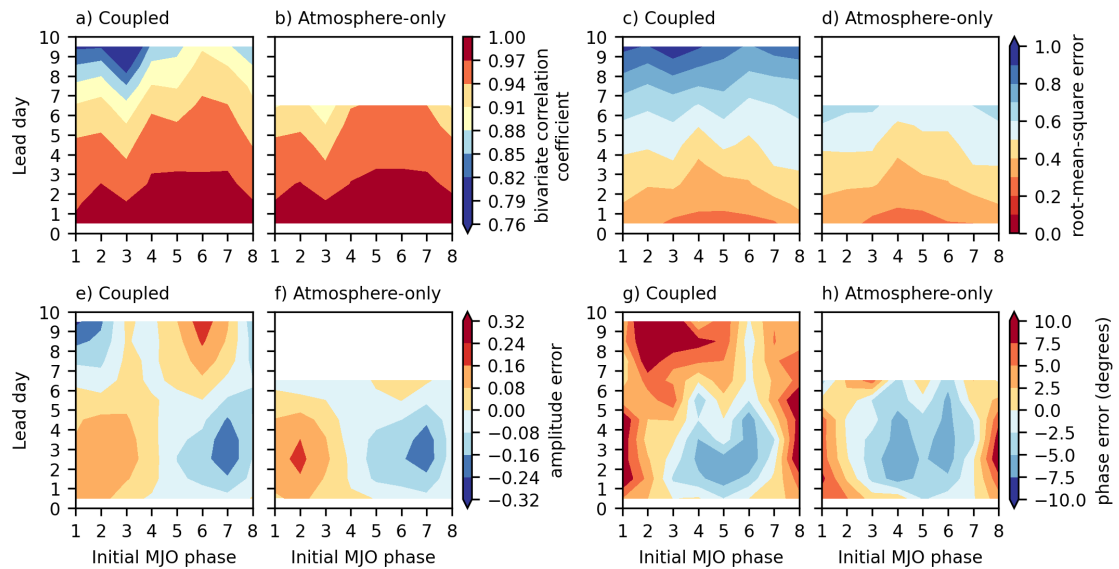


Figure A3: RMM skill metrics as a function of lead day and initial MJO phase. As in Figure 2.3 but for all boreal winter season days (November–April).

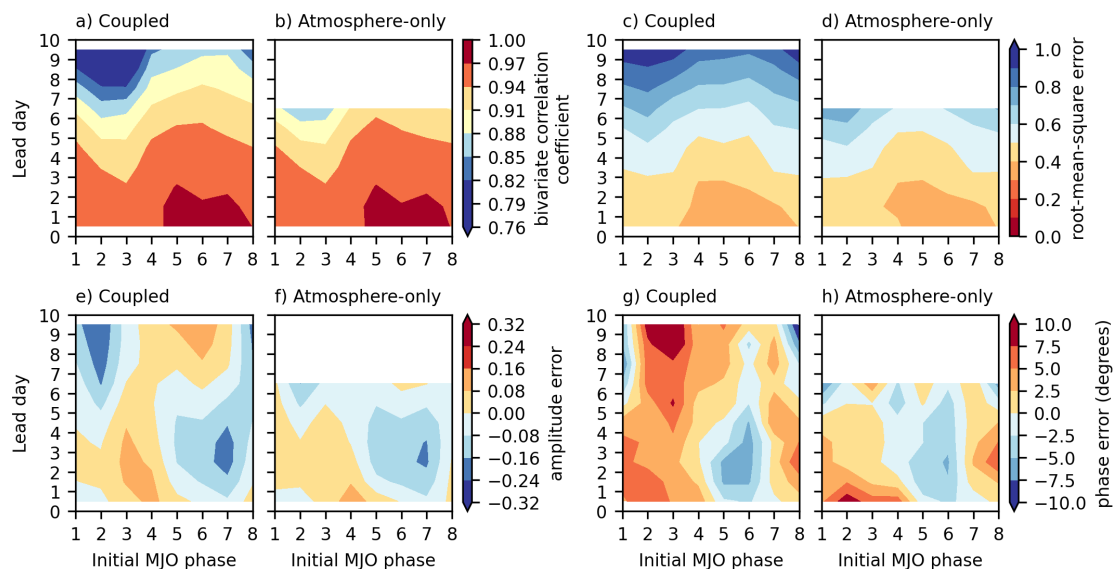


Figure A4: RMM skill metrics as a function of lead day and initial MJO phase. As in Figure 2.3 but for year-round data.

Appendix B

MJO convection across different MJO phases

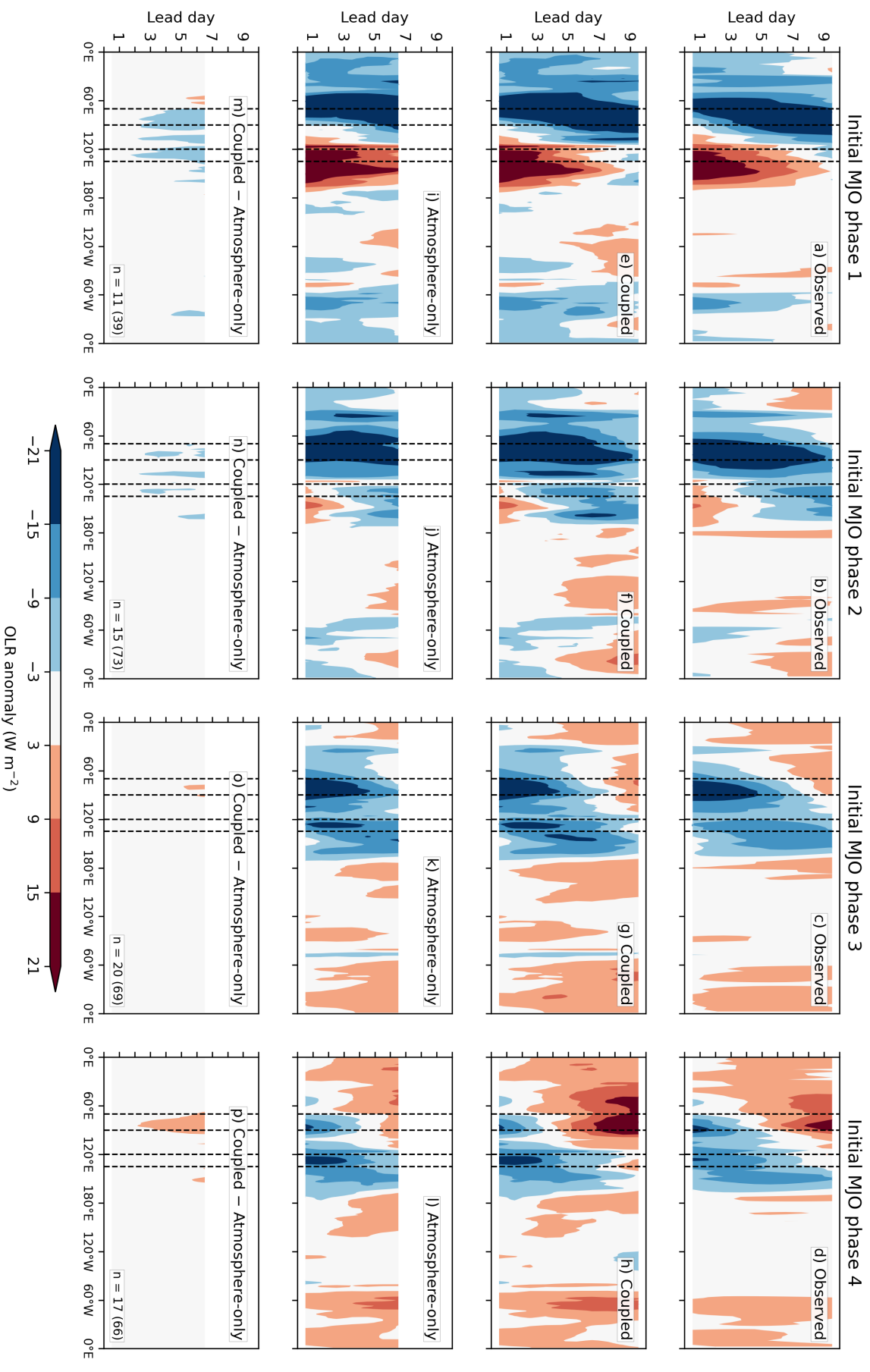


Figure B1: Hovmöller diagrams of daily mean composites of 20-200 day filtered boreal winter OLR anomaly averaged over the equatorial band (5°S–5°N), for forecasts initialised in MJO phases 1 to 4. a–d) observed; e–h) coupled model; i–l) atmosphere-only model; m–p) difference between coupled and atmosphere-only models. Vertical dashed lines represent equatorial Indian Ocean and central Maritime Continent regions. Initially active MJO forecasts only. Number n denotes the amount of independent events used in the composite (total number of days used displayed in the bracket).

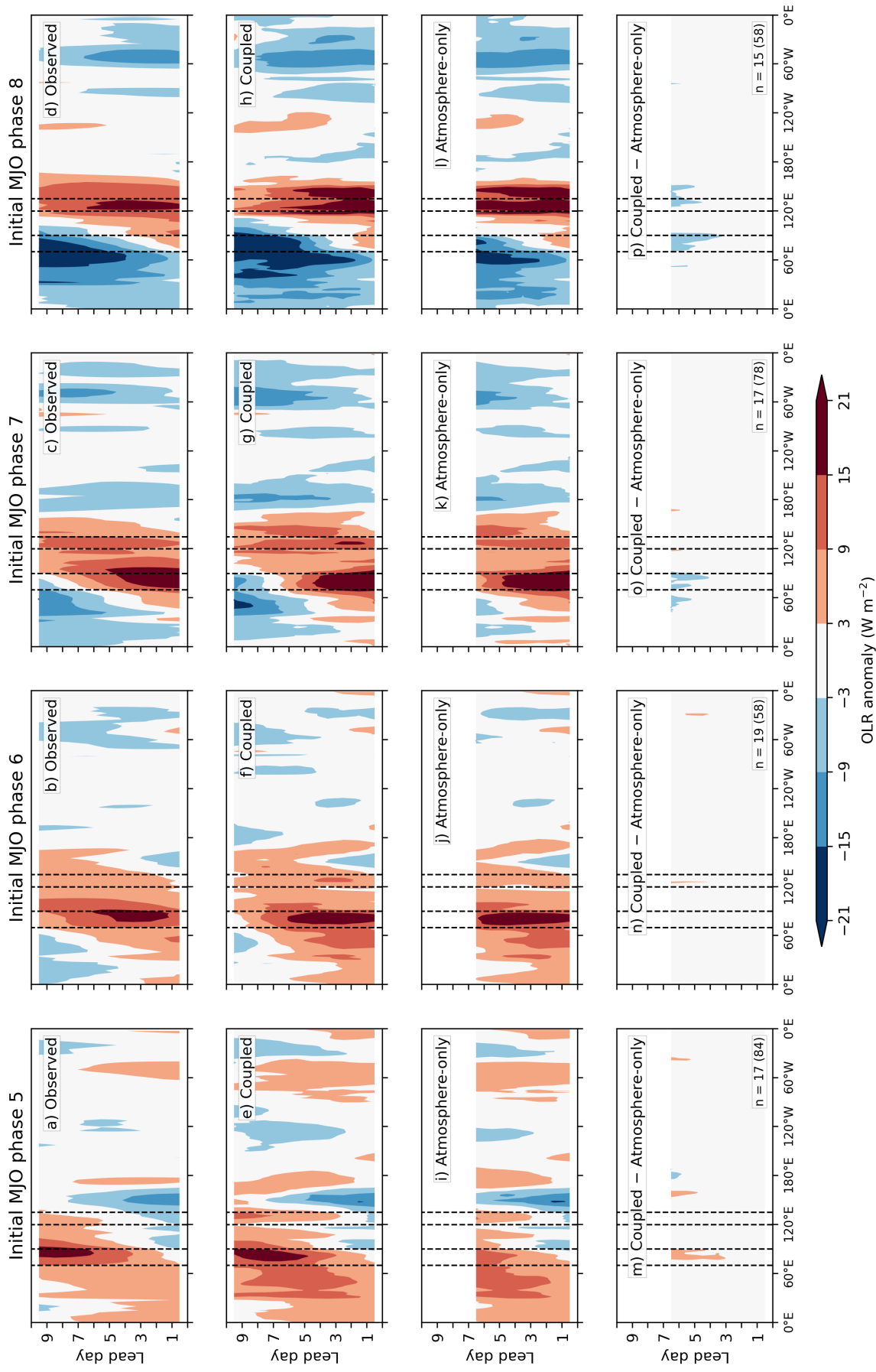


Figure B2: Hovmöller diagrams of daily mean composites of 20-200 day filtered boreal winter OLR anomaly averaged over the equatorial band (5°S-5°N), for forecasts initialised in MJO phases 5 to 8. a-d) observed; e-h) coupled model; i-l) atmosphere-only model; m-p) difference between coupled and atmosphere-only models. Vertical dashed lines represent equatorial Indian Ocean and central Maritime Continent regions. Initially active MJO forecasts only. Number n denotes the amount of independent events used in the composite (total number of days used displayed in the bracket).

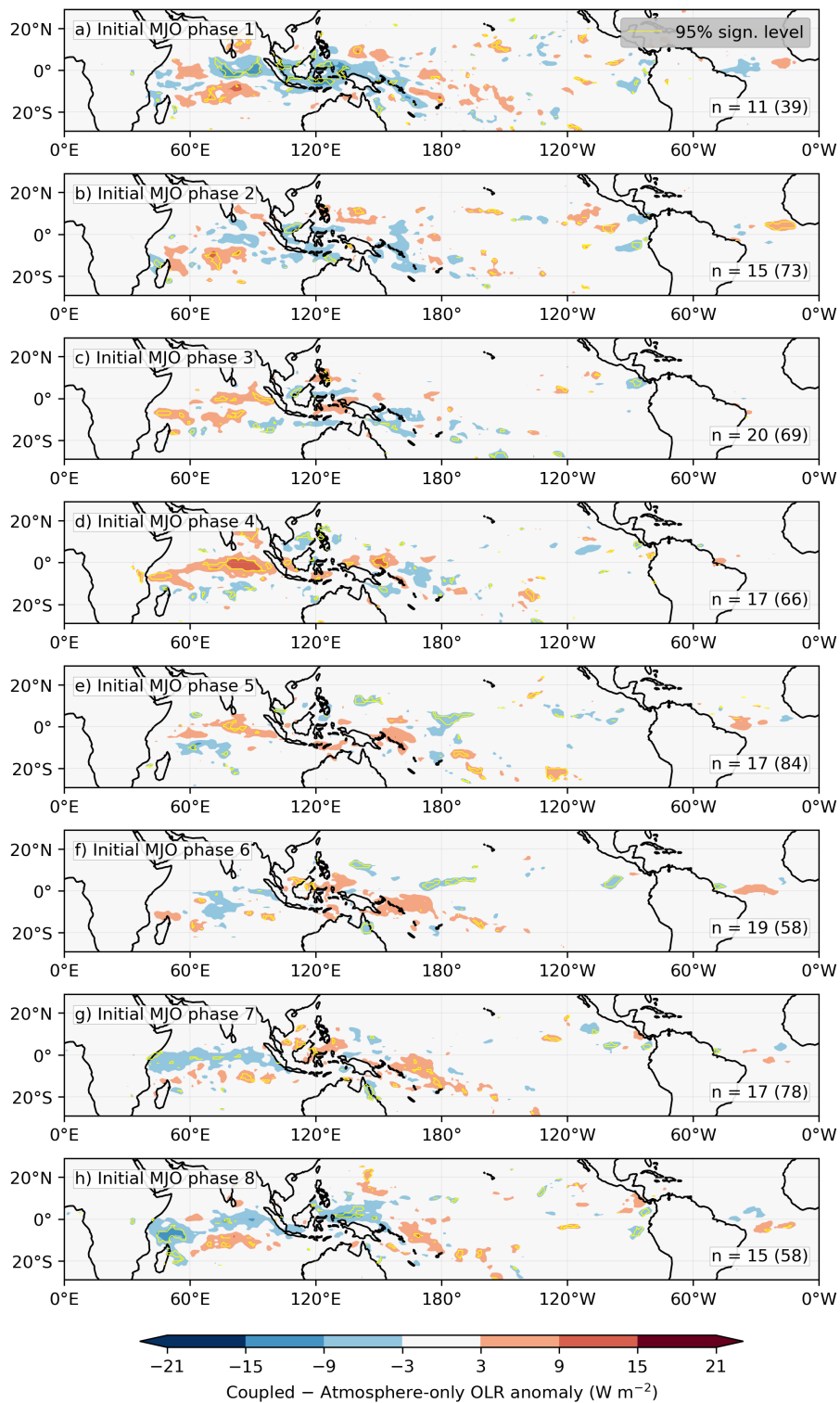


Figure B3: Difference at lead day 7 between composite daily means of coupled and atmosphere-only model 20-200 day filtered boreal winter anomaly of OLR for forecasts initialised in MJO phases 1 to 8. Initially active MJO forecasts only. Number n denotes the amount of independent events used in the composite (total number of days used is displayed in the bracket). RMM indices from Wheeler-Hendon. The yellow contour outlines differences significant at the 95% level.

Appendix C

SST and diurnal warming across different MJO phases

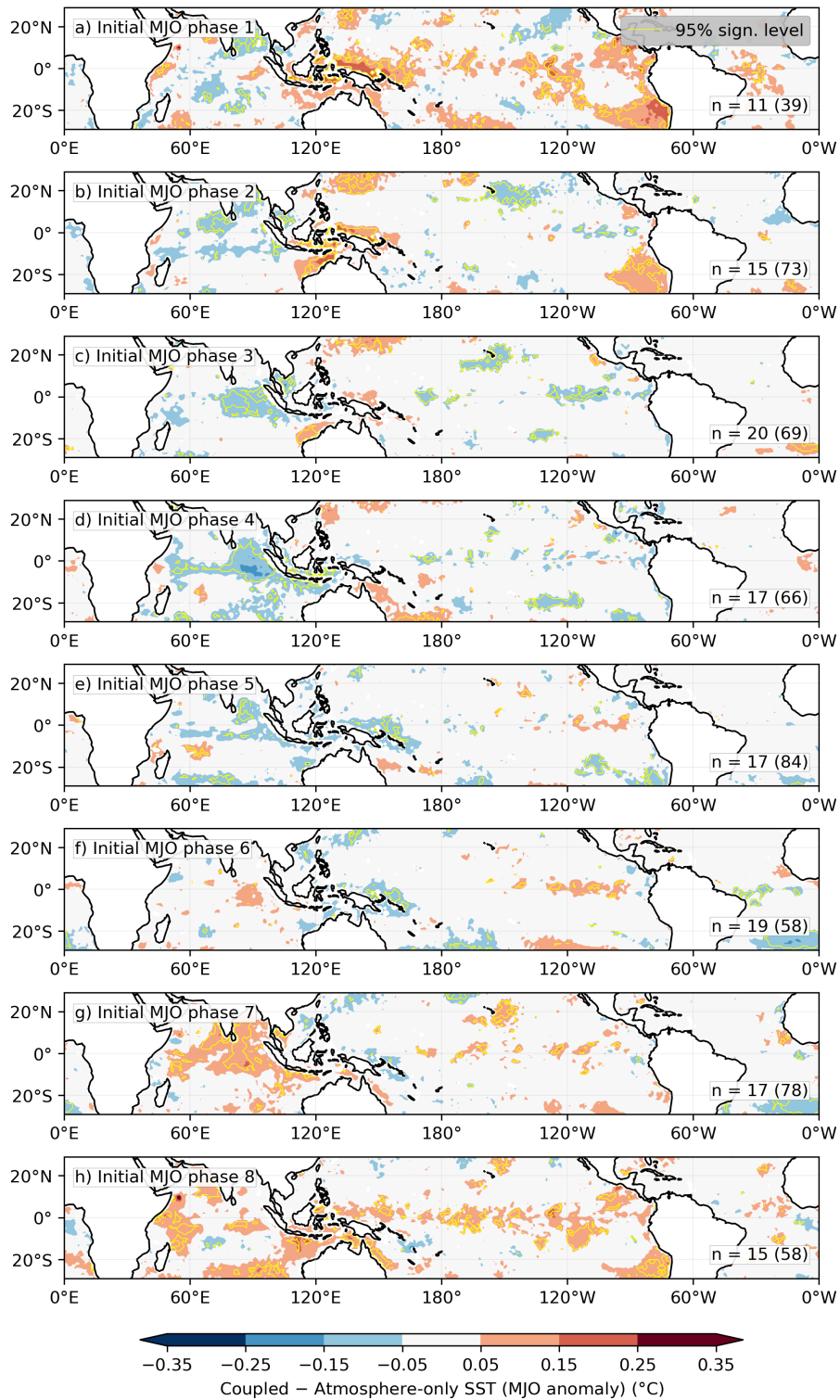


Figure C1: Composite daily mean at lead day 1 for coupled minus atmosphere-only model MJO-associated SST anomaly difference for forecasts initialised in MJO phases 1 to 8. Boreal winter and initially active MJO forecasts only. Number n denotes the amount of independent events used in the composite (total number of days used is displayed in the bracket). RMM indices from Wheeler–Hendon. The yellow contour outlines differences significant at the 95 % level.

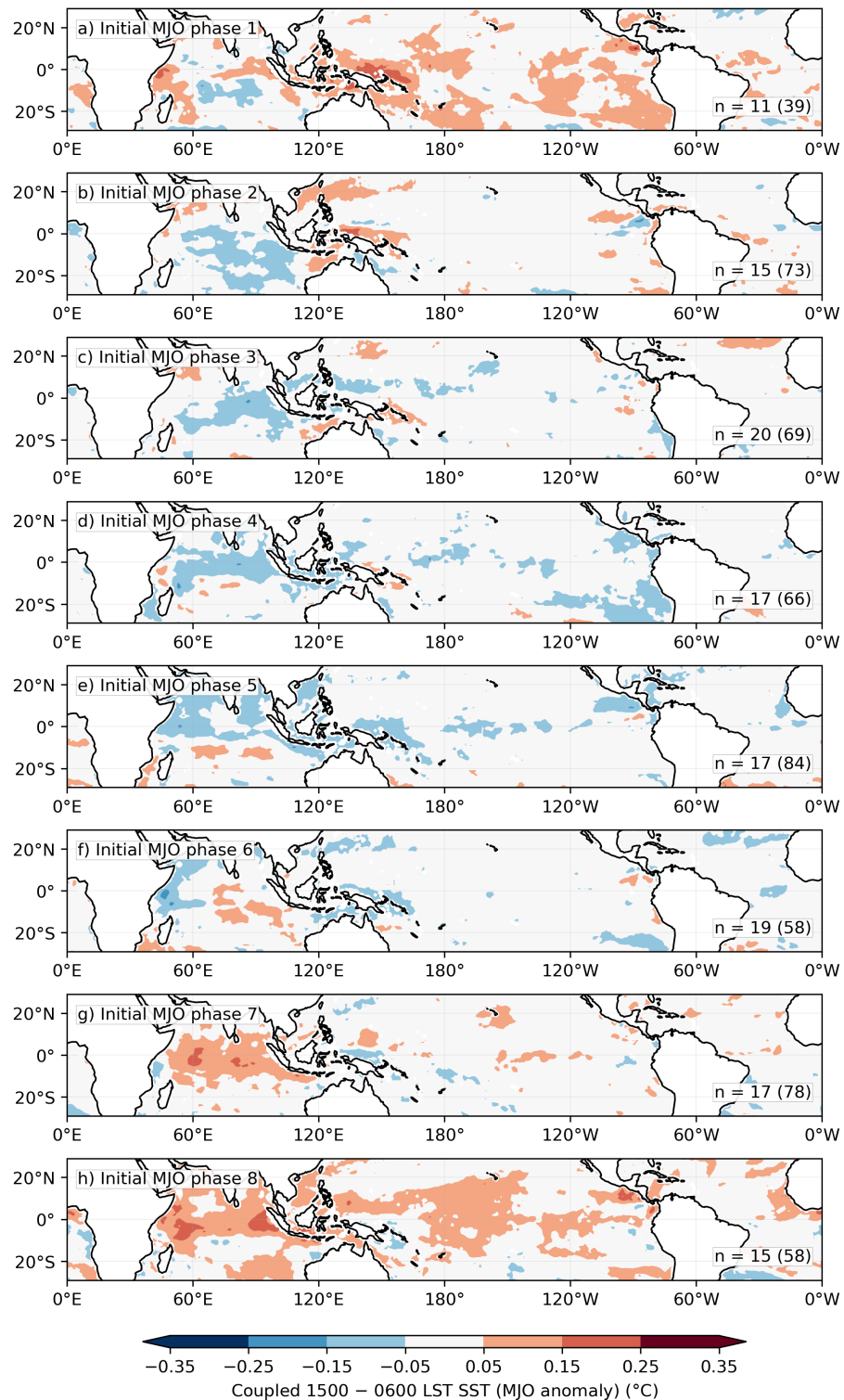


Figure C2: Composite daily mean at lead day 1 for coupled model diurnal warming of SST for forecasts initialised in MJO phases 1 to 8. Diurnal warming is defined as 1500 – 0600 local solar time (LST) SST. Boreal winter and initially active MJO forecasts only. Number n denotes the amount of independent events used in the composite (total number of days used is displayed in the bracket). RMM indices from Wheeler–Hendon.

Appendix D

Muted diurnal warming of SST

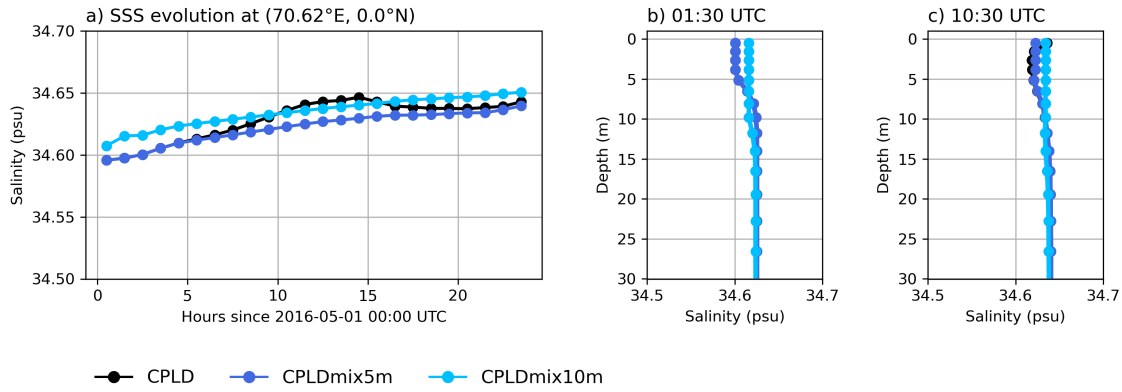


Figure D1: Sample evolution of surface diurnal warm layer for one grid point in the Indian Ocean (70.625°E , 0°N) during the first 24 hours of the forecast initialised on May 1, 2016: a) sea surface salinity (SSS), and the vertical profiles of ocean salinity at b) 0130 UTC (0610 LST) and c) 1030 UTC (1510 LST).

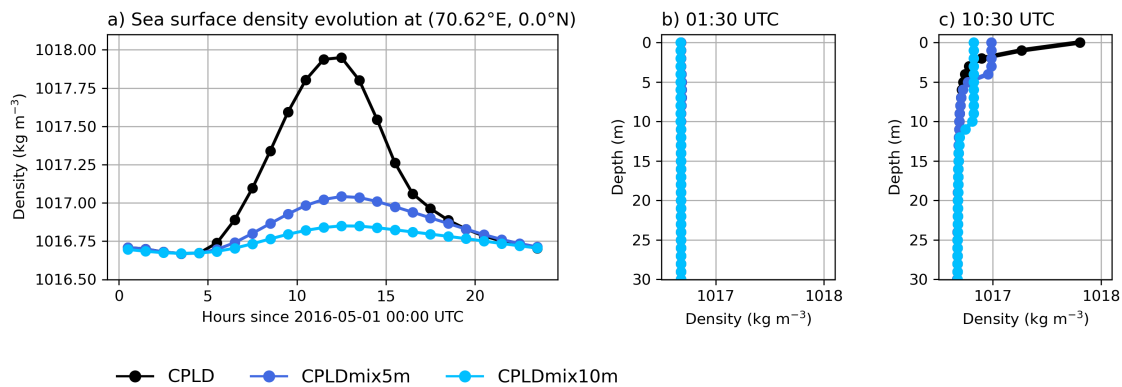


Figure D2: Sample evolution of surface diurnal warm layer for one grid point in the Indian Ocean (70.625°E , 0°N) during the first 24 hours of the forecast initialised on May 1, 2016: a) sea surface density, and the vertical profiles of ocean density at b) 0130 UTC (0610 LST) and c) 1030 UTC (1510 LST).

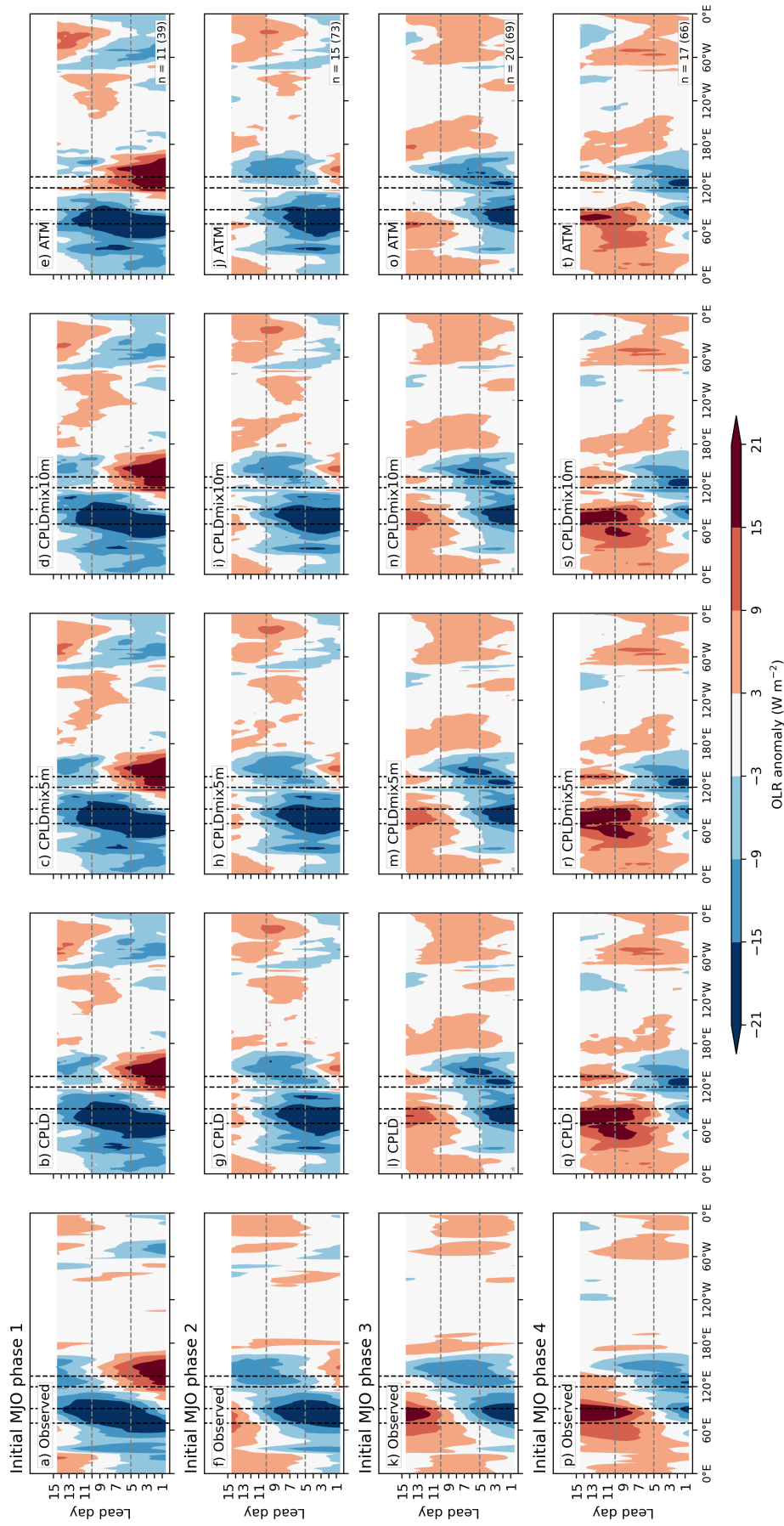


Figure D3: Hovmöller diagrams of daily mean composites of 20-200 day filtered boreal winter OLR anomaly averaged over the equatorial band (5°S - 5°N), for forecasts initialised in MJO phases 1 to 4. Panels a, f, k and p) observed; panels b, g, l and q) CPLD model; panels c, h, m and r) CPLDmix5m model; panels d, i, n and s) CPLDmix10m model; panels e, j, o and t) CPLDmix10m model. Vertical dashed lines represent equatorial Indian Ocean and central Maritime Continent regions. Initially active MJO forecasts only. Number n denotes the amount of independent events used in the composite (total number of days used displayed in the bracket). Horizontal dashed lines denote lead days 5 and 10.

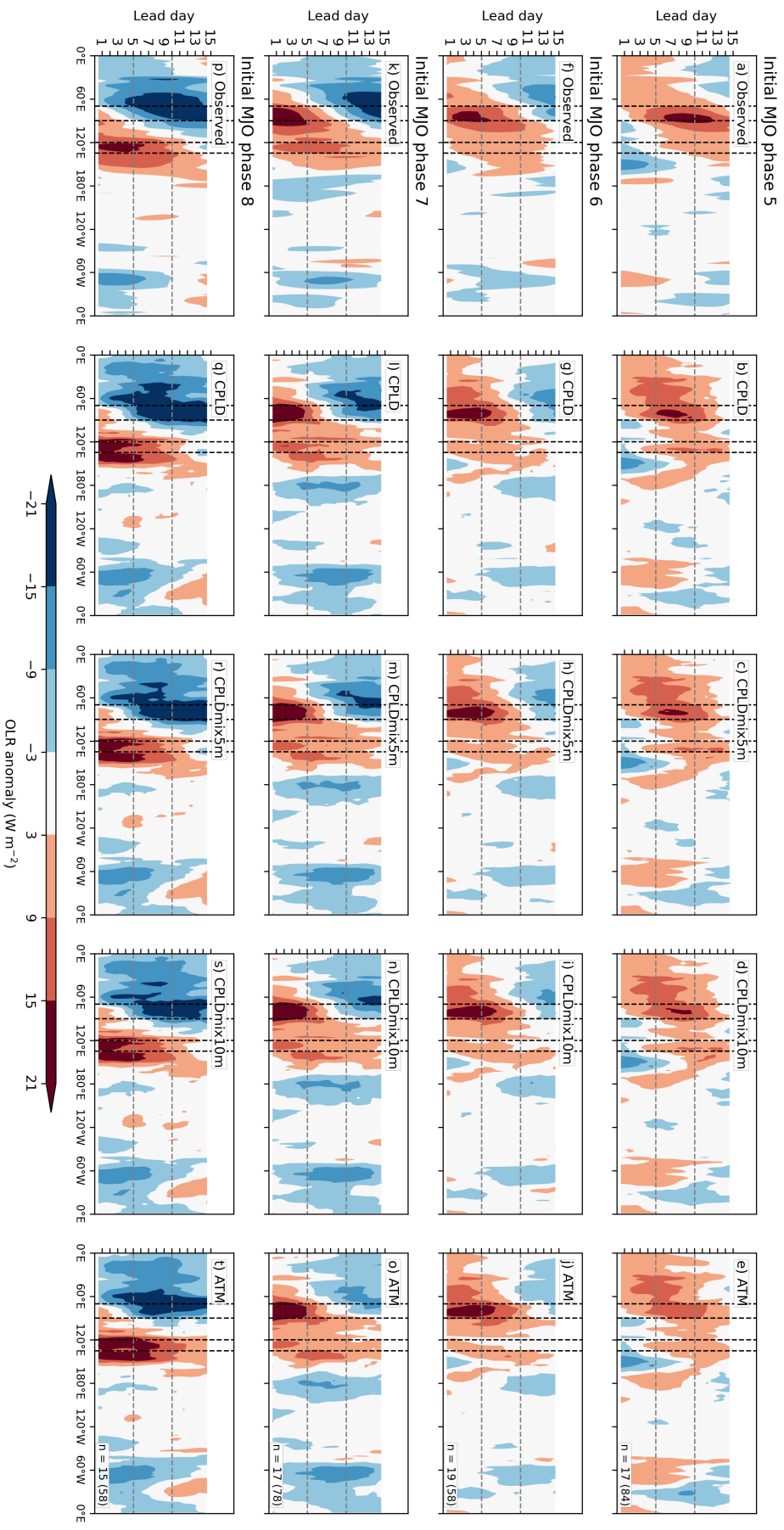


Figure D4: Hovmöller diagrams of daily mean composites of 20–200 day filtered boreal winter OLR anomaly averaged over the equatorial band (5°S – 5°N), for forecasts initialised in MJO phases 5 to 8. Panels a, f, k and p) observed; panels b, g, l and q) CPLD model; panels c, h, m and r) CPLDmix5m model; panels d, i, n and s) CPLDmix10m model. Panels e, j, o and t) CPLDmix10m model. Vertical dashed lines represent equatorial Indian Ocean and central Maritime Continent regions. Initially active MJO forecasts only. Number n denotes the amount of independent events used in the composite (total number of days used displayed in the bracket). Horizontal dashed lines denote lead days 5 and 10.

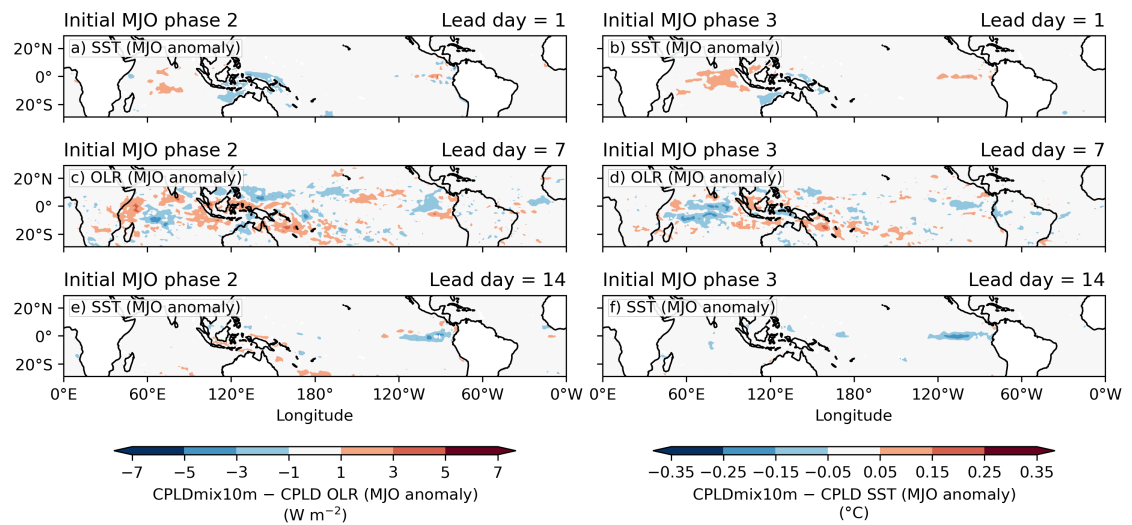


Figure D5: Composite daily mean MJO (20–200-day filtered) anomalies of CPLDmix10m minus CPLD difference for: a–b) SST at lead day 1 ; c–d) OLR at lead day 7; e–f) SST at lead day 14. Panels a, c and e are for initial MJO phase 2. Panels b, d and f are for initial MJO phase 3. Composites are calculated from boreal winter data.

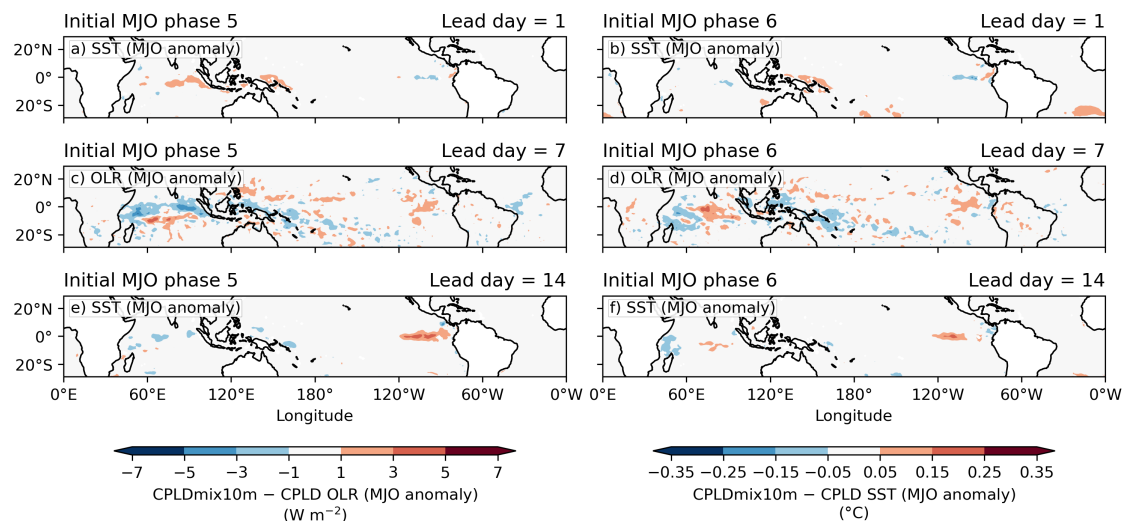


Figure D6: Composite daily mean MJO (20–200-day filtered) anomalies of CPLDmix10m minus CPLD difference for: a–b) SST at lead day 1 ; c–d) OLR at lead day 7; e–f) SST at lead day 14. Panels a, c and e are for initial MJO phase 5. Panels b, d and f are for initial MJO phase 6. Composites are calculated from boreal winter data.

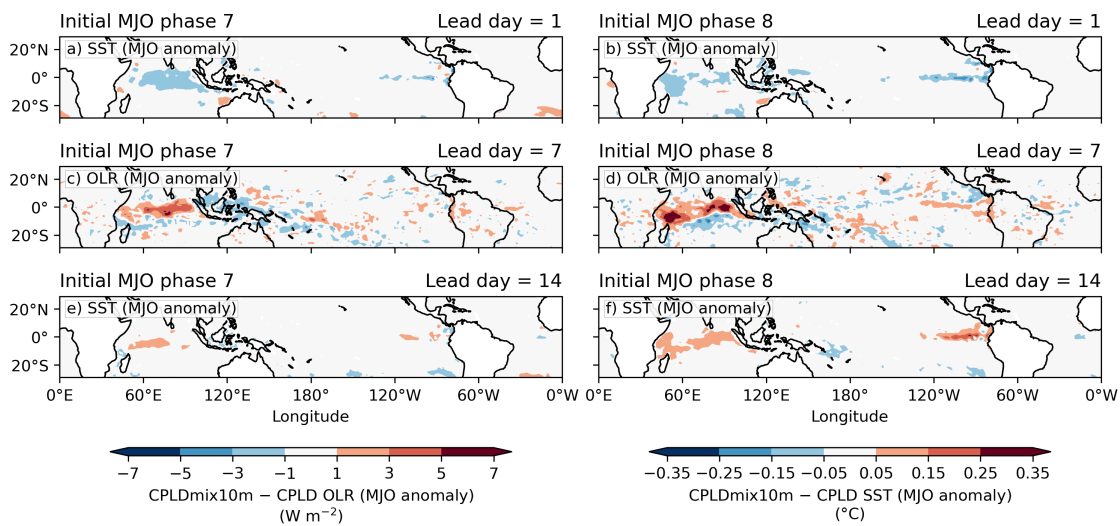


Figure D7: Composite daily mean MJO (20–200-day filtered) anomalies of CPLDmix10m minus CPLD difference for: a–b) SST at lead day 1; c–d) OLR at lead day 7; e–f) SST at lead day 14. Panels a, c and e are for initial MJO phase 7. Panels b, d and f are for initial MJO phase 8. Composites are calculated from boreal winter data.

Appendix E

Mixed layer heat budget across different MJO phases

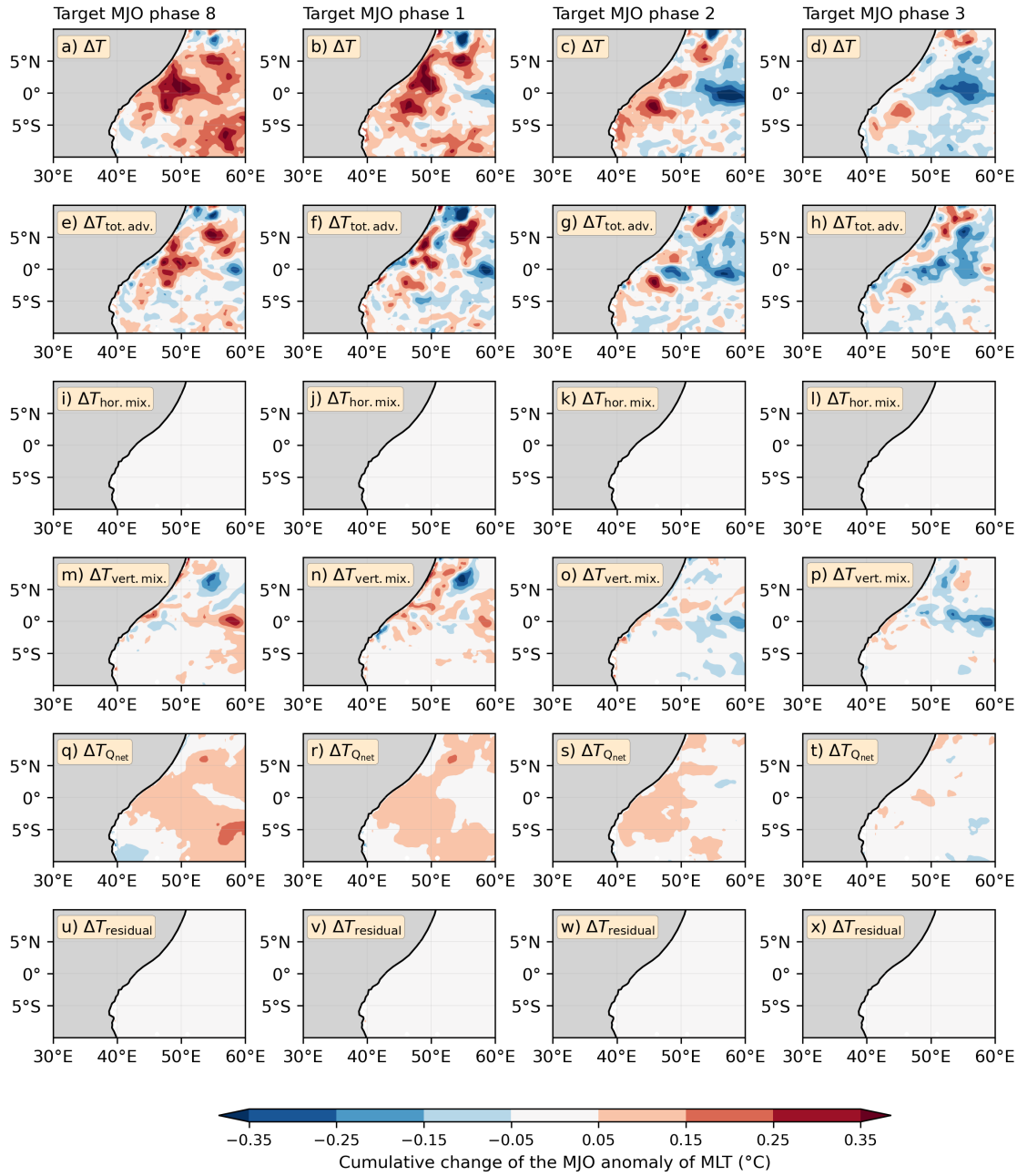


Figure E1: a–d) Cumulative change in the composite MJO anomaly of mixed layer temperature (MLT) over forecast days 1 to 10 prior to the arrival of (target) MJO phases 8, 1, 2 and 3 in the western Indian Ocean region; e–h) cumulative change of the MJO anomaly of MLT due to total advection for target MJO phases 8, 1, 2 and 3; i–l) cumulative change of the MJO anomaly of MLT due to horizontal mixing for target MJO phases 8, 1, 2 and 3; m–p) cumulative change of the MJO anomaly of MLT due to vertical mixing for target MJO phases 8, 1, 2 and 3; q–t) cumulative change of the MJO anomaly of MLT due to net heat flux for target MJO phases 8, 1, 2 and 3; u–x) residual (top row minus sum of the middle rows).

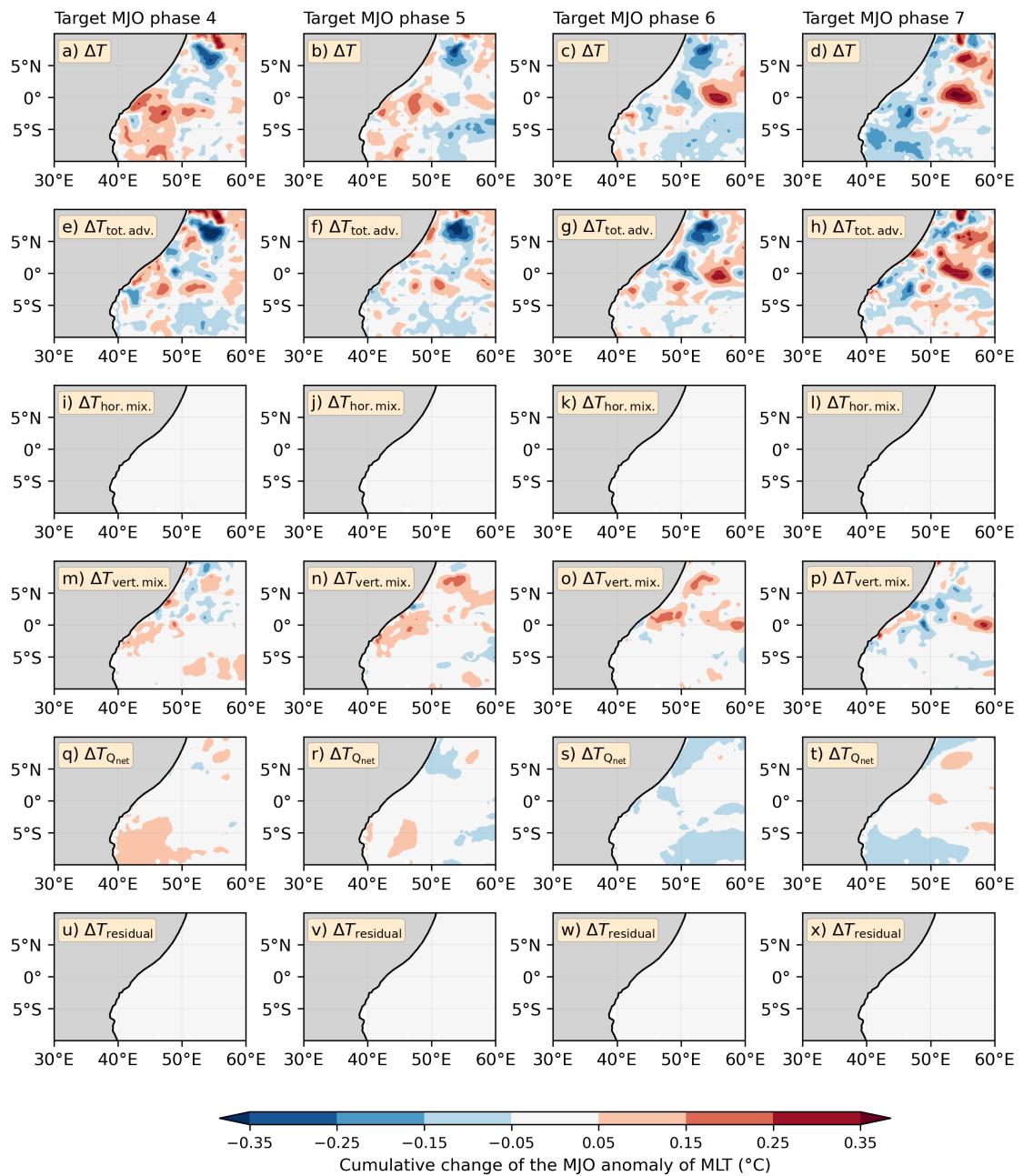


Figure E2: a–d) Cumulative change in the composite MJO anomaly of mixed layer temperature (MLT) over forecast days 1 to 10 prior to the arrival of (target) MJO phases 4, 5, 6 and 7 in the western Indian Ocean region; e–h) cumulative change of the MJO anomaly of MLT due to total advection for target MJO phases 4, 5, 6 and 7; i–l) cumulative change of the MJO anomaly of MLT due to horizontal mixing for target MJO phases 4, 5, 6 and 7; ; m–p) cumulative change of the MJO anomaly of MLT due to vertical mixing for target MJO phases 4, 5, 6 and 7; q–t) cumulative change of the MJO anomaly of MLT due to net heat flux for target MJO phases 4, 5, 6 and 7; u–x) residual (top row minus sum of the middle rows).

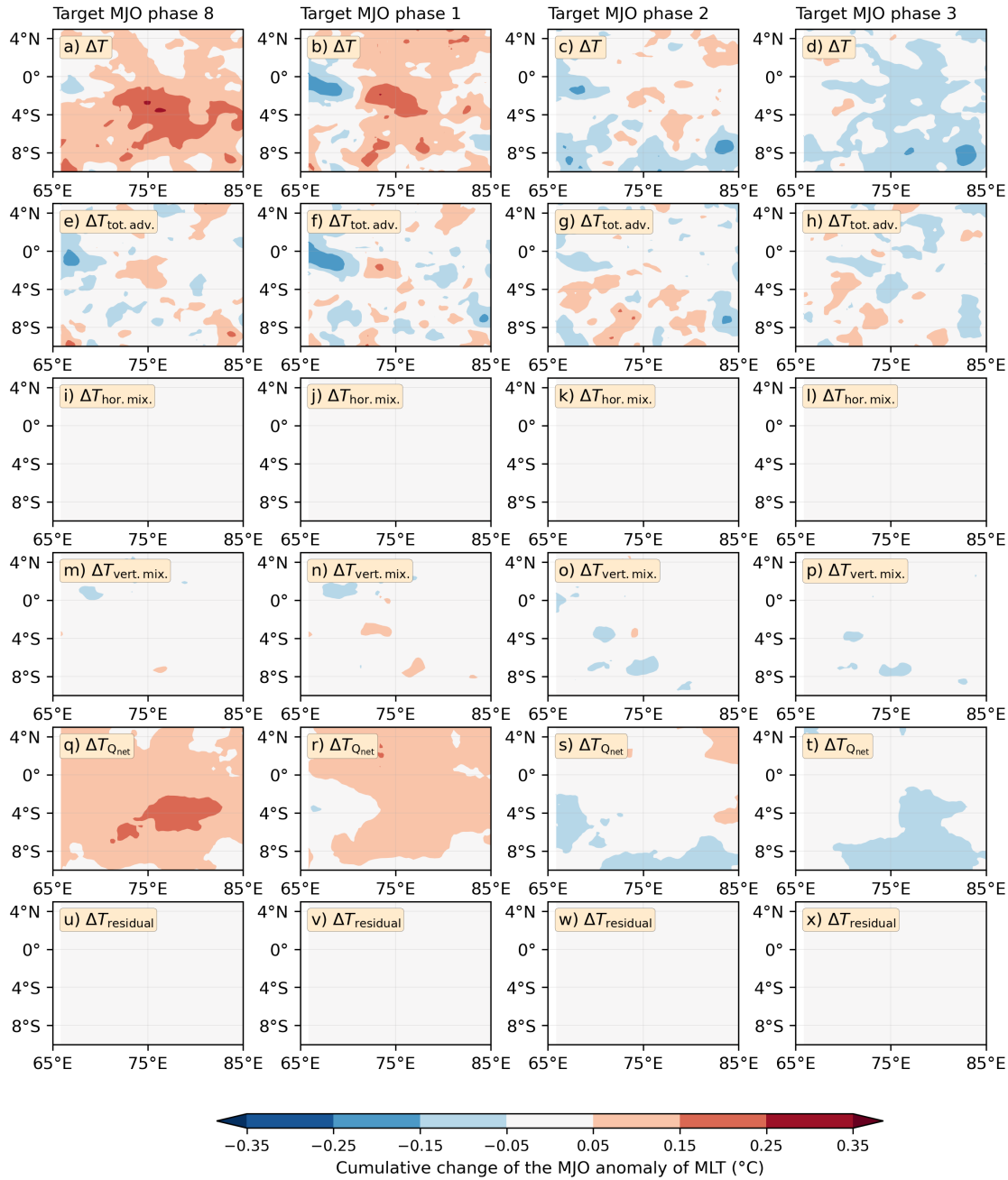


Figure E3: As in Figure E1 but for the central Indian Ocean region.

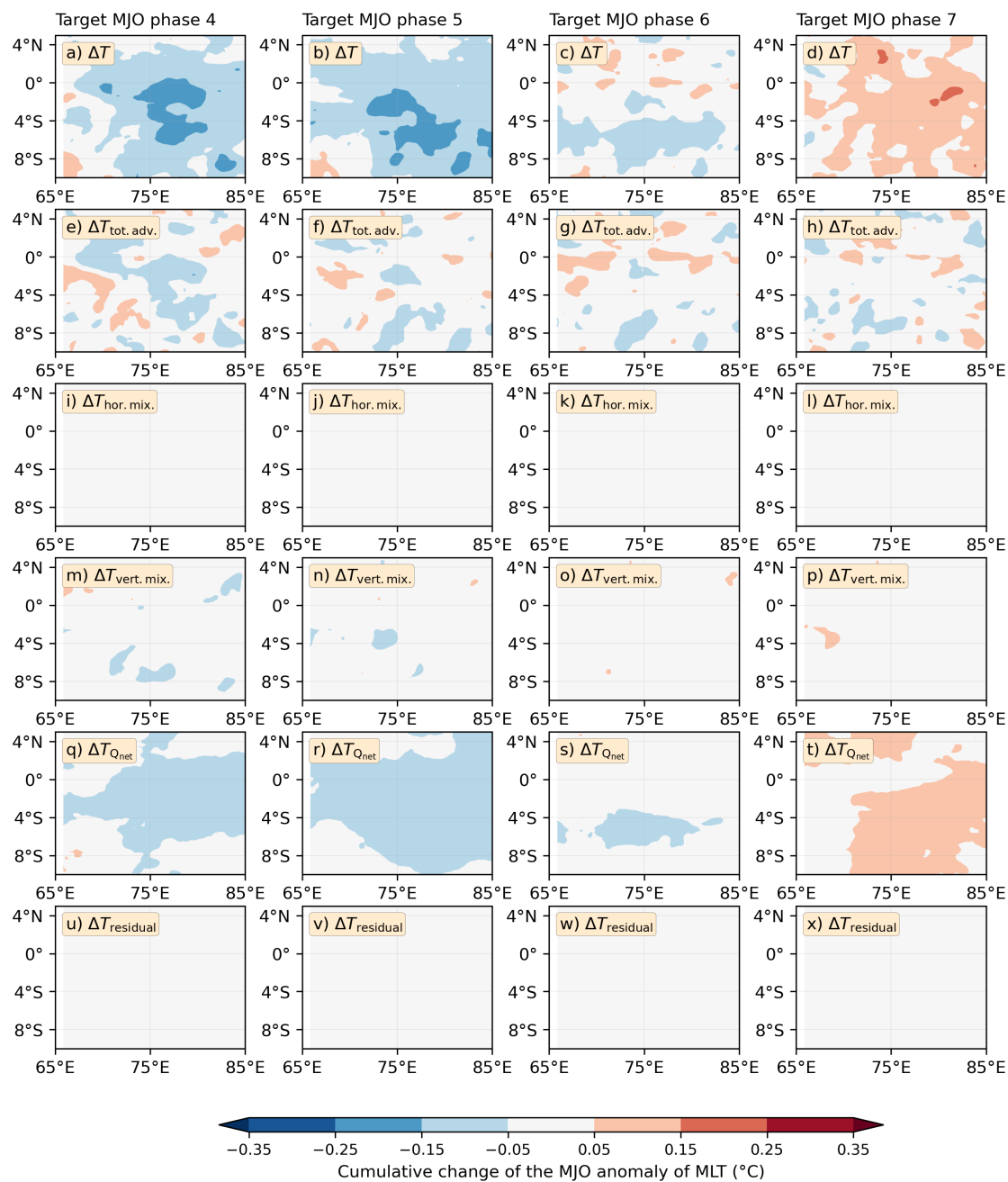


Figure E4: As in Figure E2 but for the central Indian Ocean region.

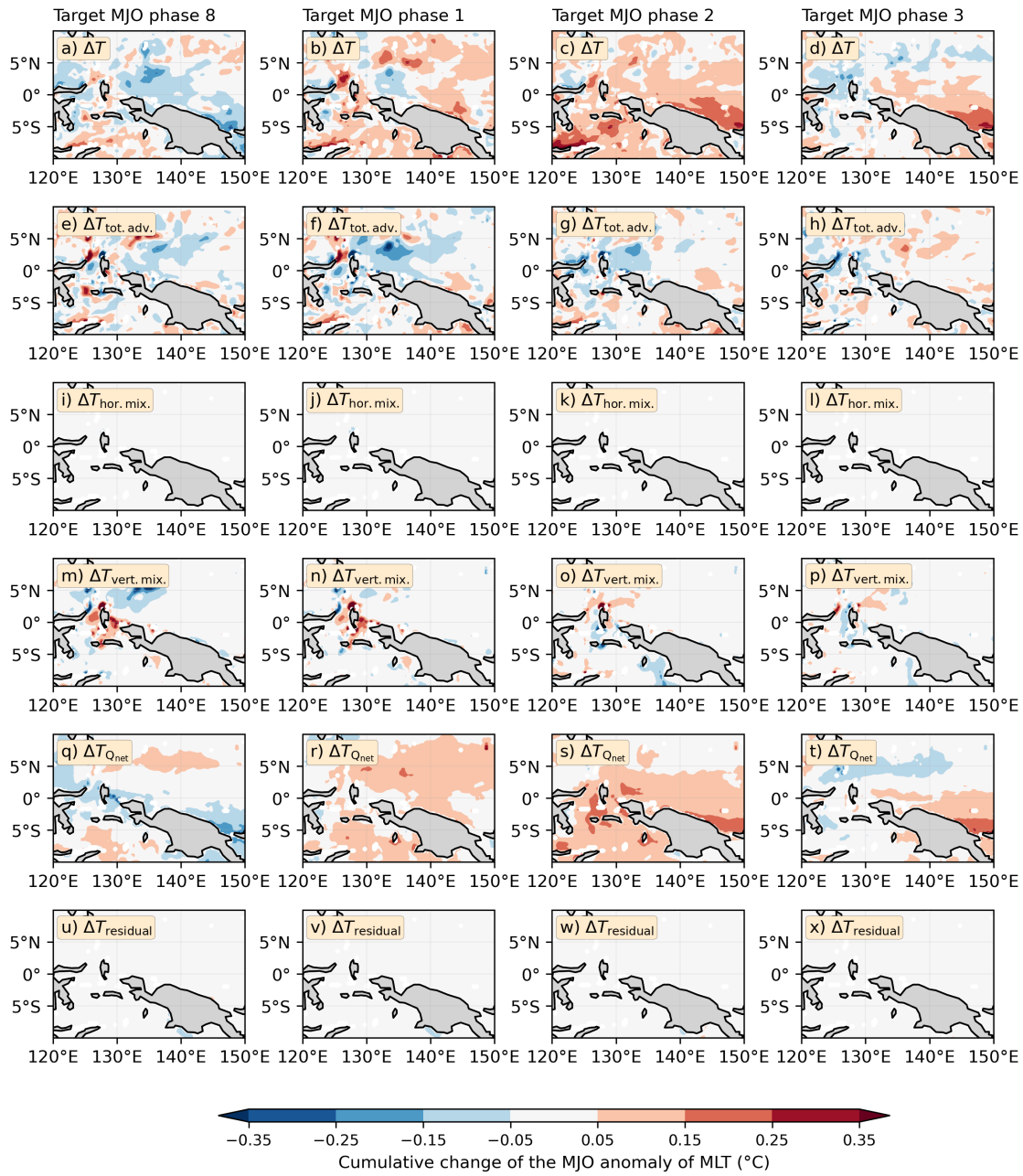


Figure E5: As in Figure E1 but for the eastern Maritime Continent region.

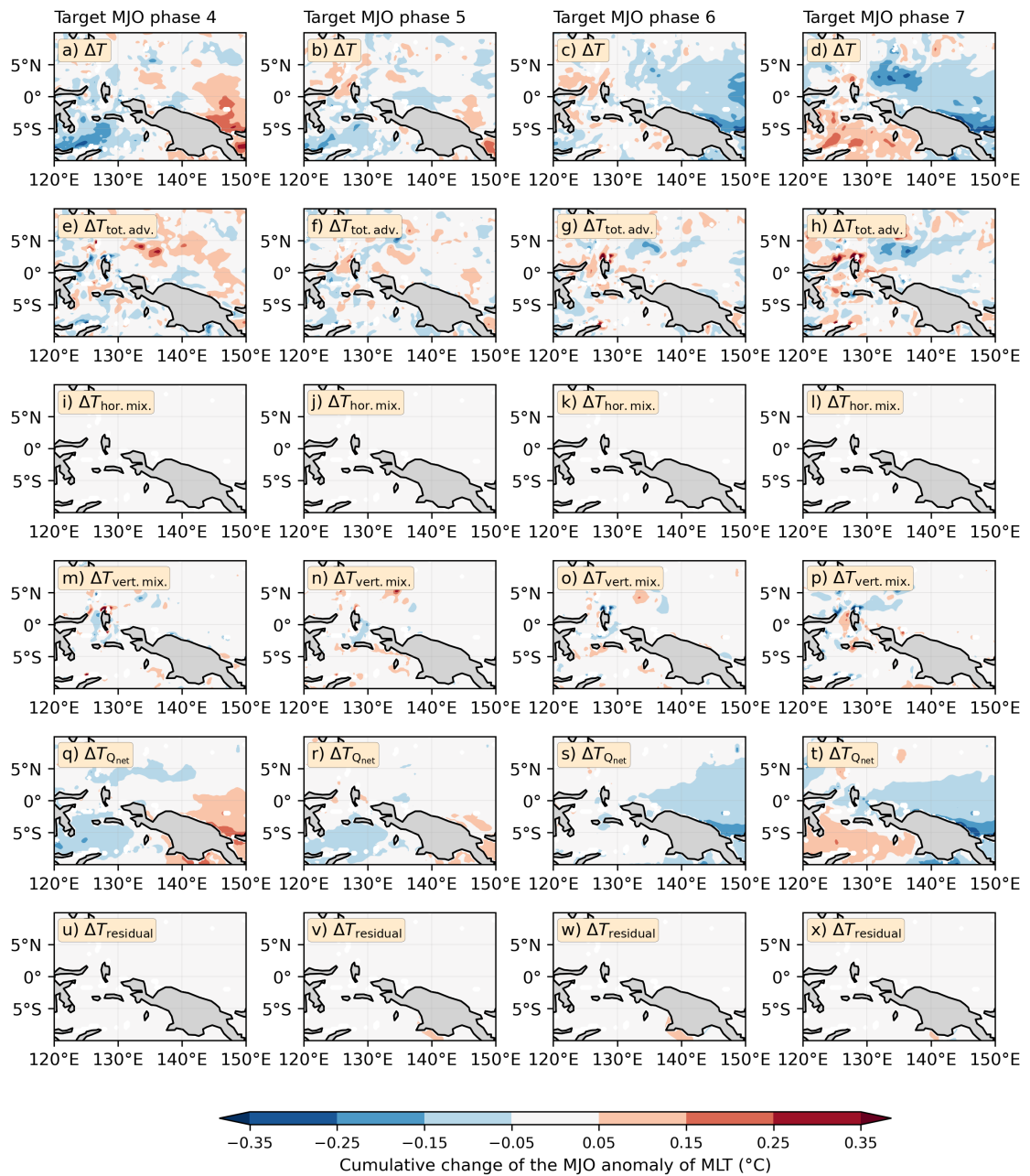


Figure E6: As in Figure E2 but for the eastern Maritime Continent region.

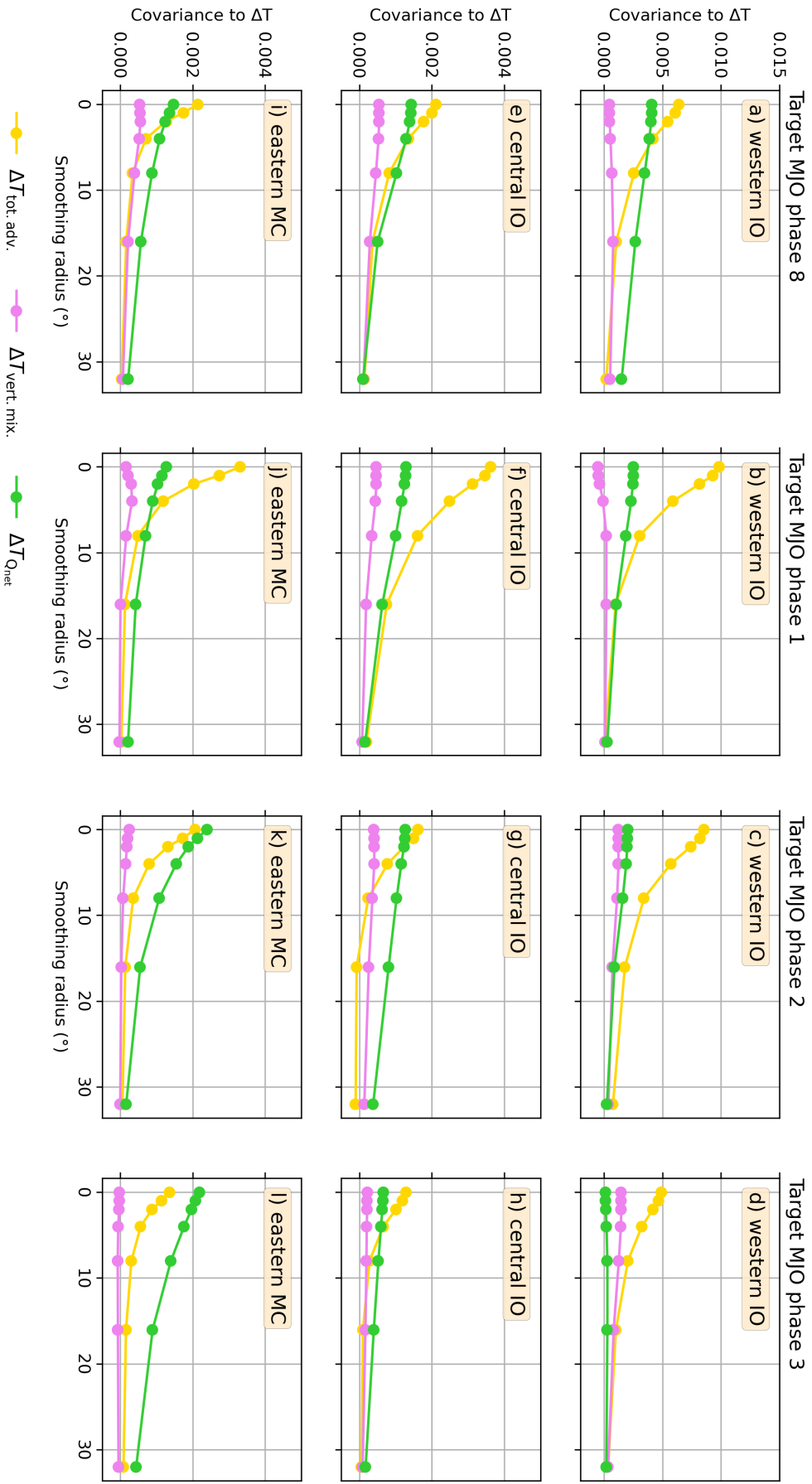


Figure E7: Covariance as a function of the smoothing radius (degree longitude). Covariance between the cumulative change in the composite MJO anomaly of mixed layer temperature (MLT, ΔT) over forecast days 1 to 10 prior to the arrival of (target) MJO phases 8, 1, 2 and 3 and $\Delta T_{\text{tot. adv.}}$ (yellow), $\Delta T_{\text{vert. mix.}}$ (pink) and $\Delta T_{Q_{\text{net}}}$ (green) for the western Indian Ocean (IO) region (panels a–d), central IO region (panels e–h) and eastern Maritime Continent region (panels i–l).

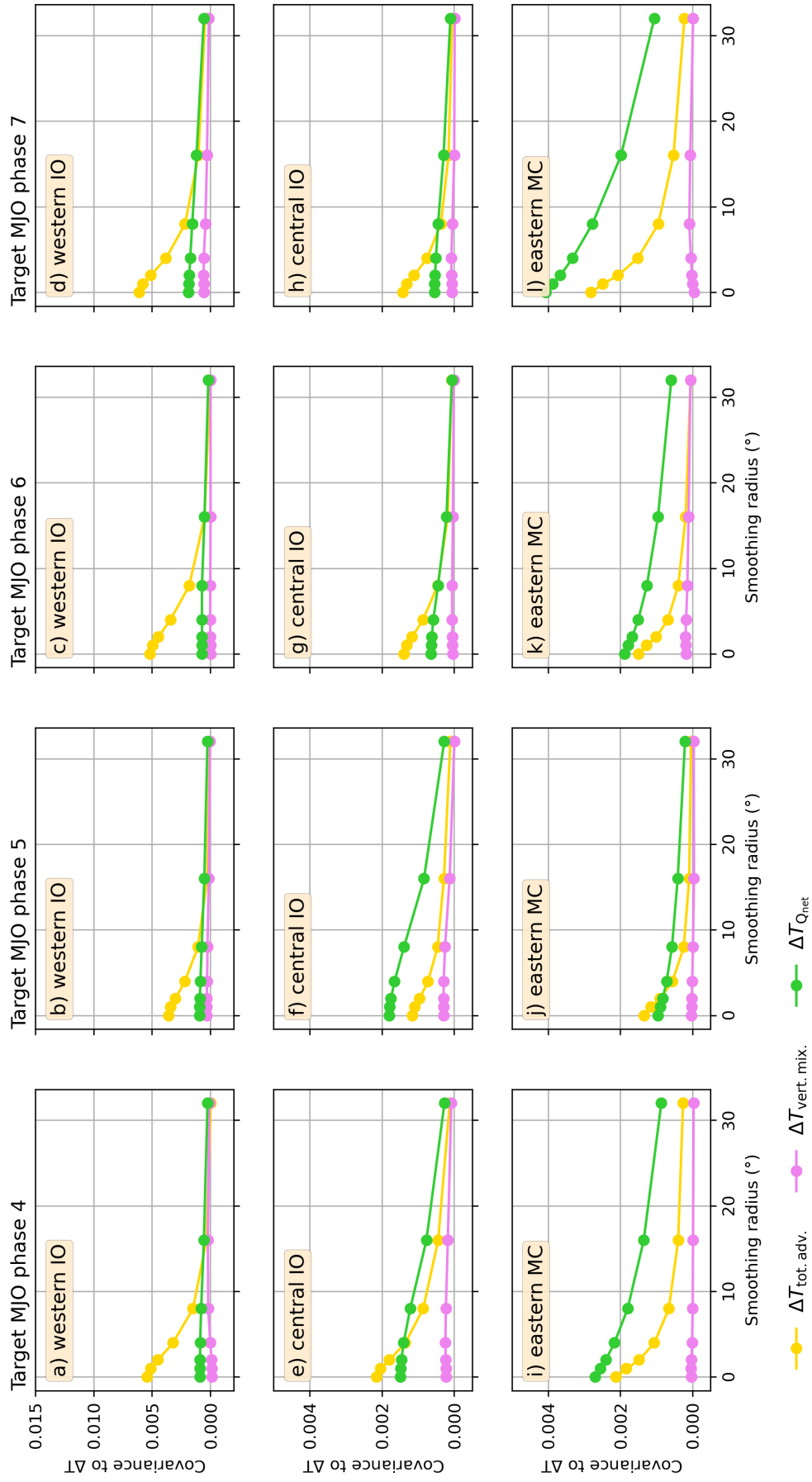


Figure E8: Covariance as a function of the smoothing radius (degree longitude). Covariance between the cumulative change in the composite MJO anomaly of mixed layer temperature (MLT, ΔT) over forecast days 1 to 10 prior to the arrival of (target) MJO phases 4, 5, 6 and 7 and $\Delta T_{\text{tot. adv.}}$ (yellow), $\Delta T_{\text{vert. mix.}}$ (pink) and $\Delta T_{\text{Q}_{\text{net}}}$ (green) for the western Indian Ocean (IO) region (panels a–d), central IO region (panels e–h) and eastern Maritime Continent region (panels i–l).

References

- Adames, Ángel F, & Kim, Daehyun. 2016. The MJO as a dispersive, convectively coupled moisture wave: Theory and observations. *Journal of the Atmospheric Sciences*, **73**(3), 913–941.
- Adams, Samantha V, Ford, Rupert W, Hambley, M, Hobson, J M, Kavčić, I, Maynard, Christopher M, Melvin, Thomas, Müller, Eike Hermann, Mullerworth, S, Porter, Andrew R, & others. 2019. LFRic: Meeting the challenges of scalability and performance portability in Weather and Climate models. *Journal of Parallel and Distributed Computing*, **132**, 383–396.
- Ahn, Min Seop, Kim, Daehyun, Sperber, Kenneth R., Kang, In Sik, Maloney, Eric, Waliser, Duane, & Hendon, Harry. 2017. MJO simulation in CMIP5 climate models: MJO skill metrics and process-oriented diagnosis. *Climate Dynamics*, **49**(11-12), 4023–4045.
- Ahn, Min Seop, Kim, Daehyun, Park, Sungsu, & Ham, Yoo Geun. 2019. Do We Need to Parameterize Mesoscale Convective Organization to Mitigate the MJO-Mean State Trade-Off? *Geophysical Research Letters*, **46**(4), 2293–2301.
- Ahn, Min-Seop, Kim, Daehyun, Ham, Yoo-Geun, & Park, Sungsu. 2020a. Role of Maritime Continent Land Convection on the Mean State and MJO Propagation. *Journal of Climate*, **33**(5), 1659–1675.
- Ahn, Min-Seop, Kim, Daehyun, Kang, Daehyun, Lee, Jiwoo, Sperber, Kenneth R., Gleckler, Peter J., Jiang, Xianan, Ham, Yoo-Geun, & Kim, Hyemi. 2020b. MJO Propagation Across the Maritime Continent: Are CMIP6 Models Better Than CMIP5 Models? *Geophysical Research Letters*, **47**(11), e2020GL087250.
- Anderson, Steven P, Weller, Robert A, & Lukas, Roger B. 1996. Surface Buoyancy Forcing and the Mixed Layer of the Western Pacific Warm Pool: Observations and 1D Model Results. *Journal of Climate*, **9**(12), 3056 – 3085.
- Arnold, Nathan P, Branson, Mark, Kuang, Zhiming, Randall, David A, & Tziperman, Eli. 2015. MJO intensification with warming in the superparameterized CESM. *Journal of Climate*, **28**(7), 2706–2724.
- Baranowski, Dariusz B., Waliser, Duane E., Jiang, Xianan, Ridout, James A., & Flatau, Maria K. 2019. Contemporary GCM Fidelity in Representing the Diurnal Cycle of Precipitation Over the Maritime Continent. *Journal of Geophysical Research: Atmospheres*, **124**(2), 747–769.

- Battisti, David S. 1988. Dynamics and thermodynamics of a warming event in a coupled tropical atmosphere–ocean model. *Journal of the Atmospheric Sciences*, **45**(20), 2889–2919.
- Bellenger, Hugo, & Duvel, Jean-Philippe. 2009. An Analysis of Tropical Ocean Diurnal Warm Layers. *Journal of Climate*, **22**(13), 3629 – 3646.
- Bernie, D J, Guilyardi, E, Madec, Gurvan, Slingo, J M, & Woolnough, S J. 2007. Impact of resolving the diurnal cycle in an ocean–atmosphere GCM. Part 1: A diurnally forced OGCM. *Climate Dynamics*, **29**, 575–590.
- Bernie, Dan J., Guilyardi, E., Madec, G., Slingo, J. M., Woolnough, S. J., & Cole, J. 2008. Impact of resolving the diurnal cycle in an ocean-atmosphere GCM. Part 2: A diurnally coupled CGCM. *Climate Dynamics*, **31**(7-8), 909–925.
- Bessafi, Miloud, & Wheeler, Matthew C. 2006. Modulation of South Indian Ocean Tropical Cyclones by the Madden–Julian Oscillation and Convectively Coupled Equatorial Waves. *Monthly Weather Review*, **134**(2), 638 – 656.
- Birch, C E, Webster, S, Peatman, S C, Parker, D J, Matthews, A J, Li, Y, & Hassim, M E E. 2016. Scale Interactions between the MJO and the Western Maritime Continent. *Journal of Climate*, **29**(7), 2471 – 2492.
- Blockley, EW, Martin, MJ, McLaren, AJ, Ryan, AG, Waters, J, Lea, DJ, Mirouze, I, Peterson, KA, Sellar, A, & Storkey, D. 2014. Recent development of the Met Office operational ocean forecasting system: an overview and assessment of the new Global FOAM forecasts. *Geoscientific Model Development*, **7**(6), 2613–2638.
- Bui, Hien X, Li, Yi-Xian, Maloney, Eric D, Kim, Ji-Eun, Lee, Sun-Seon, & Yu, Jia-Yuh. 2023. Emergence of Madden-Julian oscillation precipitation and wind amplitude changes in a warming climate. *npj Climate and Atmospheric Science*, **6**(1), 22.
- Cassou, Christophe. 2008. Intraseasonal interaction between the Madden–Julian oscillation and the North Atlantic Oscillation. *Nature*, **455**(7212), 523–527.
- Chandra, Ashneel, Keenlyside, Noel, Svendsen, Lea, & Singh, Awnesh. 2024. Processes Driving Subseasonal Variations of Upper Ocean Heat Content in the Equatorial Indian Ocean. *Journal of Geophysical Research: Oceans*, **129**(2), e2023JC020074.
- Chang, Mei Yu, Li, Tim, Lin, Pay Liam, & Chang, Ting Huai. 2019. Forecasts of MJO Events during DYNAMO with a Coupled Atmosphere-Ocean Model: Sensitivity to Cumulus Parameterization Scheme. *Journal of Meteorological Research*, **33**(6), 1016–1030.
- Chen, Yonghua, & Del Genio, Anthony D. 2009. Evaluation of tropical cloud regimes in observations and a general circulation model. *Climate Dynamics*, **32**, 355–369.

- Chi, Nan Hsun, Lien, Ren Chieh, D'Asaro, Eric A., & Ma, Barry B. 2014. The surface mixed layer heat budget from mooring observations in the central Indian Ocean during Madden–Julian Oscillation events. *Journal of Geophysical Research: Oceans*, **119**(7), 4638–4652.
- Chongyin, Li, Ruijin, Hu, & Hui, Yang. 2005. Intraseasonal oscillation in the tropical Indian Ocean. *Advances in Atmospheric Sciences*, **22**, 617–624.
- de Boyer Montégut, Clément, Madec, Gurvan, Fischer, Albert S., Lazar, Alban, & Iudicone, Daniele. 2004. Mixed layer depth over the global ocean: An examination of profile data and a profile-based climatology. *Journal of Geophysical Research: Oceans*, **109**(C12), 1–20.
- de Boyer Montégut, Clément, Mignot, Juliette, Lazar, Alban, & Cravatte, Sophie. 2007. Control of salinity on the mixed layer depth in the world ocean: 1. General description. *Journal of Geophysical Research: Oceans*, **112**(C6).
- DeMott, Charlotte A, Klingaman, Nicholas P, & Woolnough, Steven J. 2015. Atmosphere-ocean coupled processes in the Madden-Julian oscillation. *Reviews of Geophysics*, **53**(4), 1099–1154.
- DeMott, Charlotte A., Benedict, James J., Klingaman, Nicholas P., Woolnough, Steven J., & Randall, David A. 2016. Diagnosing ocean feedbacks to the MJO: SST-modulated surface fluxes and the moist static energy budget. *Journal of Geophysical Research: Atmospheres*, **121**(14), 8350–8373.
- DeMott, Charlotte A, Wolding, Brandon O, Maloney, Eric D, & Randall, David A. 2018. Atmospheric mechanisms for MJO decay over the Maritime Continent. *Journal of Geophysical Research: Atmospheres*, **123**(10), 5188–5204.
- Donlon, Craig J., Martin, Matthew, Stark, John, Roberts-Jones, Jonah, Fiedler, Emma, & Wimmer, Werenfrid. 2012. The Operational Sea Surface Temperature and Sea Ice Analysis (OSTIA) system. *Remote Sensing of Environment*, **116**(1), 140–158.
- Drushka, Kyla, Sprintall, Janet, Gille, Sarah T., & Wijffels, Susan. 2012. In Situ Observations of Madden–Julian Oscillation Mixed Layer Dynamics in the Indian and Western Pacific Oceans. *Journal of Climate*, **25**(7), 2306–2328.
- Drushka, Kyla, Sprintall, Janet, & Gille, Sarah T. 2014a. Subseasonal variations in salinity and barrier-layer thickness in the eastern equatorial Indian Ocean. *Journal of Geophysical Research: Oceans*, **119**(2), 805–823.
- Drushka, Kyla, Gille, Sarah T., & Sprintall, Janet. 2014b. The diurnal salinity cycle in the tropics. *Journal of Geophysical Research: Oceans*, **119**(9), 5874–5890.
- Du, Danni, Subramanian, Aneesh C, Han, Weiqing, Chapman, William E, Weiss, Jeffrey B, & Bradley, Elizabeth. 2024. Increase in MJO predictability under global warming. *Nature Climate Change*, **14**(1), 68–74.

- Duchon, Claude E. 1979. Lanczos filtering in one and two dimensions. *Journal of Applied Meteorology and Climatology*, **18**(8), 1016–1022.
- Fairall, C W, Bradley, Edward F, Godfrey, J S, Wick, G A, Edson, J Bo, & Young, G S. 1996. Cool-skin and warm-layer effects on sea surface temperature. *Journal of Geophysical Research: Oceans*, **101**(C1), 1295–1308.
- Feng, Zhe, Leung, L Ruby, Hardin, Joseph, Terai, Christopher R, Song, Fengfei, & Caldwell, Peter. 2023. Mesoscale convective systems in DYAMOND global convection-permitting simulations. *Geophysical Research Letters*, **50**(4), e2022GL102603.
- Fiedler, E. K., Mao, C., Good, S. A., Waters, J., & Martin, M. J. 2019. Improvements to feature resolution in the OSTIA sea surface temperature analysis using the NEMOVAR assimilation scheme. *Quarterly Journal of the Royal Meteorological Society*, **145**(725), 3609–3625.
- Fu, Xiouhua, Lee, June Yi, Hsu, Pang Chi, Taniguchi, Hiroshi, Wang, Bin, Wang, Wanqiu, & Weaver, Scott. 2013. Multi-model MJO forecasting during DYNAMO/CINDY period. *Climate Dynamics*, **41**(3-4), 1067–1081.
- Fu, Xiouhua, Wang, Wanqiu, Lee, June-Yi, Wang, Bin, Kikuchi, Kazuyoshi, Xu, Jingwei, Li, Juan, & Weaver, Scott. 2015. Distinctive Roles of Air–Sea Coupling on Different MJO Events: A New Perspective Revealed from the DYNAMO/CINDY Field Campaign. *Monthly Weather Review*, **143**(3), 794 – 812.
- Ge, Xuyang, Wang, Wanqiu, Kumar, Arun, & Zhang, Ying. 2017. Importance of the vertical resolution in simulating SST diurnal and intraseasonal variability in an oceanic general circulation model. *Journal of Climate*, **30**(11), 3963–3978.
- Giese, Benjamin S, & Harrison, D E. 1990. Aspects of the Kelvin wave response to episodic wind forcing. *Journal of Geophysical Research: Oceans*, **95**(C5), 7289–7312.
- Gill, Adrian E. 1980. Some simple solutions for heat-induced tropical circulation. *Quarterly Journal of the Royal Meteorological Society*, **106**(449), 447–462.
- Gonzalez, Alex O, & Jiang, Xianan. 2019. Distinct propagation characteristics of intraseasonal variability over the tropical west Pacific. *Journal of Geophysical Research: Atmospheres*, **124**(10), 5332–5351.
- Good, Simon, Fiedler, Emma, Mao, Chongyuan, Martin, Matthew J., Maycock, Adam, Reid, Rebecca, Roberts-Jones, Jonah, Searle, Toby, Waters, Jennifer, While, James, & Worsfold, Mark. 2020. The current configuration of the OSTIA system for operational production of foundation sea surface temperature and ice concentration analyses. *Remote Sensing*, **12**(4), 720.
- Gordon, Arnold L, Napitu, Asmi, Huber, Bruce A, Gruenburg, Laura K, Pujiana, Kandaga, Agustiadi, Teguh, Kuswardani, Anastasia, Mbay, Nurman,

- & Setiawan, Agus. 2019. Makassar Strait throughflow seasonal and interannual variability: An overview. *Journal of Geophysical Research: Oceans*, **124**(6), 3724–3736.
- Gottschalck, J., Wheeler, M., Weickmann, K., Vitart, F., Savage, N., Lin, H., Hendon, H., Waliser, D., Sperber, K., Nakagawa, M., Prestrelo, C., Flatau, M., & Higgins, W. 2010. A framework for assessing operational Madden-Julian oscillation forecasts: A clivar MJO working group project. *Bulletin of the American Meteorological Society*, **91**(9), 1247–1258.
- Gregory, D, & Allen, S. 1991. The effect of convective downdraughts upon NWP and climate simulations. *Pages 122–123 of: Ninth Conference on Numerical Weather Prediction, Denver, Colorado.*
- Gregory, D, & Rowntree, P R. 1990. A Mass Flux Convection Scheme with Representation of Cloud Ensemble Characteristics and Stability-Dependent Closure. *Monthly Weather Review*, **118**(7), 1483 – 1506.
- Hagos, Samson M, Zhang, Chidong, Feng, Zhe, Burleyson, Casey D, De Mott, Charlotte, Kerns, Brandon, Benedict, James J, & Martini, Matus N. 2016. The impact of the diurnal cycle on the propagation of Madden-Julian Oscillation convection across the Maritime Continent. *Journal of Advances in Modeling Earth Systems*, **8**(4), 1552–1564.
- Halkides, D. J., Waliser, Duane E., Lee, Tong, Menemenlis, Dimitris, & Guan, Bin. 2015. Quantifying the processes controlling intraseasonal mixed-layer temperature variability in the tropical Indian Ocean. *Journal of Geophysical Research: Oceans*, **120**(2), 692–715.
- Hao, Zhanjiu, Xu, Zhenhua, Feng, Ming, Zhang, Peiwen, You, Jia, & Yin, Baoshu. 2023. Seasonal variability of eddy kinetic energy in the Banda Sea revealed by an ocean model: An energy budget perspective. *Deep Sea Research Part II: Topical Studies in Oceanography*, **211**(10), 105320.
- Hartmann, Dennis L, Michelsen, Marc L, & Klein, Stephern A. 1992. Seasonal variations of tropical intraseasonal oscillations- A 20-25-day oscillation in the western Pacific. *Journal of the Atmospheric Sciences*, **49**(14), 1277–1289.
- Hendon, Harry H, & Glick, John. 1997. Intraseasonal Air–Sea Interaction in the Tropical Indian and Pacific Oceans. *Journal of Climate*, **10**(4), 647 – 661.
- Hendon, Harry H, Liebmann, Brant, Newman, Matthew, Glick, John D, & Schemm, J E. 2000. Medium-Range Forecast Errors Associated with Active Episodes of the Madden–Julian Oscillation. *Monthly Weather Review*, **128**(1), 69–86.
- Hersbach, Hans, Bell, Bill, Berrisford, Paul, Hirahara, Shoji, Horányi, András, Muñoz-Sabater, Joaquín, Nicolas, Julien, Peubey, Carole, Radu, Raluca, Schepers, Dinand, Simmons, Adrian, Soci, Cornel, Abdalla, Saleh, Abellan, Xavier, Balsamo, Gianpaolo, Bechtold, Peter, Biavati, Gionata,

- Bidlot, Jean, Bonavita, Massimo, De Chiara, Giovanna, Dahlgren, Per, Dee, Dick, Diamantakis, Michail, Dragani, Rossana, Flemming, Johannes, Forbes, Richard, Fuentes, Manuel, Geer, Alan, Haimberger, Leo, Healy, Sean, Hogan, Robin J., Hólm, Elías, Janisková, Marta, Keeley, Sarah, Laloyaux, Patrick, Lopez, Philippe, Lupu, Cristina, Radnoti, Gabor, de Rosnay, Patricia, Rozum, Iryna, Vamborg, Freja, Villaume, Sebastien, & Thépaut, Jean Noël. 2020. The ERA5 global reanalysis. *Quarterly Journal of the Royal Meteorological Society*, **146**(730), 1999–2049.
- Holloway, Christopher E., Woolnough, Steven J., & Lister, Grenville M.S. 2013. The effects of explicit versus parameterized convection on the MJO in a large-domain high-resolution tropical case study. Part I: Characterization of large-scale organization and propagation. *Journal of the Atmospheric Sciences*, **70**(5), 1342–1369.
- Hong, Xiaodong, Reynolds, Carolyn A., Doyle, James D., May, Paul, & O'Neill, Larry. 2017. Assessment of upper-ocean variability and the Madden-Julian Oscillation in extended-range air-ocean coupled mesoscale simulations. *Dynamics of Atmospheres and Oceans*, **78**(6), 89–105.
- Hosoda, Shigeki, Ohira, Tsuyoshi, Sato, Kanako, & Suga, Toshio. 2010. Improved description of global mixed-layer depth using Argo profiling floats. *Journal of Oceanography*, **66**(6), 773–787.
- Howard, E, Woolnough, S, Klingaman, N, Shipley, D, Sanchez, C, Peatman, S C, Birch, C E, & Matthews, A J. 2024. Evaluation of multi-season convection-permitting atmosphere – mixed-layer ocean simulations of the Maritime Continent. *Geoscientific Model Development*, **17**(9), 3815–3837.
- Hoyer, S, & Hamman, J. 2017. xarray: N-D labeled arrays and datasets in Python. *Journal of Open Research Software*, **5**(1).
- Hsu, Je Yuan, Hendon, Harry, Feng, Ming, & Zhou, Xiaobing. 2019. Magnitude and Phase of Diurnal SST Variations in the ACCESS-S1 Model During the Suppressed Phase of the MJOs. *Journal of Geophysical Research: Oceans*, **124**(12), 9553–9571.
- Hu, Yun, Wang, Xiaochun, Luo, Jing-Jia, Wang, Dongxiao, Yan, Huiping, Yuan, Chaoxia, & Lin, Xia. 2022. Forecasts of MJO during DYNAMO in a coupled tropical channel model, Part I: Impact of parameterization schemes. *International Journal of Climatology*, **42**(13), 6771–6792.
- Hunter, John D. 2007. Matplotlib: A 2D Graphics Environment. *Computing in Science & Engineering*, **9**(3), 90–95.
- Inness, Peter M, & Slingo, Julia M. 2006. The interaction of the Madden–Julian oscillation with the Maritime Continent in a GCM. *Quarterly Journal of the Royal Meteorological Society*, **132**(618), 1645–1667.

- Itterly, Kyle, Taylor, Patrick, & Roberts, J. Brent. 2021. Satellite Perspectives of Sea Surface Temperature Diurnal Warming on Atmospheric Moistening and Radiative Heating during MJO. *Journal of Climate*, **34**(3), 1203–1226.
- Jia, Wentao, Sun, Jilin, Zhang, Weimin, & Wang, Huizan. 2023. The Effect of Boreal Summer Intraseasonal Oscillation on Mixed Layer and Upper Ocean Temperature over the South China Sea. *Journal of Ocean University of China*, **22**(2), 285–296.
- Jia, Xiaolong, Li, Chongyin, Zhou, Ningfang, & Ling, Jian. 2010. The MJO in an AGCM with three different cumulus parameterization schemes. *Dynamics of Atmospheres and Oceans*, **49**(2-3), 141–163.
- Jiang, Xianan. 2017. Key processes for the eastward propagation of the Madden-Julian Oscillation based on multimodel simulations. *Journal of Geophysical Research: Atmospheres*, **122**(2), 755–770.
- Jiang, Xianan, Waliser, Duane E, Wheeler, Matthew C, Jones, Charles, Lee, Myong-In, & Schubert, Siegfried D. 2008. Assessing the skill of an all-season statistical forecast model for the Madden–Julian oscillation. *Monthly Weather Review*, **136**(6), 1940–1956.
- Jiang, Xianan, Adames, Ángel F., Kim, Daehyun, Maloney, Eric D., Lin, Hai, Kim, Hyemi, Zhang, Chidong, DeMott, Charlotte A., & Klingaman, Nicholas P. 2020. Fifty Years of Research on the Madden-Julian Oscillation: Recent Progress, Challenges, and Perspectives. *Journal of Geophysical Research: Atmospheres*, **125**(17), e2019JD030911.
- Johnson, Richard H, & Ciesielski, Paul E. 2013. Structure and properties of Madden–Julian oscillations deduced from DYNAMO sounding arrays. *Journal of the Atmospheric Sciences*, **70**(10), 3157–3179.
- Jones, Charles, & Carvalho, Leila M V. 2006. Changes in the Activity of the Madden–Julian Oscillation during 1958–2004. *Journal of Climate*, **19**(24), 6353–6370.
- Jones, Charles, Waliser, D E, Schemm, J-KE, & Lau, W K M. 2000. Prediction skill of the Madden and Julian Oscillation in dynamical extended range forecasts. *Climate Dynamics*, **16**, 273–289.
- Jones, Charles, Carvalho, Leila M V, Wayne Higgins, R, Waliser, Duane E, & Schemm, J K E. 2004. A statistical forecast model of tropical intraseasonal convective anomalies. *Journal of Climate*, **17**(11), 2078–2095.
- Kang, Daehyun, Kim, Daehyun, Ahn, Min-Seop, & An, Soon-Il. 2021. The role of the background meridional moisture gradient on the propagation of the MJO over the maritime continent. *Journal of Climate*, **34**(16), 6565–6581.
- Kara, A Birol, Rochford, Peter A, & Hurlburt, Harley E. 2000. An optimal definition for ocean mixed layer depth. *Journal of Geophysical Research: Oceans*, **105**(C7), 16803–16821.

- Karlow ska, Eliza, Matthews, Adrian J, Webber, Benjamin G M, Graham, Tim, & Xavier, Prince. 2024a. The effect of diurnal warming of sea-surface temperatures on the propagation speed of the Madden–Julian oscillation. *Quarterly Journal of the Royal Meteorological Society*, **150**(758), 334–354.
- Karlow ska, Eliza, Matthews, Adrian J, Webber, Benjamin G M, Graham, Tim, & Xavier, Prince. 2024b. The relative importance of ocean advection and surface heat fluxes during the Madden–Julian Oscillation in a coupled ocean–atmosphere model. *Journal of Geophysical Research: Oceans*, **in review**.
- Karlow ska, Eliza, Matthews, Adrian J, Webber, Benjamin G M, Graham, Tim, & Xavier, Prince. 2024c. Two-way feedback between the Madden–Julian Oscillation and diurnal warm layers in a coupled ocean–atmosphere model. *Quarterly Journal of the Royal Meteorological Society*, 1–20. Available from: <https://doi.org/10.1002/qj.4807>.
- Kawai, Yoshimi, & Wada, Akiyoshi. 2007. Diurnal sea surface temperature variation and its impact on the atmosphere and ocean: A review. *Journal of Oceanography*, **63**, 721–744.
- Kemball-Cook, Susan, Wang, Bin, & Fu, Xiouhua. 2002. Simulation of the intraseasonal oscillation in the ECHAM-4 model: The impact of coupling with an ocean model. *Journal of the Atmospheric Sciences*, **59**(9), 1433–1453.
- Kendon, E J, Prein, A F, Senior, C A, & Stirling, A. 2021. Challenges and outlook for convection-permitting climate modelling. *Philosophical Transactions of the Royal Society A*, **379**(2195), 20190547.
- Kiladis, George N, Straub, Katherine H, & Haertel, Patrick T. 2005. Zonal and vertical structure of the Madden–Julian oscillation. *Journal of the Atmospheric Sciences*, **62**(8), 2790–2809.
- Kiladis, George N, Dias, Juliana, Straub, Katherine H, Wheeler, Matthew C, Tulich, Stefan N, Kikuchi, Kazuyoshi, Weickmann, Klaus M, & Ventrice, Michael J. 2014. A Comparison of OLR and Circulation-Based Indices for Tracking the MJO. *Monthly Weather Review*, **142**(5), 1697 – 1715.
- Kim, Daehyun, Sobel, Adam H., Maloney, Eric D., Frierson, Dargan M.W., & Kang, In Sik. 2011. A systematic relationship between intraseasonal variability and mean state bias in AGCM simulations. *Journal of Climate*, **24**(21), 5506–5520.
- Kim, Daehyun, Kim, Hyerim, & Lee, Myong-In. 2017. Why does the MJO detour the Maritime Continent during austral summer? *Geophysical Research Letters*, **44**(5), 2579–2587.
- Kim, Hye-Mi, Hoyos, Carlos D, Webster, Peter J, & Kang, In-Sik. 2008. Sensitivity of MJO simulation and predictability to sea surface temperature variability. *Journal of Climate*, **21**(20), 5304–5317.

- Kim, Hye Mi, Webster, Peter J., Toma, Violeta E., & Kim, Daehyun. 2014. Predictability and prediction skill of the MJO in two operational forecasting systems. *Journal of Climate*, **27**(14), 5364–5378.
- Kim, Hye-Ryeom, Ha, Kyung-Ja, Moon, Suyeon, Oh, Hyeoun, & Sharma, Sahil. 2020. Impact of the Indo-Pacific Warm Pool on the Hadley, Walker, and Monsoon Circulations. *Atmosphere*, **11**(10).
- Kim, Hyemi, Janiga, Matthew A., & Pegion, Kathy. 2019. MJO Propagation Processes and Mean Biases in the SubX and S2S Reforecasts. *Journal of Geophysical Research: Atmospheres*, **124**(16), 9314–9331.
- Lau, William K-M, & Waliser, Duane E. 2011. *Intraseasonal variability in the atmosphere-ocean climate system*. Springer Science & Business Media.
- Lavender, Sally L, Stirling, Alison J, Whittall, Michael, Stratton, Rachel A, Daleu, Chimene L, Plant, Robert S, Lock, Adrian, & Gu, Jian-Feng. 2024. The use of idealised experiments in testing a new convective parametrization: Performance of CoMorph-A. *Quarterly Journal of the Royal Meteorological Society*, **150**(760), 1581–1600.
- Li, Kuiping, Yu, Weidong, Li, Tim, Murty, V S N, Khokiattiwong, Somkiat, Adi, T R, & Budi, S. 2013a. Structures and mechanisms of the first-branch northward-propagating intraseasonal oscillation over the tropical Indian Ocean. *Climate Dynamics*, **40**(7), 1707–1720.
- Li, Wei, Zhu, Yuejian, Zhou, Xiaqiong, Hou, Dingchen, Sinsky, Eric, Melhauser, Christopher, Peña, Malaquias, Guan, Hong, & Wobus, Richard. 2019. Evaluating the MJO prediction skill from different configurations of NCEP GEFS extended forecast. *Climate Dynamics*, **52**, 4923–4936.
- Li, Yuanlong, Han, Weiqing, Shinoda, Toshiaki, Wang, Chunzai, Lien, Ren-Chieh, Moum, James N, Wang, Jih-Wang, Li, Y, Han, W, Shinoda, T, Wang, C, Lien, R.-C, Moum, J N, & Wang, J.-W. 2013b. Effects of the diurnal cycle in solar radiation on the tropical Indian Ocean mixed layer variability during wintertime Madden-Julian Oscillations. *Journal of Geophysical Research: Oceans*, **118**(10), 4945–4964.
- Liebmann, Brant, & Smith, Catherine A. 1996. Description of a Complete (Interpolated) Outgoing Longwave Radiation Dataset. *Bulletin of the American Meteorological Society*, **77**(6), 1275–1277.
- Lim, Yuna, Son, Seok Woo, & Kim, Daehyun. 2018. MJO prediction skill of the subseasonal-to-seasonal prediction models. *Journal of Climate*, **31**(10), 4075–4094.
- Lin, Hai, Brunet, Gilbert, & Derome, Jacques. 2008. Forecast skill of the Madden-Julian oscillation in two canadian atmospheric models. *Monthly Weather Review*, **136**(11), 4130–4149.

- Lin, Hai, Huang, Zhiyong, Hendon, Harry, & Brunet, Gilbert. 2021. NAO Influence on the MJO and its Prediction Skill in the Subseasonal-to-Seasonal Prediction Models. *Journal of Climate*, **34**(23), 9425 – 9442.
- Lin, Jialin, Mapes, Brian, Zhang, Minghua, & Newman, Matthew. 2004. Stratiform precipitation, vertical heating profiles, and the Madden–Julian oscillation. *Journal of the Atmospheric Sciences*, **61**(3), 296–309.
- Liu, Lingling, Li, Yuanlong, & Wang, Fan. 2021. MJO-Induced Intraseasonal Mixed Layer Depth Variability in the Equatorial Indian Ocean and Impacts on Subsurface Water Obduction. *Journal of Physical Oceanography*, **51**(4), 1247–1263.
- Liu, Xiangwen, Wu, Tongwen, Yang, Song, Li, Tim, Jie, Weihua, Zhang, Li, Wang, Zaizhi, Liang, Xiaoyun, Li, Qiaoping, Cheng, Yanjie, & others. 2017. MJO prediction using the sub-seasonal to seasonal forecast model of Beijing Climate Center. *Climate Dynamics*, **48**(9-10), 3283–3307.
- Lorenz, David J., & Hartmann, Dennis L. 2006. The effect of the MJO on the North American monsoon. *Journal of Climate*, **19**(3), 333–343.
- Ma, Libin, & Jiang, Zijun. 2021. Reevaluating the impacts of oceanic vertical resolution on the simulation of Madden–Julian Oscillation eastward propagation in a climate system model. *Climate Dynamics*, **56**(7), 2259–2278.
- Madden, Roland A, & Julian, Paul R. 1971. Detection of a 40–50 day oscillation in the zonal wind in the tropical Pacific. *Journal of the Atmospheric Sciences*, **28**(5), 702–708.
- Madden, Roland A, & Julian, Paul R. 1972. Description of global-scale circulation cells in the tropics with a 40–50 day period. *Journal of the Atmospheric Sciences*, **29**(6), 1109–1123.
- Madec, Gurvan, Delecluse, Pascale, Imbard, M, & Levy, C. 1997. Ocean general circulation model reference manual. *Note du Pôle de modélisation*.
- Madec, Gurvan, Bourdallé-Badie, Romain, Bouttier, Pierre-Antoine, Bricaud, Clement, Bruciaferri, Diego, Calvert, Daley, Chanut, Jérôme, Clementi, Emanuela, Coward, Andrew, Delrosso, Damiano, & others. 2017. NEMO ocean engine.
- Majda, Andrew J, & Stechmann, Samuel N. 2009. The skeleton of tropical intraseasonal oscillations. *Proceedings of the National Academy of Sciences*, **106**(21), 8417–8422.
- Majda, Andrew J, & Stechmann, Samuel N. 2011. Nonlinear dynamics and regional variations in the MJO skeleton. *Journal of the Atmospheric Sciences*, **68**(12), 3053–3071.

- Maloney, Eric D, Adames, Ángel F, & Bui, Hien X. 2019. Madden–Julian oscillation changes under anthropogenic warming. *Nature Climate Change*, **9**(1), 26–33.
- Marshall, Andrew G, Alves, Oscar, & Hendon, Harry H. 2008. An enhanced moisture convergence–evaporation feedback mechanism for MJO air–sea interaction. *Journal of the Atmospheric Sciences*, **65**(3), 970–986.
- Matsuno, Taroh. 1966. Quasi-geostrophic motions in the equatorial area. *Journal of the Meteorological Society of Japan. Ser. II*, **44**(1), 25–43.
- Matthews, Adrian J. 2000. Propagation mechanisms for the Madden-Julian Oscillation. *Quarterly Journal of the Royal Meteorological Society*, **126**(569), 2637–2651.
- Matthews, Adrian J. 2004. Atmospheric response to observed intraseasonal tropical sea surface temperature anomalies. *Geophysical Research Letters*, **31**(14).
- Matthews, Adrian J. 2008. Primary and successive events in the Madden–Julian Oscillation. *Quarterly Journal of the Royal Meteorological Society*, **134**(631), 439–453.
- Matthews, Adrian J., Baranowski, Dariusz B., Heywood, Karen J., Flatau, Piotr J., & Schmidtko, Sunke. 2014. The Surface Diurnal Warm Layer in the Indian Ocean during CINDY/DYNAMO. *Journal of Climate*, **27**(24), 9101–9122.
- McDougall, Trevor J, & Barker, Paul M. 2011. Getting started with TEOS-10 and the Gibbs Seawater (GSW) oceanographic toolbox. *Scor/lapso WG*, **127**(532), 1–28.
- McKinney, Wes. 2010. *Data Structures for Statistical Computing in Python*.
- McPhaden, M. J., & Foltz, G. R. 2013. Intraseasonal variations in the surface layer heat balance of the central equatorial Indian Ocean: The importance of zonal advection and vertical mixing. *Geophysical Research Letters*, **40**(11), 2737–2741.
- McPhaden, Michael J. 1999. Genesis and evolution of the 1997-98 El Niño. *Science*, **283**(5404), 950–954.
- Megann, A P, Storkey, D, Aksenov, Y, Alderson, S, Calvert, D, Graham, T, Hyder, P, Siddorn, J, & Sinha, B. 2014. Go 5.0: The joint NERC-Met office NEMO global ocean model for use in coupled and forced applications. *Geotechnical Model Development*, **7**(3), 1069–1092.
- Met Office. 2016. *Cartopy: a cartographic python library with a matplotlib interface*. <http://scitools.org.uk/cartopy>.
- Met Office. 2020. *Iris: A Python library for analysing and visualising meteorological and oceanographic data sets*. <http://scitools.org.uk/iris>.

- Mogensen, Kristian S., Magnusson, Linus, & Bidlot, Jean Raymond. 2017. Tropical cyclone sensitivity to ocean coupling in the ECMWF coupled model. *Journal of Geophysical Research: Oceans*, **122**(5), 4392–4412.
- Moteki, Qoosaku, Katsumata, Masaki, Yoneyama, Kunio, Ando, Kentaro, & Hasegawa, Takuya. 2018. Drastic thickening of the barrier layer off the western coast of Sumatra due to the Madden-Julian oscillation passage during the Pre-Years of the Maritime Continent campaign. *Progress in Earth and Planetary Science*, **5**(1), 35.
- Neena, J. M., Lee, June Yi, Waliser, Duane, Wang, Bin, & Jiang, Xianan. 2014. Predictability of the Madden-Julian oscillation in the Intraseasonal Variability Hindcast Experiment (ISVHE). *Journal of Climate*, **27**(12), 4531–4543.
- Neena, J M, Suhas, E, & Jiang, Xianan. 2022. Modulation of the Convectively Coupled Kelvin Waves by the MJO over Different Domains. *Journal of Climate*, **35**(21), 7025 – 7039.
- Pai, D. S., Bhate, Jyoti, Sreejith, O. P., & Hatwar, H. R. 2011. Impact of MJO on the intraseasonal variation of summer monsoon rainfall over India. *Climate Dynamics*, **36**(1), 41–55.
- Paulson, Clayton A, & Simpson, James J. 1977. Irradiance measurements in the upper ocean. *Journal of Physical Oceanography*, **7**(6), 952–956.
- Peatman, Simon C., Matthews, Adrian J., & Stevens, David P. 2014. Propagation of the Madden-Julian Oscillation through the Maritime Continent and scale interaction with the diurnal cycle of precipitation. *Quarterly Journal of the Royal Meteorological Society*, **140**(680), 814–825.
- Prein, Andreas F, Langhans, Wolfgang, Fosser, Giorgia, Ferrone, Andrew, Ban, Nikolina, Goergen, Klaus, Keller, Michael, Tölle, Merja, Gutjahr, Oliver, Feser, Frauke, & others. 2015. A review on regional convection-permitting climate modeling: Demonstrations, prospects, and challenges. *Reviews of Geophysics*, **53**(2), 323–361.
- Price, James F, Weller, Robert A, & Pinkel, Robert. 1986. Diurnal cycling: Observations and models of the upper ocean response to diurnal heating, cooling, and wind mixing. *Journal of Geophysical Research: Oceans*, **91**(C7), 8411–8427.
- Rae, J. G.L., Hewitt, H. T., Keen, A. B., Ridley, J. K., West, A. E., Harris, C. M., Hunke, E. C., & Walters, D. N. 2015. Development of the Global Sea Ice 6.0 CICE configuration for the Met Office Global Coupled model. *Geoscientific Model Development*, **8**(7), 2221–2230.
- Ramadhan, Muhammad Firdaus, Sugianto, Denny Nugroho, Wirasatriya, Anindya, Setiyono, Heryoso, Maslukah, Lilik, & others. 2020. Characteristics of Halmahera Eddy and its relation to sea surface temperature, chlorophyll-a, and thermocline layer. *Page 12039 of: IOP Conference Series: Earth and Environmental Science*, vol. 530.

- Rashid, Harun A., Hendon, Harry H., Wheeler, Matthew C., & Alves, Oscar. 2011. Prediction of the Madden-Julian oscillation with the POAMA dynamical prediction system. *Climate Dynamics*, **36**(3), 649–661.
- Rawlins, F., Ballard, S. P., Bovis, K. J., Clayton, A. M., Li, D., Inverarity, G. W., Lorenc, A. C., & Payne, T. J. 2007. The met office global four-dimensional variational data assimilation scheme. *Quarterly Journal of the Royal Meteorological Society*, **133**(623), 347–362.
- Ridley, Jeff K., Blockley, Edward W., Keen, Ann B., Rae, Jamie G.L., West, Alex E., & Schroeder, David. 2018. The sea ice model component of HadGEM3-GC3.1. *Geoscientific Model Development*, **11**(2), 713–723.
- Roberts, Malcolm J., Hewitt, Helene T., Hyder, Pat, Ferreira, David, Josey, Simon A., Mizielinski, Matthew, & Shelly, Ann. 2016. Impact of ocean resolution on coupled air-sea fluxes and large-scale climate. *Geophysical Research Letters*, **43**(19), 430–10.
- Roundy, Paul E, Schreck, Carl J, & Janiga, Matthew A. 2009. Contributions of Convectively Coupled Equatorial Rossby Waves and Kelvin Waves to the Real-Time Multivariate MJO Indices. *Monthly Weather Review*, **137**(1), 469 – 478.
- Ruppert, James H., & Johnson, Richard H. 2015. Diurnally Modulated Cumulus Moistening in the Preonset Stage of the Madden-Julian Oscillation during DYNAMO. *Journal of the Atmospheric Sciences*, **72**(4), 1622–1647.
- Rutan, David A., Kato, Seiji, Doelling, David R., Rose, Fred G., Nguyen, Le Trang, Caldwell, Thomas E., & Loeb, Norman G. 2015. CERES Synoptic Product: Methodology and Validation of Surface Radiant Flux. *Journal of Atmospheric and Oceanic Technology*, **32**(6), 1121–1143.
- Rydbeck, A. V., Jensen, T. G., Smith, T. A., Flatau, M. K., Janiga, M. A., Reynolds, C. A., & Ridout, J. A. 2019. Ocean Heat Content and the Intraseasonal Oscillation. *Geophysical Research Letters*, **46**(24), 14558–14566.
- Rydbeck, Adam V, Jensen, Tommy G, & Flatau, Maria K. 2021. Reciprocity in the Indian Ocean: Intraseasonal Oscillation and Ocean Planetary Waves. *Journal of Geophysical Research: Oceans*, **126**(9), e2021JC017546.
- Rydbeck, Adam V., Christophersen, Jonathan A., Flatau, Maria K., Janiga, Matthew A., Jensen, Tommy G., Reynolds, Carolyn A., Ridout, James A., Smith, Travis A., & Wijesekera, Hemantha. 2023. Anchoring Intraseasonal Air–Sea Interactions: The Moored Moist Static Energy Budget in the Indian Ocean from Reanalysis. *Journal of Climate*, **36**(3), 959–981.
- Savarin, Ajda, & Chen, Shuyi S. 2022a. Pathways to Better Prediction of the MJO: 1. Effects of Model Resolution and Moist Physics on Atmospheric Boundary Layer and Precipitation. *Journal of Advances in Modeling Earth Systems*, **14**(6), e2021MS002928.

- Savarin, Ajda, & Chen, Shuyi S. 2022b. Pathways to Better Prediction of the MJO: 2. Impacts of Atmosphere-Ocean Coupling on the Upper Ocean and MJO Propagation. *Journal of Advances in Modeling Earth Systems*, **14**(6), e2021MS002929.
- Schreck, Carl J III. 2021. Global Survey of the MJO and Extreme Precipitation. *Geophysical Research Letters*, **48**(19), e2021GL094691.
- Senior, Natasha V, Matthews, Adrian J, Webber, Benjamin GM, Webster, Stuart, Jones, Richard W, Permana, Donald S, Paski, Jaka AI, & Fadila, Riska. 2023. Extreme precipitation at Padang, Sumatra triggered by convectively coupled Kelvin waves. *Quarterly Journal of the Royal Meteorological Society*, **149**(755), 2281–2300.
- Seo, Hyodae, Subramanian, Aneesh C., Miller, Arthur J., & Cavanaugh, Nicholas R. 2014. Coupled Impacts of the Diurnal Cycle of Sea Surface Temperature on the Madden–Julian Oscillation. *Journal of Climate*, **27**(22), 8422–8443.
- Seo, Kyong Hwan, Wang, Wanqiu, Gottschalck, Jon, Zhang, Qin, Schemm, Jae Kyung E., Higgins, Wayne R., & Kumar, Arun. 2009. Evaluation of MJO forecast skill from several statistical and dynamical forecast models. *Journal of Climate*, **22**(9), 2372–2388.
- Seo, Kyong Hwan, Lee, Hyun Ju, & Frierson, Dargan M.W. 2016. Unraveling the teleconnection mechanisms that induce wintertime temperature anomalies over the northern hemisphere continents in response to the MJO. *Journal of the Atmospheric Sciences*, **73**(9), 3557–3571.
- Shelly, Ann, Xavier, Prince, Copsey, Dan, Johns, Tim, Rodríguez, José M., Milton, Sean, & Klingaman, Nicholas. 2014. Coupled versus uncoupled hindcast simulations of the Madden-Julian Oscillation in the Year of Tropical Convection. *Geophysical Research Letters*, **41**(15), 5670–5677.
- Skinner, Daniel T., Matthews, Adrian J., & Stevens, David P. 2022. North Atlantic Oscillation response to the Madden–Julian Oscillation in a coupled climate model. *Weather*, **77**(6), 201–205.
- Smith, Gregory C., Bélanger, Jean Marc, Roy, François, Pellerin, Pierre, Ritchie, Hal, Onu, Kristjan, Roch, Michel, Zadra, Ayrton, Colan, Dorina Surcel, Winter, Barbara, Fontecilla, Juan Sebastian, & Deacu, Daniel. 2018. Impact of coupling with an ice-ocean model on global medium-range NWP forecast skill. *Monthly Weather Review*, **146**(4), 1157–1180.
- Sobel, Adam, & Maloney, Eric. 2013. Moisture Modes and the Eastward Propagation of the MJO. *Journal of the Atmospheric Sciences*, **70**(1), 187–192.
- Sobel, Adam, Wang, Shuguang, & Kim, Daehyun. 2014. Moist static energy budget of the MJO during DYNAMO. *Journal of the Atmospheric Sciences*, **71**(11), 4276–4291.

- Sobel, Adam H., Maloney, Eric D., Bellon, Gilles, & Frierson, Dargan M. 2010. Surface Fluxes and Tropical Intraseasonal Variability: a Reassessment. *Journal of Advances in Modeling Earth Systems*, **2**(1).
- Sperber, Kenneth R. 2003. Propagation and the vertical structure of the Madden–Julian oscillation. *Monthly Weather Review*, **131**(12), 3018–3037.
- Stachnik, Justin P, & Chrisler, Brett. 2020. An Index Intercomparison for MJO Events and Termination. *Journal of Geophysical Research: Atmospheres*, **125**(18), e2020JD032507.
- Stan, Cristiana, Straus, David M, Frederiksen, Jorgen S, Lin, Hai, Maloney, Eric D, & Schumacher, Courtney. 2017. Review of Tropical-Extratropical Teleconnections on Intraseasonal Time Scales. *Reviews of Geophysics*, **55**(4), 902–937.
- Storkey, David, Blaker, Adam T., Mathiot, Pierre, Megann, Alex, Aksenov, Yevgeny, Blockley, Edward W., Calvert, Daley, Graham, Tim, Hewitt, Helene T., Hyder, Patrick, Kuhlbrodt, Till, Rae, Jamie G.L., & Sinha, Bablu. 2018. UK Global Ocean GO6 and GO7: A traceable hierarchy of model resolutions. *Geoscientific Model Development*, **11**(8), 3187–3213.
- Straus, David M, & Lindzen, Richard S. 2000. Planetary-Scale Baroclinic Instability and the MJO. *Journal of the Atmospheric Sciences*, **57**(21), 3609 – 3626.
- Subramanian, Aneesh, Jochum, Markus, Miller, Arthur J, Neale, Richard, Seo, Hyodae, Waliser, Duane, & Murtugudde, Raghu. 2014. The MJO and global warming: A study in CCSM4. *Climate Dynamics*, **42**, 2019–2031.
- Suematsu, Tamaki, & Miura, Hiroaki. 2022. Changes in the Eastward Movement Speed of the Madden–Julian Oscillation with Fluctuation in the Walker Circulation. *Journal of Climate*, **35**(1), 211 – 225.
- Sui, C-H., Li, X, Lau, K-M., & Adamec, D. 1997. Multiscale Air–Sea Interactions during TOGA COARE. *Monthly Weather Review*, **125**(4), 448 – 462.
- Tamasiunas, Mariana C Nieva, Shinoda, Toshiaki, Susanto, R Dwi, Zamudio, Luis, & Metzger, E Joseph. 2021. Intraseasonal variability of the Indonesian throughflow associated with the Madden-Julian Oscillation. *Deep Sea Research Part II: Topical Studies in Oceanography*, **193**, 104985.
- Thompson, Daniel B., & Roundy, Paul E. 2013. The relationship between the Madden-Julian oscillation and U.S. violent tornado outbreaks in the spring. *Monthly Weather Review*, **141**(6), 2087–2095.
- Thual, Sulian, Majda, Andrew J, & Stechmann, Samuel N. 2014. A Stochastic Skeleton Model for the MJO. *Journal of the Atmospheric Sciences*, **71**(2), 697 – 715.

- Thyng, Kristen M, Greene, Chad A, Zimmerle, Robert D, Hetland, M, Heather, & DiMarco, Steven F. 2016. True colors of oceanography: Guidelines for effective and accurate colormap selection. *Oceanography*, **29**(3), 9–13.
- Tian, Baijun, Waliser, Duane E, Fetzer, Eric J, & Yung, Yuk L. 2010. Vertical moist thermodynamic structure of the Madden–Julian oscillation in atmospheric infrared sounder retrievals: An update and a comparison to ECMWF Interim Re-Analysis. *Monthly Weather Review*, **138**(12), 4576–4582.
- Tomassini, Lorenzo, Willett, Martin, Sellar, Alistair, Lock, Adrian, Walters, David, Whittall, Michael, Sanchez, Claudio, Heming, Julian, Earnshaw, Paul, Rodriguez, José M., Ackerley, Duncan, Xavier, Prince, Franklin, Charmaine, & Senior, Catherine A. 2023. Confronting the Convective Gray Zone in the Global Configuration of the Met Office Unified Model. *Journal of Advances in Modeling Earth Systems*, **15**(5), e2022MS003418.
- Tromeur, Eric, & Rossow, William B. 2010. Interaction of tropical deep convection with the large-scale circulation in the MJO. *Journal of Climate*, **23**(7), 1837–1853.
- Tseng, Wan Ling, Tsuang, Ben Jei, Keenlyside, Noel S., Hsu, Huang Hsiung, & Tu, Chia Ying. 2015. Resolving the upper-ocean warm layer improves the simulation of the Madden–Julian oscillation. *Climate Dynamics*, **44**(5-6), 1487–1503.
- Vellinga, Michael, Copsey, Dan, Graham, Tim, Milton, Sean, & Johns, Tim. 2020. Evaluating benefits of two-way ocean–atmosphere coupling for global NWP forecasts. *Weather and Forecasting*, **35**(5), 2127–2144.
- Ventrice, Michael J., Wheeler, Matthew C., Hendon, Harry H., Schreck, Carl J., Thorncroft, Chris D., & Kiladis, George N. 2013. A modified multivariate Madden-Julian oscillation index using velocity potential. *Monthly Weather Review*, **141**(12), 4197–4210.
- Vijith, V, Vinayachandran, P N, Webber, Benjamin G M, Matthews, Adrian J, George, Jenson V, Kannaujia, Vijay Kumar, Lotliker, Aneesh A, & Amol, P. 2020. Closing the sea surface mixed layer temperature budget from in situ observations alone: Operation Advection during BoBBLE. *Scientific Reports*, **10**(1), 7062.
- Vitart, Frédéric. 2017. Madden—Julian Oscillation prediction and teleconnections in the S2S database. *Quarterly Journal of the Royal Meteorological Society*, **143**(706), 2210–2220.
- Waliser, Duane E, Jones, Charles, Schemm, Jae-Kyung E, & Graham, Nicholas E. 1999. A statistical extended-range tropical forecast model based on the slow evolution of the Madden–Julian oscillation. *Journal of Climate*, **12**(7), 1918–1939.
- Wallace, John M, & Gutzler, David S. 1981. Teleconnections in the geopotential height field during the Northern Hemisphere winter. *Monthly Weather Review*, **109**(4), 784–812.

- Walters, David, Boutle, Ian, Brooks, Malcolm, Melvin, Thomas, Stratton, Rachel, Vosper, Simon, Wells, Helen, Williams, Keith, Wood, Nigel, Allen, Thomas, Bushell, Andrew, Copsey, Dan, Earnshaw, Paul, Edwards, John, Gross, Markus, Hardiman, Steven, Harris, Chris, Heming, Julian, Klingaman, Nicholas, Levine, Richard, Manners, James, Martin, Gill, Milton, Sean, Mittermaier, Marion, Morcrette, Cyril, Riddick, Thomas, Roberts, Malcolm, Sanchez, Claudio, Selwood, Paul, Stirling, Alison, Smith, Chris, Suri, Dan, Tennant, Warren, Luigi Vidale, Pier, Wilkinson, Jonathan, Willett, Martin, Woolnough, Steve, & Xavier, Prince. 2017. The Met Office Unified Model Global Atmosphere 6.0/6.1 and JULES Global Land 6.0/6.1 configurations. *Geoscientific Model Development*, **10**(4), 1487–1520.
- Walters, David, Baran, Anthony J., Boutle, Ian, Brooks, Malcolm, Earnshaw, Paul, Edwards, John, Furtado, Kalli, Hill, Peter, Lock, Adrian, Manners, James, Morcrette, Cyril, Mulcahy, Jane, Sanchez, Claudio, Smith, Chris, Stratton, Rachel, Tennant, Warren, Tomassini, Lorenzo, Van Weverberg, Kwinten, Vosper, Simon, Willett, Martin, Browse, Jo, Bushell, Andrew, Carslaw, Kenneth, Dalvi, Mohit, Essery, Richard, Gedney, Nicola, Hardiman, Steven, Johnson, Ben, Johnson, Colin, Jones, Andy, Jones, Colin, Mann, Graham, Milton, Sean, Rumbold, Heather, Sellar, Alistair, Ujiie, Masashi, Whitall, Michael, Williams, Keith, & Zerroukat, Mohamed. 2019. The Met Office Unified Model Global Atmosphere 7.0/7.1 and JULES Global Land 7.0 configurations. *Geoscientific Model Development*, **12**(5), 1909–1963.
- Wang, Bin, & Li, Tianming. 1994. Convective interaction with boundary-layer dynamics in the development of a tropical intraseasonal system. *Journal of the Atmospheric Sciences*, **51**(11), 1386–1400.
- Wang, Bin, & Rui, H. 1990. Dynamics of the coupled moist Kelvin–Rossby wave on an equatorial b-plane. *Journal of the Atmospheric Sciences*, **47**(4), 397–413.
- Wang, Wanqiu, Hung, Meng Pai, Weaver, Scott J., Kumar, Arun, & Fu, Xiouhua. 2014. MJO prediction in the NCEP Climate Forecast System version 2. *Climate Dynamics*, **42**(9-10), 2509–2520.
- Wang, Yanxin, Heywood, Karen J., Stevens, David P., & Damerell, Gillian M. 2022. Seasonal extrema of sea surface temperature in CMIP6 models. *Ocean Science*, **18**(3), 839–855.
- Waters, Jennifer, Lea, Daniel J., Martin, Matthew J., Mirouze, Isabelle, Weaver, Anthony, & While, James. 2015. Implementing a variational data assimilation system in an operational 1/4 degree global ocean model. *Quarterly Journal of the Royal Meteorological Society*, **141**(687), 333–349.
- Webber, Benjamin G M, Matthews, Adrian J, & Heywood, Karen J. 2010. A dynamical ocean feedback mechanism for the Madden–Julian Oscillation. *Quarterly Journal of the Royal Meteorological Society*, **136**(648), 740–754.

- Webber, Benjamin G M, Stevens, David P, Matthews, Adrian J, & Heywood, Karen J. 2012a. Dynamical ocean forcing of the Madden-Julian oscillation at lead times of up to five months. *Journal of Climate*, **25**(8), 2824–2842.
- Webber, Benjamin G. M., Matthews, Adrian J., Heywood, Karen J., & Stevens, David P. 2012b. Ocean Rossby waves as a triggering mechanism for primary Madden–Julian events. *Quarterly Journal of the Royal Meteorological Society*, **138**(663), 514–527.
- Webster, Peter J, & Lukas, Roger. 1992. TOGA COARE: The coupled ocean–atmosphere response experiment. *Bulletin of the American Meteorological Society*, **73**(9), 1377–1416.
- Wei, Yuntao, Pu, Zhaoxia, & Zhang, Chidong. 2020. Diurnal Cycle of Precipitation Over the Maritime Continent Under Modulation of MJO: Perspectives From Cloud-Permitting Scale Simulations. *Journal of Geophysical Research: Atmospheres*, **125**(13), e2020JD032529.
- Weickmann, K M. 1991. El Niño/Southern Oscillation and Madden-Julian (30–60 day) oscillations during 1981–1982. *Journal of Geophysical Research: Oceans*, **96**(S01), 3187–3195.
- Wheeler, Matthew, & Weickmann, Klaus M. 2001. Real-time monitoring and prediction of modes of coherent synoptic to intraseasonal tropical variability. *Monthly Weather Review*, **129**(11), 2677–2694.
- Wheeler, Matthew C, & Hendon, Harry H. 2004. An all-season real-time multivariate MJO index: Development of an index for monitoring and prediction. *Monthly Weather Review*, **132**(8), 1917–1932.
- Woolnough, S J, Slingo, J M, & Hoskins, B J. 2000. The Relationship between Convection and Sea Surface Temperature on Intraseasonal Timescales. *Journal of Climate*, **13**(12), 2086 – 2104.
- Woolnough, S J, Slingo, J M, & Hoskins, B J. 2001. The organization of tropical convection by intraseasonal sea surface temperature anomalies. *Quarterly Journal of the Royal Meteorological Society*, **127**(573), 887–907.
- Woolnough, S. J., Vitart, F., & Balmaseda, M. A. 2007. The role of the ocean in the Madden–Julian Oscillation: Implications for MJO prediction. *Quarterly Journal of the Royal Meteorological Society*, **133**(622), 117–128.
- Xiang, Baoqiang, Zhao, Ming, Jiang, Xianan, Lin, Shian Jiann, Li, Tim, Fu, Xiouhua, & Vecchi, Gabriel. 2015. The 3- 4-week MJO prediction skill in a GFDL coupled model. *Journal of Climate*, **28**(13), 5351–5364.
- Xu, Weixin, & Rutledge, Steven A. 2014. Convective characteristics of the Madden–Julian oscillation over the central Indian Ocean observed by shipborne radar during DYNAMO. *Journal of the Atmospheric Sciences*, **71**(8), 2859–2877.

- Yadav, Priyanka, & Straus, David M. 2017. Circulation Response to Fast and Slow MJO Episodes. *Monthly Weather Review*, **145**(5), 1577 – 1596.
- Yan, Xiao Hai, Ho, Chung Ru, Zheng, Quanan, & Klemas, Vic. 1992. Temperature and size variabilities of the Western Pacific Warm Pool. *Science*, **258**(5088), 1643–1645.
- Yan, Yunwei, Zhang, Lei, Yu, Yi, Chen, Changlin, Xi, Jingyuan, & Chai, Fei. 2021. Rectification of the Intraseasonal SST Variability by the Diurnal Cycle of SST Revealed by the Global Tropical Moored Buoy Array. *Geophysical Research Letters*, **48**(1), e2020GL090913.
- Yanai, Michio, Chen, Baode, & Tung, Wen-wen. 2000. The Madden–Julian Oscillation Observed during the TOGA COARE IOP: Global View. *Journal of the Atmospheric Sciences*, **57**(15), 2374 – 2396.
- Yang, Da, & Ingersoll, Andrew P. 2014. A theory of the MJO horizontal scale. *Geophysical Research Letters*, **41**(3), 1059–1064.
- Yoneyama, Kunio, Zhang, Chidong, & Long, Charles N. 2013. Tracking pulses of the Madden–Julian oscillation. *Bulletin of the American Meteorological Society*, **94**(12), 1871–1891.
- Zhang, C., Adames, Á. F., Khouider, B., Wang, B., & Yang, D. 2020. Four Theories of the Madden-Julian Oscillation. *Reviews of Geophysics*, **58**(3), e2019RG000685.
- Zhang, Chidong. 2005. Madden–Julian oscillation. *Reviews of Geophysics*, **43**(2).
- Zhang, Chidong. 2013. Madden-Julian oscillation: Bridging weather and climate. *Bulletin of the American Meteorological Society*, **94**(12), 1849–1870.
- Zhang, Chidong, & Gottschalck, Jonathan. 2002. SST Anomalies of ENSO and the Madden–Julian Oscillation in the Equatorial Pacific. *Journal of Climate*, **15**(17), 2429 – 2445.
- Zhang, Chidong, & Ling, Jian. 2017. Barrier effect of the Indo-Pacific Maritime Continent on the MJO: Perspectives from tracking MJO precipitation. *Journal of Climate*, **30**(9), 3439–3459.
- Zhu, Jieshun, Wang, Wanqiu, & Kumar, Arun. 2017. Simulations of MJO propagation across the Maritime Continent: Impacts of SST feedback. *Journal of Climate*, **30**(5), 1689–1704.